2007

Electrochemical behavior of aluminized steel type 2 in scale-forming waters

Leonardo Caseres
University of South Florida

Electrochemical Behavior of Aluminized Steel Type 2 in Scale-Forming Waters

by

Leonardo Caseres

A dissertation submitted in partial fulfillment
of the requirements for the degree of
Doctor of Philosophy
Department of Civil and Environmental Engineering
College of Engineering
University of South Florida

Major Professor: Alberto Sagüés, Ph.D.
Stanley Kranc, Ph.D.
Rajan Sen, Ph.D.
Noreen Poor, Ph.D.
John Wolan, Ph.D.

Date of Approval:
June 26, 2007

Keywords: cathodic behavior, modeling, EIS, galvanic corrosion, durability

Dedication

I would like to dedicate this dissertation to my lovely wife, Clara, that without her support and patient this completion would not have happened. Also, the dedication is extended to my little precious son, Maximo, for being the light of my life.

Acknowledgments

First of all, I would like to express my sincere appreciation to Dr. Alberto A. Sagüés for his guidance, encouragement, and criticism throughout my studies. His detailed scientific approach to conduct research will have, without doubt, a positive impact on my future career.

I am also very grateful to Dr. Stanley C. Kranc, Dr. Rajan Sen, Dr. Noreen Poor, and Dr. John Wolan for serving in the committee, and Dr. Scott Campbell for being the committee chairperson. Many thanks to Mr. Rodney Powers and Ivan Lassa of the Florida Department of Transportation Materials Corrosion Laboratory for providing valuable contributions to this project. I would also like to thanks to Dr. N. Birbilis of the Ohio State University for providing alloy samples and Contech Construction Products Inc. for providing the test material.

Thanks to my colleagues of the Corrosion Engineering Laboratory, in special to Mersedeh Akhoondan for her help in conducting laboratory work, Dr. Luciano Taveira, Kingsley Lau, Margareth Dugarte, Cristiane Cotrim, and Jaime Lopez Sabando for their help in the past few years. Thanks also to the undergraduate students Mr. Adam Verdon and Edward Lopez, and the staff members of the Civil and Environmental Engineering Department, the Computing and Engineering Shops.

I gratefully acknowledge the support from the Florida Department of Transportation and the Federal Highway Administration in funding this research. The opinions, findings, and conclusions expressed here are those of the author and not necessarily those of the supporting agency.

Table of Contents

List of Tables iv

List of Figures viii

Abstract xviii

Chapter 1 Introduction 1
1.1 Background on Metal Culvert Pipe Durability 1
1.1.1 The California Method 2
1.1.2 The American Iron and Steel Institute (AISI) Method 4
1.1.3 The Florida Department of Transportation (FDOT) Method 5
1.1.4 The AK Steel Method 5
1.2 Corrosion Resistance of Aluminized Steel Type 2 7
1.2.1 Manufacture and Surface Morphology 7
1.2.2 Overview of Aluminum Corrosion 8
1.2.2.1 Pitting Corrosion of Aluminum 10
1.2.3 Field Studies on the Durability of Aluminized Steel Type 2 13
1.2.4 Galvanic Corrosion of Aluminized Steel Type 2 17
1.3 Objectives of this Investigation 22
1.4 Approach 23
1.5 Significance of Research 25
1.6 Overview 26

Chapter 2 Corrosion of As-Rolled Aluminized Steel Type 2 in Scale-Forming Waters 31
2.1 Introduction 31
2.2 Experimental Procedure 32
2.3 Results 36
2.3.1 E_{OC} Trends and Direct Observations of Corrosion 36
2.3.2 Solution Composition 38
2.3.3 Impedance Behavior 39
2.4 Discussion 41
2.4.1 Direct Evidence of Corrosion Performance 41
2.4.2 Corrosion Mechanisms and Analysis of the Impedance Response 42
2.4.2.1 Solution P and Solution NP before Surface Discoloration 46
2.4.2.2 Solutions C, SW, and Solution NP after Surface Discoloration 51

2.4.3 Computation of the Nominal Corrosion Current Density 58
2.5 Implication of the Results 60
2.6 Conclusions 66

Chapter 3 Special Issues in the Cathodic Behavior of Aluminized Steel Type 2 in Scale-Forming Waters 83
3.1 Introduction 83
3.2 Experimental Procedure 85
3.3 Results 87
3.3.1 Microstructure Analysis 88
3.3.2 Solution Composition 88
3.3.3 E_{OC} and CYP Trends 89
3.4 Discussion 91
3.5 Conclusions 99

Chapter 4 Galvanic Behavior on the Corrosion Resistance of Aluminized Steel Type 2 106
4.1 Introduction 106
4.2 Experimental Procedure 107
4.3 Results 112
4.3.1 Solution Compositions 112
4.3.2 Blemished Specimens 113
4.3.2.1 E_{OC} Trends 113
4.3.2.2 Direct Observations of Corrosion 115
4.3.2.2.1 The Aluminized Coating 115
4.3.2.2.2 The Exposed Steel 118
4.3.2.3 Impedance Behavior 120
4.3.2.3.1 LCB Specimens 120
4.3.2.3.2 SCB Specimens 121
4.3.3 Macrocell Assemblies 123
4.3.3.1 E_{OC} and Macrocell Current Trends 123
4.3.3.2 Impedance Behavior 123
4.3.4 Uncoupled Steel Specimens 124
4.3.5 Coating Thickness Measurements 125
4.4 Discussion 126
4.4.1 E_{OC} Trends and Corrosion Mechanisms 126
4.4.1.1 Solution P 127
4.4.1.2 Solution NP 130
4.4.1.3 Solution C 132
4.4.1.4 Solution SW 133
4.4.2 Galvanic Macrocells 134
4.4.3 Correlation between A_R and Time to Initial Discoloration 136
4.4.4 Interpretation of the Impedance Response 137
4.4.4.1 Macrocell Assemblies 137
4.4.4.2 Blemished Specimens 138
4.4.5 Computation of the Nominal Corrosion Current Density 140

4.5 Implication of the Results 143
4.6 Conclusions 149

Chapter 5 Computation of *ac* and *dc* Current and Potential Distributions of Aluminized Steel Type 2 with Coating Breaks 187
5.1 Introduction 187
5.2 The Model System 189
5.2.1 The *dc* Model 189
5.2.1.1 Implementation of the *dc* Model 194
5.2.1.2 Cases Studied 197
5.2.2 The *ac* Model 198
5.2.2.1 Implementation of the *ac* Model 200
5.3 Results and Discussion 201
5.3.1 The *dc* Model 201
5.3.2 The *ac* Model 206
5.4 Conclusions 207

Chapter 6 Conclusions 216

References 222

Appendices 232
Appendix A: Results from Replicate Unblemished Specimens 233
Appendix B: Replicate Results of the Blemished Specimens 239
Appendix C: Interpretation of the Two-Step Reaction Mechanism 254

About the Author End Page

List of Tables

Table 2.1:	Chemical composition of steel substrate (% weight).	70
Table 2.2:	Synthetic solution compositions and properties.	70
Table 2.3:	Chemical composition of the simulated ocean water reported by the manufacturer.	70
Table 2.4:	Values of the equivalent circuit components in Figure 2.16 estimated from EIS data fit for the specimen #1 exposed to solution P.	70
Table 2.5:	Values of the equivalent circuit components in Figure 2.16 estimated from EIS data fit for the specimen #1 exposed to solution NP.	71
Table 2.6:	Values of the equivalent circuit components in Figure 2.16 estimated from EIS data fit for the specimen #1 exposed to solution SW.	71
Table 2.7:	Values of the equivalent circuit components in Figure 2.16 estimated from EIS data fit for the specimen #1 exposed to solution C.	71
Table 2.8:	Comparison of durability estimates, in yr, obtained by the application of selected forecasting methods and those obtained in this Chapter.	72
Table 3.1:	Parameters chosen for cyclical polarization modeling.	101
Table 4.1:	Average thickness measurements, per magnetic coating thickness test, and the corresponding nominal corrosion rate estimates for selected specimens.	153
Table 4.2:	Summary of visual assessment and E_{OC} trends.	154

Table 4.3: Evolution of the nominal corrosion current density for the LCB specimens #1 exposed to solutions NP, P, and SW. The parameters of the simplified analog equivalent circuits shown in Figure 4.41 are also included. Immune condition for the exposed steel was assumed when the system E_{OC} reached <-800 mV. Passive condition for the outer aluminized coating was assumed when the aluminized surface was bright with no visible pits. 155

Table 4.4: Evolution of the nominal corrosion current density for the SCB specimens #1 exposed to solutions NP, P, SW, and C. The parameters of the simplified analog equivalent circuits shown in Figure 4.41 are also included. Immune condition for the exposed steel was assumed when the system E_{OC} reached <-800 mV. Passive condition for the outer aluminized coating was assumed when the aluminized surface was bright with no visible pits. 156

Table 4.5: EIS parameters from analog equivalent circuit in Figure 4.40 and nominal corrosion current density for the aluminized and steel components in the macrocell assemblies. 158

Table 4.6: Comparison of durability estimates, in yr, obtained by application of commonly used forecasting methods and those obtained in this investigation. 159

Table 5.1: Computation parameters used for the *dc* model for all σ evaluated. 209

Table 5.2: Computation parameters used for the *ac* model for the base case. 209

Table A.1: Values of the equivalent circuit components in Figure 2.16 estimated from EIS data fit for the unblemished specimen #2 exposed to solution P. 237

Table A.2: Values of the equivalent circuit components in Figure 2.16 estimated from EIS data fit for the unblemished specimen #2 exposed to solution SW. 237

Table A.3: Values of the equivalent circuit components estimated from EIS data fit for the unblemished specimen #2 exposed to solution NP. 237

Table A.4: Values of the equivalent circuit components in Figure 2.16 estimated from EIS data fit for the unblemished specimen #2 exposed to solution C. 238

Table B.1: Evolution of the nominal corrosion current density of the steel and aluminized portions for the replicate LCB specimens exposed to solution P. The parameters of the simplified equivalent circuits shown in Figure 4.41 are also included. Immune condition for the exposed steel was assumed when the system E_{OC} reached <-800 mV. Passive condition for the outer aluminized coating was assumed when the aluminized surface was bright with no visible pits. 243

Table B.2: Evolution of the nominal corrosion current density of the steel and aluminized portions for the replicate LCB specimens exposed to solution NP. The parameters of the simplified equivalent circuits shown in Figure 4.41 are also included. Immune condition for the exposed steel was assumed when the system E_{OC} reached <-800 mV. Passive condition for the outer aluminized coating was assumed when the aluminized surface was bright with no visible pits. 244

Table B.3: Evolution of the nominal corrosion current density of the aluminized portion for the replicate LCB specimens exposed to solution SW. The parameters of the simplified equivalent circuits shown in Figure 4.41 are also included. Immune condition for the exposed steel was assumed when the system E_{OC} reached <-800 mV. 245

Table B.4: Evolution of the nominal corrosion current density of the aluminized portion for the replicate SCB specimens exposed to solution NP. The parameters of the simplified equivalent circuits shown in Figure 4.41 are also included. Immune condition for the exposed steel was assumed when the system E_{OC} reached <-800 mV. 250

Table B.5: Evolution of the nominal corrosion current density of the aluminized portion for the replicate SCB specimens exposed to solution P. The parameters of the simplified equivalent circuits shown in Figure 4.41 are also included. Immune condition for the exposed steel was assumed when the system E_{OC} reached <-800 mV. 250

Table B.6: Evolution of the nominal corrosion current density of the aluminized portion for the replicate SCB specimens exposed to solution SW. The parameters of the simplified equivalent circuits shown in Figure 4.41 are also included. Immune condition for the exposed steel was assumed when the system E_{OC} reached <-800 mV. 251

Table B.7: Evolution of the nominal corrosion current density of the aluminized portion for the replicate SCB specimens exposed to solution C. The parameters of the simplified equivalent circuits shown in Figure 4.41 are also included. Immune condition for the exposed steel was assumed when the system E_{OC} reached <-800 mV. 251

List of Figures

Figure 1.1: Refined California method chart for estimating years to perforation of 18-gage galvanized culvert pipe (California Test 643, 1999). 28

Figure 1.2: The AISI method chart for estimating years to perforation of galvanized steel pipes of 18-gage culvert pipe. Computing service life is the same as in the refined California method (Handbook of Steel Drainage & Highway Construction Products, American Iron and Steel Institute, 1994). 29

Figure 1.3: The FDOT chart for estimation years to perforation of 16-gage aluminized steel Type 2 culvert pipes (solid lines) (Cerlanek and Powers, 1993). Dashed lines correspond to service life estimation using the refined California method for galvanized steel. 29

Figure 1.4: The AK Steel method chart for estimating service life of 14-gage galvanized and aluminized steel Type 2 culvert pipes (Bednar, 1989). 30

Figure 1.5: Schematic of the typical manufacturing process of aluminized steel Type 2 (source: www.aksteel.com). 30

Figure 2.1: Cross section perpendicular to rolling direction of a 16-gage (~1.59 mm) thickness flat aluminized steel Type 2 after etching with 2% Nital solution showing the outer and inner coating layers on base steel. Light features in the outer coating are Fe-rich inclusions per SEM-EDS analysis. 72

Figure 2.2: SEM line scan conducted on the cross section of aluminized steel Type 2 (perpendicular to rolling direction) showing the main constituents in the dual coating layer and the base steel. 73

Figure 2.3: Schematic of the test cell arrangement. 73

Figure 2.4: Photograph of the test cell. 74

Figure 2.5: E_{OC} evolution of replicate specimens in solution C. End of exposure corresponds to the last datum. 74

Figure 2.6: E_{OC} evolution of replicate specimens in solution NP. End of exposure corresponds to the last datum. 75

Figure 2.7: E_{OC} evolution of replicate specimens in solution P. Arrows indicate two $CaCO_3$ additions to #1 and #2. End of exposure corresponds to the last datum. 75

Figure 2.8: E_{OC} evolution of replicate specimens exposed to solution SW. End of exposure corresponds to the last datum. 76

Figure 2.9: Evolution of the solution bulk pH with exposure time. 76

Figure 2.10: Typical EIS plot of the high-frequency limit for NP, P, and SW. 77

Figure 2.11: EIS behavior of the specimen #1 in solution NP (100 KHz - 1 mHz - 5 points/decade unless indicated otherwise). 77

Figure 2.12: EIS behavior of the specimen #1 in solution P (100 KHz - 1 mHz - 5 points/decade). 78

Figure 2.13: EIS behavior of the specimen #3 in solution P (100 KHz - 1 mHz - 5 points/decade). 78

Figure 2.14: EIS behavior of the specimen #1 in solution SW (100 KHz - 1 mHz - 5 points/decade). 79

Figure 2.15: EIS behavior of the specimen #1 in solution C (100 KHz - 1 mHz - 5 points/decade unless indicated otherwise). 79

Figure 2.16: Analog equivalent circuit used to simulate the EIS responses. 80

Figure 2.17: Evolution of the admittance parameter as a function of time for the specimens #1 in solutions NP (circles), P (squares), C (triangles), and SW (diamonds) (--- Y_F, — Y_{AL2}). Arrows indicate $CaCO_3$ additions to solution P (#1). 80

Figure 2.18: Evolution of the resistive components as a function of exposure time for the specimens #1 in solutions NP (circles), P (squares), C (triangles), and SW (diamonds) (--- R_{AL1}, — R_{AL2}). Arrows indicate $CaCO_3$ additions to solution P (#1). 81

Figure 2.19: Mott-Schottky plot of the oxide film capacitance recorded for NP and P systems (specimens #3 and #4) at ~330 hr of exposure. C_F^{-2} values obtained by EIS at E_{OC} of the duplicate specimens #1 and #2 at comparable exposure age are plotted as well (specimen # is denoted in parenthesis). 81

Figure 2.20: Nominal corrosion current density evolution for the specimens #1 in all media. No extra powdered $CaCO_3$ was added to the triplicate specimen in solution P (#3). 82

Figure 3.1: SEM images of the unexposed FG (left) and AR (right) surface conditions. Light features correspond to Fe-rich inclusions. 101

Figure 3.2: E_{OC} evolution of the AR and FG surface conditions. Specimen number is denoted in parenthesis. 101

Figure 3.3: Cyclical cathodic polarization of the AR and FG surface conditions in unstirred naturally aerated solution at 408 hr of exposure. Return scan current was always greater than for the forward scan as exemplified by arrows. 102

Figure 3.4: Cyclical cathodic polarization of the FeAl and Al1100 alloys in unstirred naturally aerated solution at 408 hr of exposure. Return scan current was always greater than for the forward scan as exemplified by arrows. 103

Figure 3.5: Cyclical cathodic polarization of the AR and FG surface conditions in unstirred deaerated solution after 650 hr of exposure. 104

Figure 3.6: Cyclical cathodic polarization of the FeAl and Al1100 alloys in unstirred deaerated solution after 650 hr of exposure. 105

Figure 3.7: Model results for the AR surface condition in the aerated solution. 105

Figure 4.1: Photograph of the test cell used to monitor galvanic currents and impedance behavior of the unblemished aluminized steel and steel components. 159

Figure 4.2: Schematic of the test cell arrangement. 160

Figure 4.3: Evolution of the solution bulk pH for the LCB configuration. 160

Figure 4.4: Evolution of the solution bulk pH for the SCB configuration. 161

Figure 4.5: E_{OC} evolution of the LCB specimens in solution P. End of exposure corresponds to the time of the last datum taken. 161

Figure 4.6: E_{OC} evolution of the LCB specimens in solution NP. End of exposure corresponds to the time of the last datum taken. 162

Figure 4.7: E_{OC} evolution of the LCB specimens in solution SW. End of exposure corresponds to the time of the last datum taken. 162

Figure 4.8: E_{OC} evolution of the SCB specimens in solution P. The test exposures were terminated ~450 hr after the last datum. 163

Figure 4.9: E_{OC} evolution as a function of time of the SCB specimens exposed to solution NP. End of exposure corresponds to the time of the last datum. 163

Figure 4.10: E_{OC} evolution as a function of time of the SCB specimens exposed to solution SW. End of exposure corresponds to the time of the last datum. 164

Figure 4.11: E_{OC} evolution as a function of time of the SCB specimens exposed to solution C. End of exposure corresponds to the time of the last datum. 164

Figure 4.12: E_{OC} evolution as a function of time of the replicate uncoupled steel specimens. End of exposure corresponds to the time of the last datum. 165

Figure 4.13: Cross section of the LCB specimen #1 exposed to solution NP showing complete outer coating loss surrounding the exposed steel. 165

Figure 4.14: SEM image: (1) 1000x magnification and (2) 5000x magnification of the surface morphology of the LCB specimen #1 in solution NP taken after the end of exposure. 166

Figure 4.15: SEM-EDS analysis of corrosion deposits on the aluminized surface of the LCB specimen #1 in solution NP. 167

Figure 4.16: Cross section of the LCB specimen #1 exposed to solution SW near the edge of the exposed steel. 168

Figure 4.17: Cross section of the SCB specimen #1 exposed to solution C showing that a pit ~0.5 mm diameter that reached the underlying steel. 168

Figure 4.18: Cross section of the SCB specimen #1 exposed to solution NP showing complete outer coating loss surrounding the exposed steel. 169

Figure 4.19: Cross section of the SCB specimen #1 exposed to solution SW near the exposed steel region. 169

Figure 4.20: Cross section of the LCB specimen #1 exposed to solution NP showing additional metal loss at the central region of the exposed steel. 170

Figure 4.21: Post-exposure photographs of selected blemished specimens. 171

Figure 4.22: Nyquist plot of the impedance response of the LCB specimen #1 in solution NP (100 KHz - 1 mHz - 5 points/decade). 172

Figure 4.23: Nyquist plot of the impedance response of the LCB specimen #1 in solution P (100 KHz - 1 mHz - 5 points/decade). 172

Figure 4.24: Nyquist plot of the impedance response of the LCB specimen #1 in solution SW (100 KHz - 1 mHz - 5 points/decade). 173

Figure 4.25: Nyquist plot of the impedance response of the SCB specimen #1 in solution NP (100 KHz - 1 mHz - 5 points/decade). 173

Figure 4.26: Nyquist plot of the impedance response of the SCB specimen #1 in solution P (100 KHz - 1 mHz - 5 points/decade). 174

Figure 4.27: Nyquist plot of the impedance response of the SCB specimen #1 in solution SW (100 KHz - 1 mHz - 5 points/decade). 174

Figure 4.28: Nyquist plot of the impedance response of the SCB specimen #1 in solution C (100 KHz - 1 mHz - 5 points/decade). 175

Figure 4.29: Nyquist plot of the impedance response of the SCB specimen #2 in solution C (100 KHz-1 mHz - 5 points/decade). 176

Figure 4.30: E_{OC} and galvanic current I_{galv} measurements for the macrocell assemblies exposed to solutions P (circles) and NP (squares). The steel components were always net cathodes. 176

Figure 4.31: Nyquist plot of the impedance response of the macrocell assembly and the individual components exposed to solution P (100 kHz–1 mHz, 5 points/decade) before (~900 hr) the E_{OC} drop. 177

Figure 4.32: Nyquist plot of the impedance response of the macrocell assembly and the individual components exposed to solution P (100 kHz–1 mHz, 5 points/decade) after (~1,780 hr) the E_{OC} drop. 177

Figure 4.33: Nyquist plot of the impedance response of the macrocell assembly and the individual components exposed to solution NP (100 kHz–1 mHz, 5 points/decade) before (~900 hr) the E_{OC} drop. 178

Figure 4.34: Nyquist plot of the impedance response of the macrocell assembly and the individual components exposed to solution NP (100 kHz–1 mHz, 5 points/decade) after (~1,780 hr) the E_{OC} drop. 179

Figure 4.35: Nyquist plot of the impedance response of the replicate uncoupled steel specimens exposed to solutions NP and P (100 kHz–1 mHz, 5 points/decade). 179

Figure 4.36: Schematic of a typical aluminized coating cross section of a LCB specimen #1 exposed to solution NP. 180

Figure 4.37: Schematic of the E_{OC} trends shown in Figures 4.5 through 4.11. 180

Figure 4.38: Schematic description of the corrosion mechanism of aluminized steel around the Fe-rich inclusion present in the outer aluminized layer: (A) development of high pH region around the inclusion due to the cathodic reaction, (B) corrosion initiation of the surrounding aluminum exposing larger inclusion area with consequent enhancement of the cathodic reaction, (C) detachment of the inclusion as a free particle from the aluminum matrix, (D) dissolution of the free particle and plating of Fe on aluminized surface, (E) development of a high pH region around the plated Fe. 181

Figure 4.39: Average of the time to initial discoloration of replicate specimens as a function of A_R. Results for A_R=0 and A_R=3 10^{-4} in solution P are minimum values as indicated by the arrows. 182

Figure 4.40: Analog equivalent circuit used to simulate the impedance response of the macrocell assemblies in solutions NP and P for the regimes before and after the E_{OC} drop. 182

Figure 4.41: Simplified equivalent circuit used to simulate the impedance response of the LCB and SCB specimens. The circuit (A) was employed solely for the LCB specimens exposed to solutions NP and P before the E_{OC} drop. The circuit (B) was used for all solutions after the E_{OC} drop. 183

Figure 4.42: Evolution of i_{corrFE} of the exposed steel portion for the LCB specimens (#1) in solutions NP and P obtained per analog equivalent circuit shown in Figure 4.41 (A) and the steel component in the macrocell assemblies obtained per the upper branch of the analog equivalent circuit in Figure 4.40. 183

Figure 4.43: Evolution of i_{corrAL} of the aluminized portion for the LCB specimens (#1) obtained using the analog equivalent circuit shown in Figure 4.41 (B) and the aluminized component in the macrocell assemblies using the lower branch of the analog equivalent circuit shown in Figure 4.40. 184

Figure 4.44: Evolution of i_{corrAL} of the aluminized portion for the SCB specimens (#1) obtained using the analog equivalent circuit shown in Figure 4.41 (B). 184

Figure 4.45: Correlation between the integrated coating loss obtained by EIS and the nominal coating thickness loss determined by magnetic coating thickness measurements for selected specimens shown in Table 4.1. 185

Figure 4.46: Cross section of the LCB specimen #1 exposed to solution NP. The dark outer layer covering the entire outer aluminized coating layer corresponds to corrosion deposits of ~10-15 μm thick. 186

Figure 5.1: Schematic of half portion of the LCB specimen (of dimensions r_0 = 1 cm, r_e = 5 cm, and H = 6.5 cm) and the two-dimensional cylindrical graded network used for the model implementation ($\Delta r = \Delta z$ = 0.1 cm). 210

Figure 5.2: Change of the total anodic and cathodic currents I_a and I_C respectively, with the number of iterations showing convergence of the *dc* model. The calculations are for the case 1 (200 μS/cm), starting potential values = -717 mV, relaxation factor α = 0.6, and O_2 concentration = 3 10^{-7} mol/cm^3. 211

Figure 5.3: Representation of the *ac* model implementation to the LCB specimen configuration. 212

Figure 5.4: Anodic current density distribution as a function of radius (— base case (2,000 μS/cm), ---- case 1 (200 μS/cm), ···· case 2 (10 μS/cm)). Bold and light lines correspond to the period before and after the E_{OC} drop, respectively. 213

Figure 5.5: Cathodic current density distribution as a function of radius (— base case (2,000 μS/cm), ---- case 1 (200 μS/cm), ···· case 2 (10 μS/cm)). Bold and light lines correspond to the period before and after the E_{OC} drop, respectively. 213

Figure 5.6: Potential distribution next to the metal surface as a function of radius. (— base case (2,000 μS/cm), ---- case 1 (200 μS/cm), ···· case 2 (10 μS/cm)). Bold and light lines correspond to the period before and after the E_{OC} drop, respectively. 214

Figure 5.7: Computed macrocell currents I_{galv} as a function of σ for the first scenario (squares), before E_{OC} drop, and the second scenario (circles), after E_{OC} drop. 214

Figure 5.8: Calculated impedance shown as Nyquist diagrams for the base case for the three reference electrode positions measured from the center of the exposed steel surface (test frequency range: 10^5 to 10^{-3} Hz and 5 points per decade). Curve (A) was obtained by assuming that all surface elements in the network are subject to a uniform *ac* potential. 215

Figure A.1: EIS behavior of the unblemished specimen #2 in solution NP (100 KHz - 1 mHz - 5 points/decade unless indicated otherwise). 233

Figure A.2: EIS behavior of the unblemished specimen #2 in solution P (100 KHz - 1 mHz - 5 points/decade). 233

Figure A.3: EIS behavior of the unblemished specimen #2 in solution SW (100 KHz - 1 mHz - 5 points/decade). 234

Figure A.4: EIS behavior of the unblemished specimen #2 in solution C (100 KHz - 1 mHz - 5 points/decade unless indicated otherwise). 234

Figure A.5: Evolution of the admittance parameter as a function of time for the unblemished specimens #2 in solutions NP (circles), P (squares), C (triangles), and SW (diamonds) (--- Y_F, — Y_{AL2}). Arrows indicate $CaCO_3$ additions to solution P (#2). 235

Figure A.6: Evolution of the resistive components as a function of exposure time for the unblemished specimens #2 in solutions NP (circles), P (squares), C (triangles), and SW (diamonds) (--- R_{AL1}, — R_{AL2}). Arrows indicate $CaCO_3$ additions to solution P (#2). 235

Figure A.7: Nominal corrosion current density evolution for the unblemished specimens #2. 236

Figure B.1: Nyquist plot of the EIS response of the LCB specimen #2 in solution NP (100 KHz - 1 mHz - 5 points/decade). 239

Figure B.2: Nyquist plot of the EIS response of the LCB specimen #3 in solution NP (100 KHz - 1 mHz - 5 points/decade). 240

Figure B.3: Nyquist plot of the EIS response of the LCB specimen #2 in solution P (100 KHz - 1 mHz - 5 points/decade). 241

Figure B.4: Nyquist plot of the EIS response of the LCB specimen #3 in solution P (100 KHz - 1 mHz - 5 points/decade). 242

Figure B.5: Nyquist plot of the EIS response of the LCB specimen #2 in solution SW (100 KHz - 1 mHz - 5 points/decade). 242

Figure B.6: Nyquist plot of the EIS response of the SCB specimen #2 in solution NP (100 KHz - 1 mHz - 5 points/decade). 246

Figure B.7: Nyquist plot of the EIS response of the SCB specimen #2 in solution P (100 KHz - 1 mHz - 5 points/decade). 247

Figure B.8: Nyquist plot of the EIS response of the SCB specimen #2 in solution SW (100 KHz - 1 mHz - 5 points/decade). 248

Figure B.9: Nyquist plot of the EIS response of the SCB specimen #3 in solution C (100 KHz-1 mHz - 5 points/decade). 249

Figure B.10: Evolution of i_{corrAL} of the aluminized portion for the replicate LCB and macrocell assemblies. 252

Figure B.11: Evolution of i_{corrAL} of the aluminized portion for the replicate SCB specimens. 252

Figure B.12: Evolution of i_{corrFE} of the exposed steel portion for the replicate LCB specimens in solutions NP and P obtained per equivalent circuit shown in Figure 4.41-A. 253

Electrochemical Behavior of Aluminized Steel Type 2 in Scale-Forming Waters

Leonardo Caseres

ABSTRACT

Aluminized steel Type 2 (AST2), often used for culvert pipes, is subject to corrosion which is the most important durability limitation factor. It was desired to determine if the outer aluminized layer will retain passivity and if protective galvanic action will develop. Thus, corrosion of unblemished and blemished AST2 surfaces was investigated in simulated natural waters.

Experiments with unblemished specimens showed passive corrosion rates (~0.06 μm/yr) in scale-forming, 0.01 M Cl^- solutions but sustained corrosion in other less protective media (with rates 3~10 μm/yr). Corrosion was manifested macroscopically by discoloration and few macro pits, but it likely proceeded also microscopically at the Fe-rich inclusion space scale. For blemished specimens, the aluminized coating galvanically protected to some extent the steel in all solutions. However, in 0.01 M Cl^- solutions, protection was delayed until after some steel corrosion had occurred. In some solutions, complete consumption of the outer aluminized coating around exposed steel was noted. Elsewhere, coating appearance was similar to that of the unblemished condition. Nominal durability projections made for 16-gage AST2 ranged from >100 yr for unblemished AST2 to ~10 yr for the blemished condition. The present findings

were used as a first step in proposing refinements of presently used durability guidelines of AST2 culvert pipe.

Cyclic cathodic polarization tests to examine O_2 and H_2 reduction at the Fe-rich inclusions showed significant hysteresis, more pronounced with decreasing scan rate. The effect was tentatively associated to the amount of Fe^{+2} being deposited during the downward scan, a hypothesis supported by results from a physical model.

A static polarization model was formulated for the blemished configuration. Results matched experimental trends and permitted evaluating the effect of solution conductivity σ beyond the experimental range. Exposed steel corrosion rates at the steel were increasingly large for decreasing σ. For the lowest σ, corrosion rates at the exposed steel center were distinctly larger than at the edge, consistent with experiments. An impedance behavior model was also formulated. Results showed frequency dependent current distribution and predicted relatively small artifacts that were and not evident experimentally, but should be considered when exploring other system conditions.

Chapter 1

Introduction

1.1 Background on Metal Culvert Pipe Durability

The durability of metallic drainage pipes plays a crucial role in the economics of highway structures. An optimum service life design for drainage pipes and other metallic components can prevent unexpected costly repairs or structure replacement. For instance, the Florida Department of Transportation (FDOT) has an extensive inventory of metallic components in direct contact with soils and waters. The metallic components include metallic culvert pipes made of clad aluminum alloy, galvanized steel, and the increasingly popular aluminized steel, in the form of aluminized steel Type 2. In addition, structural steel piling (both steel shapes and pipes), galvanized tie strips in mechanically stabilized earth walls, and buried metals are also been utilized in a variety of engineering applications. However, corrosion is the most important durability limitation factor in these components, which must operate for long design service lives (e.g. 75 yr and beyond) (Cerlanek and Powers, 1993). Therefore, it is of necessity to have in place reliable means of predicting corrosion rates so that materials selections commensurate with the desired design service lives can be made.

In actual metal forming and subsequent field application practice, galvanized steel and aluminized steel Type 2 components are liable to surface

distress that may range from minor to severe, exposing a certain amount of base steel. At present, all service life forecasting methods do not have provision for consideration of the effect of substantial localized galvanized/aluminized coating damage on the service life of these components. Such consideration would need to involve assessing the aluminized steel corrosion performance, in particular the extent of galvanic protection to the base steel, critically needed for improved forecast analysis.

This Chapter presents a description of the relevant service life predictive methods (e.g. California, AISI, FDOT, and AK Steel methods) currently in practice and areas of needed improvement are noted with emphasis on drainage aluminized steel Type 2 pipe durability exposed to environments similar to those found in Florida. Where possible, examples of the methods are given on the basis of field testing locations in this study. In addition, a literature review on the corrosion of aluminum (main component of the outer aluminized coating), the fabrication process of aluminized steel Type 2, and past studies on the corrosion of aluminized steel Type 2 are presented.

1.1.1 The California Method

The California method was developed by the California Department of Transportation (CALTRANS) in the 1950's to assess pipe durability based on the examination of ~7,000 galvanized culvert pipes (Beaton and Stratfull, 1962). A graphical analysis of the environmental parameters gathered versus pipe condition allowed to obtain the most significant parameters affecting the pipe

service life. The service life prediction method has been further refined over the years as a standardized procedure (California Test 643, 1999), which contains detailed information regarding the parameter measuring procedures as well as the use of those parameters to forecast service life of galvanized culvert pipes. The refined California method uses pH together with the minimum resistivity of both soilside and waterside (interior of a pipe) and metal gauge thickness, as key input parameters to forecast durability of galvanized steel pipe as shown in Figure 1.1.

In this refined California method, pipe durability is defined based on the number of years to first penetration of a maintenance-free corrugated metallic component. Per the latest documentation examined for this dissertation (California Test 643, 1999), the refined California method was initially intended for service life predictions of galvanized steel pipes not including provisions for aluminized steel Type 2 service life forecast. The refined method establishes that low pH and minimum resistivity values result in short service life forecasts. However, surface water may have a relatively low pH and still not be very aggressive because other dissolved species (e.g. Ca^{+2}, Mg^{+2}, CO_3^{-2}), not considered in the refined method, may precipitate a protective scale (hard waters) on the metal surface which tends to greatly decrease its corrosion rate. Conversely, high pH by itself may not guarantee extended service life if the water does not promote the formation of the protective scale (soft waters).

Substantial experimental evidence (Cerlanek and Powers, 1993 and Bednar, 1989) suggests that the refined California method yields highly

conservative predictions in hard waters and liberal results in soft non-scaling waters. Similar limitations exist for the unqualified application of resistivity, which as a parameter cannot differentiate between the presence of beneficial or of detrimental ions in the medium.

1.1.2 The American Iron and Steel Institute (AISI) Method

The American Iron and Steel Institute (AISI) developed a method, derived from the refined California method, for predicting the service life of corrugated galvanized steel culvert pipes (Handbook of Steel Drainage & Highway Construction Products, American Iron and Steel Institute, 1994). The AISI method uses pH and minimum resistivity values as in the refined California method for service life forecast as shown in Figure 1.2. Contrarily to the refined California method, the AISI method does not consider that small perforations significantly degrade pipe performance, since the consequences of those perforations are deemed to be minimal in a gravity flow pipe such as most storm sewers and culverts installed in nonerodible granular bedding. In reality, the AISI method establishes a 25% total metal loss as the practical limit for estimation of galvanized steel pipe durability, yielding service lives that are approximately twice as much as to those obtained by the refined California method. The AISI method initially applied to galvanized steel and later to aluminized steel Type 2 showed reasonably conservative predictions as reported by the Georgia Department of Transportation (Southeastern Corrugated Steel Pipe Association, 1977).

1.1.3 The Florida Department of Transportation (FDOT) Method

In the need of improving service life guidelines for highway drainage culverts, the FDOT Materials Laboratory undertook a five-year investigation to assess drainage metallic culvert performance in various environmental conditions in Florida. The field study completed in 1993 revealed that aluminized steel Type 2 outperformed galvanized steel by a factor of 2.9 when using the refined California method for predicting service life of galvanized steel culverts (Cerlanek and Powers, 1993). As a result, the FDOT introduced a durability prediction method—currently in use in Florida—derived from the refined California method for aluminized steel Type 2-coated corrugated steel that takes into account the factor of 2.9 over the refined California method in environments with pH between 5.0 and 9.0 and minimum resistivities larger than 1,000 Ω-cm as indicated by the shift in service life estimation (solid lines in Figure 1.3). For instance, in a neutral pH medium with a minimum resistivity of 4,000 Ω-cm, the FDOT method predicts service lives of ~90 yr and ~30 yr for 16-gauge aluminized and galvanized steel, respectively. As in the refined California method, durability predictions by the FDOT method do not take into account the system complexity and the variety of responses due to the existence of scale-forming waters.

1.1.4 The AK Steel Method

An alternative service life forecasting method based on field observations was proposed by AK Steel (Morris and Bednar, 1998 and Bednar, 1989) to incorporate the tendency for water scaling, mainly produced by the formation of

adherent $CaCO_3$ film on the surface of a pipe, into the service life prediction of corrugated galvanized and aluminized steel Type 2 culvert pipes. Instead of pH and minimum resistivity, the AK Steel method (shown in Figure 1.4) uses the scaling tendency parameter equal to the total hardness plus total alkalinity minus free CO_2, versus the solution conductivity (or its inverse, the resistivity).

Contrarily to the other predictive methods, the AK Steel method considers that water scaling protects the metal from subsequent corrosion. If the scaling tendency parameter versus solution conductivity falls on the straight line, a protective scale is expected to be formed on the metal surface and corrosivity of the medium would be minimal. The idealized curves labeled 50 yr, 35 yr, and 20 yr in Figure 1.4 exemplify the effect on durability of increasingly large amounts of aggressive anions such as Cl^- and SO_4^{-2} ions and/or larger amount of free CO_2 which causes scale dissolution with a consequent increase of the metal corrosion rates.

Preliminary application of this method has shown encouraging results in predicting the performance of galvanized steel and aluminized steel Type 2 culverts in tropical and subtropical environments comparable to those encountered in Florida. Experimental evidence gathered to support the applicability of this method is nevertheless limited and several important issues remain unsolved that necessitate additional laboratory experimentation. Those issues include the possibility that the aluminized coating could be susceptible to depassivation if carbonate scales promotes alkaline conditions as indicated by Porter and Hadden (1953).

1.2 Corrosion Resistance of Aluminized Steel Type 2

1.2.1 Manufacture and Surface Morphology

Several aluminizing methods suitable for steel coating have been widely used for the past decades (Suzuki, 1989). The methods differ only on the type of protection process of the steel substrate against oxidation before the hot-dipping stage. The Armco Sendzimir method, however, is commonly adopted for the bulk of production of aluminized steel Type 2 briefly explained next.

The steel to be hot-dipped is degreased by alkali cleaning or by heating at 450-600 ˚C followed by water rinsing, pickling, and water rinsing again (pretreatment process). Afterwards, the pretreated steel is cleaned by exposure to a H_2 gas atmosphere at high temperature (activating process). Cleaning the metal strip in a non-oxidizing/reducing atmosphere assures a pristine surface for coating adherence. At the end of the activating process, aluminum coating is continuously applied to the pretreated steel by hot-dipping in a closed environment at ~700 ˚C. The steel is annealed in the line and the coating thickness is controlled by the line speed, hot-dipping temperature, and air finishing knives as schematically depicted in Figure 1.5. The reaction rate between molten aluminum and steel is relatively fast, forming a duplex coating on top of the steel substrate. According to the ASTM A929 and ASSHTO M274 standard procedures, the final product must comply with a minimum coating weight of 1 oz/ft^2 which corresponds to a minimum coating thickness of ~40 μm, and a minimum tensile and yield strengths of about 310 MPa and 228 MPa, respectively.

Microscopic examination of aluminized steel Type 2 in cross section shows a nearly pearlite-free ferrite low carbon steel substrate with regular grains, a partly columnar inner alloy layer ~15 μm thick, and an outer aluminum-rich layer ~30 μm thick. The inner alloy layer is of composition Fe_2Al_5 (An et al, 2001, Li et al., 2003) although others have shown the formation of $FeAl_3$ in some cases (Serra et al., 1998, Bouche et al, 1998). The inner alloy layer is an essential ingredient of the coating protection system, supplementing the outer aluminum-rich layer and possibly providing a second line of defense against corrosion. The composition of the outer layer is predominantly a matrix of aluminum and Fe-rich intermetallic precipitates (6-11 wt% Fe) (Caseres and Sagüés, 2005). During manufacturing, small discontinuities in the aluminized coating, possibly caused by cold working can extend to the substrate steel, creating coating breaks that may result in the formation of galvanic macrocells.

1.2.2 Overview of Aluminum Corrosion

Aluminum derives its corrosion resistance from the presence of a thin protective passive oxide layer, which when in contact with air, greatly decreases the rate of metal oxidation. When in contact with water, other forms of protective layers may form being the most common the hydrated aluminum oxide with composition $Al_2O_3.3H_2O$ (Godard et al., 1967). However, the aluminum oxide film may be subject to localized breakdown resulting in accelerated dissolution of the underlying metal. In particular, aluminum oxides tend to dissolve uniformly in extreme acid or alkaline medium. In non complexing solutions of ~4<pH<~8.5,

aluminum tends to become covered with the protective oxide film as first proposed by Pourbaix (Pourbaix, 1974). Under this condition, the oxide film has very low solubility and its electronic conductivity is also very small. However, a small but finite current can be measured during metal polarization as a result of the presence of intrinsic defects in the oxide film. Others (Hunter and Fowle, 1956, Lee and Pyun, 1999) proposed that the oxide film consists of two distinctive layers. The inner oxide layer next to the metal is a compact amorphous barrier layer of thickness determined mainly by the temperature of the environment. Covering the barrier layer is a thicker, more permeable outer layer of hydrated oxide.

As mentioned earlier, in alkaline solutions (pH>~8.5) the initially protective oxide film is expected to uniformly dissolve with the formation of AlO_2^- ions. In acidic solutions (pH<~4), the oxide film decomposes to form Al^{+3} ions resulting also in considerable larger corrosion rates than otherwise. However, the predictions proposed by Pourbaix in these environmental conditions should be taken cautiously as being only general guidelines for estimation corrosion resistance in the absence of contaminants (Pourbaix, 1974).

It has been widely demonstrated that the aluminum oxide film, if present, is covered with a layer of hydroxyl groups (McCafferty, 2003), which has Lewis acid–Lewis base properties, that dictates the surface charge of the oxide film when immersed in aqueous solutions. The surface charge has close connection to the solution pH when compared with the oxide isoelectric point (typically at pH~9.5). If the solution pH<9.5, the oxide film will acquire positive charges so

that, e.g. chloride ions, can be attracted to the oxide surface. If the solution pH>~9.5, the surface will accept negative charges. The attractive forces are mainly coulombic of ion–ion interaction type. The presence of chloride ions on the aluminum surface can induce localized corrosion of aluminum even in the range of aluminum passivity. Notably, chloride ions can cause pitting of aluminum at the region of local breakdown of the passive film as discussed next.

1.2.2.1 Pitting Corrosion of Aluminum

In general, pits initiate at some chemical or physical heterogeneities at the metal surface such as inclusions, second phases, grain boundaries, flaws, mechanical damage, or surface dislocations. Pitting of aluminum is considered to be autocatalytic in nature; that is once a pit starts to grow the conditions inside the pit are such that further growth is promoted. The local pit environment becomes depleted in oxygen (assumed to be the main cathodic reactant in well aerated solutions) and enriched in hydrolyzed aluminum cationic and anionic species, maintaining charge neutrality inside the pit. As a result, the pH inside the pit is low (McCafferty, 2003). It is well documented that within aluminum pits, chloride salts exist: aluminum chloride ($AlCl_3$) and aluminum oxychlorides such as $Al(OH)_2Cl$ and $Al(OH)Cl_2$. Depending upon the kind of chloride salts, different pH values within the pit can be expected. For instance, in the presence of $AlCl_3$ the pH may be as low as 1 (Vermilyea, 1971, Hoch, 1974), and a saturated solution of $Al(OH)_2Cl$ may exhibit a pH~3 (Vijh, 1973 and Kaesche, 1974)

determined by the freezing method, whereas the pH of the bulk solution was ~11 (Wong and Alkire, 1990).

Considerable understanding of the pitting phenomenon has been achieved but an in-depth description of the steps associated with pitting corrosion is still lacking. The stages of pitting will be discussed below, from passive film breakdown, to metastable pitting, and lastly to pit growth.

The first stage of pitting is the passive aluminum film breakdown followed by pit initiation. Typically, aluminum passive films are characterized by extremely high electric fields on the order of 10^6-10^7 V/cm and by being very small in thickness (nm scale). Passive film breakdown and pit initiation can be interpreted by three mechanisms: film penetration, anionic species adsorption, or film breaking. Hoar (1965) established that the film penetration mechanism is associated with the transport by migration of aggressive anions through the passive film to the metal/oxide interface where active aluminum dissolution occurs. The penetration mechanism is supported by the existence of an induction time for pitting after chloride ions are in contact with the oxide film. Nevertheless, a critical chloride concentration in the oxide film at the metal surface has to be attained in order to display film breakdown and pit initiation. In contrast, Berzins et al. (1977), Wood et al. (1978), and Augustynski et al. (1978) found that the there is no chloride concentration threshold below which pitting will not occur and that pitting initiation and propagation depends upon the particular properties of the chloride adsorption sites at the aluminum surface.

Another approach to describe pit initiation is by the point defect model developed by Chao and coworkers (Chao et al., 1981). This approach assumes that chloride ions penetrate the outer portion of the oxide film resulting in the formation of cationic vacancies. These vacancies migrate towards the metal/oxide interface where they are consumed by the formation of cations from the metal. However, if there are more vacancies than cations formed, the vacancies remaining may condense at the metal/oxide interface creating a void. The void is presumed to be the first step in the pitting process according to this model. Optical and scanning electron microscopy conducted on ion-implanted aluminum surfaces after polarization above the aluminum pitting potential in 0.1 M NaCl has shown that the propagation of corrosion pits is associated with the formation and rupture of blisters beneath the oxide film due to electrochemical reactions occurring at the oxide/metal interface (Natishan and McCafferty, 1989) validating the postulations of the point defect model.

Foley (1986) proposed in one his early works that pit initiation involves adsorption of chloride ions at the oxide film surface followed by an oxide film penetration by the adsorbed chlorides, and a later chloride-assisted dissolution which occurs at the metal/oxide interface (Natishan and McCafferty, 1989 and later confirmed by Yu et al., 2000). After initiation, pits propagate following a series of events which lead to changes in internal pit chemistry and to the growth of pits as mentioned above.

Yet another approach, the film breaking mechanism, considers that the passive film is in a continual state of breakdown and repair caused by localized

mechanical stresses at weak sites or flaws in the passive film. This mechanism implies that local breakdown events are followed by a rapid healing process of the passive layer in non aggressive environments. In chloride containing solutions, the healing process is less likely. According to this mechanism, local passive film breakdown will lead to pitting under conditions that promote pit growth (Sato, 1971, Richardson and Wood, 1970).

1.2.3 Field Studies on the Durability of Aluminized Steel Type 2

One of the most common problems encountered while researching field corrosion findings is that there is very little standardization in the methodology used to test and to evaluate corrosion of culvert pipes. Unfortunately, it is extremely difficult to adequately define the nature of the test environments (e.g. episodic wetting, abrasion, flow) and to compare corrosion of culvert pipes. Comparison tests typically involve visual inspection to assess pipe deterioration based upon criteria set up by the investigator. In general, visual inspections lack consistency when inspections are carried out by multiple inspectors with differing biases. Despite this ambiguity, several field studies have been conducted on aluminized steel Type 2 exposed to numerous environmental conditions. The investigations more relevant to this dissertation are presented in the next paragraphs.

Ault and Ellor (1996) inspected around twenty one corrugated aluminized steel Type 2 culvert pipes located in Alabama, Oregon, and Maine. Their field studies suggested that in the absence of significant abrasion, an aluminized steel

Type 2 pipe could reach a service life of up to eight times that of a galvanized steel pipe predicted by the refined California method (if only waterside corrosion is considered, then the multiplier factor becomes 3.5). Similar results were reported by Potter et al. (1991), who suggested that the service life of aluminized steel Type 2 is ~6.2 larger than that predicted for galvanized steel. The actual service life multiplier factor varies depending on the specific environment. Under extreme conditions, however, the author stated that these materials would perform in a relatively similar manner (i.e., last a long time or fail rapidly).

The California Highway Design Manual (Section 850-13, California Department of Transportation) indicates that a 18-gage aluminized steel Type 2 pipe would have a service life equal to that of a 16-gage galvanized steel for a pH range between 5.5 and 8.5 and a minimum resistivity of 3,000 Ω-cm. However, in acid or alkaline environments the Design Manual asserts that galvanized and aluminized steels would likely show nearly equal performance as indicated by Potter et al. (1991).

A comprehensive evaluation of aluminized and galvanized steel culvert pipes conducted by Bednar (1998) showed that corrugated aluminized steel Type 2 would be considerably superior to galvanized steel in environments with resistivities higher than 950 Ω-cm and relatively high free CO_2 content. This scenario would yield a minimum 50 yr service life for aluminized coating, whereas galvanized coating would be limited to up to 20 yr in service. In overly severe environments (resistivities <600 Ω-cm), the study showed that aluminized steel typically displayed accelerated pitting corrosion and the advantage of

aluminized over galvanized coating became minimal. A later field study by Bednar and AK Steel (Bednar, 1998) on the projected service life of aluminized steel Type 2 culvert pipes exposed to nearly neutral pH solutions with low chloride concentrations showed deepest pit penetrations of ~8 mils and ~12 mils after 30 yr and 42 yr in service, respectively, indicative of low/moderate corrosion rates with pit growth of ~6.7 to ~7.2 μm/yr, for a minimum projected service life in excess of 75 yr for a 16-gage metal pipe.

The above observations of superior performance by aluminized steel Type 2 over galvanized steel have been challenged by some recent field inspections in Florida. An ongoing FDOT investigation conducted on ~3 yr old spiral rib aluminized steel Type 2 culvert pipes in the City of Saint Cloud, revealed extensive corrosion damage of aluminized steel even in mild environments with nearly neutral pH and resistivities >2,000 Ω-cm. Projected nominal service life, determined per the FDOT method (Cerlanek and Powers, 1993) for 16-gage aluminized steel Type 2, yielded service lives between 60 and 115 yr. Likewise, the AK Steel method yielded a service life in excess of 50 yr. Clearly, the extensive damage observed early on was not anticipated by either forecasting procedure. The corrosion damage indicates that the fastest corrosion rates may have locally exceeded 510 μm/yr, value significantly higher than those observed for plain steel in similar environments (~25.4 μm/yr). Firm conclusions of this ongoing investigation have not been achieved yet but it is clear that an unexpected mode of deterioration is at play, for instance through microbiologically induced corrosion.

Gartland (1987) studied the corrosion behavior of flame-sprayed aluminum coated steel immersed in natural seawater at 9 ˚C for up to 210 days. The only difference between the flame-sprayed and the hot-dipped aluminized steels is in the coating thickness (~100 μm for the flame-sprayed procedure, compared to only about half as much for hot-dipping). Open circuit potentials, potentiodynamic polarization, and linear polarization tests in the cathodic direction were conducted at different exposure times. Corrosion rates, determined at the open circuit potentials by extrapolation of the anodic and cathodic polarization curves and by linear polarization, were found to be ~4.9 to ~8.2 μm/yr at the end of exposure. It is cautioned however that this moderate corrosion rate, if sustained, would mean penetration of the aluminized layer after a decade.

The majority of the field studies reviewed revealed a superior performance of aluminized steel Type 2 over galvanized steel for 4<pH<9 and resistivities >~2,000 Ω-cm. However, the unexpected extensive corrosion damage of aluminized steel detected in some regions of central Florida generated serious concerns as what environmental factors may have been involved in the corrosion mechanism. As a result, laboratory experimentation is needed to elucidate all possible modes of metal deterioration, and to study the synergistic influence of the major environmental variables on the aluminized steel Type 2 durability.

1.2.4 Galvanic Corrosion of Aluminized Steel Type 2

Extensive research has been carried out to study the galvanic corrosion performance of aluminized steel Type 2 in various atmospheric environments as well as in high chloride concentration solutions. For instance, Legault and Pearson (1978) evaluated the atmospheric corrosion behavior of aluminized steel Type 2 test panels with uncoated cut edges (exposing the base steel) in industrial and marine environments. In their five-year investigation the corrosion rates, determined by metal weight loss ($\Delta W = k\, t^n$ where k and n are constants and t is time), were small (~0.2 μm/yr) and moderate (~0.45 μm/yr) in industrial and marine environments, respectively. Visual inspection of the test panels showed that the aluminized coating were in excellent condition except for the panels exposed to marine environments which showed small perforations of the aluminized coating with formation of uniform white corrosion product. Interestingly, the cut edges were free of corrosion in marine environments and depicted rust formation only in industrial environments indicative of insufficient galvanic protection to the exposed steel.

Similar approach was employed by Townsend and Zoccola (1979) and later by Townsend and Borzillo (1987) who tested aluminized steel Type 2 panels with cut edges exposed to severe marine, moderate marine, rural, and industrial environments. After 13 yr of exposure, aluminized steel performed well in all tests environments except for the rural atmosphere in which rust staining along the cut edges was observed. For the marine environments corrosion rates, determined by weight loss measurements, decreased with time approaching a terminal

corrosion rate of ~0.18 μm/yr. In contrast, an increasing corrosion rate trend was noted in rural and industrial atmospheres with also small terminal corrosion rates in the order of ~0.25 and ~0.16 μm/yr, respectively. The main finding of their work was that aluminized coating had in general good physical barrier properties. However, if the aluminized layer is partially disrupted, its sacrificial protection to the exposed underlying steel was not sufficient (as visually noted by the growth of rust projections at the pores and cut edges of the specimens) in all environments tested except for the marine environment. The authors stated that in aggressive environments, the aluminized coating is anodic to the exposed steel where chloride ions impair the passivity of aluminum. However, in industrial and rural atmospheres the aluminized coating passivated so that little to none galvanic protection to the underlying steel was noted.

Creus et al. (2000) investigated the corrosion behavior of aluminum coating (~10 μm thick) deposited on a 3 cm^2 4135 steel base by physical vapor deposition. The coated steels were immersed in a 3% NaCl solution, aerated, and stirred with a rotating working electrode at 500 rpm. Open circuit potentials (E_{OC}) vs saturated calomel electrode (SCE) and electrochemical impedance spectroscopy (EIS) over a frequency range from 4 mHz to 64 kHz with a 10 mV amplitude around the corrosion potential were monitored. E_{OC} stabilized around ~-705 mV_{SCE} shortly after immersion reaching ~-440 mV_{SCE} at 75 hr of exposure. Impedance diagrams after 1 hr of immersion showed two distinctive capacitive loops at high and intermediate frequency ranges, and an inductive loop at low frequencies. The authors attributed the high frequency loop to the charge transfer

resistance associated with the corrosion rate of the outer aluminized layer. The charge transfer resistance was estimated to be ~2 kΩ-cm^2, which is significantly lower than that for pure aluminum. According to the authors, this difference in resistance values results of an enhanced galvanic interaction between the steel substrate and aluminum through coating defects. Based on the charge transfer resistance value reported and assuming Tafel slopes of 160 mV/dec, a nominal aluminum corrosion rate was significantly higher (~185 μm/yr) compared to the results reported by Gartland (1987). Additional tests conducted by the authors to determine the galvanic behavior of the aluminum/4135 steel system of 3 cm^2 surface area, for an anode-to-cathode area ratio of unity, exposed to 3% NaCl solution showed a galvanic current of ~300 μA/cm^2 (aluminum being anodic to steel) at the E_{OC} of ~-712 mV_{SCE}. The authors stated that the aluminum corrosion rate was basically controlled by galvanic coupling to steel.

Shaw and Moran (1985) studied the corrosion behavior of thermally-sprayed aluminum coating specimens (7-14 cm^2 surface area with ~100 μm thick coating), with and without linear scribe marks exposed to seawater and marine atmosphere at 25 °C for ~6 months. Visual inspection of the specimens without scribe marks immersed in seawater showed small pits with no base metal corrosion. On the other hand, specimens exposed to marine atmosphere exhibited a slight buildup of corrosion products at the scribe marks but no base metal corrosion was found elsewhere on the specimen surface. Additional laboratory tests were conducted on specimens without scribe marks immersed in synthetic seawater. Corrosion potential tests monitored for 30 days stabilized at

~-800 mV_{SCE} after 10 days. During the entire exposure period, no pits were noted. Anodic polarization tests taken after 10 days of exposure showed that the aluminum coating was in passive state in the region from -800 mV_{SCE} to -550 mV_{SCE} with appearance of few well-defined pits at potentials nobler than -550 mV_{SCE}. The authors concluded that aluminum coatings on steel exhibit weak cathodic protection in marine environments, contradicting findings from Townsend and Zoccola (1979) and Creus et al. (2000).

Johnsson and Nordhag (1984) carried out an investigation to compare the sacrificial corrosion performance of several metallic coating on steel exposed to atmospheric environments and seawater for four years. Corrosion rates of uncoated cut edges aluminized steel specimens with and without scribe marks, exposing underlying steel, were determined by weight loss measurement. The atmospheric tests showed that aluminized steel was attacked mainly by pitting even after one year of exposure, especially in the marine atmosphere. The number of pits, however, does not seem to increase with time. Comparing the corrosion performance of the different metallic coatings, aluminized steel without scribe marks had the best performance except in marine environments in which galvanized steel outperformed aluminized steel. The corrosion rates varied from a low 0.2 μm/yr (urban atmosphere considered by the authors a mild environment) to a modest 1.5 μm/yr (marine atmosphere). Comparable tests conducted on the scribed specimens demonstrated the poor galvanic protection of the aluminized coating to the exposed steel in all environments and seawater,

displaying heavy red rust formation along the cut edges and at the scribe mark. This finding is in agreement with observations by Shaw and Moran (1985).

Most of the experimental investigations on the corrosion behavior of aluminized steel are related to visual corrosion assessment and gravimetric techniques. Only limited data were gathered for the evaluation of corrosion of aluminized steel using electrochemical techniques, especially EIS, which can provide a powerful means to elucidate the corrosion mechanisms and corrosion rates of aluminized steel with and without coating breaks. Thereby, laboratory experiments using this evaluation approach are needed.

Furthermore, the majority of the studies on galvanic corrosion involving aluminized steel with exposed underlying steel were conducted by atmospheric exposure or by immersion in highly aggressive solutions. Limited information exists on the galvanic behavior of aluminized steel with coating breaks exposed to fresh waters of varying scaling tendencies with moderate chloride contents, where galvanic protection may not take place at all. Studies have demonstrated discrepancies in the galvanic behavior of aluminized steel when exposed to seawater. Work is needed to clarify this issue. Implementation of a computer model of current and potential distribution in the exposed-steel/surrounding coated surface will serve to examine the effectiveness of galvanic protection of the exposed steel under various environmental and geometric regimes.

1.3 Objectives of this Investigation

In view of the unresolved issues presented above, this dissertation was focused on the study of the corrosion behavior of aluminized steel Type 2 with and without coating breaks exposed to solutions of varying scaling tendencies. The objectives of this dissertation included the following:

1. Examine the corrosion behavior of aluminized steel Type 2 of as-received surface condition in waters of varying scaling tendencies commonly found in Florida environments. Of interest is to determine if the aluminized coating is capable of retaining passivity for extended periods to support long service lives of this material.
2. Clarify important issues on the cathodic efficiency of aluminized steel Type 2 of as-received and stripped/aged surface conditions in waters of positive scaling tendency. The stripped surface condition intends to mimic long-term corrosion exposure where a fraction of the external aluminum-rich layer is consumed. Of primary interest is to evaluate the locus and strength of the cathodic reaction during metal passive state for these two surface conditions.
3. Examine the corrosion behavior of aluminized steel Type 2 with partially disrupted aluminized coating, exposing the underlying steel substrate. Of interest is to determine whether the surrounding aluminized coating will provide sufficient galvanic protection to the base steel for various coating break sizes and solution aggressivity.

4. Develop a quantitative *dc* computational model to calculate static current and potential distributions along the blemished aluminized surface for different solution aggressivity. The local anodic and cathodic kinetics at the metal surface obtained by the *dc* model are used as inputs of an *ac* computational model that accounts for complex polarization conditions and corrosion macrocells as a function of key environmental factors. The output of the *ac* model attempts to provide useful information in regards to the interpretation of the impedance response possibly complicated by uneven *ac* current distribution in the blemished system.

The results from this dissertation will support the main FDOT project goal, which is to develop a durability forecasting method based on laboratory-determined corrosion rates versus key environmental variables. It is anticipated that the durability forecasting method evaluated will take into account the effect of substantial localized aluminized coating damage. Such consideration thus needs assessing the extent of galvanic protection available under various environmental conditions. Determination of performance under those circumstances is critically needed for improved forecast analysis.

1.4 Approach

The dissertation primarily focused on the objectives specified in Section 1.3. Much of the dissertation work was focused on the first and third objectives. The first objective was addressed by conducting long term open circuit potential

and impedance measurements on the as-received aluminized steel Type 2 specimens exposed to solutions with low alkalinity and hardness (solution C), high alkalinity and low hardness (solution NP), high alkalinity and hardness (solution P), and substitute ocean water (solution SW). The solutions P and SW were expected to have positive Langelier index values so that a precipitate of $CaCO_3$ on the specimen surface was anticipated. All solutions but solution SW (~20,000 ppm) had moderate chloride concentration (~370 ppm).

To examine the effect of aluminized coating breaks (exposing the underlying steel) on the corrosion performance of aluminized steel Type 2, two coating break sizes ~3 cm^2 and ~0.03 cm^2 nominal area machined in the center of each specimen were used. On these specimens, open circuit potential and impedance measurements were conducted at selected exposure time. An experimental setup used to monitor galvanic currents as well as individual corrosion performance of the aluminized coating/steel components exposed to solutions P and NP was employed. The macroscopic distribution of corrosion due to the formation of corrosion macrocells between the aluminized surface and the underlying steel was expected to play an important role in determining the degree of corrosion severity. To examine the effectiveness of galvanic protection to the exposed steel under various environmental, a *dc* computational model to determine the current and potential distributions needed to be implemented. The *dc* model computation results also served as inputs of an *ac* computational model used to interpret the impedance response in systems with non uniform *ac* current distribution.

The issues concerning the cathodic behavior of the aluminized steel for two surface finish conditions (as-received and stripped) were studied by performing cyclical polarization tests with multiple polarization scan rates ranging from 0.05 mV/sec to 1 mV/sec. A simplified model was used to interpret the mechanism associated with the cathodic performance of aluminized steel Type 2 under those circumstances.

1.5 Significance of Research

Because premature replacement of buried metallic components damaged by corrosion is costly not only because of the price of the new unit, but also because of the associated road demolition and service outage, it is much to the benefit to have in place reliable means of predicting the corrosion rates of metals in soil and waters so that materials selections commensurate with the desired design service life can be made.

As discussed above, several service life forecasting methods have been proposed. Most of the predictive methods use pH and resistivity of the medium to predict service life of a metallic structure. A common agreement is that low values of pH (within a certain range) and resistivity forecast a short service life. However, surface water may have a relatively low pH and still not be very aggressive, because other dissolved species may precipitate a protective scale on the metal surface. Conversely, high pH by itself within the specified range may not guarantee extended service life if the water does not promote the formation of a protective scale. Furthermore, all available methods to date do not

take into consideration the effect of substantial localized metal coating damage that could complicate even more the service life forecast. This investigation gives a first insight to this problem to better forecast aluminized steel Type 2 metal pipe durability by performing laboratory experiments.

1.6 Overview

This dissertation is organized as follows:

Chapter 1 presents a general literature review and analyzes the unresolved issues on the corrosion/durability of aluminized steel Type 2. Also, this Chapter shows the research objectives, investigation approach, and the significant of this research. In Chapter 2, the electrochemical behavior of as-received aluminized steel Type 2 exposed to solutions of varying scaling tendencies is addressed. Effects of water alkalinity, hardness, and chloride content on the metal corrosion rates are also correlated. Chapter 3 presents some important issues regarding the cathodic behavior of the aluminized steel with two surface conditions: as-received and surface-stripped. Chapter 4 describes the effects of aluminized coating breaks on the corrosion performance of aluminized steel Type 2 by conducting open circuit potential and impedance measurements. Comparison with the as-received aluminized surface condition is also presented. Chapter 5 presents the theory, implementation, and results of the *dc* and *ac* computational models for the study of the effectiveness of the galvanic action of the exposed steel/aluminized coating system. Chapter 6 summarizes conclusions drawn from

the preceding chapters. A set of Appendices is included at the end of the dissertation.

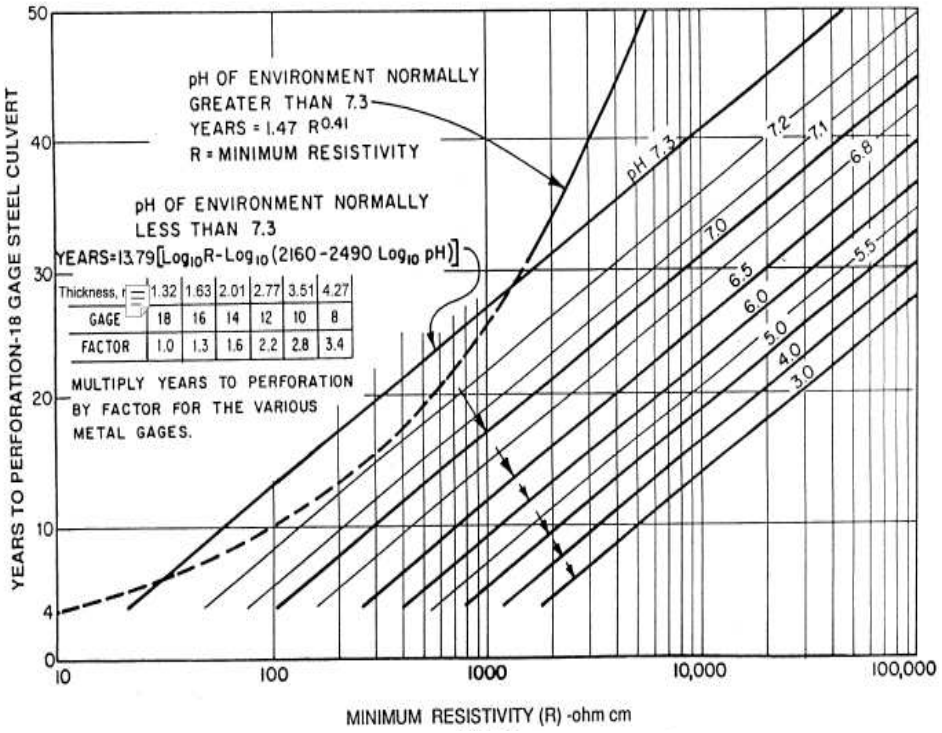

Thickness, r	1.32	1.63	2.01	2.77	3.51	4.27
GAGE	18	16	14	12	10	8
FACTOR	1.0	1.3	1.6	2.2	2.8	3.4

Figure 1.1: Refined California method chart for estimating years to perforation of 18-gage galvanized culvert pipe (California Test 643, 1999) [1].

[1] To compute the service life, the smallest pH and minimum resistivity values of either the soilside or the waterside are entered. Multipliers are given to adjust service life prediction for metal gages different than 18.

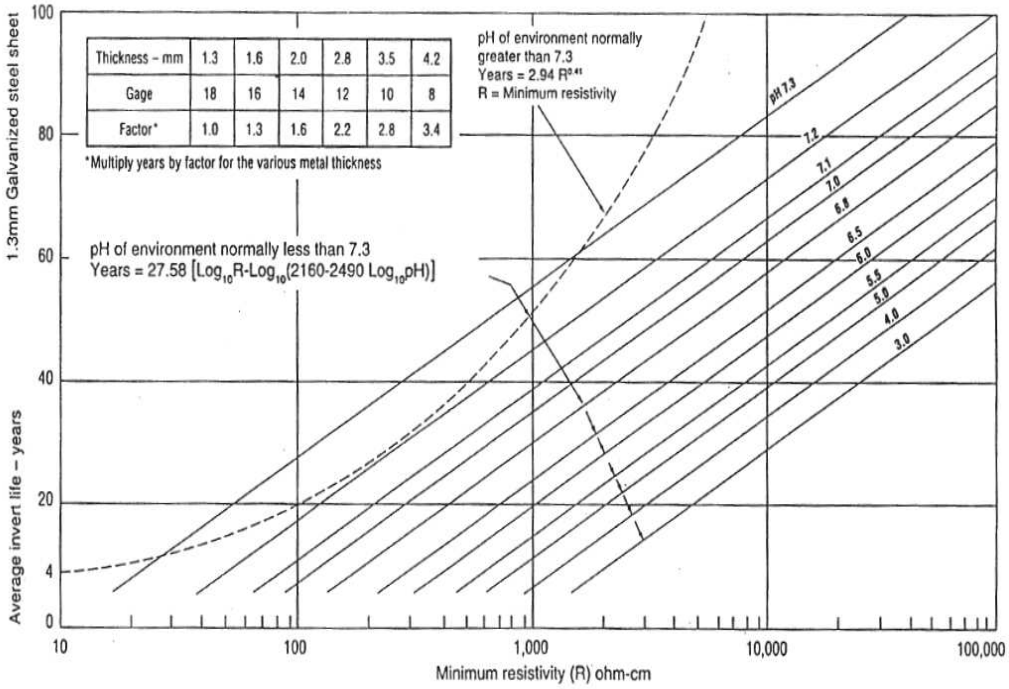

Figure 1.2: The AISI method chart for estimating years to perforation of galvanized steel pipes of 18-gage culvert pipe. Computing service life is the same as in the refined California method (Handbook of Steel Drainage & Highway Construction Products, American Iron and Steel Institute, 1994).

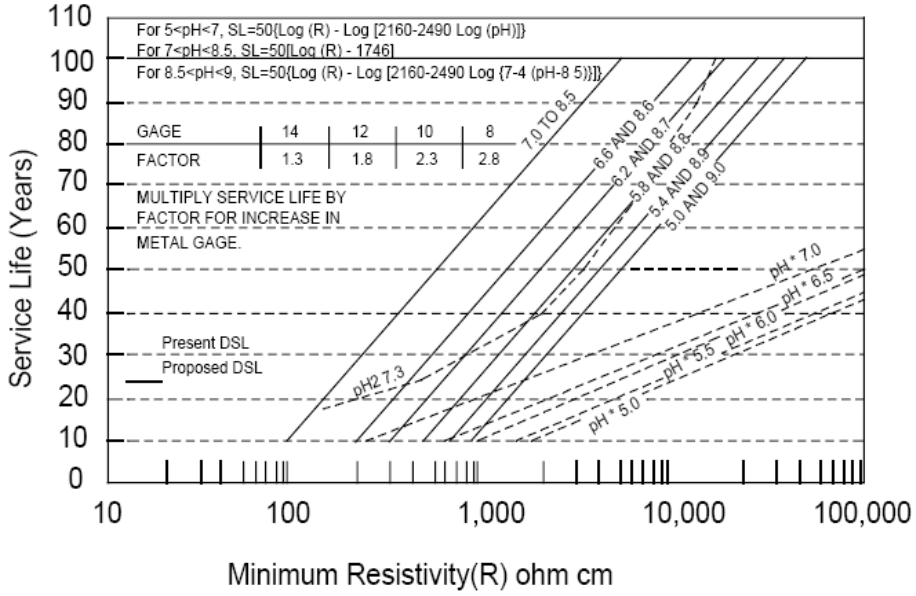

Figure 1.3: The FDOT chart for estimation years to perforation of 16-gage aluminized steel Type 2 culvert pipes (solid lines) (Cerlanek and Powers, 1993). Dashed lines correspond to service life estimation using the refined California method for galvanized steel.

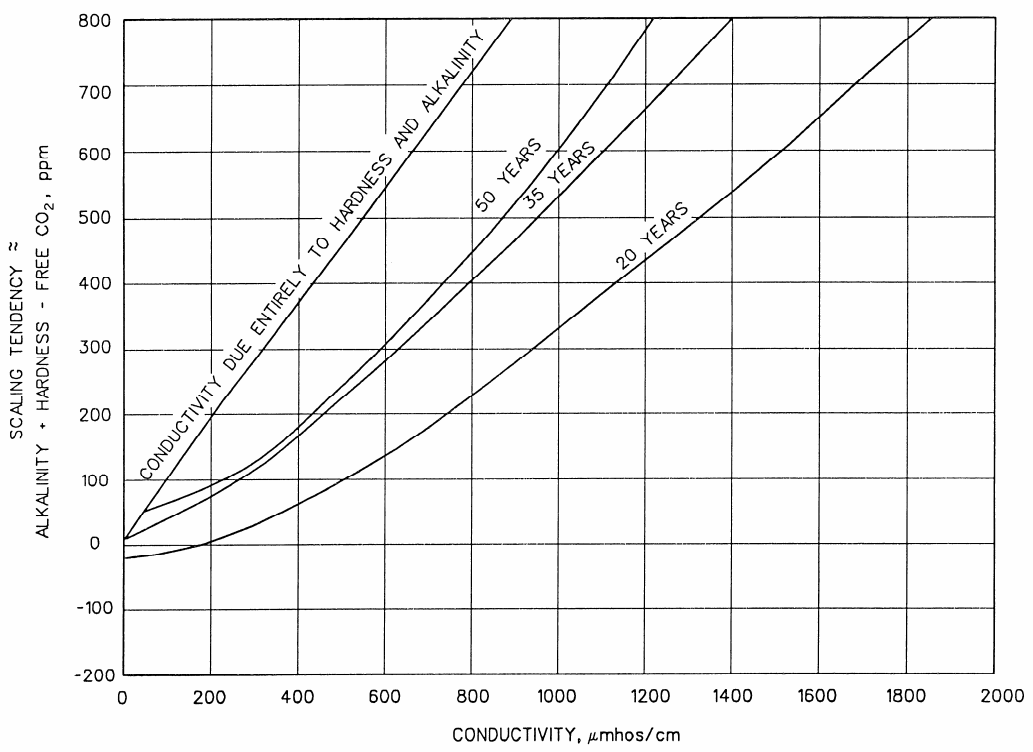

Figure 1.4: The AK Steel method chart for estimating service life of 14-gage galvanized and aluminized steel Type 2 culvert pipes (Bednar, 1989).

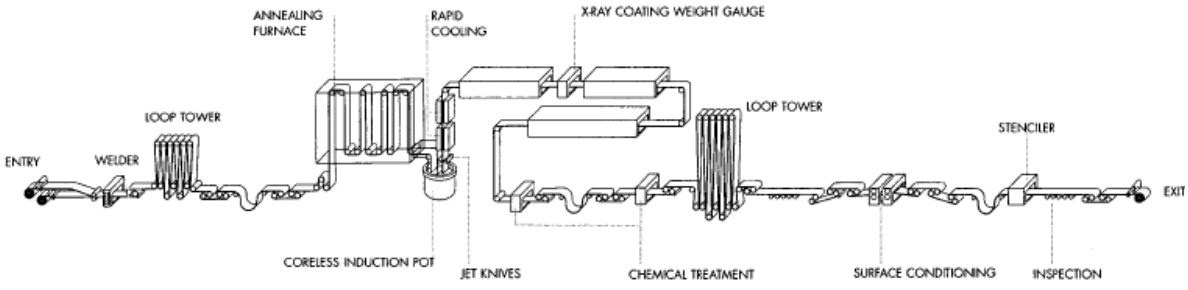

Figure 1.5: Schematic of the typical manufacturing process of aluminized steel Type 2 (source: www.aksteel.com).

Chapter 2

Corrosion of As-Rolled Aluminized Steel Type 2 in Scale-Forming Waters [2]

2.1 Introduction

As discussed in Chapter 1, aluminized steel Type 2 is produced as a steel sheet hot dip coated on both sides with commercially pure aluminum, which provides corrosion protection through low corrosion rate of the aluminum when the aluminum is in passive condition, and also may confer galvanic protection to the exposed underlying steel under certain circumstances (Kimoto, 1999). For that reason, aluminized steel Type 2 is increasingly used for metallic drainage components in contact with natural waters. However, corrosion is an important durability limitation factor in these components which are often designed for very long service life (e.g. 75 yr) (Cerlanek and Powers, 1993). As a result, mechanistic knowledge of the corrosion processes is needed to better forecasting durability in critical highway applications. In particular, it has been proposed (Morris and Bednar, 1998, and Bednar, 1989) that calcium carbonate scales formed from natural waters are protective to aluminized steel.

A common indicator of scaling tendency is the Langelier Saturation Index, $LSI = pH\text{-}pH_s$, where pH_s is the pH that would result in $CaCO_3$ precipitation

[2] This Chapter is a version of the manuscript submitted for publication in the Corrosion Journal (2006) under revision.

(Snoeyink and Jenkins, 1980). Positive values of LSI imply a tendency for $CaCO_3$ precipitation. However, the LSI parameter does not consider the reserve of species in the solution responsible for a given pH. Based on extensive field data collection, Bednar (1989) proposed that the corrosion performance of aluminized steel Type 2 in aerated media may be better predicted by the combination of an index indicating carbonate scaling tendency (scaling index (SI)=total Alkalinity (TA) plus total Hardness (TH) minus free CO_2 (FC)) and the conductivity σ of the solution in contact with the metal. However, there is concern that the aluminum-rich layer of the aluminized steel could be susceptible to depassivation if the carbonate scale promotes alkaline conditions. For example, Porter and Hadden (1953) stated that corrosion of pure aluminum was most severe in high scaling tendency natural waters.

This concern is addressed in the present Chapter, where experiments to examine the corrosion behavior of aluminized steel Type 2 in synthetic waters of varying scaling tendencies at the room temperature are reported. To focus on the stability of the aluminum-rich coating layer, this investigation uses aluminized steel Type 2 in the as-produced condition without any further forming or mechanical distress.

2.2 Experimental Procedure

As-received aluminized steel Type 2 tested came from a flat sheet stock manufactured per ASTM A929, from low carbon steel (Table 2.1) coils rolled to 16-gage (~1.59 mm thick) and hot-dipped in a bath of commercially pure

aluminum. The microstructure (Figure 2.1) had a nearly pearlite-free ferrite substrate with regular grains. The aluminized coating layer resulting from the hot-dip process included a partly columnar inner layer ~15 μm thick (Figure 2.2), of approximate intermetallic composition Fe_2Al_5 (Li et al., 2003) as determined by scanning electron microscopy (SEM) with energy dispersive x-ray analysis (EDS), and an outer layer ~25-30 μm thick. The compositions of the gray outer layer matrix and the small lighter features were predominantly aluminum with ~2.4 wt% Fe and 6-11 wt% Fe, respectively. The small light features resemble Fe-rich precipitates identified elsewhere (ASM Metals Handbook, 1972).

Circular test specimens of 95 cm^2 nominal surface area were cut out from the as-received stock, cleaned with ethanol and acetone, and stored in a desiccator prior to immersion. Specimen exposure test began typically within 24 hr after storage. Three-electrode test cell configuration (Figures 2.3 and 2.4) was used, exposing horizontally one of the specimen faces. A metal-metal oxide activated titanium mesh placed parallel ~6 cm from the specimen surface was used as a counter electrode, while a low impedance activated titanium pseudo reference electrode 0.3 cm diameter and 5 cm long (Castro et al., 1996) was placed ~1 cm from the specimen surface and periodically calibrated against a saturated calomel reference electrode (SCE). All potentials reported here are in the SCE scale unless otherwise stated. Electric contact to the specimen was made through a copper wire soldered to a copper sheet in contact with the bottom surface of the specimen not exposed to test solution. Each test cell was filled with 500 mL of solution and the cells were never replenished during the

entire length of the experiment. The relatively small electrolyte volume/specimen area ratio was intended to be representative of worst-case culvert pipe conditions with stagnant water on a pipe invert, or of occluded conditions for pore water on the soil side of a pipe.

Four test solutions were used, simulating conditions typically encountered in Florida environments. The test solutions corresponded to a carbonate precipitating condition (solution P), a mildly alkaline but non-precipitating condition (solution NP), a neutral pH of non carbonate precipitating condition and negligible alkalinity (solution C), and a substitute ocean water (solution SW) prepared according to ASTM D1141-90 standard procedure. Table 2.2 shows the compositions of the test solutions, all made from reagent chemicals and de-carbonated de-ionized water of resistivity>10^6 Ω-cm. Combinations of NaOH and NaCl (C), $NaHCO_3$, NaCl, and HCl (NP), $NaHCO_3$, NaCl, HCl, and $Ca(OH)_2$ (P), and chemical compounds commonly found in ocean water (SW) were used. The ionic constituent composition of the simulated ocean solution, reported by the manufacturer, is shown in Table 2.3. To make up for depletion of O_2, the test solutions were aerated for 30 sec at a rate of ~0.03 cm^3/sec twice a day using CO_2-free air (for solution C) and ambient air (for solutions NP, P, and SW) and isolated from the external air the rest of the time. Values of FC were calculated based on the total alkalinity and pH of the solution (Snoeyink and Jenkins, 1980):

$$FC = \frac{TA \cdot 10^{-pH}}{10^{-6.35}} \tag{2.1}$$

Test solutions C and NP had LSI = -5.9 and -0.6, respectively. Test solutions P and SW had LSI = +1.5 and +0.4, respectively. Indeed, solution P precipitated $CaCO_3$ to yield a ~0.5 mm thick powdery layer over the entire specimen surface shortly after initiation of the test exposure. To examine possible effects of thick precipitate formation in solution P tests, an additional 10 grams $CaCO_3$ reagent grade powder was poured into two of the three test cells after 312 hr and again after 480 hr to form ~5 mm and ~9 mm thick layers, respectively. In test solution SW, a very thin layer of precipitate deposited uniformly on the metal surface. The composition of that layer was expected to be mainly $CaCO_3$ since $CaCO_3$ has a lower solubility product than $Mg(OH)_2$ and is supersaturated in seawater (Mantel et al., 1992). Typically, $Mg(OH)_2$ is undersaturated at nearly neutral pH precipitating in considerable amounts at pH>9.3 (Barchiche et al., 2003). The deposits in both P and SW solutions were washed off readily during cleaning.

The immersion tests were conducted for up to ~3,100 hr at 22 ± 2°C in duplicate for solutions C, NP, and SW and in triplicate for solution P. Solution pH and electrical conductivity, and open circuit potential (E_{OC}) for each specimen were monitored at selected times. Electrochemical Impedance Spectroscopy (EIS) measurements were obtained at the E_{OC} with a Gamry® PCI4-300 potentiostat in the frequency range from 100 kHz to 1 mHz using a sinusoidal signal of 10 mV_{RMS} amplitude. At the end of the immersion test, the specimens were removed, cleaned by washing with water and ethanol, and visually examined. Additional sets of duplicate specimens placed in solutions P and NP

were used for Mott-Schottky (M-S) tests (De Gryse et al., 1975) determining nominal capacitance-potential behavior with a Solartron 1260/1287 potentiostat/electrochemical interface in the potential range from 0 to -300 mV vs. E_{OC} at a scan rate of 10 mV/sec, a fixed test frequency of 10 Hz, and a 10 mV_{RMS} amplitude. Nominal capacitance evaluation was refined by correction for the effect of the presence of a charge transfer resistance as shown later.

2.3 Results

No under-gasket crevice corrosion developed in any of the specimens for which results are reported. The results reported in this Chapter are those of the specimens #1 in each test solution unless otherwise indicated. The results of the replicate specimens (documented in Appendix A if not presented in this Chapter) was similar to that of the example unless indicated otherwise. In addition to the information provided next, the reader is referred to Table 4.2 in Chapter 4 which summarizes the visual assessment and E_{OC} evolution trends.

2.3.1 E_{OC} Trends and Direct Observations of Corrosion

Figures 2.5 to 2.8 exemplify the E_{OC} evolution of replicate specimens. Immediately after immersion, values of E_{OC} were ~-630 mV, ~-650 mV, ~-800 mV, and ~-750 mV for the solutions C, NP, P, SW, respectively.

After ~180 hr of exposure, the E_{OC} in solution C (Figure 2.5) started to drop abruptly to reach ~-920 ~-950 mV. After ~310 hr (and after ~115 hr for specimen #2), stable isolated pits (a few per specimen) became visible to the

naked eye with typical diameters of ~<0.1 mm as well as an uniform dark grayish layer that covered the entire surface. SEM-EDS analysis of a dried portion of that layer in the specimen #1 showed results consistent with the presence of aluminum hydroxide. The appearance of the strong surface discoloration was associated with a momentary increase in solution pH as explained later. Afterwards, the E_{OC} for both specimens slowly evolved toward a terminal value of ~-830 mV.

In solution NP (Figure 2.6), the E_{OC} decayed to ~-910 mV after ~500 hr of exposure and remained nearly constant afterwards. The appearance of moderate surface discoloration in solution NP did not start concurrent with the beginning of the E_{OC} drop but instead was noted after ~2,250 hr for #1 and ~1,200 hr for #2 in agreement with a moderate solution pH increase as shown later. Post exposure optical 25X examination revealed few small pits.

In solution P (Figure 2.7), the first addition of excess $CaCO_3$ to specimens #1 and #2 caused short term negative and then positive E_{OC} excursions by ~80 mV followed by a slow recovery to a terminal E_{OC} ~-770 mV, little affected by the next $CaCO_3$ addition. The specimen #3 (with no extra $CaCO_3$ addition) showed E_{OC} values ~50 mV more negative than those of the replicate specimens for exposure times ranging from 190 hr to 1,400 hr reaching ~-800 mV after 2,250 hr of exposure. In all specimens, the aluminized surface remained bright throughout the test. Post exposure optical 25X examination revealed no pit formation.

In solution SW (Figure 2.8), E_{OC} of the specimen #1 started to drop steeply immediately after exposure reaching ~-900 mV after ~165 hr. The

duplicate specimen showed noble E_{OC} values for ~265 hr followed by a slow drop to ~-840 mV after ~865 hr. Afterwards, the E_{OC} remained nearly constant for both specimens increasing to ~-805 mV for #1 and ~-835 mV for #2 after ~1,500 hr of exposure. The aluminized surface stayed bright for up to ~525 hr for #1 and ~585 hr for #2 with small isolated pits ~<0.1 mm diameter (a few per specimen) visible to the naked eye. Then, light uniform surface discoloration was noted on both specimens not concurrent with the start of E_{OC} drop.

When present, the pit depths appeared to be limited only to the outer aluminized coating layer since no reddish deposits were noted at the pit mouths. In addition, metallographic examination (detailed in Chapter 4) showed that in all cases, the damage associated with uniform aluminized surface discoloration, during the time frame investigated, appeared to be limited only to the outer coating layer.

2.3.2 Solution Composition

Figure 2.9 shows that immediately after immersion, the bulk pH of all test solutions closely approached the lowest values reported in Table 2.2. However, after equilibrium with the surrounding air was reached, the bulk pH of the solutions NP, P, and SW was expected to naturally evolve toward alkaline values despite the given buffering capacity of those solutions. In solutions P and SW, the bulk pH remained quite stable for the entire exposure increasing to only ~7.8 and ~7.9, respectively. In solution NP, however, the bulk pH increased to ~8.5 after 24 hr and reached ~8.7 near the end of the test. In solution C, the bulk pH

was ~7.7 after 3,000 hr attaining a maximum of ~9.0 at ~310 hr. The brief pH increase and later decrease was not anticipated and the cause of this trend remains unclear at present.

Total hardness and total alkalinity, determined by titration following procedures indicated in the Standard Methods for the Examination of Water and Wastewater (1992), as well as the solution conductivity are reported in Table 2.2. The Fe^{+2} content in all four solutions, measured by Atomic Absorption Spectroscopy after ~2,000 hr of immersion, was <0.01 ppm.

2.3.3 Impedance Behavior

After solution resistance subtraction, the impedance responses for solutions P, NP, and SW at the high frequency end of the impedance diagram revealed capacitive behavior with frequency dispersion that could be reasonably approximated by means of a Constant Phase Angle Element (CPE) [3] at frequencies above a compromise cutoff of ~100 Hz. Data for higher test frequencies showed more pronounced dispersion (possibly reflecting surface roughness, uneven macroscopic current distribution (De Levie, 1967) or spurious wiring effects) and were not used for quantitative impedance evaluation for these solutions (Figure 2.10).

The impedance results for solution NP (Figure 2.11) show an impedance diagram where the 1 mHz impedance modulus initially increased with time,

[3] A CPE has an impedance $Z_{CPE}=1/Y(j\omega)^n$ where $\omega=2\pi f$, Y is the admittance parameter of dimensions $\Omega^{-1}cm^{-2}\ sec^n$ (if area normalized), and n (dimensionless) is the dispersion coefficient (Hsu and Mansfeld, 2001, Lasia et al, 1999).

consistent with generally passive behavior and absence of visual evidence of active aluminized corrosion. The 1 mHz impedance modulus decreased later to values smaller than at the beginning, but even then its magnitude was large (~380 kΩ-cm^2) after ~3,000 hr of exposure. The decrease in the impedance modulus coincided with the appearance of moderate surface discoloration.

In solution P (Figure 2.12), the 1 mHz impedance magnitude of the specimen #1 (and #2 as well) was large (>6,000 kΩ-cm^2) and showed an increasing trend with time. However, upon each $CaCO_3$ addition the 1 mHz impedance modulus showed a pronounced momentary decrease to ~1,450 kΩ-cm^2 and a slow recovery later on to attain ~10,000 kΩ-cm^2 after ~3,000 hr. For the specimen #3 in solution P (Figure 2.13), the 1 mHz impedance magnitude was increasingly large as well reaching ~10,000 kΩ-cm^2 after ~3,000 hr, consistent with generally passive behavior and absence of visual evidence of active aluminized corrosion throughout the exposure in all specimens. For the frequency range analyzed, the impedance diagrams were usually describable by two overlapping loops, both approaching ideal capacitive behavior. The M-S behavior is presented in Section 2.4.2.1 keyed to the analysis of the impedance response.

The impedance results for solution SW (Figure 2.14) show an impedance diagram where the 1 mHz impedance modulus initially increased with time attaining ~365 kΩ-cm^2 at ~504 hr of exposure followed by a decreasing trend to ~270 kΩ-cm^2, consistent with the start of light surface discoloration. Afterwards, the 1 mHz impedance moduli started to increase again to attain values

comparable to those recorded at the beginning. The impedance diagrams can be describable by two distinctive loops, both approaching ideal capacitive behavior.

As will be shown below, the C system had a large Faradaic admittance component that was strongly manifested already at the highest test frequencies. Thus, for solution C the complete impedance spectra were used for the analysis with the understanding that using a CPE for simulation purposes would involve a coarser approximation than in the NP, P, and SW systems. The impedance response at the low frequency end (Figure 2.15) was initially much smaller than in the NP, P, and SW solutions, and for a short initial period there was also a low frequency inductive loop. After some exposure time the 1 mHz impedance modulus decreased even further (to ~68 kΩ-cm^2), coinciding with the appearance of strong surface discoloration, but there was a long term recovery trend toward larger 1 mHz impedance moduli. The diagrams were usually describable by two overlapping loops. Partly as a result of using the entire frequency spectrum, the high frequency loop deviated from ideal capacitive behavior more than in the cases of NP, P, and SW solutions.

2.4 Discussion

2.4.1 Direct Evidence of Corrosion Performance

The detailed direct evidence of corrosion in the various systems presented in the previous section may be summarized as follows. Visual examination of the specimen surfaces indicated no corrosion distress in solution P (which included high carbonate precipitating tendency and moderate chloride content) throughout

the entire test exposure, suggesting good corrosion performance in these environments. The addition of extra powdered $CaCO_3$ to solution P did not appear to have had harmful consequences despite momentary electrochemical disturbances as explained below. There was moderate surface discoloration with formation of few small isolated pits in solution NP (which included high total alkalinity without carbonate precipitating tendency and moderate chloride content).

A few small isolated pits followed by strong aluminized surface discoloration were noted early on in solution C, which had low alkalinity, negligible $CaCO_3$ precipitating tendency, and moderate chloride content. A few small isolated pits but only light discoloration appeared also early on in the exposure to solution SW, that had moderate alkalinity, high precipitating tendency, and high chloride content/very low resistivity.

The corrosion distress and pit penetration in all solutions was not found to extend beyond the outer aluminized layer for the time frame examined. A comprehensive summary of direct evidence of corrosion performance concerning these and subsequent experiments is provided later in Table 4.2, Chapter 4.

2.4.2 Corrosion Mechanisms and Analysis of the Impedance Response

In Chapter 1, a general introduction to corrosion phenomena in aluminum was presented. In the rest of this dissertation, the terminology used to refer to the various corrosion features and events will be used more specifically as in the following.

The term inclusions will indicate the Fe-rich intermetallic precipitate particles present in the outer aluminized surface layer. The inclusions have been identified as preferential sites for both cathodic reactions and effective pit initiation (Nisancioglu, 1990, Johnson, 1971).

Acidic oxidation of aluminum will be referred to as a process where aluminum dissolves into an acidic electrolyte according to the reaction $Al \rightarrow Al^{+3} + 3e^-$ where Al^{+3} ions are soluble. Alkaline oxidation of aluminum refers to a process of corrosion of aluminum in an alkaline environment, postulating that a film is always present on the aluminum surface (Pyun et al, 1999). As indicated in Chapter 1, such event may take place when the solution pH near the metal surface normally exceeds ~8.5 (Pourbaix, 1974). In such a case, the initially protective aluminum passive film covering most of the aluminized surface is (in the form of amorphous $Al(OH)_3$ or a comparable intermediate compound as part of the film) becomes unstable and is expected to be readily chemically attacked at the film-solution interface by OH^- ions with formation of soluble aluminate ions $Al(OH)_4^-$ (Doche et al, 1999). The resulting enhanced dissolution of aluminum ensues through enhanced transport of the relevant species through a much thinned or more defective passive film (Kolics et al, 2001, Sullivan et al, 2000). Under those conditions in the highly alkaline limit, a likely sequence of aluminum dissolution proposed by MacDonald et al (1988) and later by Chu et al (1991) is as follows:

$$Al_{SS} + OH^- \rightarrow Al(OH)_{ads} + e^- \quad (2.2\text{-A})$$

$$Al(OH)_{ads} + OH^- \rightarrow Al(OH)_{2ads} + e^- \quad (2.2\text{-B})$$

$$Al(OH)_{2ads} + OH^- \rightarrow Al(OH)_{3ads} + e^- \quad (2.2\text{-C})$$

$$Al(OH)_{3ads} + OH^- \rightarrow Al(OH)_4^- \quad (2.2\text{-D})$$

where Al_{SS} represents aluminum sites at the metal-film interface, the subsequent steps indicate metastable film formation, and the last step is the chemical dissolution at the film-electrolyte interface. It is noted that since alkaline conditions tend to develop around cathodic sites, alkaline oxidation of aluminum can be enhanced around inclusions, especially if the solution is not buffered. Such enhanced dissolution has been extensively documented in the literature (Szklarska-Smialowska, 1999, Suter and Alkire, 2001).

A pit will be referred to as an occluded acidic zone where acidic oxidation of aluminum takes place (Sasaki and Isaacs, 2004, Wiersma and Herbert, 1991, Nguyen and Foley, 1979). As mentioned in Chapter 1, several mechanisms have been proposed to describe pitting corrosion of aluminum in chloride solutions (McCafferty, 2003, Foley, 1986, McCafferty, 1995). There is common agreement that chloride ions migrate to the interior of the pit cavity once a pit initiation event took place. To maintain charge neutrality inside the cavity, H^+ ions also accumulate in the cavity, which in turn, decrease the pH there to values below the passivity range of aluminum, resulting in a self-sustaining pit (Seri and Furumata, 2002, Frankel, 1998, Verhoff and Alkire, 2000). The pit geometry needs to be such to maintain active regime inside by efficiently separating the environment inside from that outside, and/or to providing enough ohmic potential

drop between the outside and inside regions (Pickering, 2003). Inside the pit cavity acidic oxidation of aluminum takes place.

The corrosion mechanisms proposed below will be evaluated by and used in the interpretation of the results from the EIS experiments. Over the past decades, the EIS technique has been increasingly used to elucidate corrosion mechanistic issues of aluminum exposed to various environments (Mansfeld et al, 1990 and Shao et al, 2003). From the numerous investigations reviewed for this dissertation, it can be concluded that there is little consensus on the explanation of the dominant corrosion mechanisms and the models used to simulate the impedance data of aluminum alloys (De Witt and Lenderink, 1996, Aballe et al, 2001, Emregul and Abbas Aksut, 2000, Sherif and Park, 2005, Sasaki and Isaacs, 1990). It is thus noted that the mechanisms and the associated analog equivalent circuit chosen to represent the impedance response for the present case may not be unique, and that alternative mechanisms and analog equivalent circuits may explain equally well the observed impedance behavior. Indeed, other corrosion mechanisms and their corresponding analog equivalent circuits were explored as well, but the ones presented here were chosen mainly for overall simplicity and having provided a reasonable account of the observed impedance spectra. The approach used here is summarized by the analog equivalent circuit shown in Figure 2.16, which serves all the cases considered but with the meaning of some of the individual components depending on the case as detailed in the next sections.

It is noted that all the corrosion mechanisms considered in this dissertation involve abiotic systems, but the absence of microbiologically induced corrosion (MIC) has not been ruled out, other than by the lack of indications of any conspicuous biofilm in the surfaces of the test specimens. Future investigations should seek to ascertain the role, if any, that MIC phenomena can play in the deterioration of aluminized steel in the environments of interest.

2.4.2.1 Solution P and Solution NP before Surface Discoloration

The following analysis applies to solution P over the entire exposure time and solution NP for the regime before the appearance of moderate aluminized surface discoloration. In those cases, the initial system E_{OC} was quite negative reflecting the coupled potential of the inclusions with the slow passive dissolution of the larger area aluminum solid solution phase surrounding the inclusions. As time progresses, a more mature passive film is expected to experience slower dissolution with potentials drifting to moderately nobler values as observed.

The impedance response for the present passive systems is interpreted with the aid of the analog equivalent circuit shown in Figure 2.16. The resistor R_S represents the ohmic solution resistance [4]. The working assumption is made that the impedance response of the passive film (which occupies most of the specimen surface), when combined with the Helmholtz layer capacitance C_H, is predominantly capacitive and may be represented by the constant phase angle element CPE_F in the upper branch of the circuit. The film surface is taken to be

[4] All components in Figure 2.16 are expressed as surface-normalized elements by dividing/multiplying as appropriate by the nominal specimen area (95 cm^2).

the locus of a slow, nearly uniform anodic dissolution reaction as stated above, which is also only mildly potential dependent so its admittance is neglected. As mentioned earlier, the matching cathodic reaction at E_{OC} is expected to occur primarily at the inclusions (Nisancioglu, 1990, Johnson, 1971) represented by the lower branch of the circuit. The buffering capacity of these solutions is expected to neutralize the OH^- ions formed by the cathodic reaction so that increase in the local pH is minimized at least at the beginning of the exposure. To account for the observation of a low frequency loop in the impedance diagrams, the cathodic reaction is proposed to proceed in coupled steps of the type where surface coverage by an intermediate adsorbate alters the rate of the next step (Bessone et al., 1992, de Wit and Lenderink, 1996, Armstrong and Edmondson, 1973, Epelboin and Keddam, 1970). The resulting response is pseudocapacitive, (approximated by the element CPE_{AL2}) with a high-frequency limit resistance R_{AL1}, and a low frequency limit resistance $R_{AL1}+R_{AL2}$ (Armstrong and Edmondson, 1973). Consequently, the pseudocapacitive element CPE_{AL2} is placed across the resistance R_{AL2} as shown. A detailed explanation for the proposed modeling of the impedance behavior for this mechanism is shown in Appendix C.

The analog equivalent circuit in Figure 2.16 with EIS parameters reported in Tables 2.4 and 2.5 yielded good best-fit simulations of the impedance responses of both solutions, shown by the solid lines in Figures 2.11 through 2.15. Although CPEs were used in the circuit, the best fit values of n_F and n_{AL2} for both solutions were close to unity, indicating little deviation from ideal capacitive

behavior. Sometimes best fit values of n_F and n_{AL2} slightly >1 were obtained for one of the CPEs. In those cases, there was little sensitivity of the fit to the choice of which element approached ideal behavior more closely. For those cases a value n_{AL2}=1 was imposed and n_F was allowed to vary resulting in n_F values >0.93 (subscripts are keyed to the element designations in Figure 2.16).

Figures 2.17 and 2.18 show examples of the time dependence of the admittance parameters and resistive components thus calculated (the Figures contain also the results for the NP system after aluminized surface discoloration and for the other solutions as well, to be discussed later).

Throughout the test, the values for R_{AL2} and R_{AL1} for solution P were large (~2.5 10^6 Ω-cm^2 and ~1.5 10^7 Ω-cm^2, respectively), and tracked roughly together as exposure time progressed, in keeping with the above assumption of coupled steps of the associated cathodic reaction. Similar trends were noted for solution NP with large values of R_{AL2} and R_{AL1}, both reaching ~3 10^6 Ω-cm^2 before the start of aluminized surface discoloration.

The Y_{AL2} values in both solutions were much larger and variable with time than $Y_{F,}$ consistent with the assumed origin for CPE_{AL2} other than film capacitance. In solution P, Y_{AL2} values were initially ~4 10^{-5} sec$^{n_{AL2}}$/Ωcm^2 followed by a strong momentary increase to ~1.3 10^{-4} sec$^{n_{AL2}}$/Ωcm^2 only noticeable upon the first addition of extra powdered $CaCO_3$ to specimens #1 and #2 and a later decrease to a terminal value of ~2.2 10^{-5} sec$^{n_{AL2}}$/Ωcm^2. Y_{AL2} was nearly constant (~3.3 10^{-5} sec$^{n_{AL2}}$/Ωcm^2) for specimen #3 in P, which had no addition of powdered $CaCO_3$. The Y_{AL2} values for the duplicate specimens in solution NP were initially

~4.6 10^{-5} $sec^{n_{AL2}}/\Omega cm^2$ decreasing to ~1.4 10^{-5} $sec^{n_{AL2}}/\Omega cm^2$ recorded before the start of the appearance of aluminized surface discoloration.

The association of CPE_F with the passive film capacitance is further supported by the following considerations. The Y_F values were similar in both solutions (~3.4 10^{-6} to ~1 10^{-5} $sec^{n_F}/\Omega cm^2$) and changed relatively little with exposure time. In the following, the charge storage function associated with CPE_F will be quantified by a nominal capacitance C_F that has the same imaginary impedance component as CPE_F at a suitable frequency f_N. For ease of comparison with the M-S results, f_N was chosen to be 10 Hz. In fact, the sensitivity of C_F to the choice of f_N was expected to be small since n_F approached unity. Thus,

$$C_F = \frac{Y_F \cdot (2\pi \cdot f_N)^{n_F - 1}}{\sin\left(n_F \cdot \frac{\pi}{2}\right)} \tag{2.3}$$

which yielded C_F values from ~2.6 to ~7.9 $\mu F/cm^2$, numerically close to Y_F since n_F~1. These values are comparable to those reported in the literature for passive aluminum (Pyun, 1999, Bockris and Kang, 1997). If the passive film behaved as an ideal capacitor of thickness L and dielectric constant ε, its area-normalized capacitance C_i would be given by:

$$C_i = \frac{\varepsilon \cdot \varepsilon_0}{L} \tag{2.4}$$

where ε_0 is the permittivity of vacuum. Assuming L~5 nm and ε~9 (typical of thickness of naturally grown passive films on aluminum (Bessone et al., 1983, and Diggle, 1972) and of solid or hydrated aluminum oxides, respectively) yields

C_i~1.60 μF/cm^2. That value is much less than typical values of C_H (Bockris and Kang, 1997) so the combined series interfacial capacitance is still ~C_i, which approximates well the low end of the C_F value range obtained above. The approximation could be even better if it included natural surface roughness which would increase the effective value of C_i above that of the ideally flat surface assumed for Eq. 2.4. Similar general behavior on passive aluminum has been observed often (Lee and Pyun, 1999) and supports the interpretation that the high frequency loop in the spectra corresponds to the passive film.

Capacitive behavior in a semiconducting passive film often reflects the presence of a space charge zone that may extend through the entire film thickness L (the entire film thickness then acting effectively as a dielectric), or have a depth d_{SC}<L. The M-S experiments sought to elucidate that issue for the present systems since in the first case the film capacitance is not potential dependent upon brief cathodic excursions from the E_{OC}. In the latter case, however, the differential capacitance of the film is still approximately given by Eq. 2.4 but replacing L with d_{SC} which varies with potential E. For example, if the film is an n-type semiconductor as generally observed in aluminum (Bockris and Kang, 1997 and Fernandes et al, 2004) and the polarization conditions are adequate, then d_{SC}~$(2\ \varepsilon\ \varepsilon_0\ q^{-1}\ (E-E_{fb})\ N_d^{-1})^{0.5}$, where q is the electron charge, N_d is the net density of electron-donor defects (assumed to be constant for simplicity), and E_{fb} is the flatband potential (Morrison, 1980).

Assuming $C_F(E) << C_H$, $C_F(E)$ was estimated from the 10 Hz M-S impedance measurements at 100 mV intervals by:

$$C_F(E) \sim \frac{-k_C(E)}{2\pi \cdot f_N \cdot Z''(10Hz)} \quad (2.5)$$

where Z"(10Hz) is the imaginary component of the impedance and $k_C(E)$ is a correction factor close to unity. The factor $k_C(E)$ corrected for the obscuring effect of R_{AL1}, which at the lowest potentials (with R_{AL1} small) could cause the value of Z"(10Hz) to be significantly smaller than what would have resulted from the capacitive element alone [5].

Figure 2.19 shows the M-S results in duplicate in solutions NP and P for ~330 hr of exposure obtained per the above procedure. At the time of the tests, no apparent corrosion was observed in any of the specimens. The results show nearly constant capacitance with potential (from ~3.4 to ~5.9 μF/cm^2), which is therefore consistent of a space charge zone spanning the entire film thickness.

2.4.2.2 Solutions C, SW, and Solution NP after Surface Discoloration

The information collected in this investigation does not permit to clearly identify the corrosion mechanisms associated with the activation of the aluminized surface manifested by uniform discoloration and the appearance of

[5] To obtain $k_C(E)$, impedance measurements spanning the range 100 Hz-1 Hz were conducted at a few selected potentials over the same potential range as the M-S tests. Those measurements yielded at each selected potential values of Y_F and n_F which were used to calculate accurate values of $C_F(E)$ using Eq. 2.3. Therefore at the selected potentials $k_C(E) = -C_F(E)\ 2\pi\ f_N\ Z''(10Hz)$. Values of $k_C(E)$ at intermediate potentials were then assigned by polynomial interpolation.

few small macroscopic pits. Thus, additional experiments will be needed in the future to elucidate such mechanisms.

However, it can be speculated that the cases of development of aluminized surface discoloration (moderate in NP later on in the test and strong in C early on) may be attributed to macroscopically uniform alkaline oxidation on the aluminized surface. High pH conditions developed spontaneously in the bulk of solutions C (early in the exposure) and in solution NP (later on). The pH increase in C was not expected and it remains unsolved at present. The pH increase in NP was as predicted by the solution chemistry evolution toward equilibrium with the surrounding air in the pseudo-closed test cells. Those conditions coincided with aluminized surface discoloration, and with marked changes in the specimen corrosion rates (as shown later), indicative of activation of the aluminized surface. Thus, dissolution (with formation of soluble $Al(OH)_4^-$ ions per Eq. 2.2-D) of the aluminum oxide film due to alkaline conditions appears to be the main corrosion process in these cases. It is likely that, especially in the case of solution C which is unbuffered, alkaline oxidation was more intense around the rim of the inclusions due to the increase in pH there from local O_2 reduction. Thus, while macroscopically uniform, the corrosion may have been more localized at the microscopic, inclusion-scale level. As time progressed, the $Al(OH)_4^-$ concentration near the metal surface may have reached a critical value so precipitation of aluminum corrosion products in the form of hydrated $Al(OH)_3$, by the reaction $Al(OH)_4^- \rightarrow Al(OH)_3 + OH^-$, is expected to occur (Nisancioglu and Holtan, 1979). That event would explain the observed corrosion deposits and

consequent discoloration of the entire aluminized surface in the solutions C and NP. In those solutions the observed few macro pits are deemed to be relatively inconsequential because of their small number and dimensions. The resulting large combined associated ohmic resistance of the macro pits would result on a total macro pit anodic current that would be only a small fraction of the total (Oltra and Keddam, 1988). It is emphasized that the above scenario is speculative and that, in the absence of additional experimental data, other corrosion modalities cannot be completely ruled out. In particular, there could be significant micro pit activity with internal acidic corrosion, at the inclusion-scale level. Such condition is explored further in Chapter 4, where instances of discoloration of the aluminized surface in the absence of an increase in pH of the bulk solution are addressed for some of the test solutions.

The situation noted for NP and C was reversed in the case of solution SW where surface discoloration was light but the presence of a few macro pits, likely nucleated around inclusions, was notable. This condition can be explained by the strong aluminum pitting tendency in highly concentrated chloride solutions as in the solution SW (~20,000 ppm chloride concentration as opposed to only ~370 ppm in the other media used in this work). A common indicator of the pitting tendency of a particular metal in a given solution is the pitting potential E_{pit} at which pits can be initiated and sustained. As a general rule, the lower the value of E_{pit}, the easier is the development of pits as less oxidizing power is required from the electrolyte. For pure aluminum, E_{pit} is a function of chloride

concentration as originally determined by Kaesche (1962) and reproduced by Bohni and Uhlig (1969) of the form:

$$E_{pit}\ (V\ vs\ SCE) = -0.124 \cdot \log\left(Cl^{-}\right) - 0.745 \qquad (2.6)$$

For solution SW, the initial relatively positive E_{OC} was dictated by the active corrosion of the inclusions in the high chloride environment and had a value in the order of E_{pit} for pure aluminum (~-750 mV for 20,000 ppm) so pit initiation was promoted. Indeed, for aluminum alloys as in the case of the outer aluminized layer, the presence of inclusions may lower the value of E_{pit} relative to pure aluminum (Furuya and Soga, 1990) further facilitating initiation of pits under the initial exposure conditions. In unbuffered solutions inclusions may additionally facilitate pitting by local alkalinization and subsequent corrosion of the aluminum creating a groove around the perimeter of the inclusion (Nisancioglu et al, 1981, Rynders et al, 1994, Van de Ven and Koelmans, 1976). This mechanism may not have been dominant in the strongly buffered SW solution. Upon pit formation, E_{OC} drops due to enhanced electron release by aluminum corrosion within the active pits and to some extent by aluminum alkaline oxidation (again, limited in this buffered solution). The potential drop proceeded until the current for oxygen reduction at inclusions plus hydrogen evolution inside pits matched the overall rate of aluminum oxidation (oxidation of the inclusions considered to be negligible at the more negative potential). Upon the potential drop some pits may have become inactive, eventually leading to a terminal density of pits per unit area that was sustained over long periods.

Thus, in the SW medium anodic action on the aluminized surface was likely limited to the active pits and the observed light discoloration indicated only secondary global distress in the form of vestigial alkaline oxidation. In the other solutions, having only ~370 ppm chloride concentration, the value of E_{pit} for pure aluminum is ~-650 mV. While that value was reached in some cases early on (possibly accounting for the observation of some pits in those cases), the long term E_{OC} values for NP and C were much lower (-900 mV and -830 mV) so pit growth was less likely to be sustained. In solution P, the long term E_{OC} value was ~-760 mV, but early potentials were significantly more negative so initiation was likely inhibited throughout consistent with the lack of observation of macroscopic pits in that solution.

The impedance responses for solutions C, SW, and NP (after the start of active aluminized corrosion) were also simulated using the analog equivalent circuit in Figure 2.16 with R_S and CPE_F having essentially the same meaning as before. However, the proposed meaning of the components of the circuit of the lower branch is quite different to that presented for passive aluminized steel as explained next. Per the above discussion, it is tentatively proposed that the macroscopically uniform corrosion manifested by discoloration is localized to micro sites at the inclusion scale level. Corrosion is proposed to proceed simultaneously also at macro active sites in the scale of the observed macro pits. While it is recognized that alternative scenarios are also plausible, these assumptions resulted in reasonable approximations of the overall impedance behavior, and will be considered as a first step in understanding a complex

system, pending future development of experimental evidence. Per the assumptions, the local electrolytic current distribution around each micro and macro active site can be associated with a local ohmic resistance component, $R_{SL}=\sigma^{-1}/4r_{PS}$, where r_{PS} is the radius of the active zone (Oltra and Keddam, 1988). At high enough frequencies R_{SL} will, at each active site, be significantly larger than the modulus of the capacitive impedance of the site. At those high frequencies, the resistive effects from all the sites can be approximated by a simple parallel combination given by:

$$R_{AL1}^{*}=\sigma^{-1}\,(4\,A_{AL})^{-1}\,[r_{PS}\,N_{PS}+r_{PL}\,N_{PL}]^{-1} \qquad (2.7)$$

where A_{AL} is the nominal aluminized area, N_{PS} is the number of microsites (assumed for simplicity to be all of radius r_{PS}) per cm^2, and N_{PL} is the number of pits (assumed all to have radius r_{PL}) per cm^2. The relative contribution of macro and micro sites cannot be uniquely ascertained from the impedance response alone. However, the fit values of the impedance response for R_{AL1}, reported in Tables 2.5 through 2.7 for solutions C, NP, and SW, are in reasonable agreement with the values of R_{AL1}^{*} calculated for the σ values shown in Table 2.2, r_{PS}~2 μm typical of the Fe-rich particle size, r_{PL}~100 μm for typical macropit radius, $N_{PL}<5/cm^2$, and assuming $N_{PS}\sim10^3/cm^2$. Within the context of the model assumptions, such value of N_{PS} suggests that only a fraction of all possible sites were active, a situation not unusual in cases of localized corrosion (Seri and Masuko, 1985).

At high enough frequencies, the impedance is dominated by the parallel combination of R_{AL1} and the film capacitance represented by CPE_F as discussed

earlier. Each active site is assumed to have a Faradaic polarization resistance and an interfacial capacitance with some degree of non ideality. Assuming that this combination has a relatively large time constant relative to that of the resistive-film capacitance considered before, the combined behavior can be represented by the discrete parallel combination of all the polarization resistances R_{AL2} and the corresponding interfacial capacitances CPE_{AL2}.

The equivalent circuit fit calculations for solution C yielded small values (~0.89 to ~3.2 kΩ-cm^2) for R_{AL1}. Accordingly, R_{AL2} was in the order of the *lf* impedance modulus (~68 kΩ-cm^2 early on, ~495 kΩ-cm^2 near the end of the test). Both capacitive elements Y_F and Y_{AL2} had significant frequency dispersion: n_F~0.57 to 0.63 (consistent with the highly distorted appearance of the high frequency loops in Figure 2.15) and n_{AL2}~0.69 to 0.80. The values of Y_F were on the order of ~4.6 10^{-6} to ~2.9 10^{-7} sec^{nF}/Ωcm^2 at the end of the test and, considering the uncertainty inherent to the high frequency dispersion, the C_F values were consistent with the values obtained in the other solutions. Even though there is considerable deviation from ideally capacitive behavior, the values obtained for Y_{AL2} (~6.9 10^{-5} early on to ~1.7 10^{-5} sec^{nAL2}/Ωcm^2) were comparable to those obtained for solutions P and NP.

The equivalent circuit fit calculations for solution SW yielded values for R_{AL2} ranging from ~173 kΩ-cm^2 early on to ~143 kΩ-cm^2 near the end of the test), and R_{AL1} values from ~160 kΩ-cm^2 at the beginning to ~255 kΩ-cm^2 at the end of exposure. The capacitive elements Y_F and Y_{AL2} had little frequency dispersion (n_F~0.91 and n_{AL2}~0.98) as shown in Figure 2.14. The values for Y_F

ranged from ~1.4 10^{-5} to ~1.7 10^{-5} $sec^{nF}/\Omega cm^2$ by the end of the test. The nominal capacitance C_F calculated per Eq. 2.2 for a frequency f_N = 10 Hz was ~10.5 $\mu F/cm^2$ fairly invariant with time comparable to those obtained for the P system.

For the period of aluminized surface discoloration, the values of R_{AL2} and R_{AL1} for solution NP decreased to ~2 10^5 Ω-cm^2 near the end of exposure. Both capacitive elements Y_F and Y_{AL2} increased after aluminized discoloration to ~10^{-5} $sec^{nF}/\Omega cm^2$ ~10^{-4} $sec^{nAL2}/\Omega cm^2$, respectively, with little frequency dispersion (n_F~0.94 and n_{AL2}~1.00).

2.4.3 Computation of the Nominal Corrosion Current Density

The following nominal corrosion current density i_{corrAL} estimates are consistent with the proposed corrosion mechanisms and the associated analog equivalent circuit presented earlier. Figure 2.21 illustrates the i_{corrAL} evolution as a function of exposure time. Comparable results were recorded for the duplicate specimens shown in Appendix A.

For specimens in solution P over the entire test exposure and for the specimens in solution NP for the period before the appearance of uniform discoloration, a working assumption is made that the high frequency limit resistance (R_{AL1}) is approximately the same as that of a cathodic reaction under purely activation control, having a Tafel slope value β_{C2}~200 mV. The value of β_{C2} is representative to those reported for likely coupled cathodic reactions on aluminum (Armstrong and Braham, 1996) and also comparable to those obtained from cyclical polarization tests shown in Chapter 3 for unblemished aluminized

steel exposed to solution P. Since the rate of the anodic reaction was considered to be nearly potential-independent, and hence its admittance negligible, the nominal corrosion current density i_{corrAL} can then be obtained from the Stern-Geary relationship applied to the cathodic reaction only (Stern and Geary, 1957):

$$i_{corrAL} \sim \beta_{C2} (2.3 R_{AL1})^{-1} \quad (2.8)$$

To estimate i_{corrAL} for solutions C and SW, and for solution NP after the start of aluminized active corrosion, the same working assumptions were made as before but using only the value of R_{AL2} and considering for simplicity that both anodic and cathodic reaction polarizability have the same anodic and cathodic Tafel slopes $\beta_{C2}=\beta_{a2}$ and equal to 200 mV as stated previously. Thus, the i_{corrAL} under those conditions is (Lorenz and Mansfeld, 1981):

$$i_{corrAL} \sim 0.5\, \beta_{C2} (2.3 R_{AL2})^{-1} \quad (2.9)$$

The values of i_{corrAL} were extremely small for solution P (~0.03 μA/cm^2 early on to ~0.008 μA/cm^2 by the end of exposure). However, the first addition of excess $CaCO_3$ to specimens #1 and #2 caused a momentary i_{corrAL} increase to ~0.1 μA/cm^2 not observable after the next $CaCO_3$ addition. Similarly, i_{corrAL} values for the specimen #3 in P (no extra $CaCO_3$ added) were extremely small ~0.06 early on to ~0.001 μA/cm^2 by the end of the test. The values of i_{corrAL} of the duplicate specimens in solution NP before the start of aluminized discoloration were ~0.15 μA/cm^2 for both at the beginning, decreasing to ~0.03 μA/cm^2 after ~1,400 hr. The i_{corrAL} values for solution P and for solution NP for the period before the onset of aluminized discoloration were consistent with visual observation of corrosion-free aluminized steel surface.

For solution NP for the period after the onset of active aluminized corrosion, the i_{corrAL} of the duplicate specimens showed an increasing trend to reach by the end of the test a modest i_{corrAL} of ~0.2 μA/cm^2, in agreement with moderate uniform aluminized discoloration. For solution C, the duplicate specimens had i_{corrAL} values ranging from ~1.05 μA/cm^2 early on to ~0.13 μA/cm^2 after ~3,000 hr. As expected, the highest corrosion current density coincided with the appearance of uniform strong surface discoloration. The smaller i_{corrAL} values in C recorded later on are in agreement with the decrease of the solution pH back to the range of aluminum passivity. The i_{corrAL} values for the duplicate specimens in solution SW were nearly constant with time reaching ~0.3 μA/cm^2 at the end of exposure, in reasonable agreement with the results reported by Johnsson and Nordhag (1984) for aluminized steel Type 2 exposed to natural seawater at room temperature.

It is important to note that the above estimates reflect the application of a tentative interpretation of the impedance response, and that alternative scenarios should be examined in future research. Efforts should be aimed in particular at ascertaining to which extent the macroscopically uniform corrosion may be localized at the inclusion scale level.

2.5 Implication of the Results

The following tentative durability projections for a generic field application consider a total aluminized coating thickness of 45 μm (30 μm outer and 15 μm inner layers) covering uniformly a base steel 1,500 μm thick approximating a

gage 16 sheet stock, and focus on the corrosion performance of the aluminized coating layers coated on both sides of the base steel as well as the base steel itself. It is strongly emphasized that these projections are nominal in nature since test times in the present experiments were only a small fraction of the typical actual service lives involved in field applications.

Recent field inspections in Florida have shown that the inner aluminized coating layer, of nearly invariant thickness but with several small breaks especially at the rib bends in a spiral rib aluminized steel Type 2 culvert component, appears to provide little corrosion protection to the underlying steel. Even in aluminized steel without bends like those used here, breaks not related to corrosion in the inner layer were clearly noted. Based on this observation, no durability credit was assigned to the inner coating layer in this investigation. Hence, the projected service life SL is defined as the number of years to penetration through the base steel and the outer aluminized layer on both sides of the base steel, considering that penetration occurs from both sides of the metal as it is usually observed in field exposures. For the present calculations, it is also assumed that similar environments exist on each side of a pipe so the corrosion rates at both sides are equal. Thus, the projected SL is for simplicity taken to be equal to the sum of the SL of the outer layer on either pipe side plus the amount of time needed to penetrate half of the thickness of the base steel.

The values of i_{corrAL} as a function of exposure time obtained in the laboratory experiments are summarized in Tables 2.4 through 2.7. Those discrete i_{corrAL} values were used to estimate SL of the outer aluminized layer in all

solutions for the exposure period from t=0 to t_f where t_f is the time for the end of the test and $i_{corrAL}(t_i)$ is the time evolution corrosion current density obtained from the EIS measurements where i=1 to n represents each EIS measurement. Thus, SL for the outer coating layer is computed as:

$$SL = 30 \cdot \left[\frac{A_W}{t_f \cdot n \cdot F \cdot \rho_{AL}} \cdot \sum_{1}^{n-1} i_{corrAL_i} \cdot (t_{i+1} - t_i) + i_{corrAL_1} \cdot t_1 + i_{corrAL_n} \cdot (t_f - t_n) \right]^{-1} = 30 \cdot CR_{AL}{}^{-1} \quad (2.10)$$

where A_W is the aluminum atomic weight, n=3 for the Al/Al^{+3} reaction, ρ_{AL} is the aluminum density, and the term in brackets corresponds to the aluminum corrosion rate CR_{AL}.

For solution P, which may be taken as representative of media with high carbonate scaling tendency, nearly neutral pH, and moderate chloride content, the extremely small CR_{AL} (<0.24 μm/yr) recorded in this investigation if sustained at these levels would indicate a full consumption of the outer layer in >100 yr of service, consistent with the projected SL computed from corrosion rate estimates of field culvert pipes exposed to tropical environments of composition similar to solution P (Bednar, 1989). Additions of extra $CaCO_3$ emulating solutions with higher carbonate precipitating tendencies caused short-term increase to ~1 μm/yr, but even this transient larger rate did not cause visual corrosion damage to the outer aluminized steel.

Durability projections become distinctly more pessimistic for some of the other conditions investigated. For instance, for solution NP which may be representative of media with high alkalinity but low hardness, high pH, and moderate chloride content, CR_{AL} was modest (~1.04 μm/yr). If this rate is

maintained, it would mean a full outer coating loss in ~30 yr of service. The high rate observed for this solution mainly ascribed to the high pH of the solution bulk above the aluminum passivity range is in agreement with the results obtained from field studies conducted on aluminized steel Type 2 exposed to environments with solution pH>9 (Pyskadlo and Ewing, 1987). For solution C, which may be taken to be representative of media with both low alkalinity and hardness, high pH, and moderate chloride content, CR_{AL} was ~3.16 μm/yr, which would indicate a full outer coating layer consumption in only ~10 yr, consistent with the strong aluminized surface discoloration observed early on in the exposure.

For solution SW emulating seawater composition, the CR_{AL} was modest (~3.25 μm/yr) indicating a full outer layer consumption in ~9 yr of service. While subject to considerable uncertainty, the corrosion rate becomes important considering that the corrosion is strongly localized, with consequent risk of aluminized layer penetration early in the life of a component exposed to similar media. This finding is in agreement with the observations reported by Perkins et al (1982) and Stavros (1984), who asserted that severe pitting corrosion of aluminized steel exposed to very aggressive environments is determinant when forecasting durability in this type of medium.

After full consumption of the outer aluminized layer, corrosion of the base steel starts and is expected to proceed at the rates of ~12 μA/cm^2 in SW and ~10 μA/cm^2 in the other media as reported in Chapter 4. Those values are in agreement with corrosion rates reported by McCafferty (1974), Oh et al (1999),

and Sander et al (1996). The corresponding projected SL values for the base steel would be ~6 yr for SW and ~8 yr for the other media.

Table 2.8 summarizes the overall SL estimates (SL of the outer layer plus that of the base steel) obtained in this investigation.

As mentioned in Chapter 1, a variety of predictive methods have been proposed for forecasting the service life of metallic components. Nevertheless, special consideration is given to the most relevant forecasting methods, e.g. the AK Steel, the California, the AISI, and the FDOT methods. The computed SL estimates using those methods, reported in Table 2.8, were determined based on the solution compositions shown in Table 2.2 for a 16-gage aluminized steel Type 2. Comparison between the SL projections from the present experiments and those obtained from the forecasting methods are presented in the next paragraphs.

For solutions with high scaling tendencies, moderate chloride content, and nearly neutral pH (solution P), the SL estimates computed by the FDOT and AISI forecasting methods were somewhat conservative (and overly conservative in the case of the AK Steel and California methods) compared to the SL projections obtained here. For the solution with high alkalinity/low hardness, moderate chloride content, and high pH (solution NP), SL estimates obtained from the FDOT method were in good agreement with the results reported in this investigation. On the other hand, the AISI, California, and AK Steel methods yielded either liberal or conservative estimates compared with the present findings. For solutions with moderate chloride content, low both alkalinity and

hardness, and high pH (solution C), SL projections were in close agreement with those determined by the AK Steel, California, and FDOT methods and overly conservative compared to durability projections obtained by the AISI method. In extremely aggressive solutions of low resistivity, high chloride content, and nearly neutral pH (solution SW), the AISI method yielded comparable estimates of durability relative to the present findings, whereas the California method projected shorter service lives. In highly aggressive environments, no durability credit is given by the FDOT method and no SL projections are given by the AK Steel method for solutions with scaling indexes beyond ~800 ppm.

Based on the above, for unblemished aluminized steel the present findings would support retaining the present FDOT guidelines regardless of scaling tendency for environments with moderately low resistivity such as those used in the tests (e.g. ~500 Ω-cm to ~1,000 Ω-cm) and neutral to mildly alkaline conditions (e.g. ~7.5<pH<~9.0). The results also support exploring the use of alternative guidelines such as the AISI method for environments with extremely high chloride contents (e.g. resistivity <50 Ω-cm) and nearly neutral pH. Eventual changes in existing guidelines should consider not only the specific results of this investigation but also the entirety of the performance record of aluminized steel pipe. It is also strongly cautioned that other corrosion processes, such as MIC, may be active in the field but have received little attention in prior performance studies and were not addressed in this investigation. Factors like MIC may be important in the performance of aluminized steel, and need additional determination for possible inclusion in future durability forecasting methods.

It is also noted that the above findings apply to aluminized steel with an initially unblemished metallic coating. In actual metal forming and subsequently field application practice, the aluminized steel component (e.g. culvert pipes) is liable to surface distress that may range from minor to severe, exposing a certain amount of base steel. Determination of corrosion performance in those circumstances is addressed later in Chapter 4.

2.6 Conclusions

1. In >3,000 hr tests, unblemished aluminized steel Type 2 showed extremely low nominal corrosion rates (<~0.008 μA/cm^2) by the end of the test period in an environment with moderate chloride content but of high carbonate precipitating tendencies (the solution P), supporting prior evidence in favor of a carbonate scale tendency criterion to predict corrosivity.
2. In a high total alkalinity, but non-scale forming medium with moderate chloride content (the solution NP), unblemished aluminized steel Type 2 showed low/moderate nominal corrosion rates (<~0.10 μA/cm^2) for most of the test exposure. However, electrochemical impedance measurements revealed higher nominal corrosion rates (~0.22 μA/cm^2) by the end of exposure concurrent with the appearance of uniform discoloration, indicative that corrosion may be of importance over longer periods upon evolution of solution pH to higher values.
3. Exposure to moderate chloride content but in the absence of total alkalinity and carbonate scaling tendency (solution C) led to strong uniform

aluminized surface discoloration and the appearance of few macro pits early on, consistent with early development of high solution pH likely responsible for the severe initial corrosion. Early on, nominal corrosion rate was large (~1 $\mu A/cm^2$) but it decrease to ~0.15 $\mu A/cm^2$, consistent with a decrease in solution pH to nearly neutral values.

4. Exposure to high chloride content and high carbonate scaling tendency (solution SW) led to early formation of few small macro pits as well as light uniform discoloration of the aluminized surface with nearly constant nominal corrosion rates of ~0.3 $\mu A/cm^2$ throughout the test exposure.
5. Macro pits and surface discoloration appeared to be limited to the outer aluminized coating layer at least for the time frame examined in all solutions. The macro pits were usually small and infrequent on the corroding aluminized surface so they appeared to play a secondary role for the solutions C and NP and a primary form of corrosion for solution SW. The macroscopically uniform nature of the corrosion may be a manifestation of micro pits at the scale of the finely distributed Fe-rich inclusions present in the outer aluminized coating layer.
6. It is tentatively proposed that the mechanism of activation of the aluminized surface in solutions NP and C may involve alkaline dissolution of aluminum as a result of a high pH of the solution bulk (early on for C and later in the test for NP), which would cause aluminum dissolution possibly more localized at the microscopic, inclusion-scale level, and later precipitation of

aluminum corrosion products, covering the entire specimen surface, consistent with visual evidence of uniform surface discoloration.

7. For solution P over the entire test time and solution NP before the appearance of aluminized surface discoloration, impedance response was described assuming coupled cathodic reactions acting on the inclusions where surface coverage by an intermediate adsorbate alters the rate of the next step resulting in a pseudocapacitive behavior.
8. For solutions C and SW, and solution NP after the appearance of aluminized surface discoloration, the impedance response was assumed to be dominated at high frequencies by the parallel combination of the local ohmic resistance of all micro and macro active sites and the aluminum oxide film capacitance, and at low frequencies by the discrete parallel combination of the Faradaic polarization resistance and an interfacial capacitance at all active sites.
9. Tentative durability projections made for unblemished 16-gage aluminized Type 2 flat sheet durability were >100 yr for the least aggressive environment (P), and between 15 and 36 yr for the other media based on the assumptions in this investigation. It is emphasized that the projections are nominal in nature considering the short test times of the present experiments. The results obtained in this investigation were used as a first step in proposing refinements of presently used durability guidelines of aluminized steel Type 2 culvert pipe based on environmental composition.

10. The present findings would support retaining the present FDOT guidelines for durability predictions of unblemished aluminized steel Type 2 regardless of scaling tendency for environments with moderately low resistivity such as those used in the tests (e.g. ~500 Ω-cm to ~1,000 Ω-cm) and neutral to mildly alkaline conditions (e.g. ~7.5<pH<~9.0). The results also support exploring the use of alternative guidelines such as the AISI method for environments with extremely high chloride contents (e.g. resistivity <50 Ω-cm) and nearly neutral pH. Eventual changes in existing guidelines should consider not only the specific findings of this investigation but also the entirety of the performance record of aluminized steel pipe.

Table 2.1: Chemical composition of steel substrate (% weight).

C	Mn	P	S	Si	Cu	Al	Cb	Ni	Cr	Ti	N	Mo	Fe
0.05	0.20	0.006	0.012	0.01	0.03	0.04	0.002	0.017	0.03	0.002	0.004	0.003	Bal.

Mill test report provided by Contech Construction Products Inc.

Table 2.2: Synthetic solution compositions and properties.

Solution	TA	TH	FC	BI	pH_L (pH_H)	Ca^{+2} mg/L	Cl^- mg/L	σ µmho/cm
C (control)	6	2	0	8	~7.4 (~9.0)	0	372	1,140
NP (non precipitating)	480	2	11	471	~7.8 (~8.7)	0		1,850
P (precipitating)	184	52	13	223	~7.4 (~7.8)	200		1,390
SW (precipitating - high chloride)	210	8,280	12	8,480	~7.3 (~7.9)	†	†	40,000

Legend: TA: total alkalinity expressed as mg/L $CaCO_3$, TH: total hardness expressed as mg/L $CaCO_3$, σ: solution conductivity, pH_L, pH_H: lowest and highest pH values, respectively.
† See Table 2.3 for detailed simulated ocean water composition.

Table 2.3: Chemical composition of the simulated ocean water reported by the manufacturer.

Ionic species	Cl^-	Na^+	SO_4^{-2}	Mg^{+2}	Ca^{+2}	K^+	HCO_3^-	Br^-	Sr^{+2}	B^{+3}
Concentration/ppm	19,846	11,024	2,768	1,326	419	400	145	67.1	13.8	4.72

Table 2.4: Values of the equivalent circuit components in Figure 2.16 estimated from EIS data fit for the specimen #1 exposed to solution P.

Time hr	R_S Ω	R_{AL1} kΩ	Y_F s^{n_F}/Ω	n_F	R_{AL2} kΩ	Y_{AL2} $s^{n_{AL2}}/\Omega$	n_{AL2}	i_{corrAL} µA cm^{-2}
48	17.8	27.0	3.19E-04	0.94	27.0	3.83E-03	1.00	0.034
216	17.7	55.5	3.49E-04	0.94	37.6	3.83E-03	1.00	0.016
312	18.3	79.6	3.51E-04	0.94	47.8	3.24E-03	1.00	0.011
336	17.1	10.1	4.00E-04	0.94	7.6	1.25E-02	1.00	0.091
480	19.5	18.4	4.11E-04	0.94	16.5	7.75E-03	1.00	0.050
504	20.2	10.7	4.28E-04	0.94	9.9	9.78E-03	1.00	0.085
624	20.7	17.2	4.36E-04	0.94	15.9	6.31E-03	1.00	0.053
1248	22.1	22.5	5.09E-04	0.94	20.7	2.75E-03	0.98	0.041
2376	20.9	74.8	5.41E-04	0.93	32.5	1.84E-03	1.00	0.012
3072	21.6	110.4	5.39E-04	0.93	25.4	2.08E-03	1.00	0.008

Nominal specimen area A_{AL} = 95 cm^2.

Table 2.5: Values of the equivalent circuit components in Figure 2.16 estimated from EIS data fit for the specimen #1 exposed to solution NP.

Time hr	R_S Ω	R_{AL1} kΩ	Y_F s^{n_F}/Ω	n_F	R_{AL2} kΩ	Y_{AL2} $s^{n_{AL2}}/\Omega$	n_{AL2}	i_{corrAL} μA/cm^2
24	14.8	6.6	3.69E-04	0.95	9.6	4.42E-03	1.00	0.14
144	15.3	13.9	4.20E-04	0.95	17.5	2.44E-03	1.00	0.07
360	14.9	8.7	4.85E-04	0.94	13.6	2.86E-03	0.99	0.10
624	15.0	20.4	4.98E-04	0.94	30.5	1.14E-03	0.95	0.04
864	14.9	24.4	5.06E-04	0.94	27.9	1.31E-03	0.99	0.04
1368	15.3	28.1	5.59E-04	0.94	31.2	1.29E-03	0.99	0.03
2376	14.7	7.9	7.03E-04	0.94	6.6	2.74E-03	1.00	0.07
3048	14.5	2.1	9.62E-04	0.94	2.0	9.92E-03	1.00	0.22

Nominal specimen area A_{AL} = 95 cm^2.

Table 2.6: Values of the equivalent circuit components in Figure 2.16 estimated from EIS data fit for the specimen #1 exposed to solution SW.

Time hr	R_S Ω	R_{AL1} kΩ	Y_F s^{n_F}/Ω	n_F	R_{AL2} kΩ	Y_{AL2} $s^{n_{AL2}}/\Omega$	n_{AL2}	i_{corrAL} μA cm^{-2}
384	0.48	1.7	1.30E-03	0.92	1.8	2.46E-02	0.97	0.25
504	0.51	2.2	1.35E-03	0.92	2.1	2.47E-02	0.98	0.21
648	0.48	2.0	1.37E-03	0.92	2.0	2.54E-02	0.98	0.23
864	0.48	1.7	1.53E-03	0.92	1.4	3.10E-02	0.98	0.34
1200	0.49	1.7	1.64E-03	0.91	1.3	3.07E-02	0.97	0.35
1464	0.51	2.3	1.63E-03	0.91	1.6	3.06E-02	0.99	0.28
1680	0.50	1.9	1.67E-03	0.91	1.3	3.01E-02	0.98	0.35
1896	0.51	2.4	1.65E-03	0.91	1.5	2.98E-02	0.99	0.30
2424	0.49	2.4	1.64E-03	0.91	1.5	2.73E-02	0.97	0.30
2760	0.51	2.6	1.62E-03	0.91	1.5	2.96E-02	0.99	0.30
3096	0.51	2.7	1.63E-03	0.91	1.5	3.03E-02	0.99	0.30

Nominal specimen area A_{AL}= 95 cm^2.

Table 2.7: Values of the equivalent circuit components in Figure 2.16 estimated from EIS data fit for the specimen #1 exposed to solution C.

Time hr	R_S Ω	R_{AL1} kΩ	Y_F s^{n_F}/Ω	n_F	R_{AL2} kΩ	Y_{AL2} $s^{n_{AL2}}/\Omega$	n_{AL2}	i_{corrAL} μA/cm^2
24	19.5	150	4.36E-04	0.93	4.9	1.94E-03	0.93	0.09
360	17.6	9.4	9.59E-05	0.57	0.7	6.59E-03	0.69	0.63
504	18.6	12.1	6.57E-05	0.60	1.3	4.29E-03	0.72	0.34
648	18.4	13.5	5.24E-05	0.62	1.8	3.43E-03	0.74	0.26
864	19.0	15.9	4.24E-05	0.63	2.4	2.70E-03	0.76	0.19
960	18.1	15.6	4.00E-05	0.64	2.2	2.65E-03	0.76	0.21
1392	16.9	19.1	3.78E-05	0.62	2.9	2.21E-03	0.77	0.16
2400	17.5	28.9	2.89E-05	0.63	4.1	1.81E-03	0.79	0.11
3048	17.6	35.2	2.74E-05	0.63	5.2	1.65E-03	0.80	0.09

Nominal specimen area A_{AL} = 95 cm^2.

Table 2.8: Comparison of durability estimates, in yr, obtained by the application of selected forecasting methods and those obtained in this Chapter.

Test solution	AK Steel	California	AISI	FDOT	This Chapter
P	<20	29	57	56	>100 (>100)
NP	<20	25	50	33	36 (38)
SW	NA	7	15	NA	15 (19)
C	<20	30	62	27	19 (23)

Numbers in parenthesis correspond to the results from duplicate specimens.

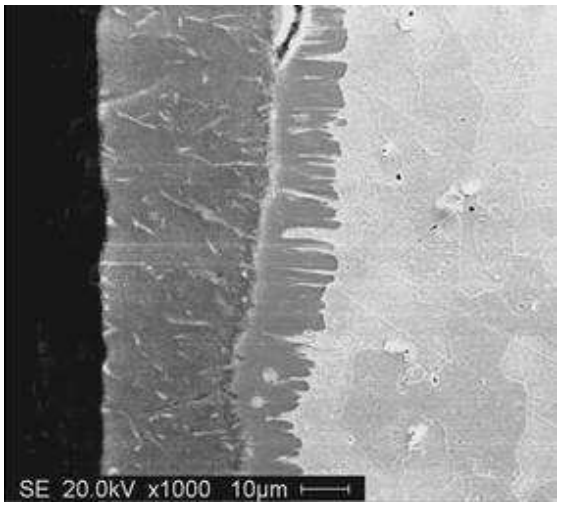

Figure 2.1: Cross section perpendicular to rolling direction of a 16-gage (~1.59 mm) thickness flat aluminized steel Type 2 after etching with 2% Nital solution showing the outer and inner coating layers on base steel. Light features in the outer coating are Fe-rich inclusions per SEM-EDS analysis.

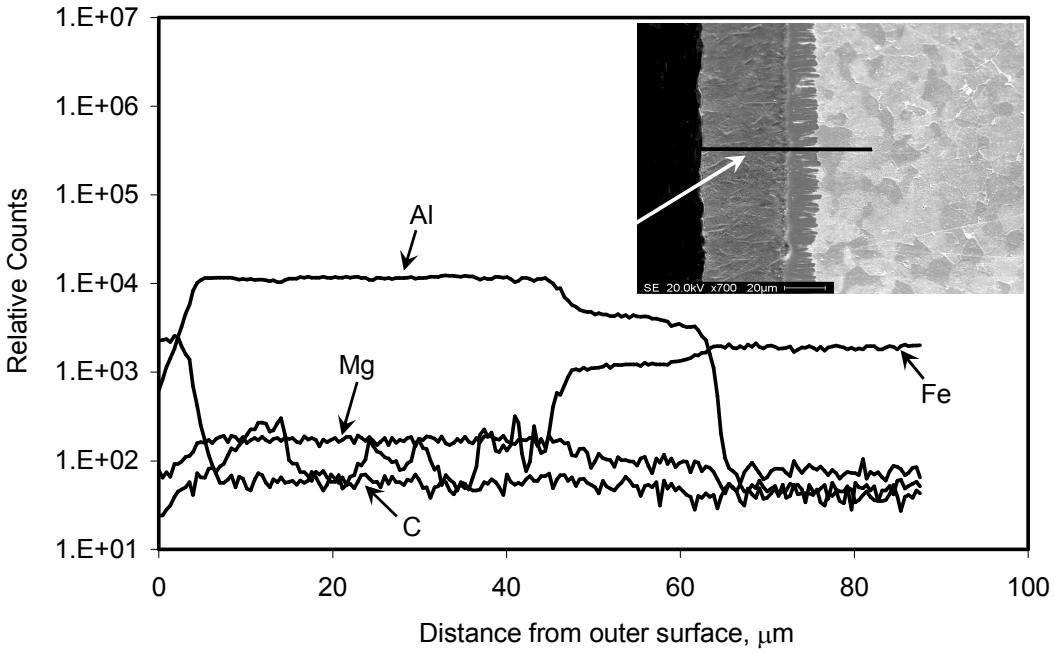

Figure 2.2: SEM line scan conducted on the cross section of aluminized steel Type 2 (perpendicular to rolling direction) showing the main constituents in the dual coating layer and the base steel.

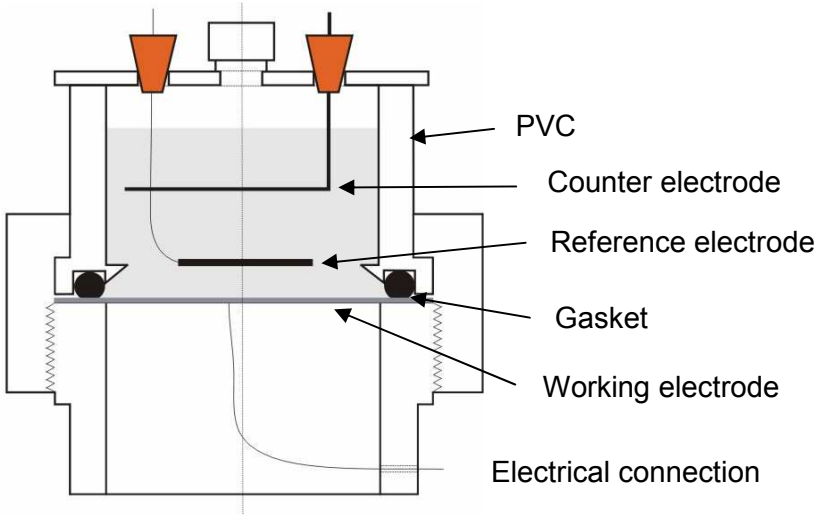

Figure 2.3: Schematic of the test cell arrangement.

Figure 2.4: Photograph of the test cell.

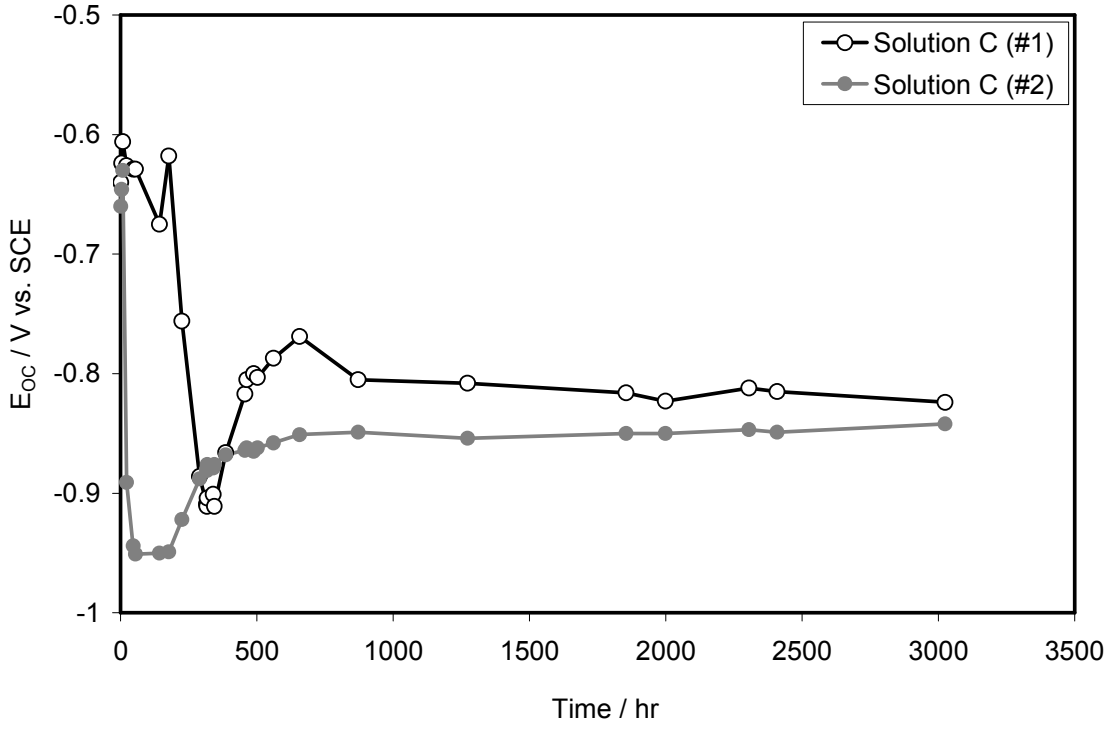

Figure 2.5: E_{OC} evolution of replicate specimens in solution C. End of exposure corresponds to the last datum.

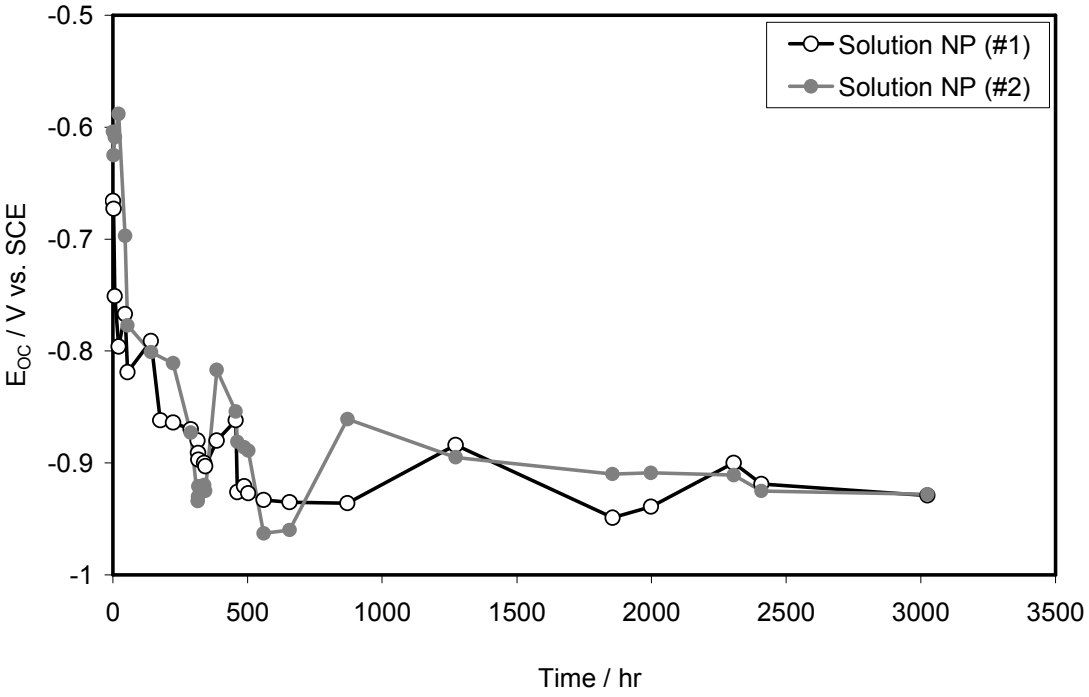

Figure 2.6: E_{OC} evolution of replicate specimens in solution NP. End of exposure corresponds to the last datum.

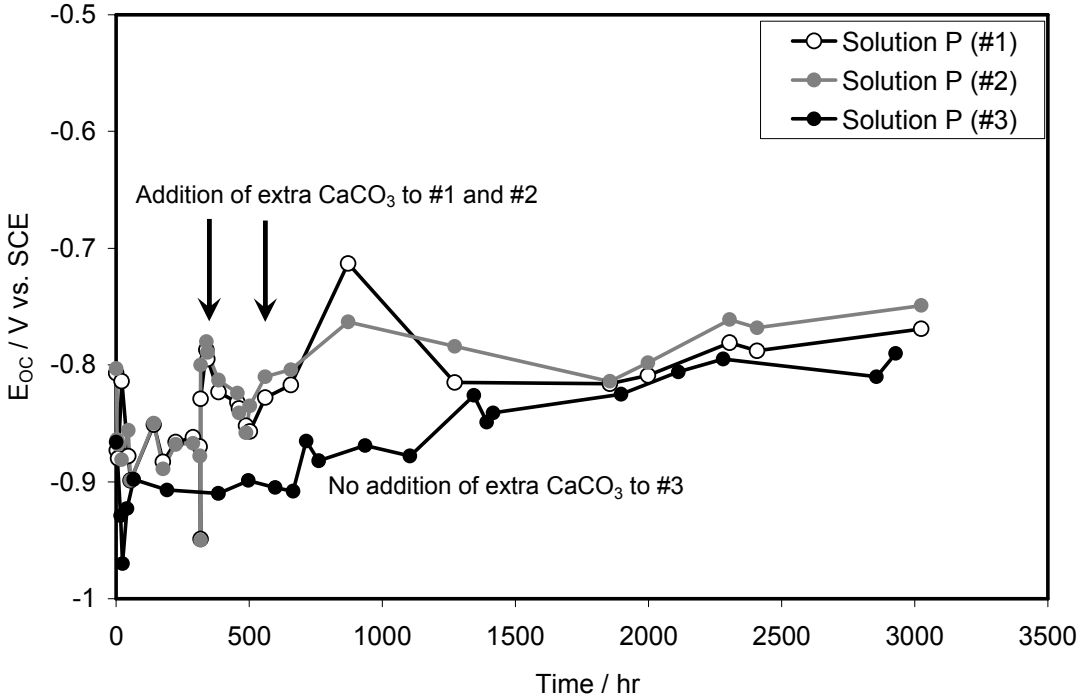

Figure 2.7: E_{OC} evolution of replicate specimens in solution P. Arrows indicate two $CaCO_3$ additions to #1 and #2. End of exposure corresponds to the last datum.

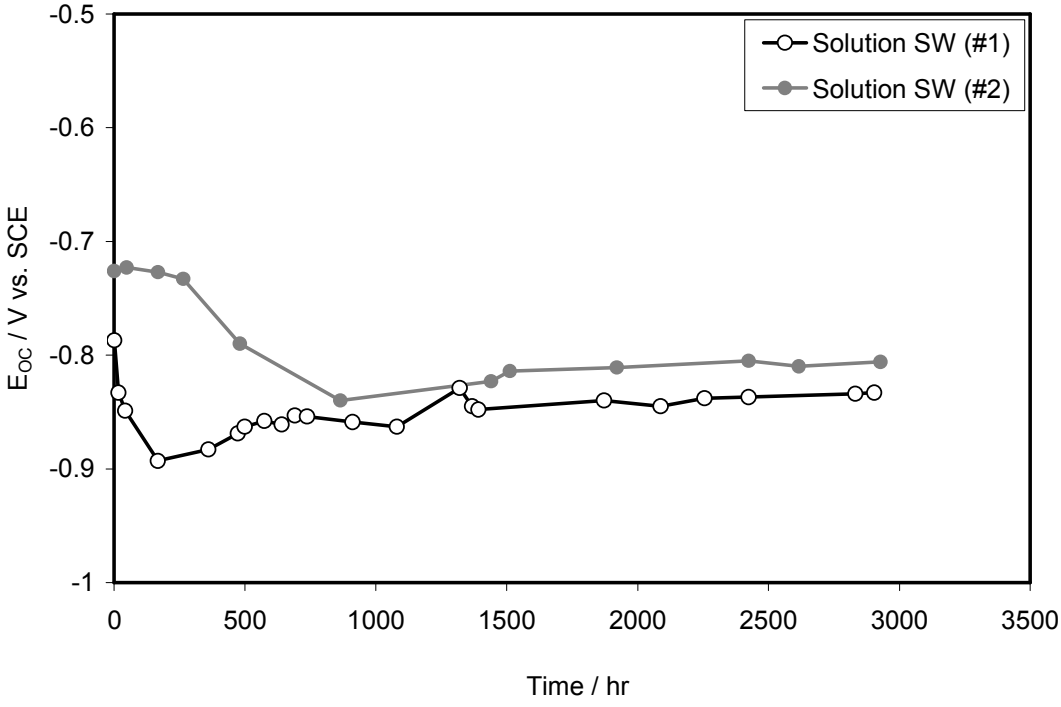

Figure 2.8: E_{OC} evolution of replicate specimens exposed to solution SW. End of exposure corresponds to the last datum.

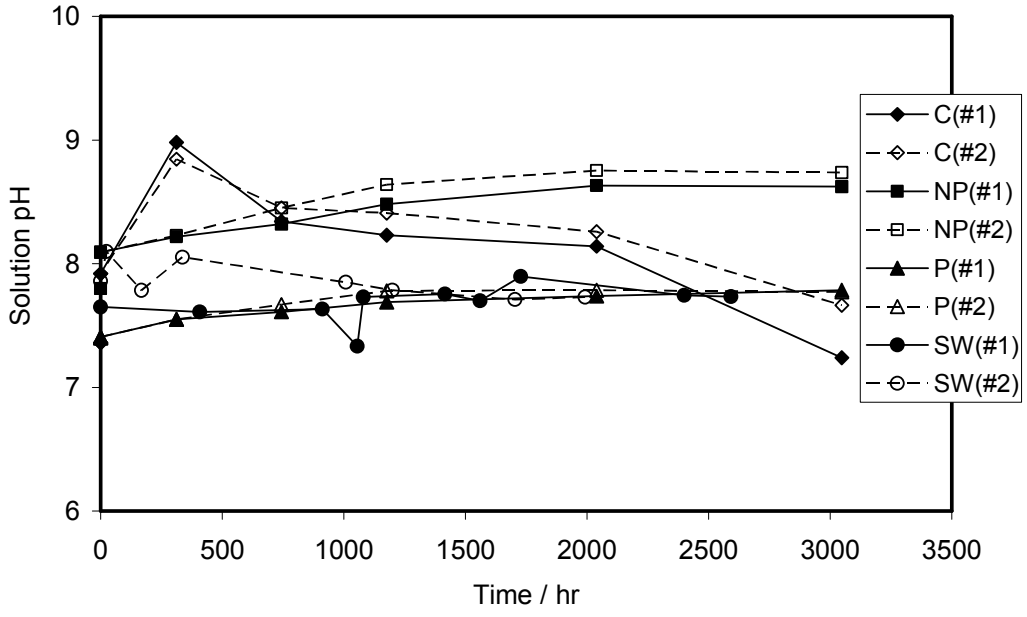

Figure 2.9: Evolution of the solution bulk pH with exposure time.

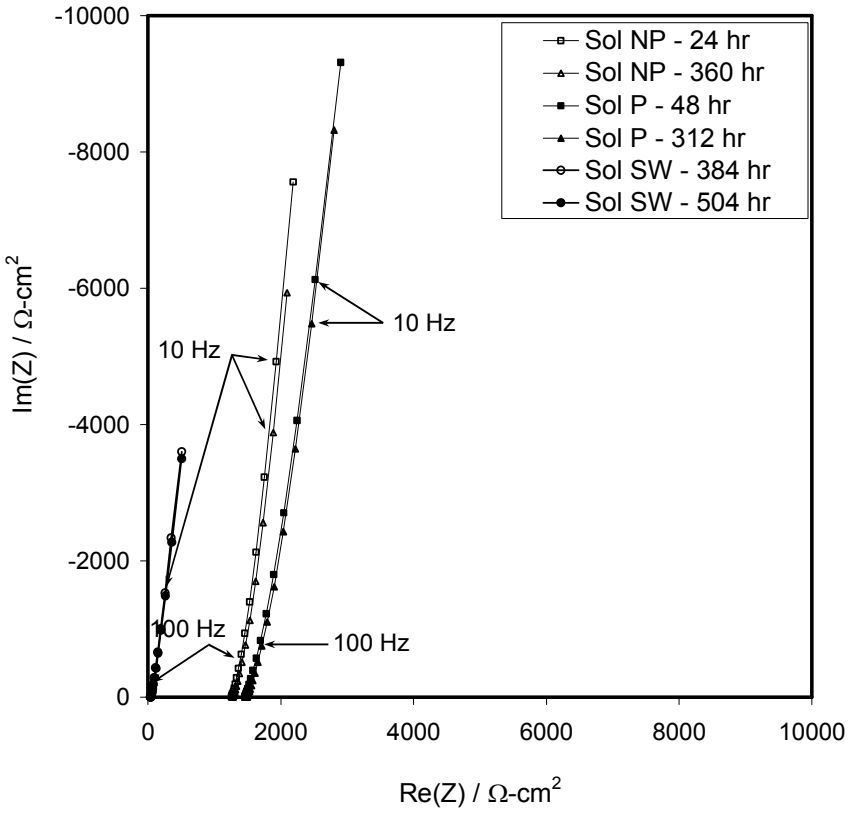

Figure 2.10: Typical EIS plot of the high-frequency limit for NP, P, and SW.

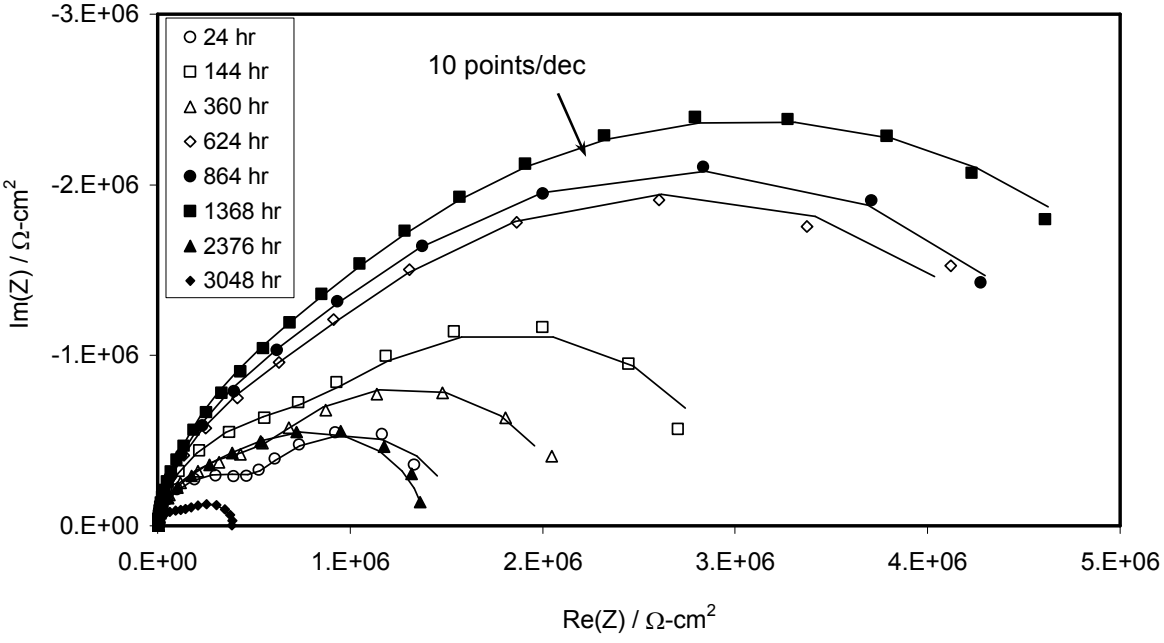

Figure 2.11: EIS behavior of the specimen #1 in solution NP (100 KHz - 1 mHz - 5 points/decade unless indicated otherwise).

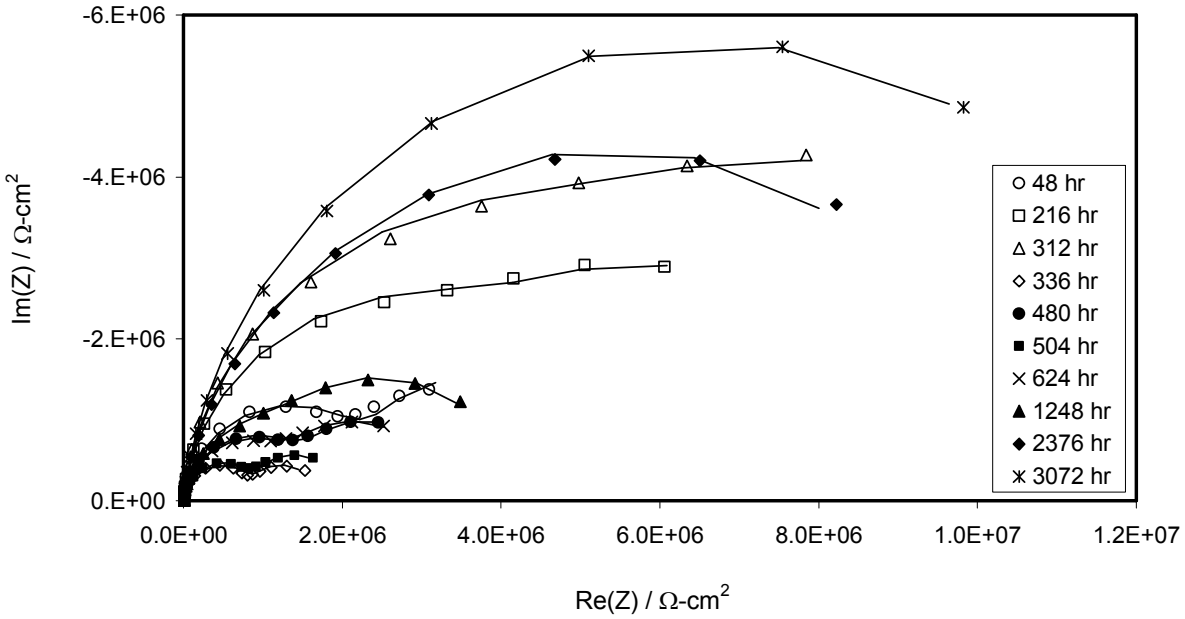

Figure 2.12: EIS behavior of the specimen #1 in solution P (100 KHz - 1 mHz - 5 points/decade).

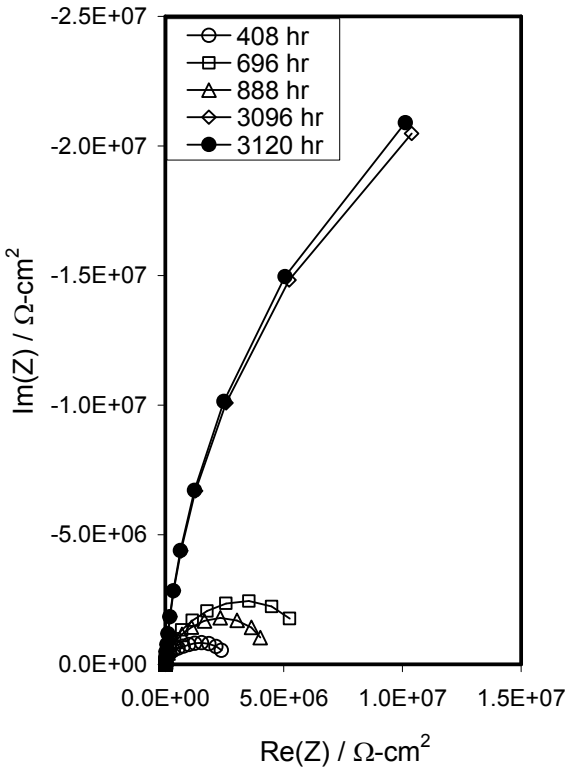

Figure 2.13: EIS behavior of the specimen #3 in solution P (100 KHz - 1 mHz - 5 points/decade).

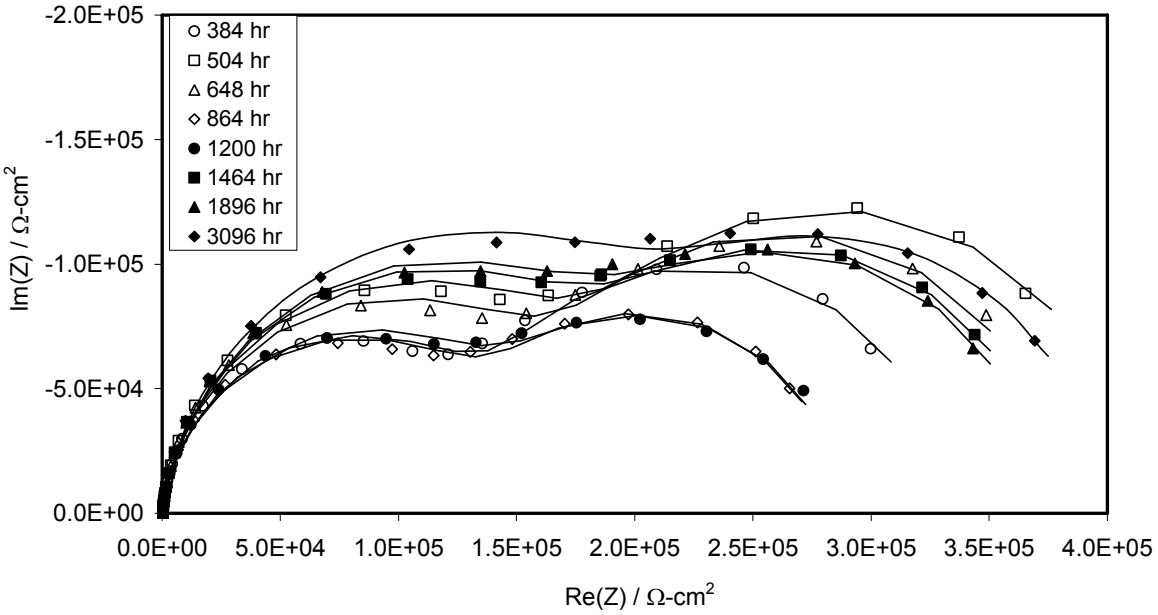

Figure 2.14: EIS behavior of the specimen #1 in solution SW (100 KHz - 1 mHz - 5 points/decade).

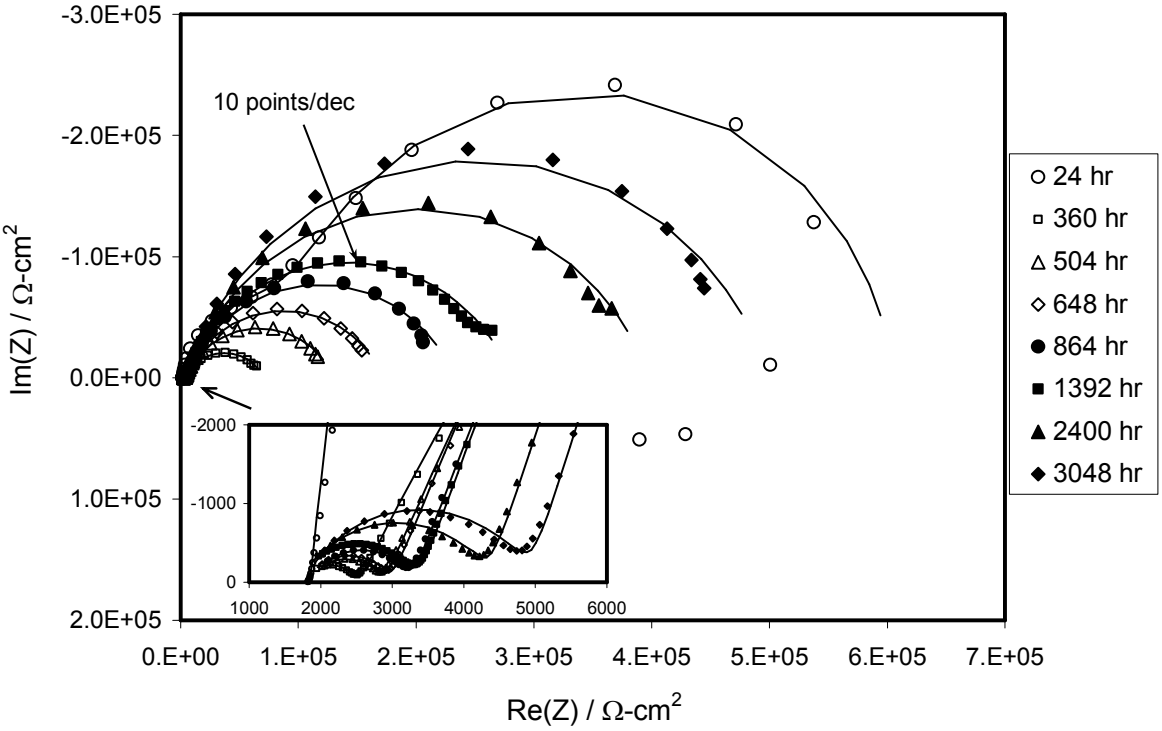

Figure 2.15: EIS behavior of the specimen #1 in solution C (100 KHz - 1 mHz - 5 points/decade unless indicated otherwise).

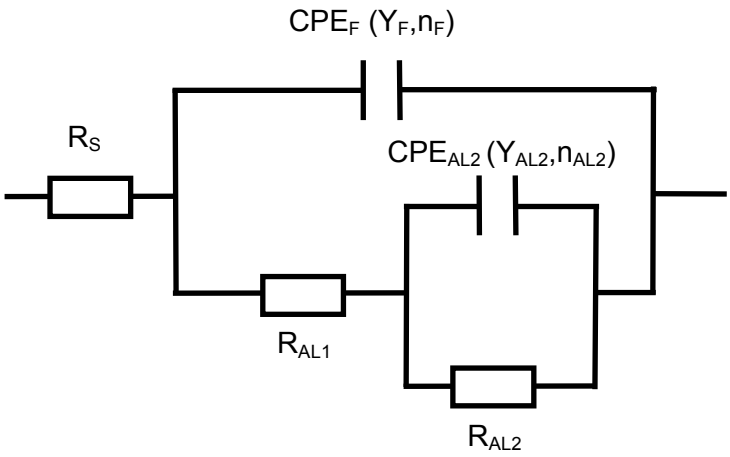

Figure 2.16: Analog equivalent circuit used to simulate the EIS responses.

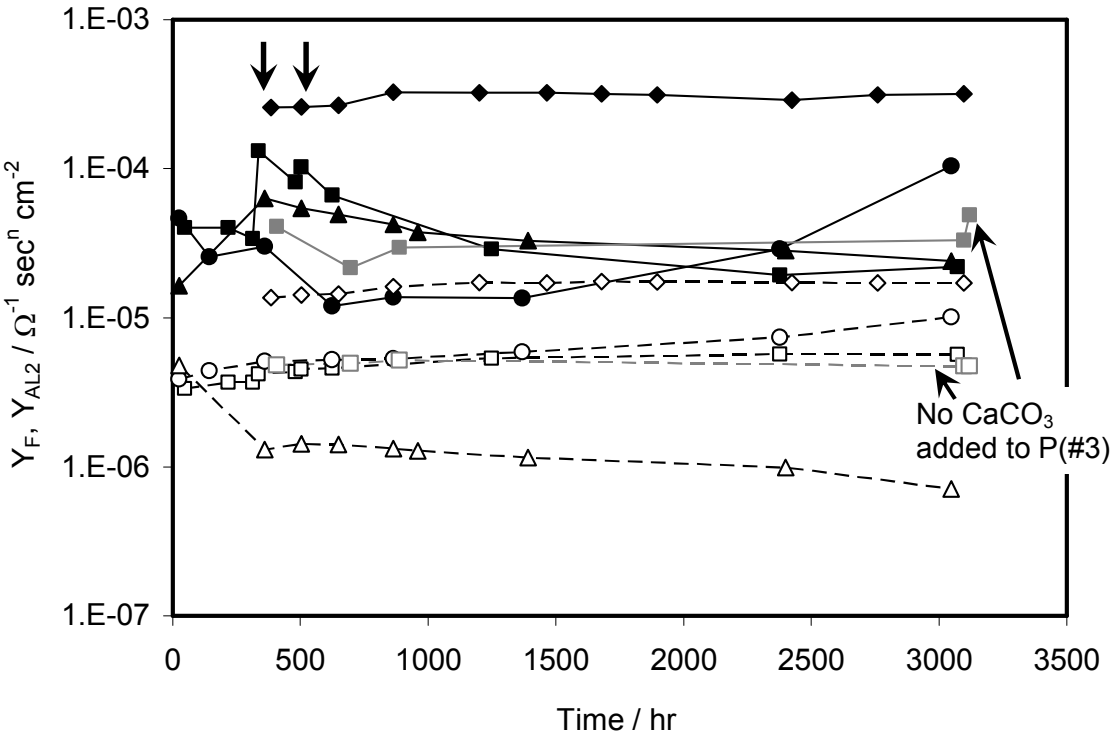

Figure 2.17: Evolution of the admittance parameter as a function of time for the specimens #1 in solutions NP (circles), P (squares), C (triangles), and SW (diamonds) (--- Y_F, — Y_{AL2}). Arrows indicate $CaCO_3$ additions to solution P (#1).

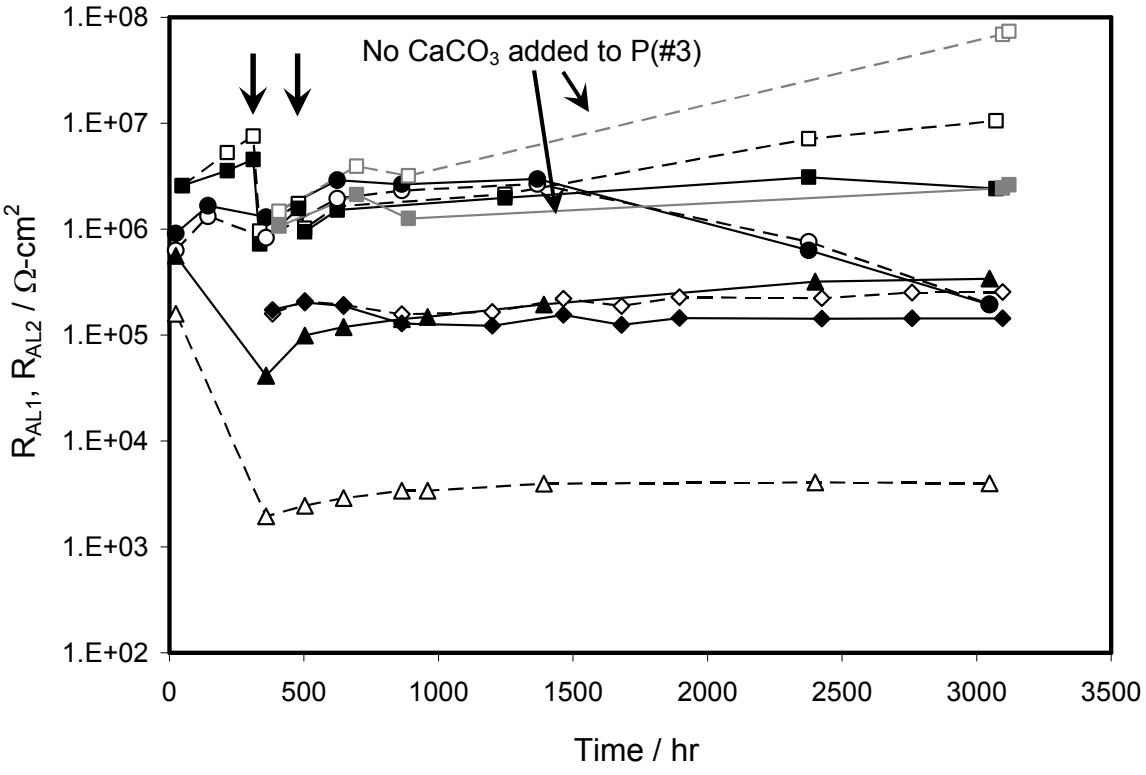

Figure 2.18: Evolution of the resistive components as a function of exposure time for the specimens #1 in solutions NP (circles), P (squares), C (triangles), and SW (diamonds) (--- R_{AL1}, — R_{AL2}). Arrows indicate $CaCO_3$ additions to solution P (#1).

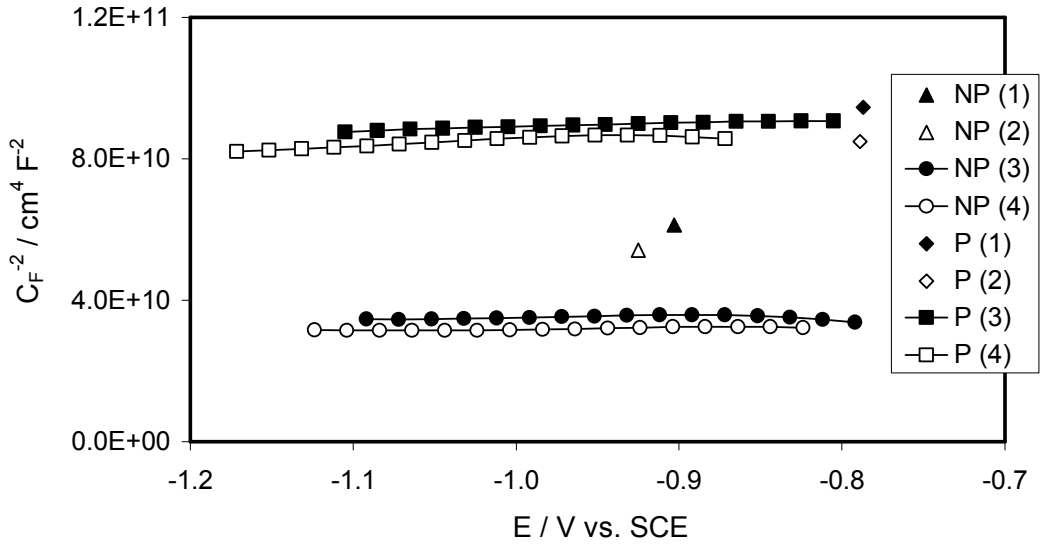

Figure 2.19: Mott-Schottky plot of the oxide film capacitance recorded for NP and P systems (specimens #3 and #4) at ~330 hr of exposure. C_F^{-2} values obtained by EIS at E_{OC} of the duplicate specimens #1 and #2 at comparable exposure age are plotted as well (specimen # is denoted in parenthesis).

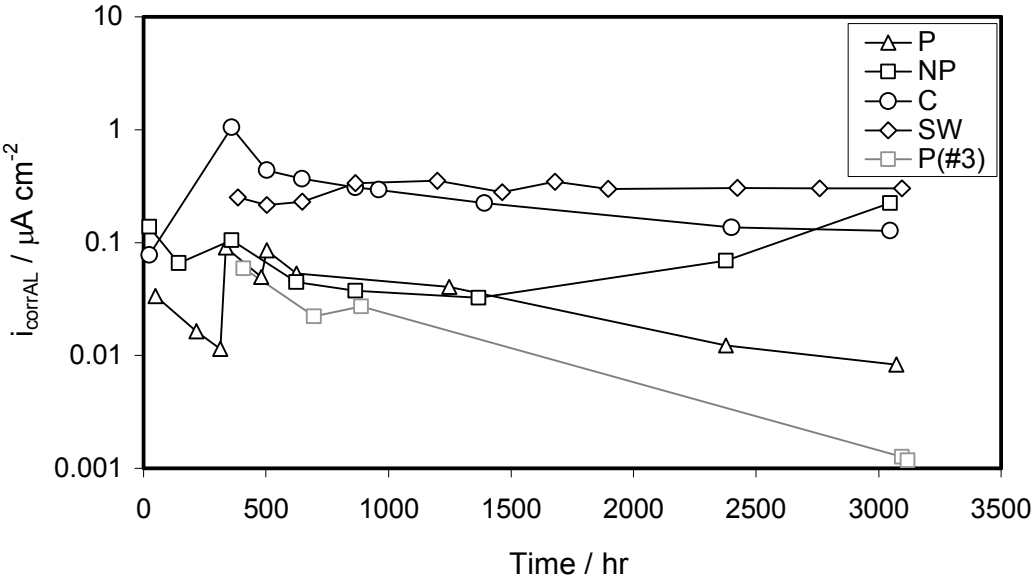

Figure 2.20: Nominal corrosion current density evolution for the specimens #1 in all media. No extra powdered $CaCO_3$ was added to the triplicate specimen in solution P (#3).

Chapter 3

Special Issues in the Cathodic Behavior of Aluminized Steel Type 2 in Scale-Forming Waters

3.1 Introduction

As mentioned in Chapter 1, aluminized steel Type 2 is commonly used as a component for applications in drainage culvert pipe that are designed to operate for long service lives, so that extremely low corrosion rates are desirable (Cerlanek and Powers, 1993). As even low corrosion rates may be important, their detection requires sophisticated techniques with associated inherent uncertainty. Therefore, understanding of mechanistic issues is critical to increase the level of confidence in the corrosion rate estimation. A key mechanistic question is the nature and extent of the cathodic reaction taking place on the micrometer-scale Fe-rich constituent inclusions, e.g. $FeAl_3$ and Fe_2Al_5 embedded in the solid-solution aluminum matrix (Park et al., 1999, Nisancioglu, 1990, and Nisancioglu et al., 1981) as the cathodic reaction will control the overall rate of metal dissolution. Consequently, experiments intending to obtain additional information on the cathodic behavior on aluminized steel in scaling-forming water were performed and are addressed in this chapter.

To isolate the cathodic reaction, experiments were performed by cyclically polarizing to potentials more negative than those encountered under normal E_{OC}

conditions (e.g. <-900 mV). The experiments produced some kinetic parameter information useful for calibrating predictive models, but also revealed enhanced cathodic activity at the more negative polarization regimes that merits detailed discussion. The following describes the results and sets the stage for future investigation of the causes of that behavior.

As discussed earlier, the inclusions not only act as microsites for cathodic reaction but also can promote localized corrosion of aluminum surrounding the inclusions. For instance, Gundersen and Nisancioglu (1990) proposed that aluminum containing ~3% Fe exposed to nearly neutral pH solutions with negligible buffering capacity is preferentially dissolved in the vicinity of the inclusions as a consequence of a local pH increase due to the cathodic reaction occurring at the inclusions. Effectively, this leads to increased exposure of the inclusions at the metal surface, and therefore, an enhancement of the cathodic reaction with consequent further increase in the aluminum dissolution rate. In buffered solutions, however, localized alkalinization in the vicinity of the inclusions may be prevented by neutralization of OH^- ions. Thereby preferential aluminum dissolution around inclusions is minimized, as confirmed by Nisancioglu and Holtan (1979) and later by Bjoergum et al (1995) on AA1100 in buffered neutral pH, NaCl solutions.

At present, there is some controversy in regards to the type of dominant cathodic reaction at the potentials of interest in aluminum containing Fe-rich inclusions. Previous investigations (Seri and Furumata, 2002) conducted to determine the cathodic behavior of commercially pure aluminum exposed to

aerated unbuffered 0.05 M NaCl solution at neutral pH identified H_2 evolution under activation control as the main cathodic reaction for potentials ranging from ~-750 mV to ~-1400 mV. Seri's results were in agreement with those reported by Gartland (1987) for aluminum-coated steel exposed to aerated seawater. However, Rynders et al (1994) and Park et al (1999) reported O_2 reduction as the dominant cathodic reaction for AA6061 in aerated 0.6 M NaCl solution for up to ~-1,000 mV_{SCE}.

Other types of inclusions, e.g. Cu compounds, have also been reported to act as sites for cathodic reaction sharing possibly similarities to Fe inclusions in the interpretation of the cathodic reaction mechanisms. For example, Vukmirovic et al (2002) and later Jakab et al (2005) documented that cathodic polarization of AA2024-T3 containing Cu-rich particles in unbuffered NaCl solution caused detachment of Cu inclusions (by undercutting due to corrosion of the surrounding aluminum) from the aluminum matrix. The mechanically/electrically detached metallic Cu adopted its own corrosion potential leading to formation of Cu^{+2} ions that later replated on the metal surface, resulting in an increase in the cathodic reaction rate.

3.2 Experimental Procedure

The aluminized steel Type 2 used in this part of the investigation came from the same batch as those used in previous Chapters. Circular unblemished specimens of 95 cm^2 nominal surface area were cut out from the as-received aluminized steel sheet. The surface had no blemishes detectable by unaided

visual inspection. Two specimen surface conditions were tested: as-received (AR) and finely ground (FG). The FG surface, indented to simulate an aged condition after rolling finish may have wasted away and better exposed inclusions, was prepared by hand-rubbing 1 μm diamond metallographic polishing compound with a soft paper which removed ~5 μm of the outer aluminized layer. Both AR and FG surfaces were ultrasonically cleaned with ethanol and stored in a desiccator before immersion. A 500 mL three-electrode test cell was used exposing horizontally one of the specimen faces (Figures 2.3 and 2.4). All potentials are reported in the SCE scale.

For comparison, limited tests were conducted with as-melted bulk alloy specimens[6] of composition Fe_2Al_5, similar to that found as intermetallics in aluminized steel, and with commercially pure aluminum (AA1100-H14) sheet stock with nominal Al composition of ~99% and ~1% Fe maximum[7]. The specimens were mounted in an epoxy resin exposing 1.4 cm^2 and 4 cm^2 for the intermetallic and the AA1100 respectively, wet-ground to a 600-grit surface finish, placed in a three electrode configuration corrosion cell (Princeton Applied Research®) with a ~0.5 cm Luggin capillary to specimen surface distance.

Solution P was used in this part of the investigation with composition and properties the same as that shown in Table 2.2 in Chapter 2. The calculated LSI value was +1.4, a condition that was manifested by the formation of a precipitate of $CaCO_3$ to yield a ~0.5 mm thick powdery layer on the specimen surface shortly after exposure.

[6] Supplied courtesy of Dr. N. Birbilis, Ohio State University.
[7] Supplied by Metal Samples Inc.

The immersion tests were conducted in duplicate for nearly 1,700 hr at 22 ±2 °C. The solution was in contact with laboratory air through a small opening for the first ~410 hr of exposure followed by deaeration with pure N_2 gas. E_{OC} and solution conductivity were monitored periodically. Also, cathodic cyclic polarization (CYP) tests were conducted sequentially at three different scan rates (1, 0.5, and 0.05 mV/sec) at selected exposure times with potentials shifted first from E_{OC} to ~-1.15 V (forward scan) and then back to E_{OC} (reverse scan). The potentials were corrected afterwards for ohmic drop taking into account the solution resistance R_S determined from the high frequency limit of EIS measurements. Given the buffering capacity of the solution, pH fluctuations at the metal surface were expected to be minimized during cathodic polarization. At the end of the immersion test, all specimens were examined by 40X optical microscopy and with a Scanning Electron Microscope (SEM). The Fe^{+2} concentration of the solution bulk was measured at the end of exposure by Atomic Absorption Spectroscopy.

3.3 Results

Experimental trends exemplified in this Chapter are for single specimens unless otherwise noted. Trends obtained for duplicate specimens were comparable to those shown here. CYP tests of both surface conditions were conducted when the metals were still in passive state. No under-gasket crevice corrosion developed in any of the specimens for which results are reported.

3.3.1 Microstructure Analysis

A SEM view of the typical microstructure of the near-surface cross section of the as-received aluminized specimens is shown in Figure 2.1 (Chapter 2). The unexposed surface morphology of the AR and FG conditions is shown in Figure 3.1. The light features are ~1.6 to 3.3 μm Fe-rich inclusions of approximate composition ~85% Al and ~15% Fe. The FG surface appearance was comparable to that of the AR material except that the inclusions covered respectively ~7.6% and ~5.5% of the total specimen surface. The matrix surrounding the inclusions was, as expected, richer in aluminum with average composition of ~98% Al and ~2% Fe. After long term exposure, ~2-10 μm diameter isolated pits were observed in the FG specimens but none in the AR specimens. In addition, light discoloration of the aluminized coating was noted on the FG specimens after ~800 hr of exposure whereas no discoloration was observed for the AR specimens even after ~1,700 hr exposure.

3.3.2 Solution Composition

The initial solution pH closely approached the lowest values reported in Table 2.2, increasing to 8.20 after 1,500 hr. Solution resistivity was also constant and close to the value reported in Table 2.2. The Fe^{+2} concentration in solution for both surface conditions at the end of exposure was below the minimum detection level of the instrument (0.01 ppm).

3.3.3 E_{OC} and CYP Trends

Figure 3.2 exemplifies the E_{OC} evolution for up to ~1,700 hr for the duplicate specimens. Trends were similar for both FG and AR surface conditions. Shortly after immersion, E_{OC} values were ~-750 mV, and remained nearly constant for 24 hr after which the potential gradually decreased toward a terminal value of ~-900 mV, consistent with the E_{OC} trends obtained in Chapter 2. There unblemished as-received aluminized steel was documented was found the have extremely low nominal corrosion rates and correspondingly clean surface appearance for up to 3,000 hr of exposure in a solution similar to that used in this part of the investigation.

Typical CYP (E vs. i_C where i_C is the cathodic current density normalized to total specimen area) behavior of the FG and AR conditions in the naturally aerated solution is exemplified in Figure 3.3. Additional CYP tests conducted at different exposure times and in well-agitated solution showed comparable trends. At the two fastest scan rates both AR and FG conditions had similar CYP trends, with negligible hysteresis at 1 mV/sec and moderate hysteresis at 0.5 mV/sec. The curves for both surface conditions seemingly exhibited a typical activation polarization regime with apparent cathodic Tafel slopes of ~170-250 mV/dec, comparable to those reported by Armstrong and Braham (1996) for commercially pure aluminum in NaCl solution, and values of i_C at the starting E_{OC} of ~10^{-8} - 7 10^{-8} A/cm^2. At the apex potential, i_C for the AR condition was ~2 10^{-6} A/cm^2 at 1 mV/sec, approximately two times smaller than that for the FG conditions. At the lowest scan rate, 0.05 mV/sec, the polarization curves showed much more

pronounced hysteresis and greater current densities at the apex potential for both surface conditions than in the faster tests. In all cases, the i_C values at each potential for the reverse scan was larger than those recorded for the forward scan, suggesting a large signal pseudoinductive response of the system for negative potential excursions from E_{OC}.

Figure 3.4 shows comparable tests for the FeAl and Al1100 specimens. Those were normally kept polarized at -850 mV (potential representative of the typical E_{OC} of aluminized steel), which was not their natural E_{OC} so the starting point of their CYP curves is not at zero current density but rather at the steady state polarizing current density (>~0.2 μA/cm^2 for both materials). Additional CYP tests conducted at different exposure times showed comparable trends. For all scan rates, hysteresis was relatively large for FeAl, but not for Al1100. The curves showed steep cathodic slopes in agreement with the results reported by Seri and Furumata (2002), with i_C values for the reverse scan larger than those for the forward scan. Values of i_C at the apex potential were comparable to those obtained for the FG specimens. Additional experiments conducted on specimens exposed to a well-agitated solution did not cause a significant change in i_C.

Figures 3.5 and 3.6 show results of tests as in Figures 3.3 and 3.4, respectively, but conducted while deaeration had been in progress for at least 72 hr. Additional CYP tests conducted at different exposure times showed comparable trends to those in Figures 3.5 and 3.6. The CYP curves at the faster scan rates for the two surface conditions and the alloys showed comparable trends to those under aeration. However, at 0.05 mV/sec there was less

hysteresis than in the aerated case notably for the AR and FG conditions but also for the alloys. The starting E_{OC} values were in general more negative (~40 mV) than for the aerated solution for both AR and FG conditions, although the i_C values at the apex potential were not much changed. After solution reaeration for >48 hr, the starting E_{OC} and CYP behavior reverted in all cases to that obtained before deaeration.

3.4 Discussion

In both the aerated and deaerated tests the i_C values at a given potential for the AR and FG conditions were in a ratio ~2:1, respectively, while the SEM examination indicated a ratio of the same order (~1.4:1) for the area fraction covered by Fe-rich inclusions. The shape of the polarization curves during the forward scan at the fast scan rates and the lack of sensitivity to solution agitation suggest activation-limited control over much of the test cycle. Those observations are consistent with the Fe-rich inclusions acting as microelectrodes for the cathodic reaction, to an extent that depends strongly on the amount of those inclusions as noted elsewhere (Nisancioglu, 1990) for comparable systems.

The nature of the main cathodic reaction(s) active in the potential regime examined is not entirely clear, a situation not uncommon in studying aluminum alloys (Moon and Pyun, 1998). O_2 reduction (OR) can be expected under aeration to be the dominant cathodic reaction at ~-900 mV E_{OC}. Since that is in the order of the reversible potential for the water/hydrogen system at the near neutral pH of the system, H_2 evolution (HE) may not yet be important. This

expectation is supported by the observed decrease in E_{OC} to more negative values upon deaeration. However, the decrease was modest (~40 mV) considering that deaeration was effectively ~99% based on dissolved oxygen measurements. It is possible then that HE was proceeding at an incipient rate at the former E_{OC}, and that the 40 mV decrease was enough added overpotential for the rate of HE to be sufficient for establishing a new mixed potential when combined with the anodic reaction.

Another reason to expect HE to be important at the more negative potentials is that the cathodic reaction maintained its activation-limited behavior after deaeration, at the rates that were comparable to or even higher than before in some cases. The size and typical separation of the inclusions, which is only a few μm (Figure 3.1), is significantly less than the depth δ of the Nernst layer (e.g. several hundred μm (Kaesche, 1985) typically encountered under the nearly stagnant/lightly stirring conditions used. Thus, the diffusion-controlled current density would be given approximately by $i_L=nFC_BD/\delta$ where n, C_B and D are the valence, bulk concentration and diffusivity of the species undergoing reduction. For OR, n=4, D~2 10^{-5} cm^2/sec and C_B~3 10^{-7} M under aeration, so for the expected δ values i_L would be >~10^{-5} A/cm^2 which is larger than most of the forward scan i_C values observed. However, under deaeration i_L for OR would become about two orders of magnitude smaller, with values in the order of 10^{-7} to 10^{-6} A/cm^2, but such limitation was not observed in the cathodic curves under deaeration even at the low scan rates. Yet, if the diffusional transport were not an issue, the sustained high cathodic reaction rates under deaeration would also be

inconsistent with the usual first order kinetics for OR, were i_C is proportional to the concentration of O_2 in the electrolyte. Those discrepancies do not apply to HE, which at the solution pH is most likely to proceed by direct water reduction, which is neither subject to concentration polarization nor greatly dependent on O_2 concentration.

It would appear then that while OR is significant (at least for the forward scans) near the aerated E_{OC}, HE becomes dominant at the more negative potentials perhaps aided by having a smaller Tafel slope than that of OR. It is cautioned that invoking HE does not explain all the polarization effects observed upon deaeration. For example, upon averaging results of multiple specimens, cathodic currents were somewhat higher after deaeration. In the context of a simple mixed potential scenario, it would be necessary to propose an increase in the rate of both the anodic and the cathodic reactions, in the appropriate proportions, to explain both a decrease in E_{OC} as well as an increase in the cathodic reaction rates. The present evidence is insufficient to identify if and how an anodic rate increase takes place upon deaeration and this issue shall remain for later investigation.

Setting aside the issue of the identification of the cathodic reaction, the most striking feature demanding explanation is the strong hysteresis present in the return cathodic curve, notably for the FG condition, as well as the much lesser extent of hysteresis upon deaeration. Clearly, the extent, direction, and scan rate dependence of the observed hysteresis indicate that the aluminized surface became an increasingly better cathode as the cathodic reactions

progressed, but the mechanism for such increase and its dependence on aeration is not evident.

Detailed elucidation of the above issues would require additional experimental evidence such as surface analytical data and controlled transport experiments (e.g. using a rotating disk electrode (Newman, 1966)) that are beyond the scope of the present investigation. Instead, a tentative scenario will be presented below that accounts for the observed behavior in the aerated condition, and for some of the features seen after deaeration. The scenario may serve as a first step in formulating a future specialized study of the problem. The approach is inspired by well-documented models of cathodic enhancement in aluminum-copper alloys by deposition of copper dissolved in aqueous media (Vukmirovic, 2002).

Analogous to those models, it is speculated that upon cathodic polarization below the starting E_{OC} a species that serves as an efficient host for the operating cathodic reaction (in the following assumed to be only HE for simplicity) deposits somewhere on the aluminized surface. That new surface is in addition to the initially present inclusions, and may have a higher exchange current density for the cathodic reaction than the inclusions. Thus, a small amount of deposition may have a strong effect so that even a small initial concentration of the depositing species in the solution could suffice and even not become exhausted from the solution throughout the entire polarization cycle. The rate of deposition is finite, so consistent with observation the effect would be stronger at the lower scan rates. On first approximation, the cathodic current due

to the deposition reaction may be considered to be small compared to that of the main cathodic reaction. Also as an approximation, only a single anodic reaction will be assumed for the cathodic potential regime explored, modeled as potential-independent passive Al dissolution at a constant rate i_{P2}.

The tentatively proposed deposition reaction is Fe reduction ($Fe^{+2}+2e^{-} \rightarrow Fe$), where the Fe^{+2} ions are available from prior preferential dissolution of the inclusions. The inclusions may have been in electronic contact with the rest of the metal, or as free particles separated from the matrix due to undercutting cathodic corrosion of the surrounding aluminum (Vukmirovik et al, 2002, Park et al, 1999). Assuming equilibrium with some metallic Fe on the surface at the beginning of the potential scan, the initial Fe^{+2} ion concentration in the pH range of interest is given by $[Fe^{+2}]_i = 10^{(E_{OC}-E_0)/0.03}$ where E_0 = -681 mV is the standard Fe^{+2}/Fe redox potential (Bockris and Reddy, 1970). The typical E_{OC} values of -900 mV and -940 mV for the aerated and deaerated conditions, respectively, correspond then to $[Fe^{+2}]_i$ values of ~3.6 10^{-8} M to ~3.6 10^{-9} M (0.002 ppm and 0.0002 ppm), which are consistent with the upper bound concentration observed by Atomic Absorption Spectroscopy. The Fe^{+2} ions present in the solution at the beginning of the polarization cycle increasingly reduce to deposited Fe as cathodic polarization progresses. For simplicity, a high cathodic reaction exchange current density on the newly formed surface will be assumed, so the required amount and rate of deposition is small and $[Fe^{+2}]$ can be treated as being approximately constant over the polarization cycle. Given a slow enough scan rate, the Fe deposition will become significant and the main cathodic

reaction rate will be noticeably greater in the return scan, thus resulting in pseudoinductive hysteresis as observed experimentally.

The observation of lesser hysteresis for the deaerated than for the aerated solution in AR and FG surface conditions may be explained by the effect of aeration on the starting E_{OC} (~40 mV higher than in the deaerated solution). The order-of-magnitude leaner initial Fe^{+2} concentration noted above for the deaerated solution would result in a correspondingly lower extent of new Fe deposition, and hence, less pronounced hysteresis. At the more negative starting E_{OC} under deaeration, there would have been some Fe deposition on the surface, which might account for the similar or greater cathodic reaction rates observed after deaeration compared with before. As indicated above, it would be however necessary to invoke a stronger anodic reaction rate upon deaeration (an increase of i_{P2} in the above simplified assumptions) to explain a more negative E_{OC} in the face of similar or increased cathodic action. That hypothesis and its operating mechanism would necessitate additional experimental evidence for evaluation, so the following will focus on the response observed under aerated conditions.

The predictions of the above scenario for aerated conditions were evaluated by a simplified quantitative model that was formulated by assigning Tafel kinetics to both HE and Fe deposition, with nominal exchange current densities i_{0Ci}, equilibrium potentials $Eeqc_i$, and cathodic Tafel slopes β_{Ci} where the subscript i is replaced by 1 for Fe and by 2 for HE accordingly. HE is assumed to take place at the Fe-rich inclusions initially present, and at the newly

deposited metallic Fe surface. The region where Fe deposition takes place is not known, so a cathodic current density for Fe deposition will be nominally assigned to act on the specimen surface not initially occupied by the inclusions or any previously deposited Fe, leaving it up to the choice of i_{0C1} and related parameters to obtain appropriate scaling factors. The aluminum on the rest of the surface is assumed to be experiencing slow passive dissolution at a current density i_{P2}. The solution has high conductivity so the ohmic potential drop is neglected.

Per the assumptions above, the time-dependent total cathodic current under activation control comprises that of HE and Fe deposition such that:

$$I_{CT}(t) = I_{C2I}(t) + I_{C2N}(t) + I_{C1}(t) = I_{C2}(t) + I_{C1}(t) \tag{3.1}$$

where I_{C2I} and I_{C2N} are the HE currents on the inclusions and on the newly deposited Fe, respectively, and I_{C1} is the Fe deposition current on the rest of the surface. It is also assumed that HE on both inclusions and newly deposited Fe has the same kinetic parameters except for the exchange current density, which is i_{0C2} on the inclusions and greater by a multiplier factor k_2 on the deposited Fe. Thus, $I_{C2}(t)$ can be written as:

$$I_{C2}(t) = i_{0C2} \cdot \left(A_{C0} + \frac{k_1 \cdot k_2}{2F} \int_0^t I_{C1}(\tau) d\tau \right) \cdot 10^{\frac{Eeqc_2 - E(t)}{\beta_{C2}}} \tag{3.2}$$

where F is the Faraday constant, E(t) is the applied potential, A_{C0} is the initial Fe-rich inclusion area, and $\frac{k_1}{2F} \int_0^t I_{C1}(\tau) d\tau$ gives the area of the deposited Fe. The parameter $k_1 = A_S N_A$ is the Fe coverage constant in cm^2 per moles of Fe^{+2}, N_A is the Avogadro's number, and A_S represents the area described by a simple cubic

structure of Fe atoms with a typical lattice parameter of 0.28 nm (Kepaptsoglou et al, 2007).

Per the assumed locus of Fe deposition:

$$I_{C_1}(t) = i_{0C1} \cdot \left(A - \left(A_{C0} + \frac{k_1}{2F} \int_0^t I_{C_1}(\tau) d\tau \right) \right) \cdot 10^{\frac{Eeqc_1 - E(t)}{\beta_{C1}}} \tag{3.3}$$

where A the total specimen area. Then, the net cathodic current is:

$$I_{net}(t) = I_{C2}(t) + I_{C1}(t) - i_{P2} \cdot \left(A - \left[A_{C0} + \frac{k_1}{2F} \int_0^t I_{C_1}(\tau) d\tau \right] \right) \tag{3.4}$$

Figure 3.7 show solutions to Eq. (3.4) numerically calculated by finite differences for the aerated condition, respectively. Typical values of β_{C1} and i_{0C2} (Kaesche, 1985) were chosen along with values of β_{C2} and i_{P2} numerically calculated from the CYP tests conducted at 1 mV/sec (see Table 3.1). Consistent with specimen dimensions and surface analysis, A was set to 95 cm^2 and A_{C0} to 5 cm^2 (AR condition). A nominal initial Fe^{+2} concentration equal to 0.002 ppm was chosen, calculated as above. Plausible input values of i_{0C1} and k_2 were chosen such that the model calculations simulated a typical CYP trend of the AR condition at 0.05 mV/sec. Those input values were used for the other scan rates as well.

The model results were in reasonable agreement with the experimental trends. However, a slight discrepancy of the model results respect to the experimental data is noted for the return scan at 0.05 mV/sec for the aerated solution. A momentary increase of the experimental cathodic current density followed by a steeper slope was observed for the slowest return scan, not quite

well reproduced by the simplified model. This observation is not clear at this moment but it can be speculated that if the Fe deposition mechanism is assumed to be a very slow process compared to the slowest scan rate examined, then its response to the potential change is not instantaneous so that Fe^{+2} ions continue to deposit even during the return scan. The resulting effect yields a pseudoinductive behavior in accordance with the experimental results.

3.5 Conclusions

1. Cyclic polarization tests conducted on the as received and finely ground surface unblemished aluminized steel Type 2 exposed to a solution with high scaling tendency, high alkalinity and moderate chloride content yielded cathodic current densities for the finely ground surface condition that were about twice as much as those recorded for the as-received surface condition, consistent with larger amounts of Fe-rich inclusions noted on the finely ground surface.
2. Experimental evidence presented here suggests that there is no clear indication about the type of the cathodic reaction(s) taking place at the Fe-rich inclusions. However, experimental results (e.g. change in E_{OC} due to solution deaeration) permitted to speculate that O_2 reduction was the main reaction at potential of ~-900 mV and H_2 evolution reaction took over at more negative potentials.
3. Cyclic polarization tests also showed that for the smallest scan rate examined (0.05 mV/sec) a significant hysteresis existed between the cathodic current

densities for the forward and reverse scans. The amount of hysteresis decreased for increasing scan rates (0.5 and 1 mV/sec) associated to the amount of Fe^{+2} ions being deposited during polarization. It is proposed that larger hysteresis was observed for the aerated solution compared to the deaerated solution, especially at the smallest scan rate, because the amount of Fe^{+2} ions is larger in the aerated solution.

4. The results obtained from a simplified quantitative model were in reasonable agreement with the experimental results.

Table 3.1: Parameters chosen for cyclical polarization modeling.

β_{C2} mV dec^{-1}	β_{C1} mV dec^{-1}	i_{0C2} A cm^{-2}	i_{0C1} A cm^{-2}	i_{P2} A cm^{-2}	k_2	k_1 cm^2 mol^{-1}
200	120	10^{-8}	10^{-10}	$5\ 10^{-8}$	100	$4.7\ 10^{8}$

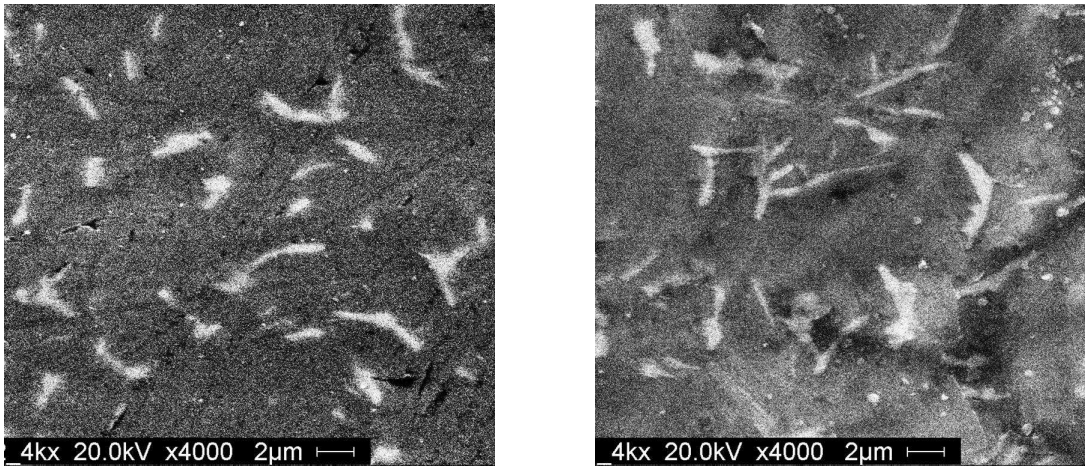

Figure 3.1: SEM images of the unexposed FG (left) and AR (right) surface conditions. Light features correspond to Fe-rich inclusions.

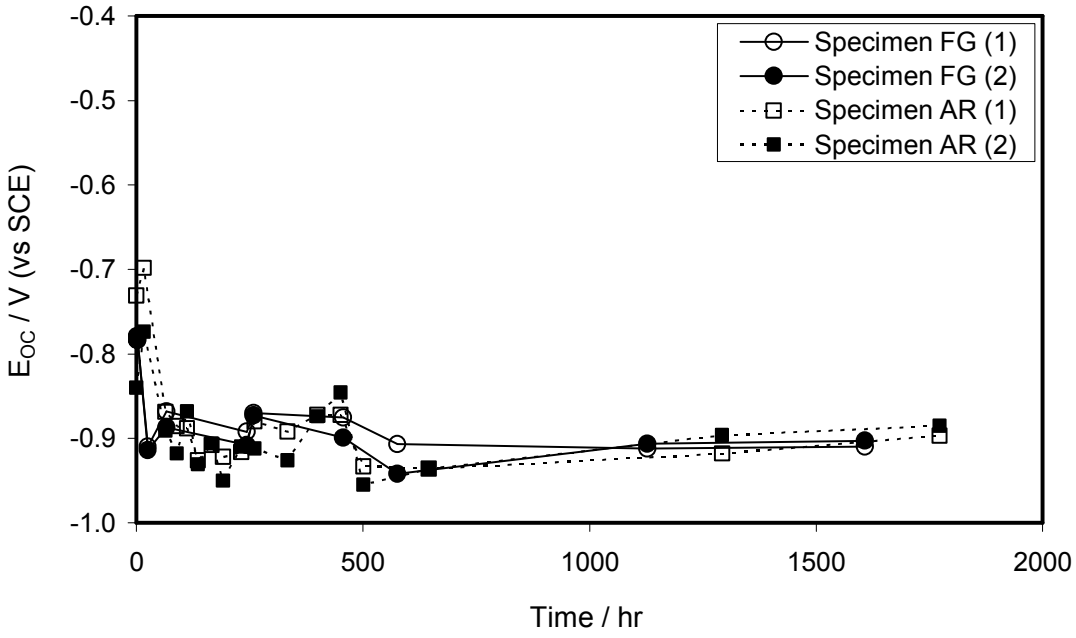

Figure 3.2: E_{OC} evolution of the AR and FG surface conditions. Specimen number is denoted in parenthesis.

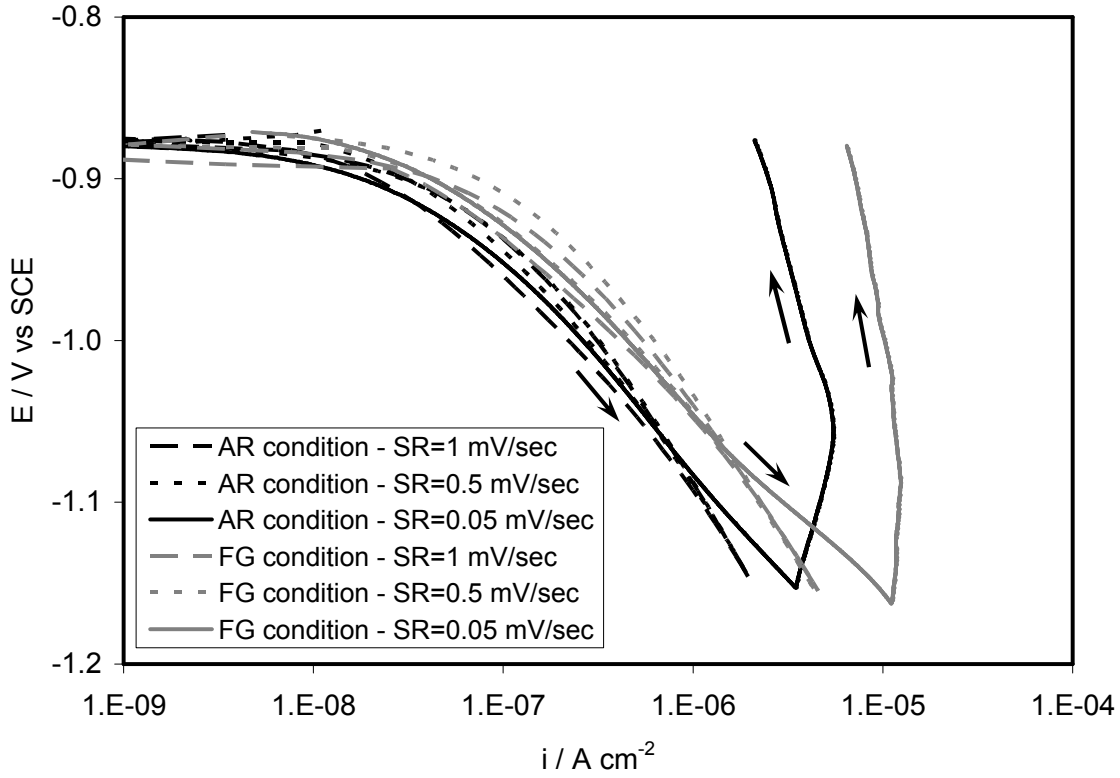

Figure 3.3: Cyclical cathodic polarization of the AR and FG surface conditions in unstirred naturally aerated solution at 408 hr of exposure. Return scan current was always greater than for the forward scan as exemplified by arrows.

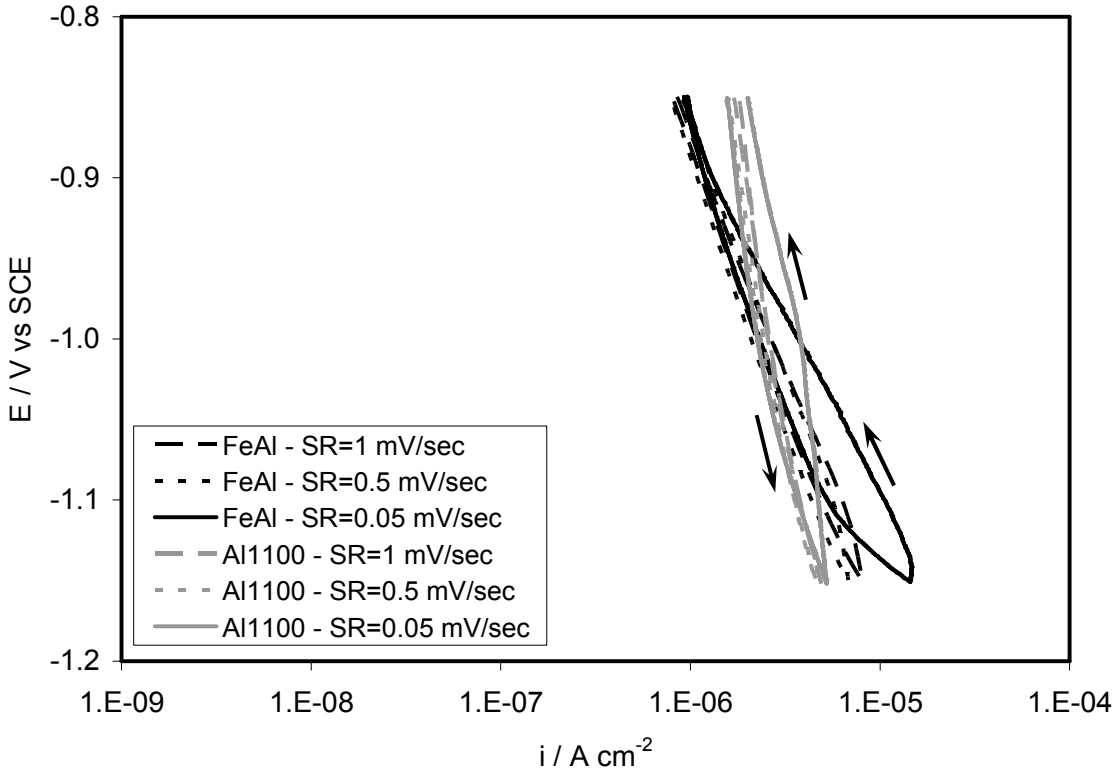

Figure 3.4: Cyclical cathodic polarization of the FeAl and Al1100 alloys in unstirred naturally aerated solution at 408 hr of exposure. Return scan current was always greater than for the forward scan as exemplified by arrows.

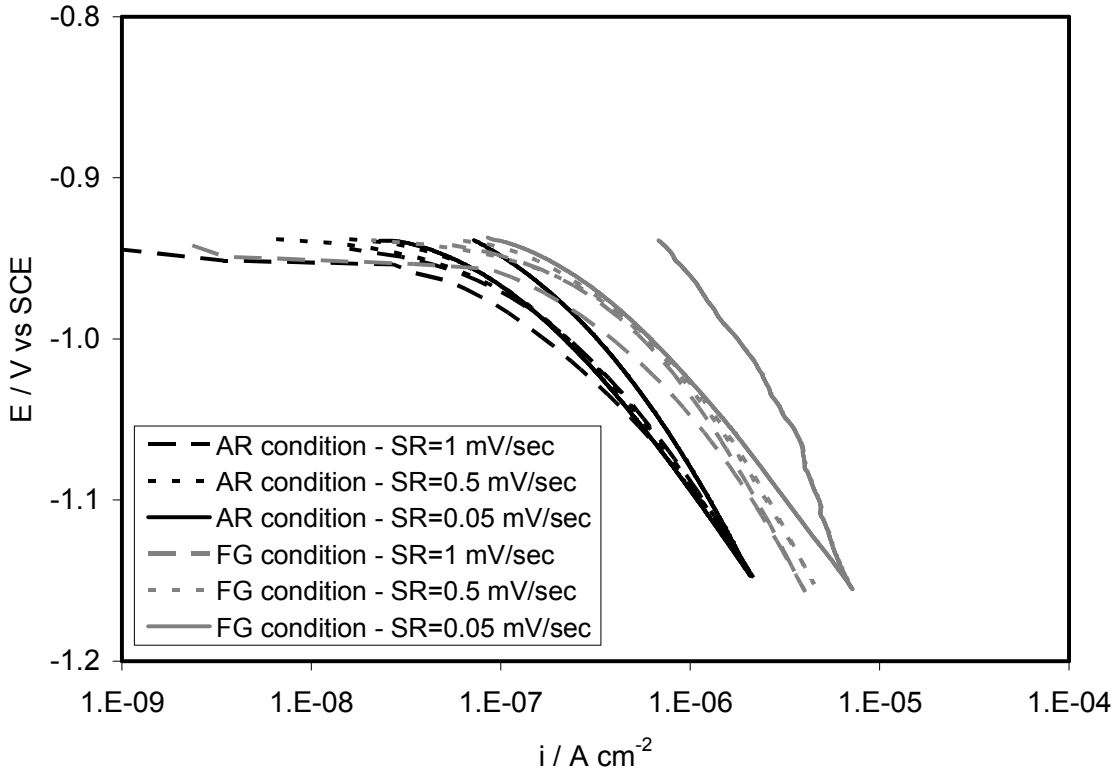

Figure 3.5: Cyclical cathodic polarization of the AR and FG surface conditions in unstirred deaerated solution after 650 hr of exposure.

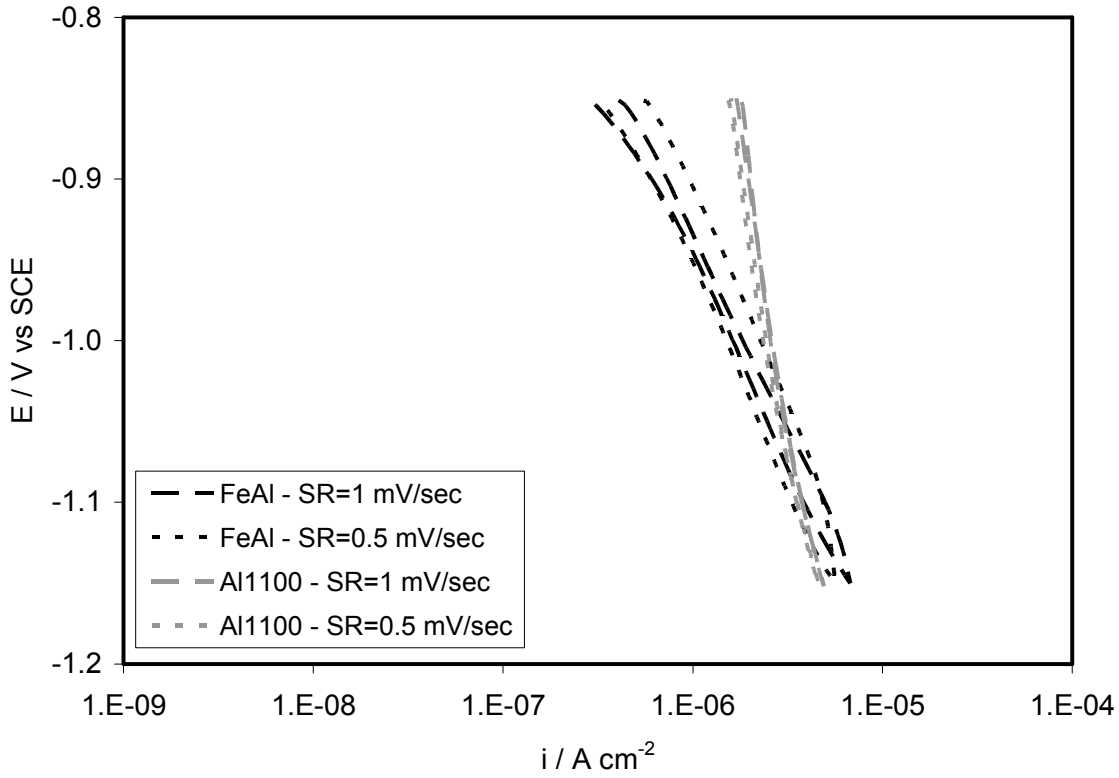

Figure 3.6: Cyclical cathodic polarization of the FeAl and Al1100 alloys in unstirred deaerated solution after 650 hr of exposure.

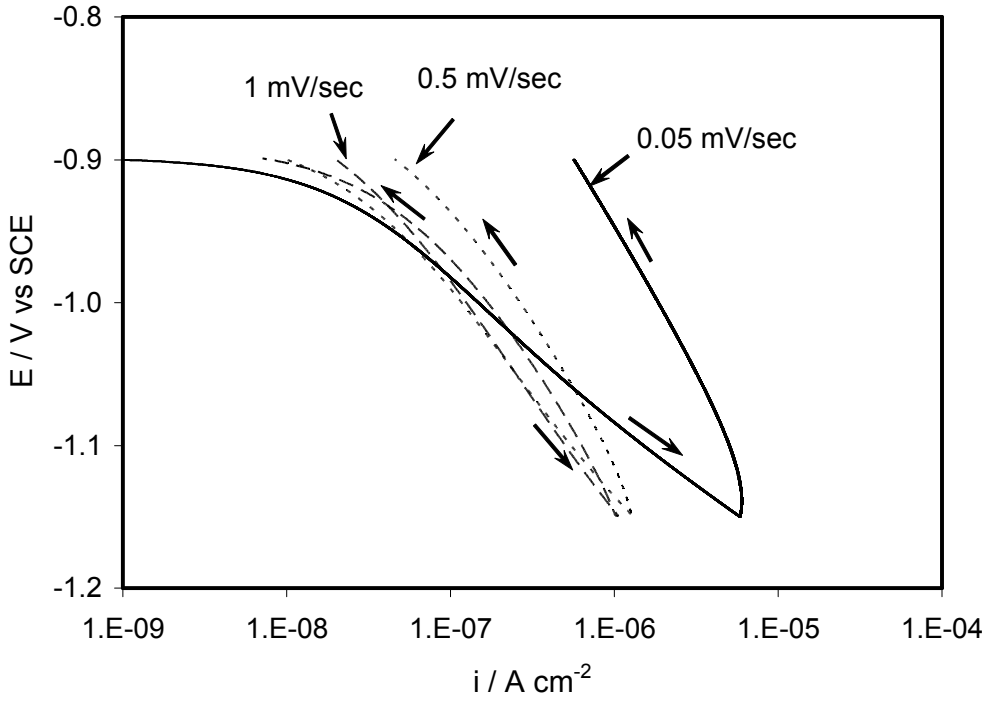

Figure 3.7: Model results for the AR surface condition in the aerated solution.

Chapter 4

Galvanic Behavior on the Corrosion Resistance of Aluminized Steel Type 2

4.1 Introduction

As mentioned in previous Chapters, aluminized metallic coatings have excellent intrinsic corrosion resistance compared to other metallic coatings. As shown in Chapter 2, outer aluminized coating can maintain passivity for extended exposure times in scale-forming environments so that long service lives of unblemished aluminized steel components could be expected. However, the aluminized coating may be mechanically partially disrupted in common use exposing the underlying base steel. In such case, it is important to know if the aluminized coating will galvanically protect the exposed steel, and to which extent the size of the exposed steel portion will be important when exposed to environments commonly encountered in Florida.

This Chapter aims at determining the corrosion behavior of mechanically distressed aluminized steel Type 2 with exposed underlying steel substrate, immersed in waters of varying scaling tendencies with moderate and high chloride contents bracketing compositions typically found in Florida waters. These conditions are of interest as environmental aggressivity may be sufficient to cause significant corrosion of the exposed steel, but not enough to promote

adequate galvanic current delivered by the outer aluminized coating. Of importance is to determine the amount of current delivered by the outer aluminized coating when coupled to steel of different areas, and the mechanisms associated with the galvanic corrosion processes relevant to better forecasting durability in critical highway applications. Advanced forecasting will be addressed in a future investigation.

4.2 Experimental Procedure

The aluminized steel Type 2 used in this part of the investigation came from the same batch as those used in previous Chapters. Circular unblemished specimens of 95 cm^2 nominal surface area were cut out from the as-received aluminized steel sheet, and coating breaks 2 cm and 0.2 cm diameters and 300 μm deep were machined in the center of one of the specimen faces exposing the underlying steel. The blemished specimens are identified hereon as LCB and SCB for the large and small coating breaks, respectively. The exposed steel/aluminized coating area ratio A_R was ~0.03 for the LCB specimens and ~3 10^{-4} for the SCB specimens. Traces of metal shavings were removed from the machined breaks with a razor blade. A magnetic coating thickness gauge was used to verify that the exposed steel was free of aluminized coating. Afterwards, the blemished specimens were ultrasonically degreased with acetone and ethanol, and stored in a desiccator. A 500 mL three-electrode test cell configuration similar to that schematically shown in Figure 2.3 in Chapter 2 was used, exposing horizontally the blemished face. A metal-metal oxide activated

titanium mesh was used as a counter electrode placed at ~6 cm from the metal surface and a 0.8 cm long and 0.2 cm diameter titanium wire used as a pseudo reference electrode (Castro et al., 1996) periodically calibrated against a SCE momentarily placed in the liquid. Unless specified, all the potentials reported here will be given on the SCE scale. To determine the electrochemical behavior of the underlying steel, additional experiments were conducted in duplicate on uncoupled steel specimens of ~3 cm^2 nominal surface area, made by mechanically stripping the aluminized coating from the same aluminized steel stock and wet ground to a 320-grit surface finish, placed in a companion cell. For those experiments, a SCE electrode was placed momentarily in each test solution for the duration of the electrochemical measurements.

To monitor galvanic currents between the exposed steel and the surrounding aluminized coating as well as the electrochemical impedances of the individual macrocell components, a test cell shown in Figures 4.1 and 4.2 was used. The test cell consisted of an as-received unblemished aluminized steel specimen of 95 cm^2 nominal surface area placed at the bottom of the cell and a separate but normally interconnected (except during EIS and galvanic measurements) 3 cm^2 nominal surface area steel specimen positioned ~2 cm parallel to the aluminized surface. The macrocell assemblies had an A_R~0.03. The steel component was made by mechanically stripping the aluminized coating from the same aluminized steel stock, and wet ground to a 320-grit surface finish. Electrical connection was made using a stainless steel wire spotted welded to the back side of the steel. Afterwards, the back side and the edges of the steel were

coated with epoxy. Both the aluminized and the steel components were cleaned with acetone and ethanol and stored in a desiccator prior to immersion.

All test cells were never replenished with new solution for the entire exposure. The relatively small electrolyte volume/total specimen area ratio was intended to be representative of worst-case culvert pipe conditions with stagnant water on the pipe invert, or of occluded conditions for pore water on the soil side of a pipe.

The test solutions evaluated were C, NP, P, and SW per the nomenclature in Chapter 2 and compositions shown in Tables 2.2 and 2.3. The test solutions were quiescent and naturally aerated through a small opening in the test cells. In such case, the test solutions were expected to be in equilibrium with the partial pressure of CO_2 of the surrounding air. The equilibrium solution compositions, calculated by the Mineql+® software, for the open system were comparable to those for the pseudo-closed system used in Chapter 2. Solution pH was measured by a research grade combination pH electrode (model 476086 from Corning Inc.) with an internal Ag/AgCl reference system connected to a Corning Model 140 pH meter (Scientific Instruments, Science products, Corning Glass Works) with an input impedance of ~10^{12} Ω set as a voltmeter. An auxiliary multimeter was connected to the voltmeter output to achieve a resolution of 0.1 mV. The pH electrode was calibrated before and after use using pH=4, pH=7 and pH=10 buffer solutions corrected by the appropriate solution temperature factor. A conductance bridge (model 31A from YSI Co. Inc., Yellow Springs, OH) with platinum-iridium electrodes was used for conductivity measurements.

The immersion tests were conducted in duplicate and in some cases in triplicate for up to ~3,500 hr at 22 ± 2 ˚C. Solution pH and electrical conductivity were monitored at selected times. Open circuit potentials (E_{OC}) were periodically measured as a function of exposure time with a multimeter of 200 MΩ input resistance. To map the potential profile with radius a Luggin capillary placed at ~1 mm from the metal surface was manually scanned over the surface in duplicate LCB specimens exposed to solutions P and NP. In addition, EIS measurements were regularly conducted at the E_{OC} with a Gamry® PCI4-300 potentiostat in the frequency range from 100 kHz to 1 mHz taken 5 data points per decade using sinusoidal signals of 10 mV_{RMS} amplitude. Galvanic currents between the aluminized and steel components were periodically measured with a 0.1 Ω input resistance ammeter (Model HP 34401A). By convention, net anodic currents were assigned positive signs. Measurements of E_{OC} of the interconnected components were recorded right before measurements of galvanic currents. To evaluate the individual impedance response of the two macrocell components in the galvanic couple, the components were disconnected and a battery-operated *dc* current source of impedance at least one order of magnitude above the impedance of each component of the couple was connected across the components, to preserve the individual static polarization conditions (see Figure 4.2). The component to be tested was then connected to the EIS system as usual. The other component of the couple remained *dc*-polarized but nearly free of *ac* excitation current during the test. At

the end of long term exposure, all specimens were removed, cleaned, and examined by 40X optical microscopy.

Direct assessment of the corrosion rate of the aluminized portion conducted in selected specimens shown in Table 4.1 was accomplished by performing coating thickness measurements after the end of exposure using a magnetic coating thickness gauge (model Mikrotest® III by ElektroPhysik), reported by the manufacturer to have an accuracy of ±5% of the reading. The measuring protocol included the selection of six locations on the aluminized surface distributed as follows: three locations at the unexposed rim of the specimen that approximated conditions before exposure, and three locations on the exposed aluminized surface where it had retained deposits in the form of corrosion products or other precipitates. Afterwards, the deposits at those three locations were stripped from the aluminized surface by lightly hand rubbing with 600-grit abrasive paper until revealing the bare aluminized surface underneath. Similar rubbing on the unexposed locations was found to result in no detectable metal loss per magnetic gauge indications. A total of three measurements were taken at each location by three independent operators, each selecting different spots in each specimen following the measuring protocol above. Then, the results were combined for each location, and the resulting average and standard deviation were calculated. Nominal average coating loss was roughly estimated by subtracting the remaining coating thickness (after removing deposits) from that measured at the unexposed metal, and then converted to nominal average corrosion rate by dividing by the corresponding test duration. The nominal

average coating loss was then compared to the integrated material loss computed from EIS measurements as shown in Section 4.4.4.

4.3 Results

Table 4.2 summarizes visual assessment and E_{OC} evolution trends of the blemished specimens as well as the unblemished specimens reported in Chapter 2. The corresponding detailed comments including electrochemical impedance results in the form of Nyquist diagrams of the blemished specimens are given in the following sections. Treatment of the EIS data presented in this Chapter was the same as that employed in Chapter 2. Impedance trends are in some instances exemplified for single specimens (labeled as #1 hereon). Comparable impedance results were obtained for the duplicates (labeled as #2 hereon) and for the triplicates (labeled as #3 hereon) unless otherwise noted. Triplicate specimens, available in some cases, were tested for trend confirmation when needed. Results for replicates not given in this Chapter are documented in Appendix B. Results for the LCB specimens exposed to solution C and for the macrocell assemblies in solutions C and SW are not available because significant crevice corrosion developed underneath the sealing gasket in all replicate specimens so the results were discarded.

4.3.1 Solution Compositions

Figures 4.3 and 4.4 show the pH evolution for up to 3,000 hr for the LCB and SCB specimens, respectively. Immediately after immersion, bulk pH values

were ~7.8 for NP, ~7.5 for P, ~7.3 for C, and ~7.6 for SW, close to the values reported in Table 2.2 in Chapter 2. As time progressed, the bulk pH for solution P steadily increased to ~7.7 and ~8.2 for the LCB and SCB configurations, respectively, up to ~1,200 hr and remained nearly constant afterwards. The bulk pH for solution NP showed an increase to terminal pH values of ~9.0 (SCB) after ~200 hr and ~8.8 (LCB) near the end of the exposure. The bulk pH for the solution SW for both SCB and LCB configurations increased to ~8.0 by the end of the test. In solution C, the bulk pH showed pH fluctuations (around a pH unit) around the terminal pH of ~7.5. Comparable pH trends were also observed for the macrocell assemblies exposed to solutions NP and P.

Total hardness and total alkalinity, determined by titration following procedures indicated in the Standard Methods for the Examination of Water and Wastewater (1992), as well as the solution conductivity are reported in Table 2.2. The Fe^{+2} concentration in all solutions, measured by Atomic Absorption Spectroscopy after ~2,000 hr, was below the minimum detection limit of the instrument (0.01 ppm).

4.3.2 Blemished Specimens

4.3.2.1 E_{OC} Trends

Figures 4.5 through 4.11 show the E_{OC} evolution for up to ~3,000 hr for the LCB and SCB specimens, respectively.

The LCB specimens exposed to solution P (Figure 4.5) showed E_{OC} values of ~-780 mV immediately after immersion, increasing to nearly constant

values of ~-745 mV for a period ranging from ~1,200 hr to ~1,700 hr of exposure. At the end of that stage, E_{OC} started a gradual decrease to attain terminal values of ~-910 mV after ~2,000 hr. The SCB specimens exposed to solution P (Figure 4.8) showed E_{OC} values of ~-760 mV immediately after immersion, then decreased to ~-900 mV after ~180 hr and slowly recovered to ~-820 mV near the end of the test. Values of E_{OC} obtained with a Luggin probe placed at ~1 mm above the surface at various radial locations of replicate LCB specimens in solution P at ~72 hr and ~200 hr of exposure, were nearly constant only ~1-2 mV more positive over the exposed steel than over the aluminized surface. The E_{OC} distribution next to the metal surface for the LCB configuration, calculated using a *dc* computational model presented in Chapter 5, was in agreement with the E_{OC} profiles observed here.

The LCB specimens exposed to solution NP (Figure 4.6) showed E_{OC} values of ~-770 mV immediately after immersion, increasing to ~-730 mV for periods ranging from ~500 hr to ~1,600 hr. At the end of that period, E_{OC} decayed to ~-930 mV for periods ranging from ~900 hr to ~2,000 hr. For up to ~1,200 hr, the LCB specimen #2 did not display a decrease in E_{OC} possibly associated with a premature test termination. The SCB specimens (Figure 4.9) showed E_{OC} values of ~-750 mV immediately after exposure to solution NP, decreasing to ~-900 mV for periods ranging from ~50 hr to ~200 hr. The SCB specimen #1 showed long term (days-weeks) E_{OC} fluctuations for up to ~1,500 hr followed by a stabilization period around the terminal E_{OC}. Long-term E_{OC} fluctuations were unnoticeable in the duplicate specimen.

The LCB and SCB specimens exposed to solution SW (Figure 4.7 and Figure 4.10, respectively) showed comparable E_{OC} trends. For a very few hrs after immersion, E_{OC} values were ~-750 mV followed by a sharp decrease to a terminal E_{OC} around ~-880 mV.

The SCB specimens exposed to solution C (Figure 4.11) showed E_{OC} values of ~-620 mV a few hrs after immersion followed by a gradual drop to ~-810 mV after ~1,000 hr, and then recovered slowly reaching ~-710 mV by the end of exposure.

Figure 4.12 illustrates the E_{OC} evolution for up to ~500 hr for the uncoupled steel specimens exposed to solutions C, NP, and P. Immediately after exposure, the E_{OC} was ~-380 mV for solution NP and ~-430 mV for C and P. A few hrs after immersion, the E_{OC} decayed steeply to nearly constant terminal values around ~-720 mV for solutions NP and P and ~-630 mV for solution C. These terminal E_{OC} values were comparable to those recorded for the LCB and SCB specimens in the same solutions before the start of the E_{OC} decay.

4.3.2.2 Direct Observations of Corrosion

4.3.2.2.1 The Aluminized Coating

In the LCB specimens exposed to solutions NP and P, the beginning of the E_{OC} drop was concurrent with the appearance of grayish discoloration of the aluminized surface around the perimeter of the exposed steel spot. The discoloration, moderate in P and darker in the NP system, later covered uniformly the entire aluminized surface forming an adherent layer ~10-15 μm (NP) and <1

μm (P) thick as measured by a magnetic thickness gauge after the end of the exposure. Specimen autopsy showed that corrosion damage associated with uniform discoloration appeared to be mainly associated with changes in the outer coating layer as confirmed by metallographic analysis. Metallographic examination conducted on a cross section near the aluminized/steel edge of the LCB specimen #1 (and the specimen #2 as well) exposed to solution NP (Figure 4.13) showed an annulus ~70 μm wide surrounding the exposed steel spot of severe corrosion, not noted in any of the specimens in solution P. As a result, the outer aluminized coating layer in NP was completely consumed exposing the inner layer which appeared to remain intact for the time frame examined. A SEM image (Figure 4.14) of the discolored surface of the LCB specimen #1 in solution NP taken at the end of exposure showed a tight, compact layer covering uniformly the aluminized surface. Further SEM-EDS analysis (Figure 4.15) of a dried portion of that layer was consistent with the presence of aluminum hydroxide $Al(OH)_3$ in agreement with the results reported in Chapter 2 and the results shown elsewhere (Davis, 1999). Few isolated small pits were observable only under magnification (indicative of pit diameter <0.1 mm) in both solutions NP and P.

On the other hand, the LCB specimens exposed to solution SW showed isolated small visible pits (indicative of pit diameter ~0.1 mm) on the aluminized surface early on followed by the appearance of uniform light discoloration, forming an adherent layer <1 μm thick, but the appearance of that layer (at ~360 hr of exposure) was not coincident with the start of the E_{OC} decay. The light

surface discoloration in SW did not start near the exposed steel perimeter but instead at several locations on the aluminized surface. Interestingly, metallographic examination conducted on the specimen #1 in SW (Figure 4.16) showed that the aluminized coating surrounding the exposed steel did not display signs of severe corrosion with both outer and inner coating layers in place.

During exposure, a similar grayish discoloration was noted starting at the aluminized surface in the vicinity of the exposed steel of all SCB specimens in solutions NP and C, and at various spots on the aluminized surface in SW. The discoloration, dark for solutions C and NP and lighter for SW, progressed until covering uniformly the entire aluminized surface, forming an adherent layer ~5-10 μm (NP), <2 μm (C), and <1 μm (SW) thick. The appearance of initial discoloration was concurrent with the E_{OC} drop for solution C (~545 hr after immersion). For solutions NP and SW, the appearance of initial discoloration was not concurrent with the beginning of the E_{OC} drops (which took place after short exposure times) but instead were noted (for the specimens #1) at ~1,030 hr and ~275 hr for NP and SW, respectively. In contrast, the aluminized surface of the SCB specimens exposed to solution P did not show discoloration or pits throughout the entire test period.

Autopsy of the SCB specimens showed that corrosion damage associated with uniform discoloration appeared to be mainly associated with changes in the outer coating layer as confirmed by metallographic examination. In addition, few pits visible to the naked eye (~0.1 mm diameter) in solutions C and SW were noted on the aluminized surface shortly after exposure. Some of those pits in

solution C appeared to have reached the underlying steel since reddish deposits were detected at some pit mouths as shown in Figure 4.17. Few isolated small pits were observable only under magnification (indicative of pit diameter <0.1 mm) in solution NP. As in the LCB specimens in the NP system, the SCB specimens in solutions NP and C as well showed a ~50 μm wide annulus of severe corrosion surrounding the exposed steel as shown in Figure 4.18. It can be noted that the outer aluminized layer was completely consumed exposing the inner coating layer, which appeared to have remained intact throughout the exposure. Contrarily, the SCB specimens in SW and P did not show severe corrosion around the exposed steel as exemplified in Figure 4.19 for the SW solution.

4.3.2.2.2 The Exposed Steel

A few hrs after immersion, visual examination conducted on the exposed steel of the LCB and SCB specimens exposed to solutions P and NP (and the individual steel specimens in P and NP solutions as well) showed a uniform reddish/black scale (likely rich in Fe^{+2}/Fe^{+3}) formed over the entire steel surface. Later on, the scale in those specimens developed until forming a layer ~300 μm thick. At ~450 hr of exposure, the central ~0.3 cm^2 of the exposed steel area of all LCB and individual steel specimens in solutions P and NP developed a 1-3 mm thick porous reddish growth. There was noticeable additional steel metal loss underneath the central growth in the LCB and individual bare steel specimens in NP, but less so in P. A metallographic examination (Figure 4.20) carried out in

the LCB specimen #1 exposed to solution NP showed that the metal loss at the exposed steel was estimated to be ~0.1 grams. No such central growth was observed in the SCB specimens exposed to those solutions. At ~500 hr, formation of small crystals appeared on top of the Fe-rich scale in both LCB, SCB, and individual steel specimens immersed in solution P. SEM-EDS analysis of few crystals obtained from the LCB specimens in P was consistent with the presence of $CaCO_3$. During post-exposure cleaning, the scales on the exposed steel of the LCB, SCB, and uncoupled steel specimens in solution NP were easily removed, but were more adherent in solution P.

The exposed steel of the SCB specimens in solution C showed corrosion in only one (#1) of the triplicate specimens, an early formation of a thin reddish scale (likely rich in Fe^{+2}) that later developed to form a layer ~<300 μm thick on top of the steel. No signs of corrosion were observed in either replicate #2 or #3, where the steel spot remained bright over the entire test period. The replicate individual steel specimens in solution C showed early formation of corrosion deposits distributed over the entire surface of similar appearance to that noted in the SCB specimen #1.

The exposed steel of the SCB specimens in solution SW was bright and free of corrosion scale throughout the entire exposure, and there was only very light steel discoloration with no corrosion deposits of the LCB specimens in solution SW.

Selected photographs of the LCB and SCB specimens taken after exposure and after cleaning are shown in Figure 4.21.

4.3.2.3 Impedance Behavior

4.3.2.3.1 LCB Specimens

Figures 4.22 through 4.24 show the non area normalized impedance evolution for up to ~2,400 hr for the LCB specimens exposed to solutions P, NP, and SW.

Figures 4.22 and 4.23 show the EIS results for solutions NP and P, respectively, before and after the onset of the E_{OC} drop. For the period before the onset of the E_{OC} drop, the 1 mHz impedance moduli in both solutions were small (~<1.5 kΩ for NP and P) for up to ~1,300 hr of exposure. Per visual assessment of the specimen surface, the impedance behavior during that period was expected to be dominated mainly by the impedance of the steel portion by itself since corrosion scales there were notable, indicative of significant corrosion rates and correspondingly large integrated admittance. In contrast, the aluminized surface remained bright, suggesting passive behavior with consequent very small integrated admittance despite the large aluminized surface. After the onset of the E_{OC} drop, the 1 mHz impedance moduli decreased even further to ~150 Ω (NP) and ~250 Ω (P), consistent with active corrosion of the aluminized surface in both solutions. At that stage, the impedance behavior was expected to be dominated mainly by the impedance of the uniformly corroding aluminized portion, whereas the exposed steel was cathodically protected by the surrounding aluminized surface. That expectation was supported by the evidence presented in the subsequent sections.

Figure 4.24 shows the EIS results for solution SW for the period after the onset of E_{OC} drop. The 1 mHz impedance moduli ranged from ~2.5 kΩ to ~4.5 kΩ throughout the test, expected to be dominated by localized corrosion of the large aluminized portion. As before, the exposed steel was cathodically protected by the surrounding aluminized surface as discussed in the subsequent sections.

4.3.2.3.2 SCB Specimens

Figures 4.25 through 4.29 shows the non area normalized impedance [8] evolution for up to ~2,700 hr for the SCB specimens exposed to solutions NP, P, SW, and C.

Figure 4.25 shows the EIS results for solution NP where the 1 mHz impedance moduli initially increased with time to reach ~30 kΩ for up to ~1,000 hr, despite the early corrosion scales deposited on the exposed steel. After ~1,000 hr, the 1 mHz impedance moduli started to decrease, consistent with the start of aluminized discoloration, to values smaller than at the beginning (~600 Ω). Figure 4.26 shows the EIS results for solution P where the 1 mHz impedance moduli increased with time from ~30 kΩ to ~80 kΩ after ~2,500 hr, consistent with generally passive behavior and the absence of visual evidence of active corrosion of the aluminized surface over the entire test exposure.

Figure 4.27 shows the EIS results for solution SW where the 1 mHz impedance moduli ranged from ~3 kΩ to ~5 kΩ throughout the exposure.

[8] The EIS measurements conducted on the SCB specimens in all solutions were obtained after the onset of the E_{OC} drop took place.

Figures 4.28 and 4.29 show the EIS results for the specimens #1 and #2 in solution C. The EIS results for the triplicate specimen were comparable to those of the duplicate. The 1 mHz impedance moduli in those cases were initially large approaching ~12 kΩ for #1 and ~50 kΩ for #2 at ~120 hr of exposure. Afterwards, the 1 mHz impedance moduli started to decrease to reach ~2 kΩ for #1 and ~4.5 kΩ for #2 after ~650 hr, coinciding with the appearance of the dark grayish layer on the aluminized surface in both specimens. After ~1,000 hr, there was a long-term recovery toward larger 1 mHz impedance moduli for both specimens.

In all cases, the EIS behavior was expected to be dominated mainly by the impedance of the active (NP, SW, and C systems) and passive (P system) aluminized surface. The exposed steel in all cases remained cathodically protected so its impedance was expected to be comparably large to that of the aluminized coating and that expectation was supported by the evidence presented in the subsequent sections.

In the LCB specimens in NP and the SCB specimens in C and NP, the amount of electric charge consumed by the corrosion of the annulus region calculated by the Faraday's law was <2.7 Coulombs which represents a local impedance of >170 kΩ. This value was considerably larger than the 1 mHz impedance moduli determined after aluminized discoloration (~150 Ω for NP and ~2-4.5 kΩ), thus, its contribution to the overall anodic dissolution of the aluminized surface can be neglected.

4.3.3 Macrocell Assemblies

4.3.3.1 E_{OC} and Macrocell Current Trends

Visual appearance and E_{OC} trends for the macrocell assemblies are summarized in Table 4.2. The E_{OC} trends, rust evolution at the steel component, and changes in the appearance of the aluminized coating generally paralleled those of the LCB specimens exposed to the same environments. In addition to that information, measurements in these macrocell assemblies provided the galvanic current (I_{galv}) between the steel and aluminized components. The evolution of I_{galv}, as well as the mixed E_{OC} is shown in Figure 4.30 for up to ~2,700 of exposure (data available only for P and NP). In both solutions, the unblemished aluminized steel component of the couple was always a net anode while the steel component was a net cathode. The initial I_{galv} values were ~14 μA and ~1.5 μA for solutions NP and P, respectively. Upon the later start of E_{OC} drop, the I_{galv} values in both solutions started to increase reaching terminal values of ~60 μA and at ~35 μA for solutions NP and P, respectively.

4.3.3.2 Impedance Behavior

The impedance responses of the coupled macrocell assemblies and the individual components exposed to solutions P and NP before (~900 hr) and after (~1,780 hr) the onset of the low E_{OC} regimes are illustrated in Figures 4.31 through 4.34.

Before the E_{OC} drop (Figures 4.31 and 4.33), the 1 mHz impedance moduli of the aluminized component were large (~55 kΩ for P and ~13 kΩ for

NP), consistent with generally passive behavior and the absence of visual evidence of active corrosion. The 1 mHz impedance modulus for the steel component was ~1 kΩ for both solutions, in agreement with the observation of early corrosion deposits on the steel surface in both environments. Notably, the overall impedance responses of the coupled macrocell assemblies in both solutions nearly equaled that of the steel component by itself, indicating that the steel ruled the impedance behavior of the coupled system.

After the onset of the low E_{OC} regime (Figures 4.32 and 4.34), the 1 mHz impedance moduli of the aluminized component greatly decreased to ~1 kΩ in solution P and to ~2 kΩ in solution NP, consistent with the appearance of uniform discoloration (strong for NP and moderate for P) and light pitting indicative of ongoing corrosion in both solutions. In addition, the impedance diagrams of the steel component in both solutions resembled a nearly straight line rather than the earlier depressed semicircular appearance. The 1 mHz impedance magnitudes of the coupled assemblies nearly matched those of the aluminized component by itself, indicating that the aluminized coating dominated the impedance behavior of the coupled system for the low E_{OC} regime.

4.3.4 Uncoupled Steel Specimens

Figure 4.35 shows the non area normalized impedance of the uncoupled steel specimens recorded after ~216 hr of exposure to solution NP and ~72 hr to P. The 1 mHz impedance modulus for the steel component was ~500-800 Ω for both solutions, in agreement with the observation of early corrosion deposits on

the steel surface in both environments. The overall impedance trends in both solutions were in good agreement with those recorded for the LCB specimens and the coupled macrocell assemblies exposed to the same solutions for the period before the E_{OC} drop despite the larger solution resistances R_S observed for the uncoupled steel specimens attributed to the larger separation between the metal surface and the reference electrode sensing point. Again, this observation confirms that the impedance response for the aluminized/steel system for the period before the E_{OC} drop is largely dominated by that of the steel.

4.3.5 Coating Thickness Measurements

Figure 4.36 exemplifies schematically a typical aluminized coating cross section of an aluminized steel Type 2 that has been exposed for extended periods of time. Table 4.1 summarizes the average coating thickness measurements (comprising both inner and outer layers) obtained from three independent operators for the conditions before and after exposure obtained for selected specimens. Thickness measurements were measured with a standard deviation of ~±7.6 μm. Table 4.1 also includes estimates of the nominal corrosion rates for the aluminized portion obtained per methodology shown in Section 4.2. For instance, nominal corrosion rates of the aluminized components for the macrocell assemblies in solutions NP and P were large (~16-20 μm/yr in NP and ~13-25 μm/yr in P) in agreement with the visual observation of uniform surface discoloration noted on those specimens. Nominal corrosion rates were also large for the LCB specimens in NP (~21-33 μm/yr) and smaller but modest for the LCB

specimens in P (~7 μm/yr) also consistent with visual observation of surface discoloration in those cases. The LCB specimens in SW showed the smallest nominal corrosion rates (~2 μm/yr) of all specimens examined, in agreement with light uniform corrosion.

4.4 Discussion

4.4.1 E_{OC} Trends and Corrosion Mechanisms

Figure 4.37 is a schematic of the typical E_{OC} evolution trends shown in Figures 4.5 through 4.11 for the LCB and SCB specimens. Macrocell assemblies, where available for the corresponding environments, had E_{OC} trends essentially identical to those of the LCB specimens and will not be discussed separately here.

Shortly after exposure, the E_{OC} values of the specimens with large A_R (LCB and macrocell assemblies) in solutions P and NP (~-700 mV ~-730 mV) were nobler (~100-150 mV) than those with smaller A_R (SCB) exposed to the same solutions and comparable to those measured for the uncoupled steel specimens (~-720 mV) exposed to solutions P and NP. Inasmuch as the active steel showed a small degree of polarizability compared with the more polarizable passive aluminized coating early on in the test, the resulting E_{OC} trends were then dominated largely by the E_{OC} of the large exposed steel corroding at a moderate rate. For the specimens with small A_R in solutions NP, P, and SW and with large A_R in SW, nobler E_{OC} values were maintained for a few hrs after immersion before the E_{OC} decay took place.

In the following the corrosion mechanism of blemished aluminized steel will be discussed, keeping in mind the mechanisms proposed in Chapter 2 for the baseline unblemished material condition. The discussion is keyed to each of the solutions evaluated.

4.4.1.1 Solution P

The behavior of the small coating break (SCB) specimens was similar to that of the unblemished specimens, except that at the very beginning (first day or so) the E_{OC} was relatively positive, likely dominated by that of the small exposed base steel, which initially developed rust as mentioned above. After that period, the E_{OC} dropped to that of the unblemished system, suggesting that the rust layer on the steel acted as an obstacle to O_2 reduction there. From there on, the E_{OC} was such that the exposed steel was cathodically protected by the rest of the system (likely only a very small current is needed for that). The aluminized surface remained passive thereon.

In the specimens with a larger amount of exposed steel (LCB and macrocell assemblies), the E_{OC} was initially quite positive, dictated by the corrosion potential of the large exposed steel spot corroding at a moderate rate in the low Cl^-, scale forming solution as mentioned above. The most striking feature of these systems was that after an interval of typically ~1,500 hr the aluminized surface experienced macroscopically uniform activation and the potential dropped dramatically, with the aluminized surface acting as a strong protecting anode to the exposed steel. The bulk solution pH remained neutral,

and about 2 μm of the outer aluminized layer were macroscopically uniformly consumed in the next 2,000 hr or so.

The activation of the aluminized surface was manifested by light gray discoloration and the appearance of a few small macroscopically apparent pits. As observed in Chapter 2 for similar conditions, the few active macro pits are deemed to be inconsequential because of their small number and dimensions, and their consequently large combined associated ohmic resistance, which would yield only a small fraction of the observed macrocell current. Thus, the macro pits will not be further discussed.

It is tentatively proposed that this macroscopically uniform corrosion reflects the combined presence of many micro pits distributed on a spatial scale comparable to that of the inclusions. Some alkaline dissolution is expected to have taken place as well, but likely to be of secondary importance (except during the initial activation stages as speculated further below) because of the relatively large buffering capacity of solution P. The discoloration is viewed as the result of precipitation of hydrated alumina outside the mouths of those pits. The large cathodic current at the exposed steel plus additional cathodic action at inclusions (minus the current needed to balance any alkaline dissolution) sustains the combined anodic processes at the micro pits.

The above proposal is speculative in that the conditions needed to support that modality of pitting in a 0.01 M Cl^- solution such as solution P would need to be ascertained in future work. In that connection, the following questions could be formulated: (1) Why are the proposed micro pits so uniformly distributed and

stable?, and (2) Why was there a long incubation period (effectively unlimited in the case of small coating breaks) before activation of the aluminized surface?

A possible answer to (1) is that since the exposed steel zone was a strong cathode, competitive action between adjacent pits was less important than otherwise, and larger pits will have less of the cathodic protection action in immediate neighbors that would have tended to lower active pit density. The cathodic action in the small break case is deemed not to be large enough to provide the required cathodic sustaining action. With regards to (2), it is speculated that some degree of alkaline dissolution is needed to start the micro pits (likely nucleated around the inclusions as discussed in Chapter 2). That process is initially slow due to the high potentials prevalent early in the test. The necessary degree of dissolution takes place first at the rim of the exposed steel where pH is mildly elevated through a mechanism (Evans, 1926) where the rim is a net cathode, hence more alkaline, and the center is a net anode, as confirmed by the presence of a central depression on the steel. The alkalinization is mild and etching around the inclusions in the ring around the exposed steel is slow. After a long time (e.g. 1,500 hr) micro pit activation of the aluminized surface immediately around the steel finally takes place. As those micro pits develop and local potential drops further, the active zone slowly expands away from the exposed steel, with consequent expansion of the mildly alkaline zone (but with likely enhanced local action around inclusions at the lower prevalent potentials), until micro pits affect the entire aluminized surface. Experiments to test the validity of this speculative scenario in future research may include (and not be

limited to) the following: (a) detailed local pH measurements to ascertain that mild alkalinization is a pre-micro pitting step; (b) verification that micro pits have etching around inclusions as precursors; (c) exploring solution chemistry spontaneous changes (for example due to exhaustion of buffering capacity because of interaction with air or with products of steel corrosion) as an alternative trigger to the aluminum excitation and (d) exploration of the potential for microbiology induced corrosion in the system.

4.4.1.2 Solution NP

In these solutions, there was also delayed onset of macroscopically uniform active corrosion in blemished specimens, although it is recalled that enhanced corrosion also developed in the unblemished specimens late in the test (Chapter 2). Some of the processes proposed above for specimens with large coating breaks in solution P are likely to be present here too, with the important difference that this solution evolves spontaneously with time to increasingly higher bulk pH values (~9.0) as result of interaction with open air. The onset of the high corrosion regime then appears to be associated with the pH increase, and alkaline oxidation is probably the dominant form of deterioration as it was in the case of the unblemished specimens but aggravated by the coupling with the strongly cathodic steel surface. Consistent with this interpretation, in both small and large coating break systems there was severe aluminized surface corrosion (with complete consumption of the outer coating layer) immediately around the perimeter of the exposed steel region as expected

from the local increase in pH from O_2 reduction at the rim of the exposed steel. As shown by modeling in Chapter 5, corrosion of the aluminized surface next to the rim is also expected to be aggravated by macrocell coupling since the resistive path is lowest there. As noted in Chapter 2, while macroscopically uniform, the corrosion of the aluminized surface may have been more localized at the microscopic level, likely involving aluminum surrounding inclusions, where increasingly higher pH takes place because of O_2 reduction, or because of some extent of micro pit formation around those inclusions following the initial alkaline oxidation undercutting. Solution NP has significant buffering strength, but the effects of local alkalinization around inclusions may be still important because they would be additional to that of the already enhanced high bulk pH of the solution. Macro pits were few in these systems and appear to be secondary per the arguments exposed earlier.

Finally, it is noted that in the small coating break specimens, the E_{OC} dropped a long time before the onset of surface discoloration and associated fast corrosion. It is thought that the early E_{OC} drop reflected less efficient O_2 reduction at the small central steel spot, because of the early buildup of a compact steel corrosion product scale there. Since the steel area was small compared with the rest of the system, local steel polarization and consequent overall E_{OC} drop were expected to be substantial. In the large coating break specimens, the steel surface was larger, and occluding effects would have been proportionally less important.

4.4.1.3 Solution C

In this solution, only small coating break specimens could be evaluated, but delayed onset of active aluminum corrosion took place as well. Unlike the other solutions, solution C has negligible buffering power and the effects of local alkalinization at inclusions are likely to be important. In the case of the blemished specimens the bulk solution pH remained nearly neutral, so widespread alkaline oxidation as proposed for solution NP does not appear to be the main cause of the observed discoloration. Instead, localized alkalinization may have been responsible for generation of finely dispersed micro pits at the inclusion size scale, which would then represent the main form of aluminum attack. Such mechanism is subject to the same caveats noted above for the case of solution P. In solution C, however, the initiation of micro pits is facilitated by the lower buffering capacity, which may explain why activation took place even though the coating break was small.

It is noted that in the case of unblemished specimens the mechanism responsible for the activation of the aluminized surface in solution C was probably a result of a temporary early surge in solution pH in the pseudo closed-cell conditions used there. Those experiments should be repeated under open cell conditions for relevant comparison with the blemished specimen test results.

For completeness, the process of alkalinization and undercutting of inclusions is described here in more detail, keyed to the pictorial description in Figure 4-38 adapted from sources that include Nisancioglu (1990) and Park et al (1999). The increase in the local pH from the cathodic reactions tends to elevate

the OH^- ion concentration in the vicinity of the cathodic reaction locus (Figure 4.38-A). Furthermore, the aluminum activation surrounding the inclusions may cause an increase in the effective area of the inclusions which further catalyses the cathodic reaction, enhancing aluminum dissolution there (Figure 4.38-B).

If conditions are propitious, some of the inclusions can eventually become non-faradically separated as free particles from the aluminum matrix, due to undercutting enhanced-pH corrosion of the surrounding aluminum as proposed by Vukmirovic et al. (2002) (Figure 4.38-C). The free particles would corrode more readily as they are not cathodically protected by the surrounding corroding matrix (Figure 4.38-D), forming Fe^{+2} ions. Those ions can be electrochemically redeposited (by $Fe^{+2}+2e^- \rightarrow Fe$) on the surface either uniformly or, more likely, around the perimeter of the inclusions. The Fe deposition phenomenon was described in detail in Chapter 3. The plated Fe, which is a strong cathode, may promote further aluminum corrosion if high local pH develops around the plated Fe (Figure 4.38-E). As time progresses, more undercutting corrosion of aluminum and the subsequent plating of Fe is expected at many finely dispersed locations with macroscopically uniform appearance.

4.4.1.4 Solution SW

The main aspects described in Chapter 2 for the unblemished condition apply also to the blemished specimens. In the blemished condition, the E_{OC}, initially dictated by corroding inclusions and the central exposed steel zone, is thought to meet or exceeds E_{pit}. The rest of process should be qualitatively as in

the unblemished condition, except that because of coupling with the exposed steel one would have expected an even faster initiation of the pitting regime and a more positive terminal E_{OC} here. However, that was not the case in either count. That observation suggests that even for large coating breaks the cathodic current from the exposed steel spot (3% of total area) at the operating potentials was not large compared with the total cathodic current at inclusions (initially) and inclusions plus pits (later on) on the aluminized surface. Protection of the exposed steel was excellent because activation of the aluminized surface was prompt, so the steel surface remained virtually free of corrosion products.

4.4.2 Galvanic Macrocells

The E_{OC} trends and the appearance of aluminized surface discoloration of the LCB specimens in solutions NP and P were consistent with the macrocell galvanic current trends recorded for the coupled macrocell assemblies exposed to the same solutions. Measurements of galvanic currents for which data are available (P and NP, Figure 4.30) demonstrated that the outer aluminized coating layer behaved always as net anode upon contact with steel. However, the amount of macrocell current delivered by the outer coating layer in those solutions was insufficient to prevent rust formation on the steel surface early on in the exposure. This observation was also noted in the specimens with small A_R exposed to the same solutions. This weak early galvanic action could be attributed to a predominantly passive condition of the outer aluminized coating layer, as manifested by its large impedance moduli in both solutions early on.

Larger galvanic currents were expected in both solutions for the A_R examined upon signs of corrosion of the outer aluminized coating later on in the test.

There were no macrocell current measurements available for solution SW, but the steel in the specimens with small A_R in that solution did not show signs of corrosion over the entire exposure time, and the steel in the specimens with large A_R in solution SW showed only very light discoloration. Those results indicate strong galvanic protection by the surrounding aluminized coating in the SW solution as well, consistent with observation of pitting of the aluminized surface and some secondary macroscopically uniform corrosion. In solution SW, the protective regime was established soon, as manifested by the drop of E_{OC} into protective potentials after only about two days of exposure for specimens with both small and large A_R.

The galvanic behavior of the specimens with small A_R in solution C showed variability, in that one of three specimens showed signs of steel corrosion but in all cases an annulus of aluminized outer layer corrosion wastage around the steel was noted. It is intriguing, however, that the relatively positive E_{OC} (~-620 mV) in all replicate specimens existed for at least ~1 hr up to ~100 hr and clearly protective potentials did not develop until about ~600 hr, yet the steel showed no signs of corrosion in two cases. For those cases, however, it should be recalled that aluminized corrosion was limited to the aforementioned annulus of severe coating loss around the steel. With such tight macrocell configuration, the local steel potential could have been significantly more negative than that

measured by the reference electrode several diameters away, so the recorded E_{OC} values may have be misleading.

4.4.3 Correlation between A_R and Time to Initial Discoloration

Figure 4.39 shows the time for the initial appearance of discoloration of the aluminized surface as a function of A_R for the unblemished, blemished specimens, and the macrocell assemblies. The time to initial discoloration, obtained by averaging the results of replicate specimens for each A_R, was largest for the specimens with A_R=0 (unblemished specimens) in solutions NP, P, and SW and did not show significant difference when varying A_R from 3 10^{-4} (SCB specimens) to 0.03 (LCB and macrocell specimens) in solutions NP and SW. For solution P arrows in Figure 4.39 indicate minimum values since no discoloration was observed for the specimens with smaller A_R. The trends obtained for solution P, NP, and SW are not unexpected since for large A_R (large cathode/anode area ratio), enhanced macrocell action between the large exposed steel and the small aluminized coating could be established, and hence, large corrosion rates of the aluminized coating would be expected with consequent earlier appearance of aluminized surface discoloration. However, the trend for solution C is opposite to those obtained for the other solutions in that smaller time to discoloration was attained when going from unblemished condition to a finite A_R. This discrepancy for the C system can be explained by recalling that while there was a high bulk pH excursions (to ~9.0, Chapter 2, Figure 2.9) shortly after immersion for the unblemished specimens, the specimens with A_R=3 10^{-4} maintained a nearly

neutral solution pH throughout the exposure (Figure 4.4). The early pH elevation in the unblemished specimens triggered early global depassivation with consequent strong uniform surface discoloration of the unblemished specimens but not for the blemished specimens.

4.4.4 Interpretation of the Impedance Response

4.4.4.1 Macrocell Assemblies

The analog equivalent circuit chosen to simulate the impedance response of the macrocell assemblies is shown in Figure 4.40. It is assumed that the overall interfacial admittance can be divided into two branches as explained below.

The upper branch in Figure 4.40 is for the exposed steel (and the individual steel specimens as well) and describes scenarios for both before and after the E_{OC} drop. For the period before the E_{OC} drop, the circuit consists of a polarization admittance (R_{a1}^{-1}) for the activation polarization of the anodic reaction ($Fe \rightarrow Fe^{+2}+2e^{-}$) in parallel with a Constant Phase Angle Element CPE_1 representing the interfacial charge storage at the steel surface, and an admittance (series combination of the polarization admittance $R_{C1}^{-1}=2.3\ i_{C1}/\beta_{C1}$ and the diffusional component W_1) governed by activation/concentration polarization of the cathodic reaction. The latter is likely to be $O_2+2H_2O+4e^{-} \rightarrow 4OH^{-}$ and it is assumed to be so and, for simplicity, to occur under simple one-dimensional conditions. The resulting impedance for the exposed steel has the form $Z_1(\omega)=[1/R_{a1}+1/Z_{C1}(\omega)]^{-1}$ where $R_{a1}^{-1}=2.3\ i_{a1}/\beta_{a1}$ and $Z_{C1}^{-1}(\omega)= 2.3$

$i_{C1}/\beta_{C1}+2.3\ (i_L-i_{C1})\ \beta_{C1}^{-1}\ (j\omega\delta^2\ D^{-1})^{0.5}\ (\tanh\ (j\omega\delta^2\ D^{-1})^{0.5})^{-1}$ (Bard and Faulkner, 2000) where i_{a1} and i_{C1} are the anodic and cathodic current densities, respectively. After the E_{OC} drop, the exposed steel (which may or may not have corrosion products on the surface depending on the case) is polarized down to potential levels where the Fe/Fe^{+2} reaction is near equilibrium (Pourbaix, 1974). The corresponding equilibrium current density is expected to be small with correspondingly small admittance. The remaining reaction of importance is expected to be O_2 reduction, occurring at a diffusion-limited, potential-independent value.

The lower branch of the equivalent circuit in Figure 4.40 is for the aluminized component and describes scenarios for both before and after active corrosion of the outer aluminized coating layer as described in Sections 2.4.2.1 and 2.4.2.2 in Chapter 2.

4.4.4.2 Blemished Specimens

The analog equivalent circuit in Figure 4.40 is deemed to be simplified to be applicable to the LCB and SCB configurations. The simplified equivalent circuits shown in Figure 4.41 were consistent with the assumptions presented in Section 4.4.1 and the observations made earlier.

For the period before the E_{OC} drop, the impedance response (dominated largely by the anodic and cathodic reactions at the exposed steel as stated earlier) of the LCB specimens in solutions P and NP was modeled using solely the upper branch of the equivalent circuit in Figure 4.40 but replacing CPE_1 by

the parallel combination of CPE_1 and CPE_F (keyed as CPE*) as shown in the simplified equivalent circuit in Figure 4.41-A. This simplification is valid only if the passive aluminized portion has cathodic and anodic admittances significantly smaller than those of the active exposed steel as it is observed for the period before the E_{OC} drop. After the E_{OC} drop, however, the impedance response for all the cases was modeled using the simplified equivalent circuit in Figure 4.41-B. The anodic polarization resistance R_{AL2} in Figure 4.41-B represents the active aluminized corrosion (either by pitting in solution SW or by uniform corrosion in the other solutions) in parallel with the diffusional cathodic impedance of the exposed steel, under the assumption that the majority of the cathodic reaction took place there as mentioned earlier and considering that the value of the resistance R_{AL1} (representing the parallel combination of the local electrolytic current distribution around each pit associated with an ohmic resistance component as stated in Chapter 2) is expected to be considerably smaller than R_{AL2} so that R_{AL1} can be neglected. The element CPE** in Figure 4.41-B encompasses the parallel combination of CPE_1, CPE_F, and CPE_{AL2}. After the E_{OC} drop took place, the anodic admittance of the exposed steel in all solutions were nearly zero as a result of the proximity of the system potential to that of the Fe/Fe^{+2} equilibrium reaction as mentioned earlier, thus R_{a1} is infinity.

However, the EIS interpretation used for the macrocell assemblies and the blemished specimens do not account for the presence of non-uniform *ac* current distribution commonly encountered in arrangements involving interconnected dissimilar metals (Kranc and Sagüés, 1993). This experimental artifact may lead,

if not properly quantified, to an incorrect EIS interpretation and therefore to inaccurate corrosion rate estimates. To account for uneven *ac* current distribution for the LCB specimen geometry, an *ac* computational model is introduced in Chapter 5. The results from the *ac* computational model indicate that negligible non uniform *ac* current distribution can be expected in these systems even though there is a substantial difference in the polarization resistance of the steel and the aluminized components, especially early on in the exposure. Thus, the use of the analog equivalent circuits proposed in this Chapter to fit the EIS data is valid.

4.4.5 Computation of the Nominal Corrosion Current Density

Per the assumptions above and the observations made earlier, for the period before the onset of the E_{OC} drop a rough estimation of the nominal corrosion current density for the exposed steel i_{corrFE} was made by computing the charge transfer resistance $R_{CT} = [R_{a1}^{-1}+R_{C1}^{-1}]^{-1}$, where the resistors R_{a1} and R_{C1} were obtained by fitting the EIS data using the analog equivalent circuits in Figures 4.40 (upper branch for the macrocell assemblies and the individual steel specimens) and 4.41-A (for the LCB specimens in NP and P systems) [9].

[9] For before the E_{OC} drop regime, values of i_{corrFE} for the LCB specimens in SW and the SCB specimens in all test solutions are not available, since all EIS measurements in those cases were taken after E_{OC} had reached an arbitrary potential <-800 mV. In that case, the values of i_{corrFE} were expected to be nearly zero as a result of the proximity of the system potential to that of the Fe/Fe^{+2} equilibrium reaction as mentioned earlier.

From the Stern-Geary relationship (Stern and Geary, 1957), the values of i_{corrFE} are computed as follows:

$$i_{corrFE} \sim B\ (A_{FE}\ R_{CT})^{-1} \quad (4.1)$$

where A_{FE} is the nominal steel area and the parameter B is called the Stern-Geary constant equal to $\beta_{a1}\beta_{C1}[2.3(\beta_{a1}+\beta_{C1})]^{-1}$ for the assumed values of the Tafel slopes β_{a1}=60 mV/dec and β_{C1}=120 mV/dec (Kaesche, 1985).

For the macrocell assemblies in solutions NP and P for the period before the E_{OC} drop, the nominal corrosion current density for the aluminized component i_{corrAL} was computed using Eq. 2.8 following the assumptions presented for passive unblemished aluminized steel in Section 2.4.2.1 in Chapter 2. Values of R_{AL1} computed here were obtained by fitting the EIS data using solely the lower branch of the analog equivalent circuit in Figure 4.40 (the same as that in Figure 2.16 in Chapter 2) [10]. For the period after active aluminized surface corrosion, the values of i_{corrAL} in all cases were computed using Eq. 2.9 in Chapter 2 with values of R_{AL2} obtained by fitting the EIS data using the corresponding simplified analog equivalent circuits shown in Figures 4.40 and 4.41-B.

The time evolutions of i_{corrFE} and i_{corrAL} for the blemished specimens and the macrocell assemblies is shown in Figures 4.42 through 4.44 with the EIS parameters shown in Tables 4.3 through 4.5.

[10] Values of i_{corrAL} for the LCB and the SCB specimens in all test solutions before E_{OC} drop are not available, since all EIS measurements in those cases were taken either after E_{OC} had reached an arbitrary potential <-800 mV or the overall impedance response was largely dominated by the small impedance of the active steel compared to the much larger impedance of the passive aluminized portion.

For the steel portion in the LCB specimens (Figure 4.42), the values of i_{corrFE} ranged from ~10 μA/cm^2 early on to ~30 μA/cm^2 by the end of the positive E_{OC} trend for NP, and from ~10 μA/cm^2 early on to ~5 μA/cm^2 for solution P. Those values were roughly in agreement with the results of the steel component in the macrocell assemblies and the individual steel specimens exposed to the same solutions and also consistent with the observed corrosion deposits over the steel surface in both solutions early on in the exposure.

For the regime after the E_{OC} drop, the i_{corrAL} values of the LCB specimens (Figure 4.43) were modest for solutions P and NP (~3 μA/cm^2) and smaller for solution SW (~0.1 μA/cm^2), consistent with the appearance of moderate/strong aluminized surface discoloration for P and NP, and light in SW. The i_{corrAL} values for the aluminized component in the macrocell assemblies (Figure 4.43) were ~0.5 μA/cm^2 and ~5.1 μA/cm^2 for solutions P and NP, respectively, also consistent with moderate in P and strong aluminized surface discoloration in NP. For the SCB specimens (Figure 4.44), the i_{corrAL} value obtained by the end of exposure was extremely small for P (~0.003 μA/cm^2), consistent with absence of aluminized corrosion throughout the entire test exposure. Values of i_{corrAL} by the end of exposure were ~1.5 μA/cm^2, ~0.1 μA/cm^2, and ~0.03 μA/cm^2, for NP, SW, and C, respectively.

The integrated aluminized coating loss, during the exposure period from t=0 to t_f where t_f is the time for the end of the test, was evaluated by using the time evolution of $i_{corr}(t_i)$ obtained from the EIS measurements where i=1 to n

represents each EIS measurement. The integrated material loss was then calculated from the charge density such that:

$$Q = \sum_{1}^{n-1} i_{corr_i} \cdot (t_{i+1} - t_i) + i_{corr_1} \cdot t_1 + i_{corr_n} \cdot (t_f - t_n) \quad (4.3)$$

The integrated coating loss during exposure is $L_{INT} = Q\, A_W\, (nF\rho)^{-1}$, A_W is the aluminum atomic weight, and ρ is the aluminum density. Figure 4.45 compares the integrated coating loss obtained by EIS and the nominal coating thickness loss determined by magnetic coating thickness measurements in a log-log representation. The comparison shows reasonable agreement between both estimates, in support of the assumptions made for interpretation of the EIS data. Figure 4.46 shows a metallographic analysis conducted on the LCB specimen #1 exposed to solution NP. Corrosion deposits noted on top of the outer aluminized layer were ~10-15 μm thick which yields a nominal corrosion rate of ~40 μm/yr, using the appropriate exposure time. This result is in good agreement with that determined by magnetic coating measurements and EIS measurements. However, magnetic coating thickness does not have the capability to detect pitting loss in the case of e.g. the solution SW, where pitting was the main form of corrosion. As a result, measurements of magnetic coating thickness may underestimate the actual corrosion rates in those cases.

4.5 Implication of the Results

In the following, the same analysis and assumptions presented in Section 2.5 in Chapter 2 are used here to tentatively project durability of aluminized steel

Type 2 with coating breaks exposing the underlying steel, and will not be discussed in this section unless clarification is needed. It is strongly emphasized that the durability projections obtained in this investigation are nominal in nature since the present experiments were conducted for relatively short times, compared to the actual service lives involved in field applications.

The extent and morphology of coating breaks is assumed to resemble the conditions examined experimentally. Those would apply for example to a pattern of breaks of small aspect ratio spaced a small fraction of 1 meter (a few inches) apart, at the bottom of a shallow pool of stagnant water as it may occur between corrugations in the culvert invert. It is assumed for simplicity that the medium is replenished only infrequently, during episodic flow events. Once the post-potential drop regime is established, corrosion rates are considered to proceed at a space- and time-uniform rate until the outer coating layer is exhausted.

The values of i_{corrAL} and i_{corrFE}, reported in Tables 4.3 through 4.5, were used to compute the SL for the aluminized coating and the base steel using Eq. 2.10 in Chapter 2, replacing accordingly the aluminum parameters by those of the steel.

In solution P which represented conditions of carbonate scale forming solutions, that is high total alkalinity and total hardness, full outer layer consumption would be projected to occur in ~2 yr for A_R~0.03 (consistent with moderate aluminized surface discoloration as the main mode of deterioration), but in excess of 100 yr for A_R~3 10^{-4}. It is also noted that for A_R=0 as in the unblemished aluminized steel as reported in Chapter 2 a negligible nominal

corrosion rate and bright appearance was noted for solution P, so the outer layer durability projection would also be in excess of 100 yr.

Projections become distinctly more pessimistic for solutions of high alkalinity, negligible carbonate scaling tendency and moderate chloride content (solution NP). Severe corrosion was noted around the exposed steel perimeter for both A_R~0.03 and ~3 10^{-4} with complete consumption of the outer aluminized coating layer after only a few weeks. It is not clear at this moment if corrosion would tend to progress even further specifically at the aluminized ring around the steel. It can be noted however that since the inner coating layer had remained in place at least for the duration of the experiment, it is suspected that uniform corrosion would take place in this case. If that would be the case, full outer layer consumption would be projected to occur in only ~2 yr for A_R~0.03, and after ~7 yr for A_R~3 10^{-4}, both values in agreement with strong discoloration of the aluminized surface. Longer SL of the outer aluminized layer was obtained for A_R=0 (~30 yr).

In solution SW simulating seawater composition, full outer layer consumption would be projected to occur in ~30 yr of service for both A_R~3 10^{-4} and ~0.03, and ~9 yr for A_R=0. However, the strong localized corrosion as opposed to a light uniform corrosion distress was the main form of corrosion in this solution for all A_R. Those values become important considering that the corrosion is strongly localized, with consequent risk of aluminized layer penetration of a component exposed to similar media.

In solution C which represented solutions with low alkalinity, low carbonate scaling tendency, and moderate chloride content, severe corrosion was noted around the exposed steel (for A_R~3 10^{-4}) with complete consumption of the outer aluminized coating layer at that spot after a few weeks of exposure. However, metallographic evidence permitted to infer that since the inner coating layer had remained in place at least for the duration of the experiment, corrosion would mainly take place uniformly over the entire aluminized surface. If that would be the case, full outer layer consumption would be projected to occur in ~20 yr of service for A_R~3 10^{-4}. For A_R=0 (Chapter 2), outer layer consumption would be consumed in ~10 yr of service. The shorter durability projections for A_R=0 can be related to a momentary increase in solution pH (>8.8) observed early in the test, not noted for the cases of A_R~3 10^{-4}.

After consumption of the outer aluminized layer (assuming that the inner coating layer provides little to none corrosion protection to the base steel as described in Chapter 2), corrosion of the base steel starts and is expected to proceed at rates of ~12 μA/cm^2 in SW and ~10 μA/cm^2 in the other media. Per the assumptions presented in Chapter 2, the projected SL for the base steel would be ~6 yr in SW and ~8 yr in the other media.

The overall SL estimates summarized in Table 4.6 were computed following the considerations presented in Chapter 2. Table 4.6 also includes the projected durability computed by the predictive methods (the AK Steel, the California, the AISI, and the FDOT) repeated from Table 2.8 for convenience.

For the specimens with A_R~3 10^{-4} (and for A_R=0 as well) in solution P (high scaling tendency, ~7.5<pH<~8.5 and moderate chloride content), the forecasting methods examined projected shorter durability estimates than the findings obtained in this investigation. For A_R~0.03, however, the AK Steel method was in close agreement with the results obtained here whereas the other methods overestimated durability by >20 yr.

For A_R~3 10^{-4} and ~0.03 in solution NP (high alkalinity, ~7.5<pH<~9, and moderate chloride content), the durability estimates obtained from the AK Steel method were in reasonable agreement with the results reported here. In contrast, the other methods overestimated SL by >10 yr compared with the present findings.

In solution SW (extremely aggressive solutions of low resistivity, nearly neutral pH, and high chloride content), the AISI method was in close agreement relative to the present findings for all A_R, whereas the California method projected shorter service lives. In highly aggressive environments, no durability credit is given by the FDOT method and no SL projections are given by the AK Steel method for solutions with scaling indexes beyond ~800 ppm.

In solution C (low scaling tendency, nearly neutral pH, and moderate chloride content), SL projections were in close agreement with those determined by the AK Steel, California, and FDOT methods and overly conservative compared to durability projections obtained by the AISI method.

The results presented in Chapter 2 for unblemished steel supported considering retaining present FDOT durability guidelines regardless of scaling

tendency for environments with moderately low resistivity such as those used in the tests (e.g. ~500 Ω-cm to ~1,000 Ω-cm) and neutral to mildly alkaline conditions (e.g. ~7.5<pH<~9.0). However, for blemished surface conditions with exposed base steel, the findings in this section suggest that the AK Steel method may be a more appropriate alternative in those environmental conditions. The results in this section would still support exploring the use of alternative guidelines such as the AISI method for environments with extremely high chloride contents (e.g. resistivity <50 Ω-cm) and nearly neutral pH, as it was also the case in Chapter 2 for unblemished surface conditions. As before, it is strongly cautioned that other environmental parameters such as microbiology-induced corrosion may influence the corrosion performance of the Al/Fe system, and that eventual changes in existing guidelines should consider not only the specific results of this investigation but also the entirety of the performance record of aluminized steel pipe.

In closing, it is noted too that the above results indicate that corrosion products from the steel portion may play a role in creating or accelerating corrosion of the aluminized coating, in part resulting from the limited electrolyte volume involved in the tests. The small electrolyte volume was intended to be representative of worst-case culvert pipe conditions with stagnant water, or of occluded conditions for pore water on the soil side of a pipe. It is noted that long term conditions may be more benign if there is frequent electrolyte renewal. Furthermore, the findings from the present investigation apply to aluminized steel with a surface condition resembling scratched or otherwise distressed material,

with an exposed steel area representing ~3% and 0.03% of the total area. In actual metal forming and subsequently field application practice, the aluminized steel component (e.g. culvert pipe) is liable to surface distress, especially at the sharp bent regions which may expose base steel. The exposed steel area in those cases may be considerably less than 0.03%. To obtain additional information on performance under those circumstances, sharply bent as well as unprotected cut end specimens are being examined in a continuing investigation.

4.6 Conclusions

1. Galvanic protection was provided by the surrounding aluminized surface to base steel exposed at coating breaks in all the environments tested. However, in the less aggressive media (e.g. the solution P) protection developed only after a period of thousands of hours at which the open circuit potential was ~-720 ~-750 mV (comparable to those of the steel), when some corrosion of the base steel had already taken place.
2. At the end of that positive potential trend period, the aluminized surface of specimens with exposed steel (except for the specimens with small A_R in solution P) showed signs of developing a macroscopically uniform active condition. The open circuit potentials at that stage were ruled by the aluminized coating.
3. The positive potential period was shorter for the more aggressive media (NP, C, and SW), where the base steel remained bright throughout the test period

in SW. Positive potential period was also shorter when the area ratio of exposed steel to aluminized surface was greater.

4. Impedance spectroscopy estimates of the long-term corrosion rates of the outer aluminized layer in the active conditions for the LCB configuration (largest steel/aluminized area ratio) were ~30 μm/yr for solutions P and NP, and ~1.5 μm/yr for SW. For the SCB configuration (small steel/aluminized area ratio), long-term corrosion rates of the outer aluminized layer in the active conditions were ~15 μm/yr for NP, ~0.03 μm/yr for P, ~1 μm/yr for SW, and 0.4 μm/yr for C. Those estimates were approximately consistent with direct measurements of thickness loss. Notably, the most nominally aggressive solutions did not result in the highest outer aluminized layer corrosion rates.
5. The results for blemished/macrocell specimens have trends that extrapolate reasonably to the limit case of unblemished aluminized surfaces addressed in Chapter 2 (zero steel/aluminized area ratio). In that limit, the active aluminized surface condition was never reached in the least aggressive medium (P) during the 3,000 hr test. However, active conditions developed on the unblemished aluminized surfaces in the more aggressive media after incubation times comparable to those encountered for blemished specimens with the smallest area ratio (~3 10^{-4}). Long-term corrosion rates in that condition were ~3-5 μm/yr.
6. As in Chapter 2, corrosion macro pits were usually small and infrequent on the corroding aluminized surface so they appeared to play a secondary role

for the solutions C, NP, and P, and a primary form of corrosion for solution SW. The macroscopically uniform appearance of the corrosion indicates that aluminum corrosion products may have deposited uniformly on the aluminized surface.

7. The mechanism of activation of the aluminized layer may involve local alkalinization from enhanced cathodic reaction at the inclusions (especially in the low buffering capacity solution C), which would activate aluminum in the form of micro pits at the scale of the finely distributed inclusions present in the outer aluminized coating layer. Alkalinization may have been greater next to the steel region due to faster O_2 reduction rates there, consistent with the observation of a discoloration front radiating from the central exposed steel area.
8. Plating of Fe (from inclusion particles separated from the matrix by undercutting corrosion and/or from initial corrosion of the exposed steel) on the aluminized surface may have further enhanced cathodic action in an autocatalytic manner that could account for the observation of the positive open circuit potential period, especially in solutions with low buffering capacity (solution C).
9. Tentative durability projections were made for 16-gage aluminized sheet assuming penetration from both sides of the metal and considering consumption of the outer aluminized layer and of the base metal, using the corrosion rates estimated from the EIS measurements and focusing on stagnant water conditions. For blemished surfaces, the projected service life

was >100 yr for the least aggressive environment (P) and the smallest coating break, whereas for the largest coating break service life was shortened to ~10 yr. For the other media, durability projections were between 16 and 33 yr. Caveats on the meaning of these long term extrapolations, noted in Chapter 2, apply here as well.

10. For blemished surface conditions with exposed base steel, the findings in this section suggest that the AK Steel method may be a more appropriate alternative to that suggested in Chapter 2 for environments with moderately low resistivity such as those used in the tests (e.g. ~500 Ω-cm to ~1,000 Ω-cm) and neutral to mildly alkaline conditions (e.g. ~7.5<pH<~9.0). The results would still support exploring the use of alternative guidelines such as the AISI method for environments with extremely high chloride contents (e.g. resistivity <50 Ω-cm) and nearly neutral pH. As before, it is strongly cautioned that other environmental parameters such as microbiology-induced corrosion may influence the corrosion performance of the Al/Fe system, and that eventual changes in existing guidelines should consider not only the specific results of this investigation but also the entirety of the performance record of aluminized steel pipe.

Table 4.1: Average thickness measurements, per magnetic coating thickness test, and the corresponding nominal corrosion rate estimates for selected specimens.

Specimen	Thickness / μm		Exposure time hr	Nominal corrosion rate μm/yr
	Before exposure	After exposure		
LCB Solution SW (2)	45.7	45.5	2,800	2
SCB Solution NP(2)	45.0	40.9	3,400	10
LCB Solution NP(1)	47.8	38.1	2,600	33
LCB Solution NP(3)	47.0	40.9	2,600	21
LCB Solution P(1)	51.8	49.8	2,650	7
LCB Solution P(2)	49.0	47.5	2,650	6
Macrocell assembly P(1)	52.3	48.3	2,700	13
Macrocell assembly P(2)	50.8	45.0	1,900	25
Macrocell assembly NP(1)	48.5	43.4	2,700	16
Macrocell assembly NP(2)	48.8	43.2	2,500	20

Thickness measurements are the average values obtained by three independent operators. Thickness measurements were determined with a standard deviation of ±7.6 μm.

Table 4.2: Summary of visual assessment and E_{OC} trends.

Test solution	Unblemished (A_R=0)		SCB (A_R~3 10^{-4})			LCB (A_R~0.03)			Macrocell assemblies (A_R~0.03)		
	E_{OC} (mV)	Aluminized Surface	E_{OC} (mV)	Steel Surface	Aluminized Surface	E_{OC} (mV)	Steel Surface	Aluminized Surface	E_{OC} (mV)	Steel Surface	Aluminized Surface
P	1: 0-3 hr: ~-805 2: 0-3 hr: ~-800 3: 0-5 hr: ~-800 1: Terminal: ~-760 2: Terminal: ~-770 3: Terminal: ~800	Bright over the entire exposure time. No visible pits.	1: 0-20 hr: ~-760 2: 0-20 hr: ~-760 1: Terminal: ~-820 2: Terminal: ~-820	Uniform black/reddish scale from start.	Bright over the entire exposure time. No visible pits.	1: 0-1200 hr: ~-745 2: 0-1200 hr: ~-745 3: 0-1500 hr: ~-740 1: Terminal: ~-920 2: Terminal: ~-920 3: Terminal: ~-905	Uniform black/reddish scale from start. At ~450 hr central reddish deposit spot. No preferential corrosion at spot.	Moderate discoloration Few small isolated pits.	1: 0-1600 hr: ~-710 2: 0-1700 hr: ~-740 3: 0-1100 hr: ~-730 1: Terminal: ~-885 2: Terminal: ~-885 3: Terminal: ~-885	Uniform black/reddish scale from start. At ~440 hr, central reddish deposit spot. No preferential corrosion at spot.	Moderate discoloration. Few small isolated pits.
NP	1: 0-5 hr: ~-650 2: 0-5 hr: ~-600 1: Terminal: ~-895 2: Terminal: ~-930	Moderate discoloration after ~2,250 hr (1,200 hr). Few small isolated pits.	1: 0-160 hr: ~-720 2: 0-2 hr: ~-750 1; Terminal: ~-900 2: Terminal: ~-900	Uniform reddish scale from start.	Strong discoloration after ~1,030 hr (~890 hr). ~50 µm outer aluminized coating layer around steel fully lost. Few small isolated pits.	1: 0-1600 hr: ~-725 2: 0-1200 hr: ~-725 3: 0-500 hr: ~-735 1: Terminal: ~-930 2: Terminal: ~-725 3: Terminal: ~-930	Uniform reddish scale from start. At ~460 hr central porous reddish deposit spot. Preferential corrosion at spot.	Strong discoloration in #1 and #3 and ~70 µm outer aluminized coating layer around steel fully lost. No discoloration in #2. Few small isolated pits in #1 and #3. No visible pits in #2.	1: 0-800 hr: ~-710 2: 0-1400 hr: ~-710 3: 0-850 hr: ~-710 1: Terminal: ~-810 2: Terminal: ~-830 3: Terminal: ~-925	Uniform reddish scale from start. At ~400 hr central porous reddish deposit spot. Preferential corrosion at spot.	Strong discoloration. Few small isolated pits.
C	1: 0-175 hr: ~-630 2: 0-8 hr: ~-645 1: Terminal: ~-840 2: Terminal: ~-830	Strong discoloration after ~310 hr (~115 hr). Few isolated pits.	1: 0-1 hr: ~-615 2: 0-90 hr: ~-630 3: 0-20 hr: ~-610 1: Terminal: ~-695 2: Terminal: ~-730 3: Terminal: ~-720	Uniform reddish scale from start in #1. No corrosion scale or discoloration in #2 and #3.	Strong discoloration after ~545 hr (~648 hr) ((~624 hr)). ~50 µm outer aluminized coating layer around steel fully lost. Few isolated visible pits.	Undergasket corrosion. Data discarded			Undergasket corrosion. Data discarded		
SW	1: 0-3 hr: ~-780 2: 0-10 hr: ~-730 1: Terminal: ~-805 2: Terminal: ~-835	Light discoloration after ~525 hr (~585 hr). Few isolated visible pits.	1: 0-1 hr: ~-750 2: 0-1 hr: ~-750 1: Terminal: ~-840 2: Terminal: ~-850	No corrosion scale or discoloration.	Light discoloration after ~275 hr (415 hr). Few isolated visible pits.	1: 0-48 hr: ~-750 2: 0-30 hr: ~-750 1: Terminal: ~-850 2: Terminal: ~-850	No scale. Very slight discoloration as test progressed.	Light discoloration after ~380 hr (~360 hr). Few isolated visible pits.	Undergasket corrosion. Data discarded		

A_R = exposed steel/aluminized surface area ratio. Aluminized surface discoloration appeared concurrent with the initiation of E_{OC} drop for the LCB specimens and macrocell assemblies in solutions NP and P, and the SCB specimens in solution C. Initially, the aluminized surface was bright in all specimens. Later on, discoloration, when taking place, was uniformly spread over the entire aluminized surface.

Table 4.3: Evolution of the nominal corrosion current density for the LCB specimens #1 exposed to solutions NP, P, and SW. The parameters of the simplified analog equivalent circuits shown in Figure 4.41 are also included. Immune condition for the exposed steel was assumed when the system E_{OC} reached <-800 mV. Passive condition for the outer aluminized coating was assumed when the aluminized surface was bright with no visible pits.

Solution NP (#1) – Before the E_{OC} drop								
Time hr	R_S Ω	W_1 Ω	R_{C1} Ω	R_{a1} Ω	Y* $sec^{n*}\ \Omega^{-1}$	n*	i_{corrFE} μA cm^{-2}	i_{corrAL} μA cm^{-2}
72	8.30	44.4	682.5	1378	1.65E-03	0.68	12.13	Passive
264	8.48	79.2	401.2	1631	1.67E-03	0.70	17.20	
408	8.42	55.6	294.5	1636	1.71E-03	0.70	22.19	
456	6.11	11.1	358.6	1689	2.04E-03	0.64	18.72	
720	7.01	10.9	345.3	1556	1.83E-03	0.68	19.60	
1008	8.75	14.4	203.2	1430	1.50E-03	0.75	31.13	
Solution NP (#1) – After the E_{OC} drop								
Time hr	R_S Ω	W_1 Ω	R_{C1} Ω	R_{AL2} Ω	Y** $sec^{n**}\ \Omega^{-1}$	n**	i_{corrFE} μA cm^{-2}	i_{corrAL} μA cm^{-2}
1752	9.05	9.0	499	1123	2.36E-03	0.81	Immune	0.42
2088	9.03	8.8	470	902	2.34E-03	0.83		0.52
2424	9.05	8.7	456	172.4	2.13E-03	0.86		2.75

LCB Solution P (#1) – Before the E_{OC} drop								
Time hr	R_S Ω	W_1 Ω	R_{C1} Ω	R_{a1} Ω	Y* $sec^{n*}\ \Omega^{-1}$	n*	i_{corrFE} μA cm^{-2}	i_{corrAL} μA cm^{-2}
48	6.8	74.5	3508	808	1.05E-03	0.78	8.44	Passive
192	7.5	55.6	2832	873	9.77E-04	0.80	8.30	
552	7.3	5.0	1634	980	1.13E-03	0.77	9.04	
960	7.4	4.8	2418	1496	1.01E-03	0.78	5.99	
1224	7.7	3.3	3177	1805	8.99E-04	0.80	4.81	
LCB Solution P (#1) – After the E_{OC} drop								
Time hr	R_S Ω	W_1 Ω	R_{C1} Ω	R_{AL2} Ω	Y** $sec^{n**}\ \Omega^{-1}$	n**	i_{corrFE} μA cm^{-2}	i_{corrAL} μA cm^{-2}
1920	8.1	3.3	546	843	3.23E-03	0.85	Immune	0.56
2400	8.1	3.3	436	163	7.22E-03	0.86		2.91

Table 4.3: (Continued)

LCB Solution SW (#1)								
Time hr	R_S Ω	W_1 Ω	R_{C1} Ω	R_{AL2} Ω	Y** $sec^{n**}\ \Omega^{-1}$	n**	i_{corrFE} μA cm^{-2}	i_{corrAL} μA cm^{-2}
168	0.23	19.5	2602	4452	1.39E-03	0.90	Immune	0.11
192	0.23	33.6	2796	4108	2.02E-03	0.87		0.12
360	0.23	18.6	2824	4080	1.41E-03	0.92		0.12
528	0.22	13.6	2509	2718	1.54E-03	0.92		0.17
720	0.23	14.0	2828	2669	1.61E-03	0.92		0.18
840	0.24	14.1	3448	2988	1.66E-03	0.92		0.16
1008	0.24	14.6	4199	3499	1.68E-03	0.92		0.14
1248	0.24	11.9	3933	3012	1.70E-03	0.92		0.16
1536	0.25	12.5	5224	3819	1.68E-03	0.92		0.12
1752	0.24	12.6	4450	3267	1.70E-03	0.92		0.14
2256	0.24	13.8	5534	3761	1.67E-03	0.92		0.13
2784	0.24	14.2	7125	4704	1.64E-03	0.91		0.10

Table 4.4: Evolution of the nominal corrosion current density for the SCB specimens #1 exposed to solutions NP, P, SW, and C. The parameters of the simplified analog equivalent circuits shown in Figure 4.41 are also included. Immune condition for the exposed steel was assumed when the system E_{OC} reached <-800 mV. Passive condition for the outer aluminized coating was assumed when the aluminized surface was bright with no visible pits.

SCB Solution NP (#1)								
Time hr	R_S Ω	W_1 Ω	R_{C1} Ω	R_{AL2} Ω	Y** $sec^{n**}\ \Omega^{-1}$	n**	i_{corrFE} μA cm^{-2}	i_{corrAL} μA cm^{-2}
96	6.8	274	4080	5694	5.97E-04	0.91	Immune	0.08
168	6.7	211	3236	7159	6.39E-04	0.91		0.06
288	6.8	456	7244	15250	6.78E-04	0.91		0.03
432	7.0	333	3898	8293	7.72E-04	0.91		0.06
648	6.9	974	11570	16650	7.81E-04	0.91		0.03
840	7.2	1196	16520	21460	8.16E-04	0.91		0.02
1032	7.3	1819	37620	38930	8.15E-04	0.91		0.01
1272	7.0	1046	12820	10820	8.91E-04	0.91		0.04
1440	7.2	780	10510	8455	9.32E-04	0.92		0.05
1944	7.2	846	1231	343	1.30E-03	0.93		1.33

Table 4.4: (Continued)

SCB Solution P (#1)								
Time hr	R_S Ω	W_1 Ω	R_{C1} kΩ	R_{AL2} kΩ	Y** sec^{n**} Ω^{-1}	n**	i_{corrFE} μA cm^{-2}	i_{corrAL} μA cm^{-2}
96	7.1	74.5	44.5	55.4	3.59E-04	0.92	Immune	0.017
168	7.5	62.2	16.1	15.8	4.25E-04	0.92		0.058
288	7.9	121.1	38.7	35.1	4.67E-04	0.93		0.026
432	7.9	64.7	27.2	20.3	5.03E-04	0.92		0.045
648	8.2	100.6	79.7	43.6	5.15E-04	0.91		0.021
840	8.1	170.4	288.9	71.9	5.18E-04	0.92		0.013
1008	8.1	157.4	533.4	86.9	5.09E-04	0.92		0.011
1272	8.3	291.3	2921	112.5	5.06E-04	0.92		0.008
1440	8.5	539.1	1.5E5	189.1	4.94E-04	0.92		0.005
1704	7.9	292.6	1.7E5	156.4	4.98E-04	0.92		0.006
2160	8.2	335.2	1.9E5	372.2	4.83E-04	0.93		0.002

SCB Solution SW (#1)								
Time hr	R_S Ω	W_1 Ω	R_{C1} Ω	R_{AL2} Ω	Y** sec^{n**} Ω^{-1}	n**	i_{corrFE} μA cm^{-2}	i_{corrAL} μA cm^{-2}
96	0.32	18.1	2216	3144	8.29E-04	0.92	Immune	0.15
168	0.35	11.6	3718	6144	9.27E-04	0.92		0.07
288	0.35	5.9	4251	3895	1.20E-03	0.91		0.12
432	0.35	6.2	5031	3419	1.39E-03	0.90		0.13
624	0.35	6.8	5256	3208	1.49E-03	0.90		0.14
840	0.37	7.8	7455	4202	1.51E-03	0.90		0.11
1272	0.37	9.0	9400	4698	1.48E-03	0.90		0.10
1440	0.39	9.4	10420	4907	1.45E-03	0.90		0.09
1536	0.35	9.1	8856	4148	1.47E-03	0.90		0.11
1680	0.35	8.9	8838	4539	1.45E-03	0.90		0.10
1944	0.37	9.6	10590	4871	1.40E-03	0.90		0.09
2112	0.37	9.7	10560	4816	1.40E-03	0.90		0.10
2496	0.37	9.7	14450	5881	1.37E-03	0.90		0.08
2688	0.37	4.7	11350	5062	1.38E-03	0.90		0.09

Table 4.4: (Continued)

SCB Solution C (#1)							
Time hr	R_S Ω	W_1 Ω	R_{C1} Ω	R_{AL2} Ω	Y^{**} sec^{n**} Ω^{-1}	n**	i_{corrAL} μA cm^{-2}
120	11.3	827.1	28220	11910	3.67E-04	0.91	0.04
168	10.6	553.1	11440	8569	4.14E-04	0.91	0.05
288	10.4	278.7	3489	5792	6.05E-04	0.91	0.08
432	10.2	182.5	2137	3519	8.64E-04	0.92	0.13
648	10.1	120.2	1290	1715	1.29E-03	0.93	0.27
840	10.3	54.9	660	858	1.80E-03	0.94	0.53
1296	10.4	71.0	1853	1892	2.61E-03	0.90	0.24
1440	10.4	113.7	4506	4228	2.35E-03	0.91	0.11
1608	10.7	108.6	8494	7126	2.21E-03	0.91	0.06
1704	10.3	70.5	7674	5444	2.25E-03	0.91	0.08
1968	10.9	170.4	13860	9269	2.18E-03	0.91	0.05
2160	10.6	181.8	13180	11060	2.16E-03	0.91	0.04
2496	10.9	226.3	16780	15450	2.09E-03	0.91	0.03
2664	10.5	219.9	16640	14470	2.09E-03	0.91	0.03

Table 4.5: EIS parameters from analog equivalent circuit in Figure 4.40 and nominal corrosion current density for the aluminized and steel components in the macrocell assemblies.

Specimen	Time hr		Sol.	R_S Ω	R_{a1} kΩ	R_{C1} kΩ	W_1 Ω $sec^{-0.5}$	Y_1 sec^n/Ω	n_1	i_{corrFE} μA/cm^2
Steel component	Before E_{OC} drop	900	P	175.1	0.9	0.6	17.9	3.2E-03	0.75	16.1
		900	NP	59.8	1.2	0.3	51.1	5.0E-03	0.55	24.2
	After E_{OC} drop	1780	P	210.6	3.8	0.1	5.1	6.4E-03	0.75	Immune
		1780	NP	50.1	3.3	0.2	54.4	1.1E-03	0.55	

Specimen	Time hr		Sol.	R_S Ω	R_{AL1} kΩ	Y_{AL2} sec^{n2}/Ω	n_{AL2}	R_{AL2} kΩ	Y_F sec^{nF}/Ω	n_F	i_{corrAL} μA/cm^2
Aluminized component	Before E_{OC} drop	900	P	57.4	9.9	9.8E-04	0.98	71.2	5.2E-04	0.94	0.09
		900	NP	16.5	6.9	3.4E-03	0.99	24.6	7.9E-04	0.94	0.13
	After E_{OC} drop	1780	P	55.7	0.2	3.2E-02	0.84	1.0	1.3E-03	1.00	0.46
		1780	NP	16.7	0.05	1.3E-01	0.80	0.09	1.2E-02	0.85	5.08

Table 4.6: Comparison of durability estimates, in yr, obtained by application of commonly used forecasting methods and those obtained in this investigation.

Test solution	AK Steel	California	AISI	FDOT	This investigation		
					A_R=0	A_R~3 10^{-4}	A_R~0.03
P	<20	29	57	56	>100 (>100)	>100 (>100)	10 (11, 11)
NP	<20	25	50	33	36 (38)	16 (15)	10 (10)
SW	NA	7	15	NA	15 (19)	33 (28)	27 (30)
C	<20	30	62	27	19 (23)	27 (28, 24)	-

Numbers in parenthesis correspond to the results from replicate specimens.

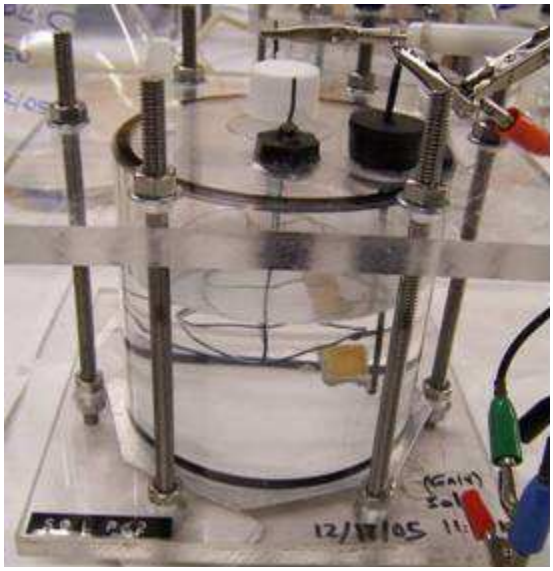

Figure 4.1: Photograph of the test cell used to monitor galvanic currents and impedance behavior of the unblemished aluminized steel and steel components.

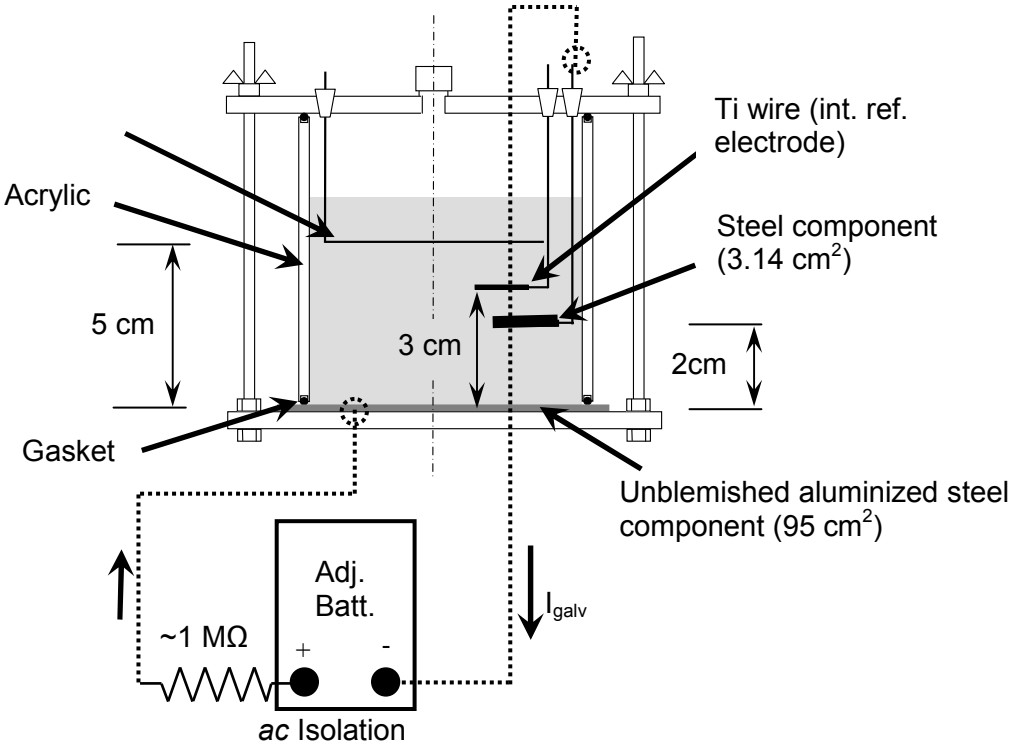

Figure 4.2: Schematic of the test cell arrangement.

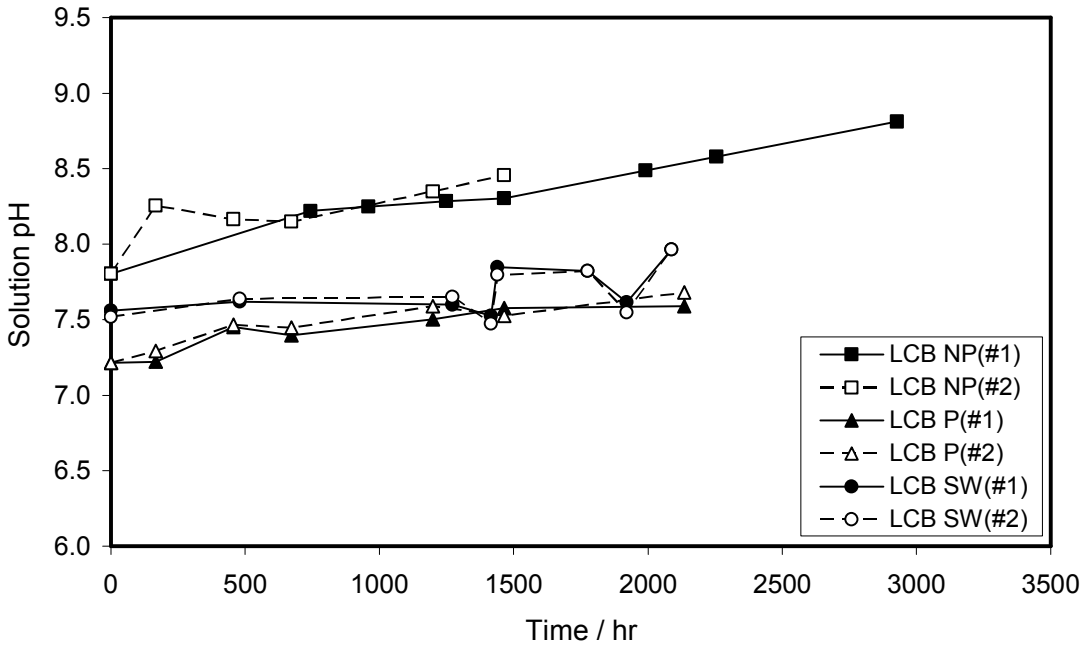

Figure 4.3: Evolution of the solution bulk pH for the LCB configuration.

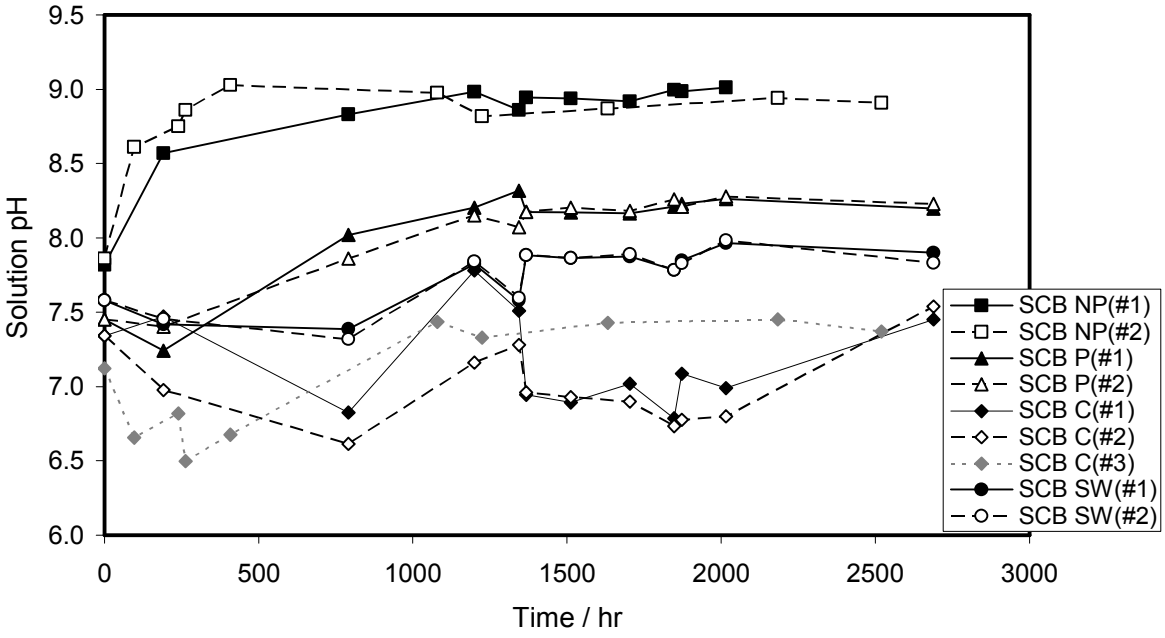

Figure 4.4: Evolution of the solution bulk pH for the SCB configuration.

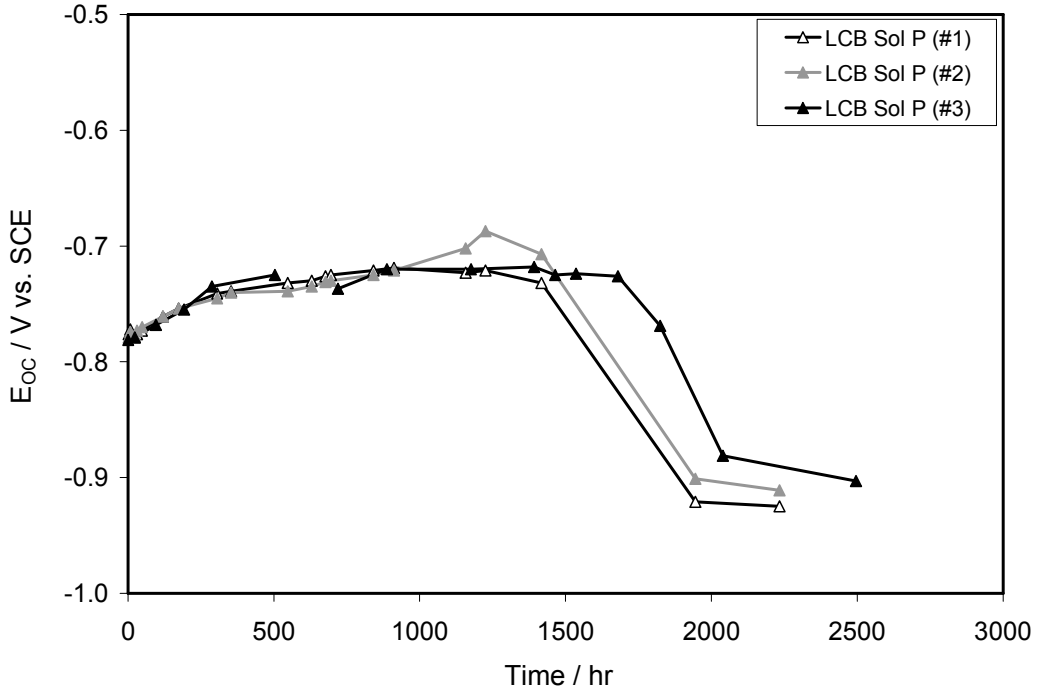

Figure 4.5: E_{OC} evolution of the LCB specimens in solution P. End of exposure corresponds to the time of the last datum taken.

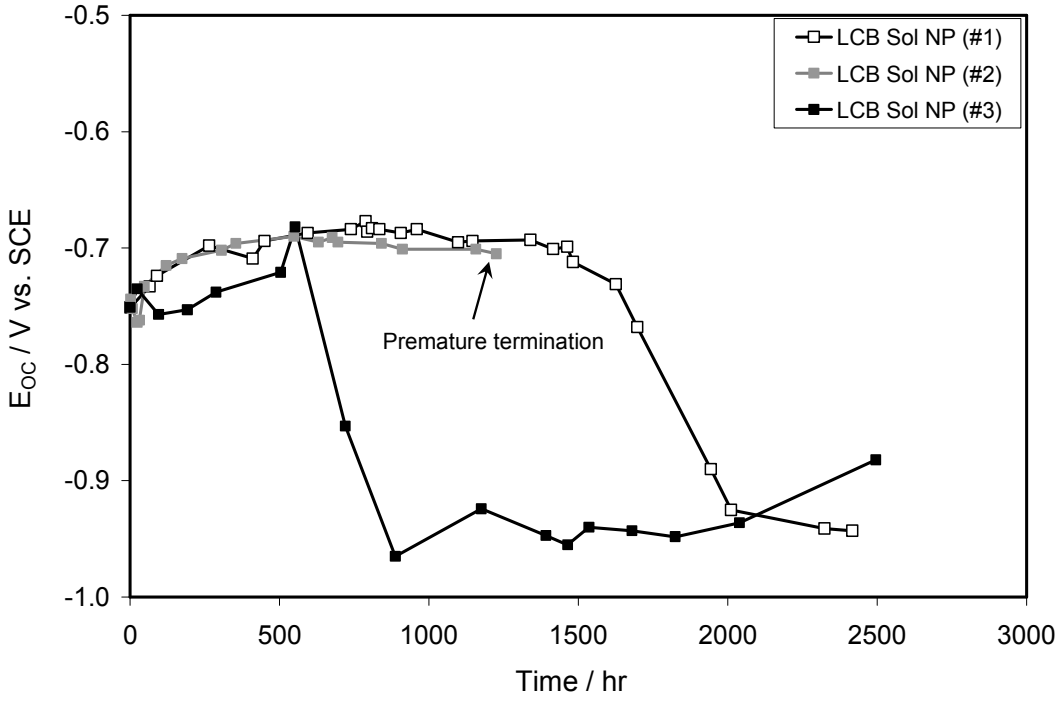

Figure 4.6: E_{OC} evolution of the LCB specimens in solution NP. End of exposure corresponds to the time of the last datum taken.

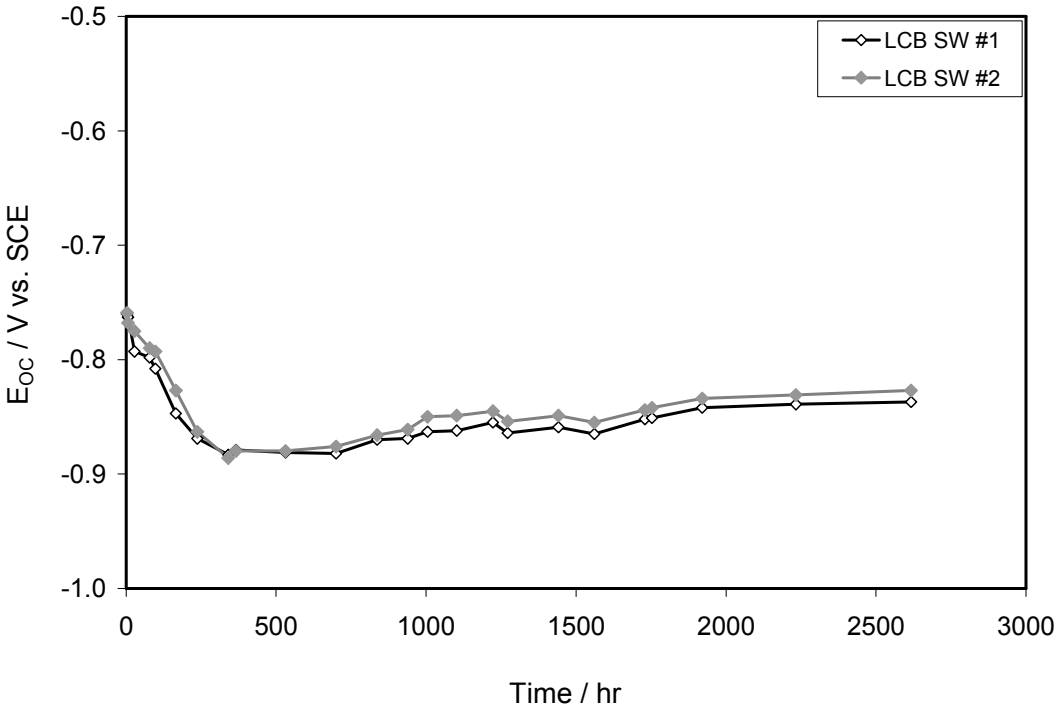

Figure 4.7: E_{OC} evolution of the LCB specimens in solution SW. End of exposure corresponds to the time of the last datum taken.

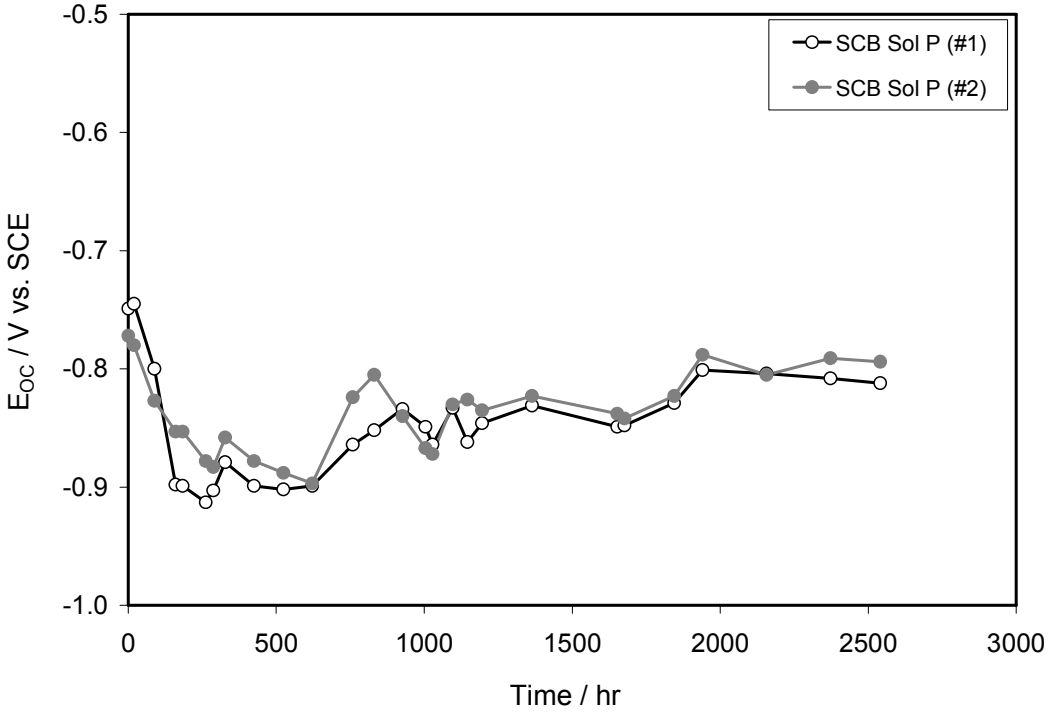

Figure 4.8: E_{OC} evolution of the SCB specimens in solution P. The test exposures were terminated ~450 hr after the last datum.

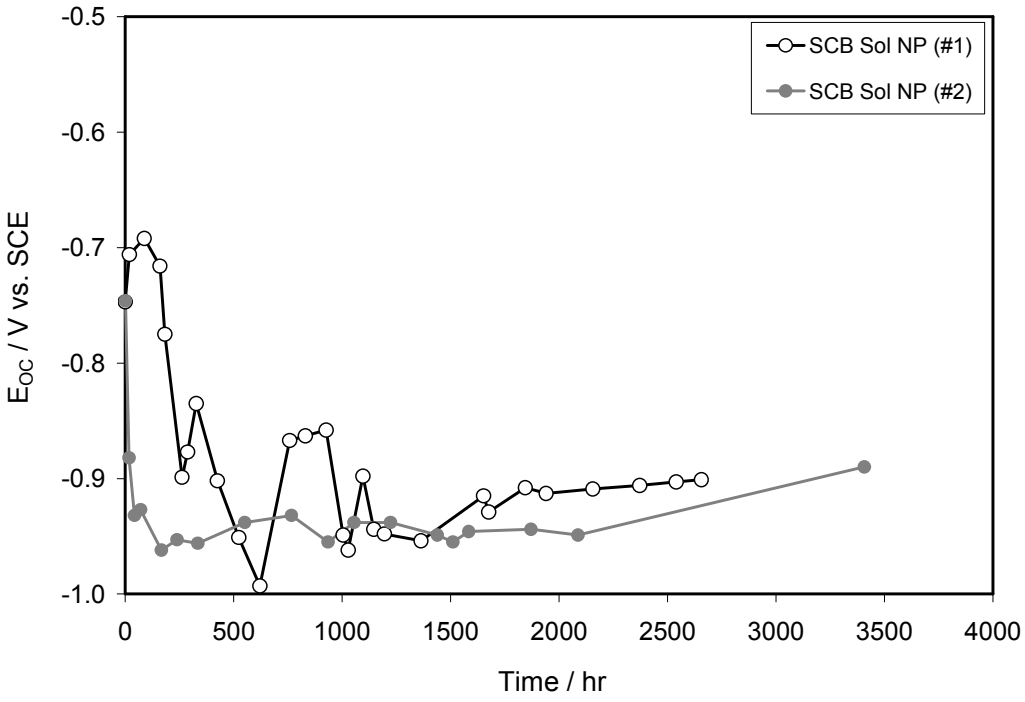

Figure 4.9: E_{OC} evolution as a function of time of the SCB specimens exposed to solution NP. End of exposure corresponds to the time of the last datum.

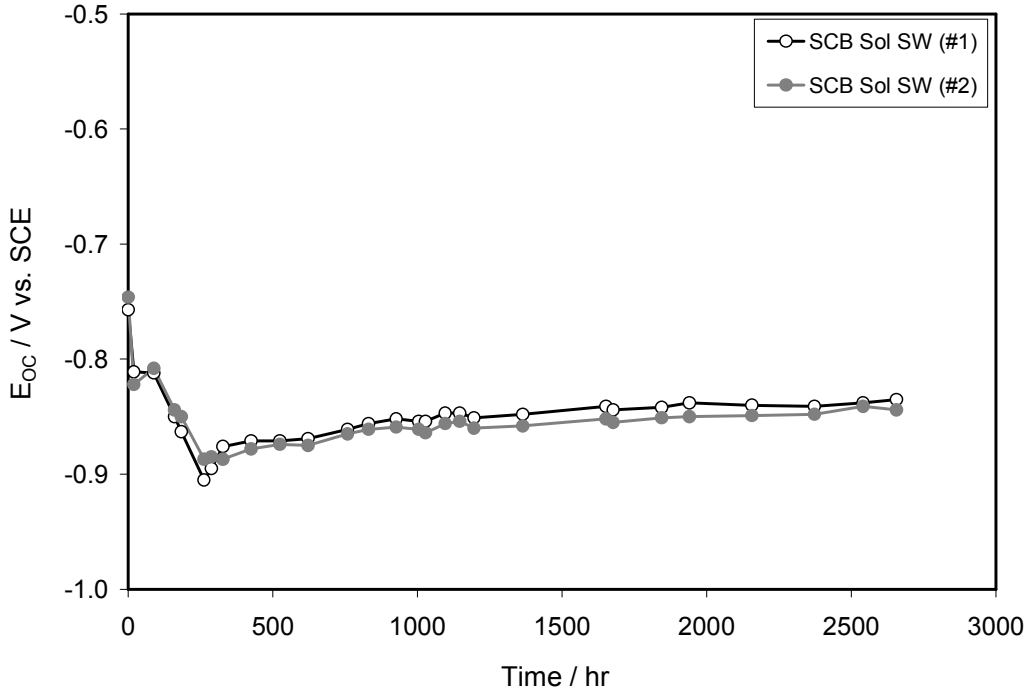

Figure 4.10: E_{OC} evolution as a function of time of the SCB specimens exposed to solution SW. End of exposure corresponds to the time of the last datum.

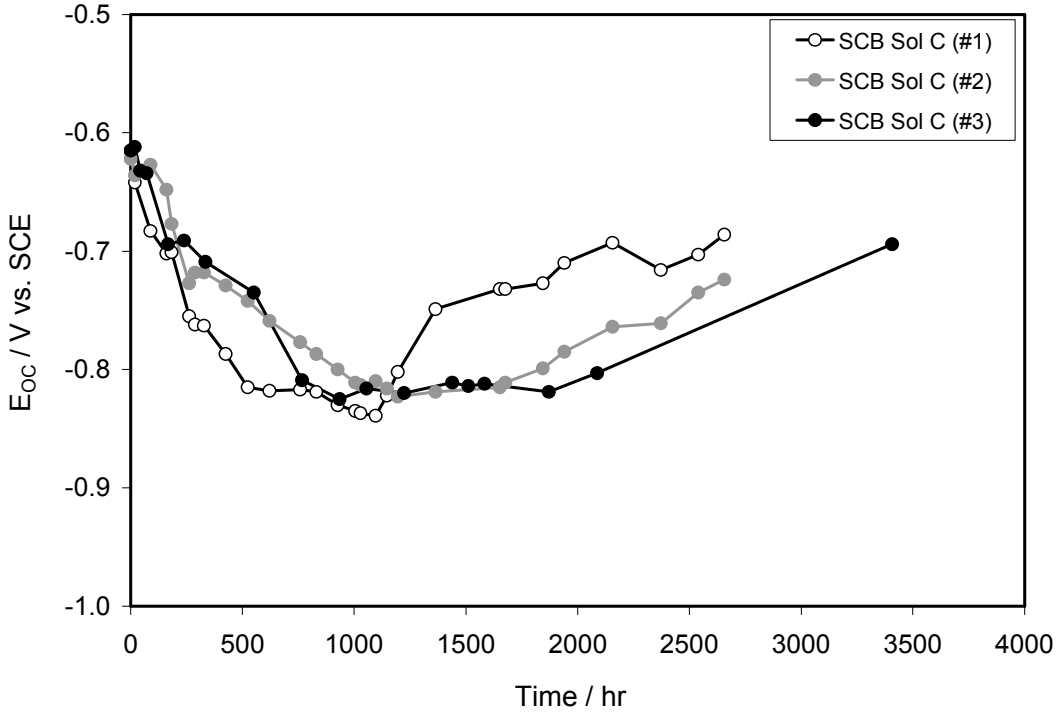

Figure 4.11: E_{OC} evolution as a function of time of the SCB specimens exposed to solution C. End of exposure corresponds to the time of the last datum.

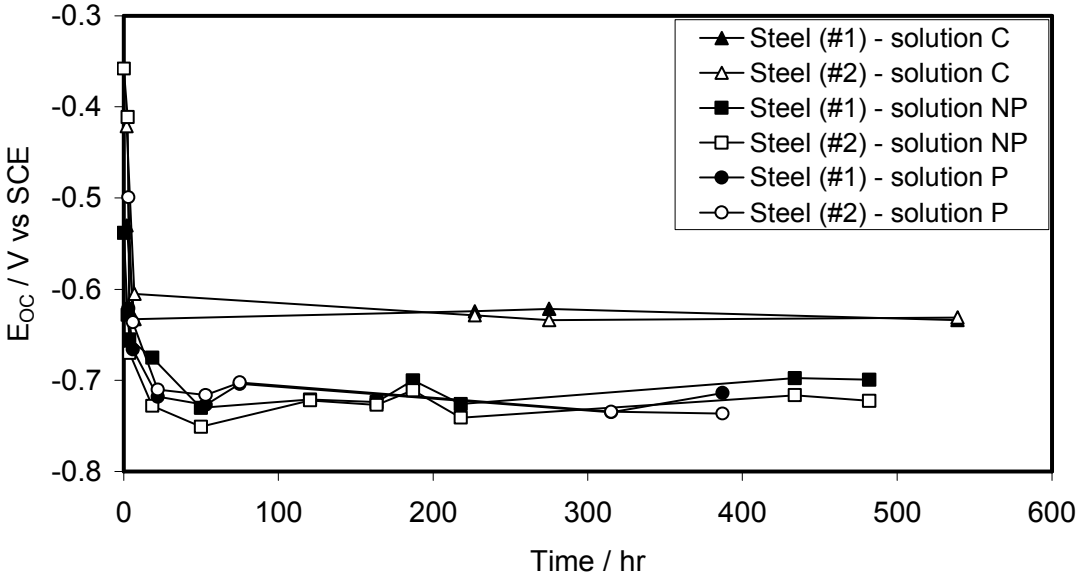

Figure 4.12: E_{OC} evolution as a function of time of the replicate uncoupled steel specimens. End of exposure corresponds to the time of the last datum.

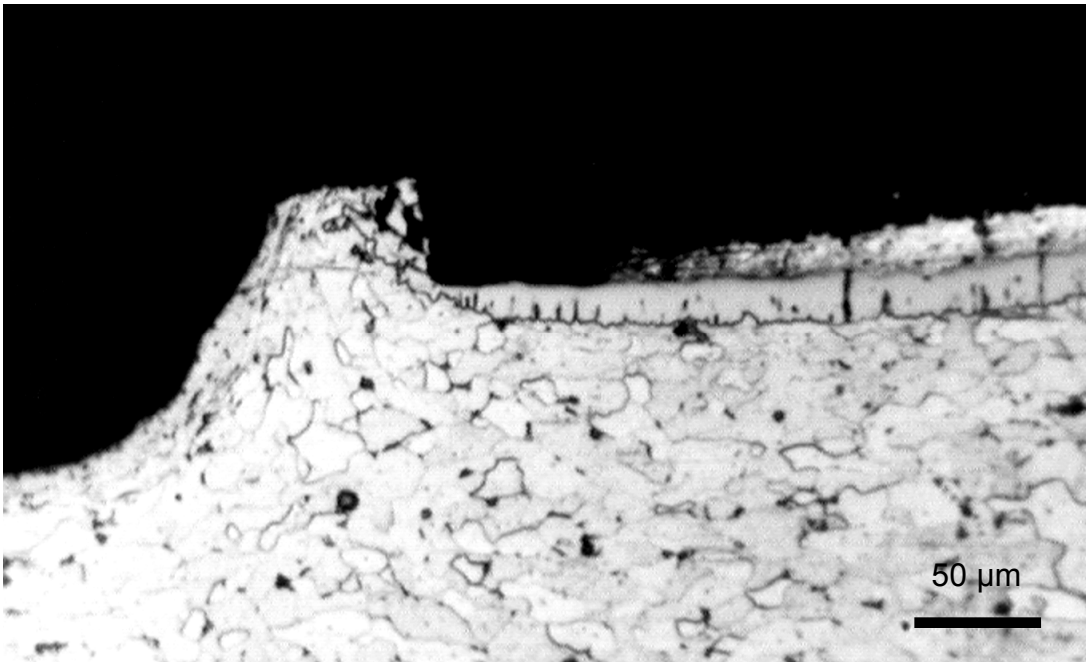

Figure 4.13: Cross section of the LCB specimen #1 exposed to solution NP showing complete outer coating loss surrounding the exposed steel.

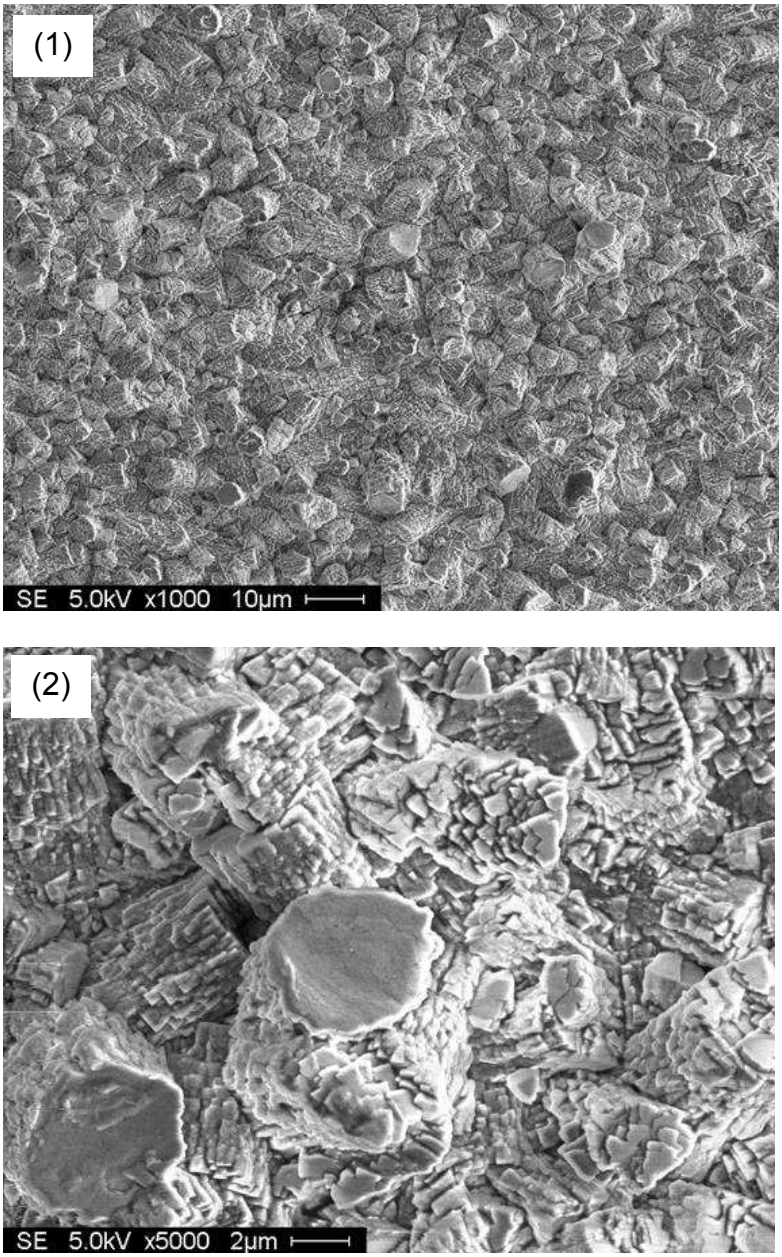

Figure 4.14: SEM image: (1) 1000x magnification and (2) 5000x magnification of the surface morphology of the LCB specimen #1 in solution NP taken after the end of exposure.

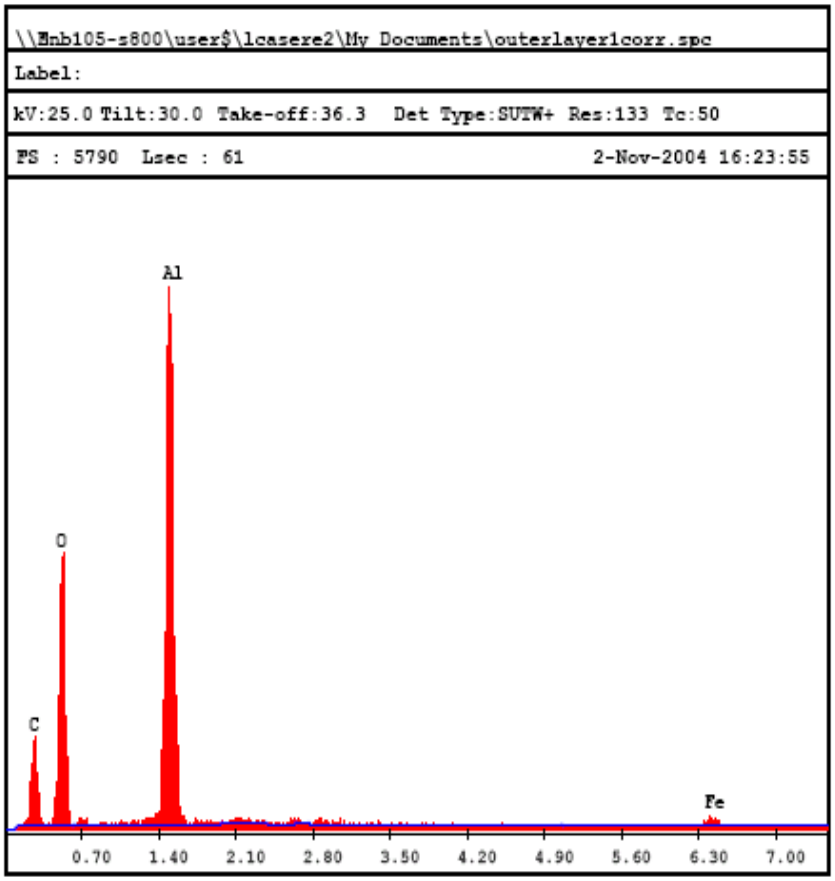

EDAX ZAF Quantification (Standardless)
Element Normalized
SEC Table : Default

Element	Wt %	At %	K-Ratio	Z	A	F
O K	49.44	62.82	0.1967	1.0352	0.3840	1.0008
AlK	48.20	36.32	0.3123	0.9673	0.6699	1.0000
FeK	2.36	0.86	0.0211	0.8870	1.0054	1.0000
Total	100.00	100.00				

Element	Net Inte.	Bkgd Inte.	Inte. Error	P/B
O K	226.84	2.79	0.86	81.33
AlK	585.91	7.16	0.53	81.83
FeK	13.42	4.13	4.43	3.25

Figure 4.15: SEM-EDS analysis of corrosion deposits on the aluminized surface of the LCB specimen #1 in solution NP.

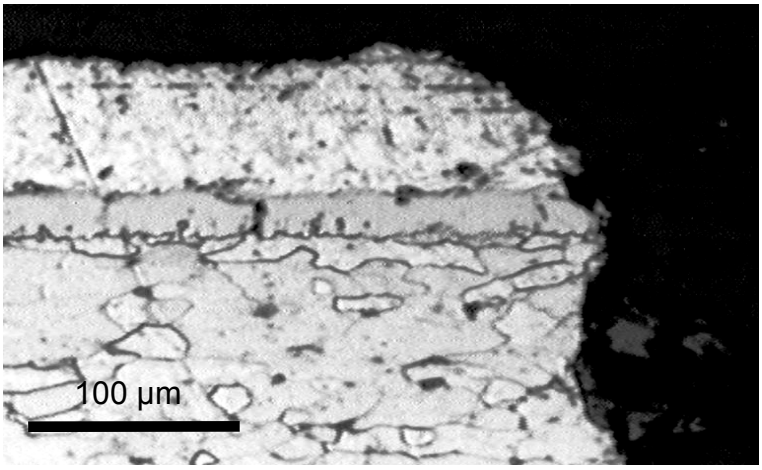

Figure 4.16: Cross section of the LCB specimen #1 exposed to solution SW near the edge of the exposed steel.

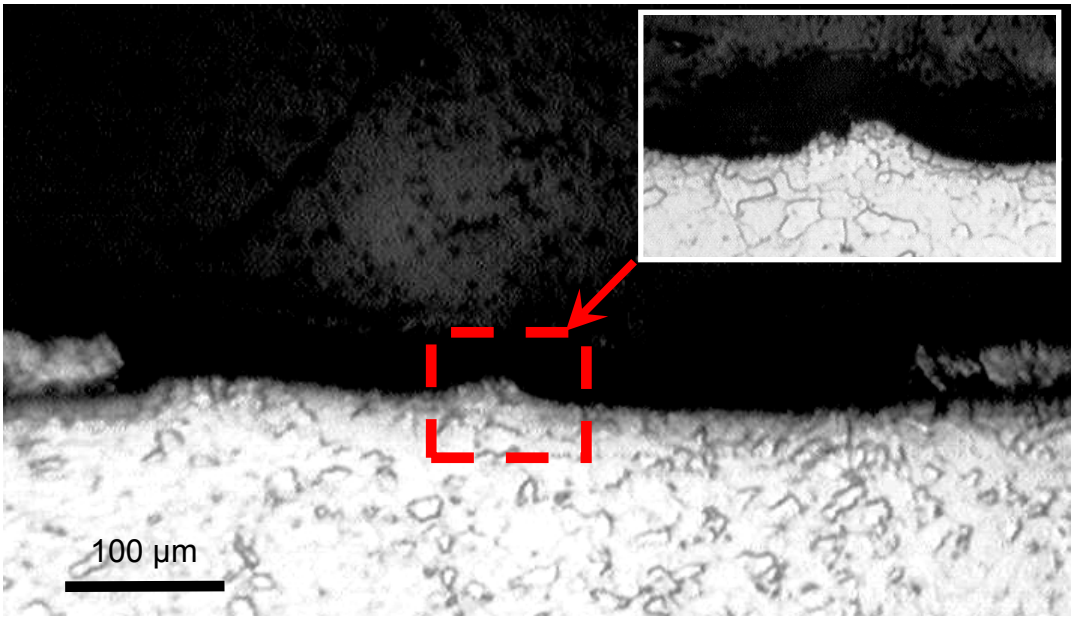

Figure 4.17: Cross section of the SCB specimen #1 exposed to solution C showing that a pit ~0.5 mm diameter that reached the underlying steel.

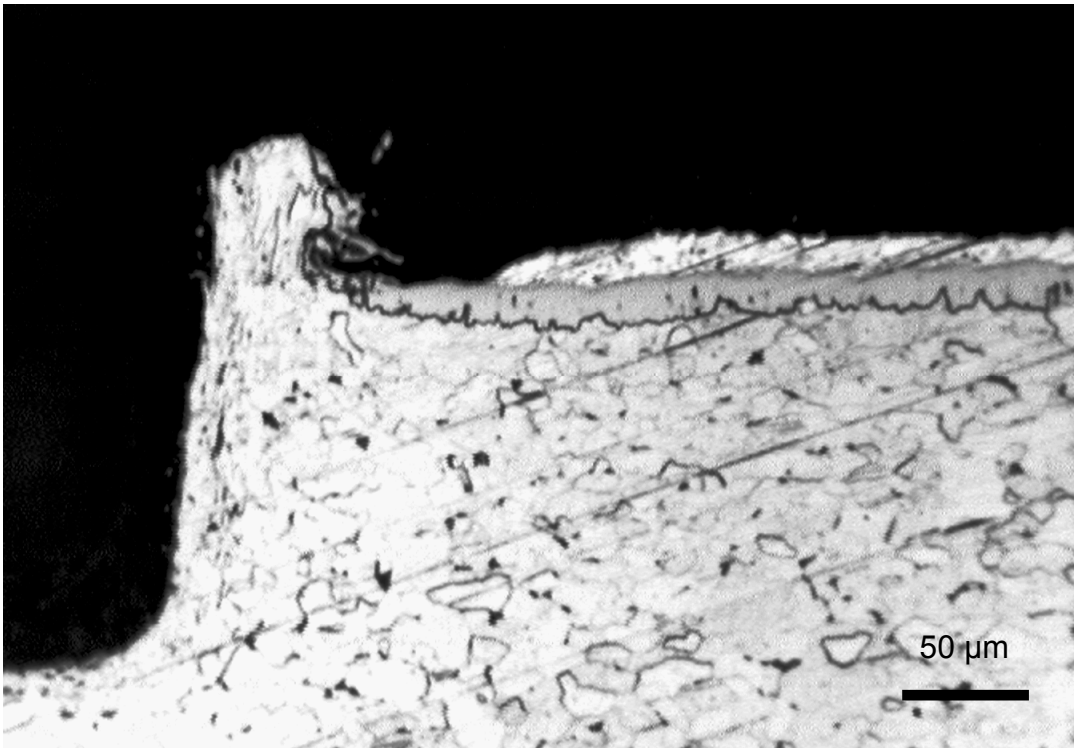

Figure 4.18: Cross section of the SCB specimen #1 exposed to solution NP showing complete outer coating loss surrounding the exposed steel.

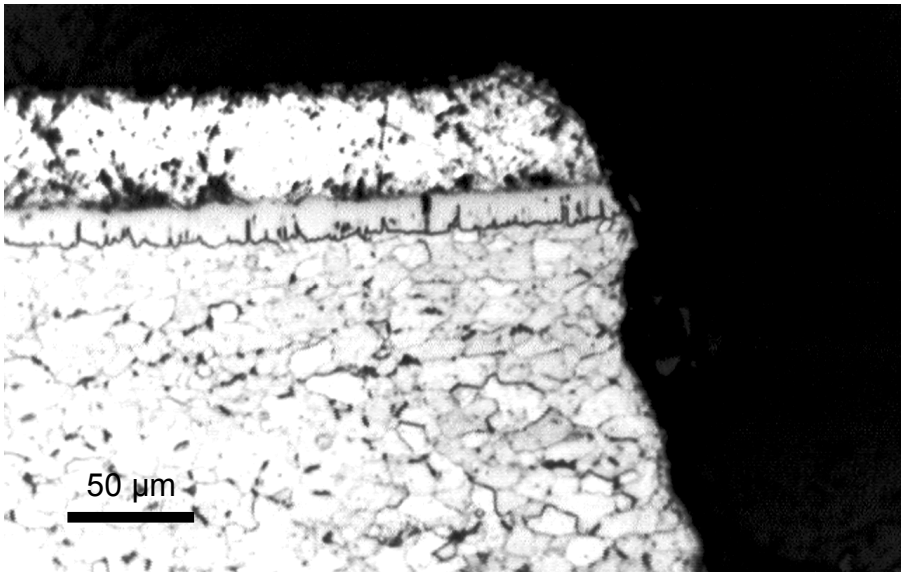

Figure 4.19: Cross section of the SCB specimen #1 exposed to solution SW near the exposed steel region.

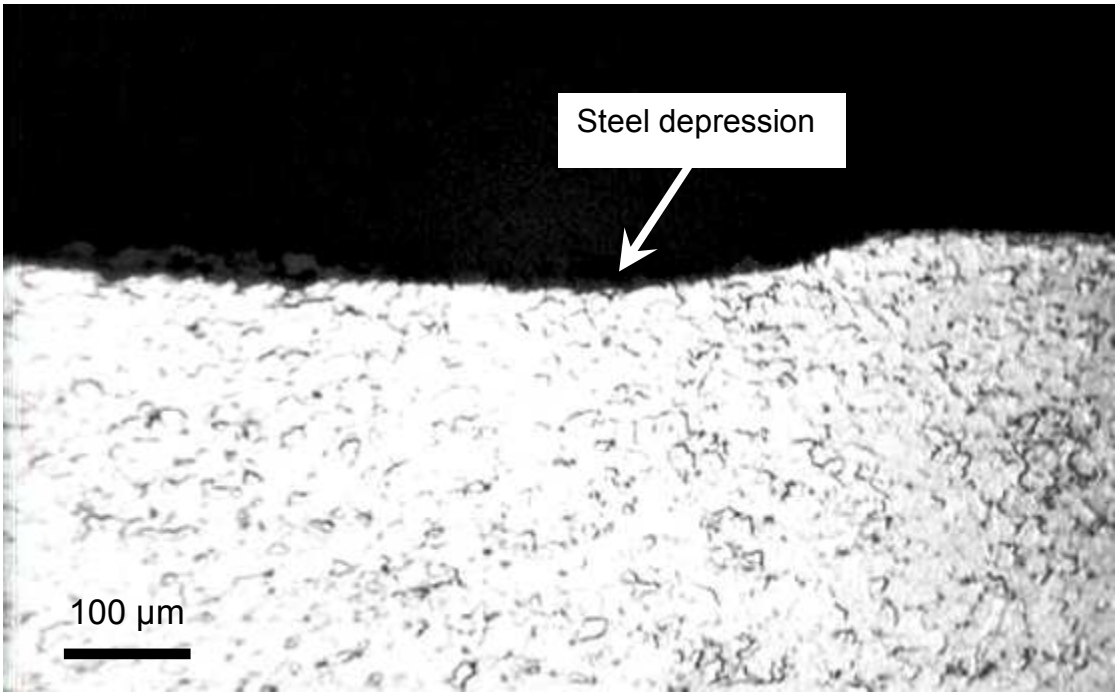

Figure 4.20: Cross section of the LCB specimen #1 exposed to solution NP showing additional metal loss at the central region of the exposed steel.

SCB specimen (#1) in Sol NP

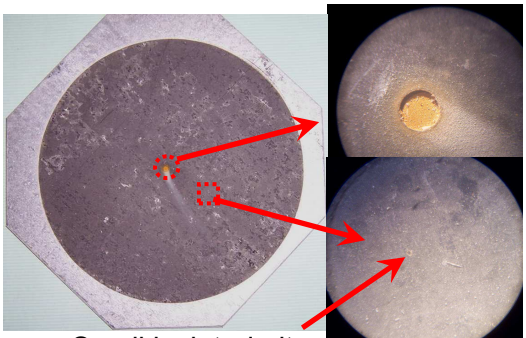

Small isolated pits

SCB specimen (#1) in Sol P

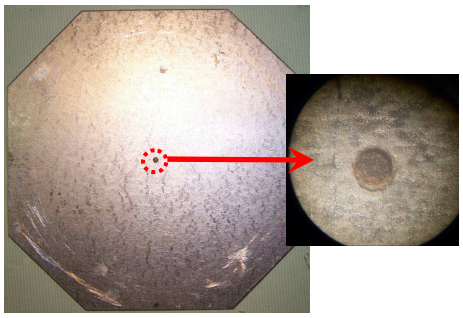

SCB specimen (#1) in Sol SW

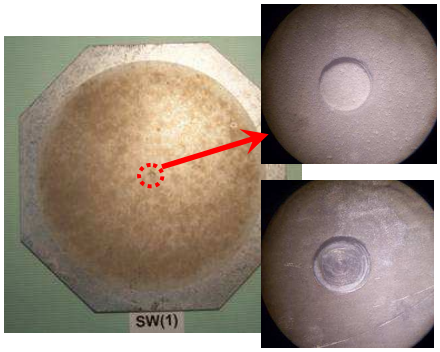

SCB specimen (#2) in Sol C

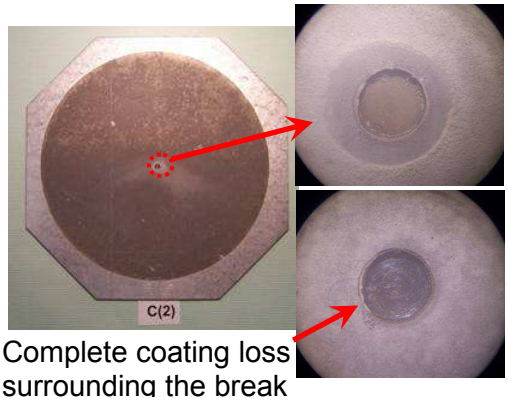

Complete coating loss surrounding the break

LCB specimen (#1) in Sol SW

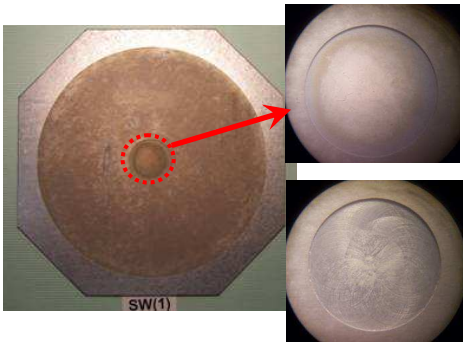

LCB specimen (#2) in Sol P

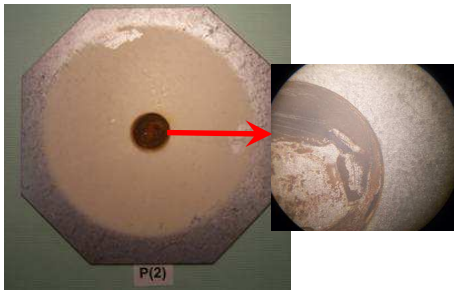

LCB specimen (#1) in Sol NP

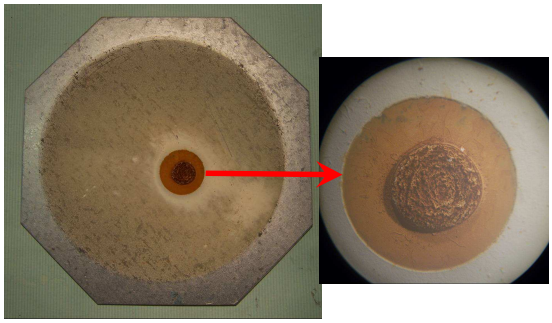

Two distinctive precipitate formation. Central growth was ~1-3 mm thick

Figure 4.21: Post-exposure photographs of selected blemished specimens.

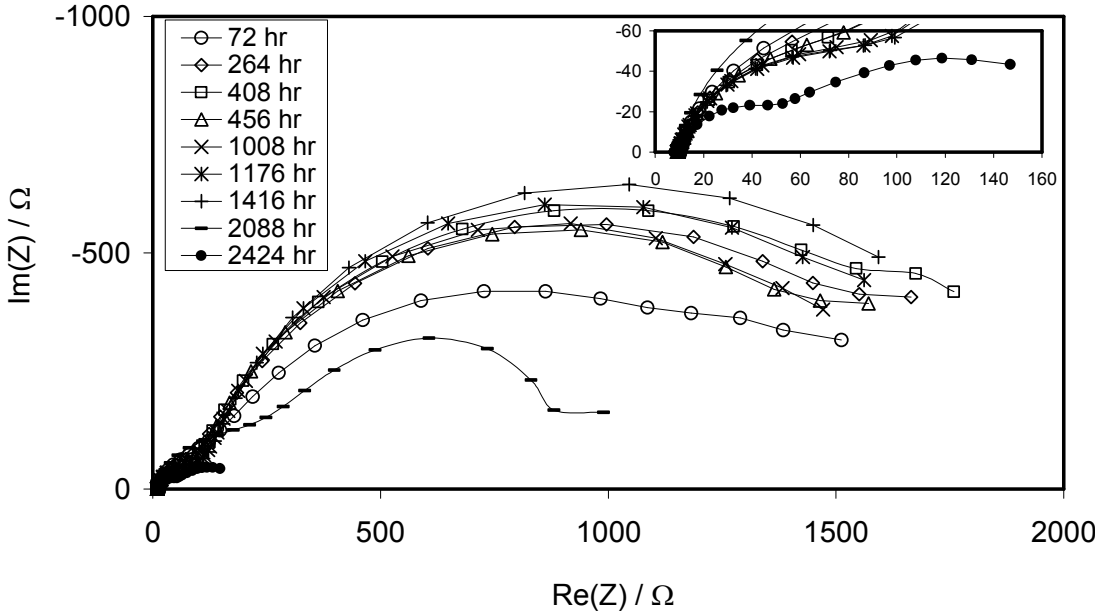

Figure 4.22: Nyquist plot of the impedance response of the LCB specimen #1 in solution NP (100 KHz - 1 mHz - 5 points/decade).

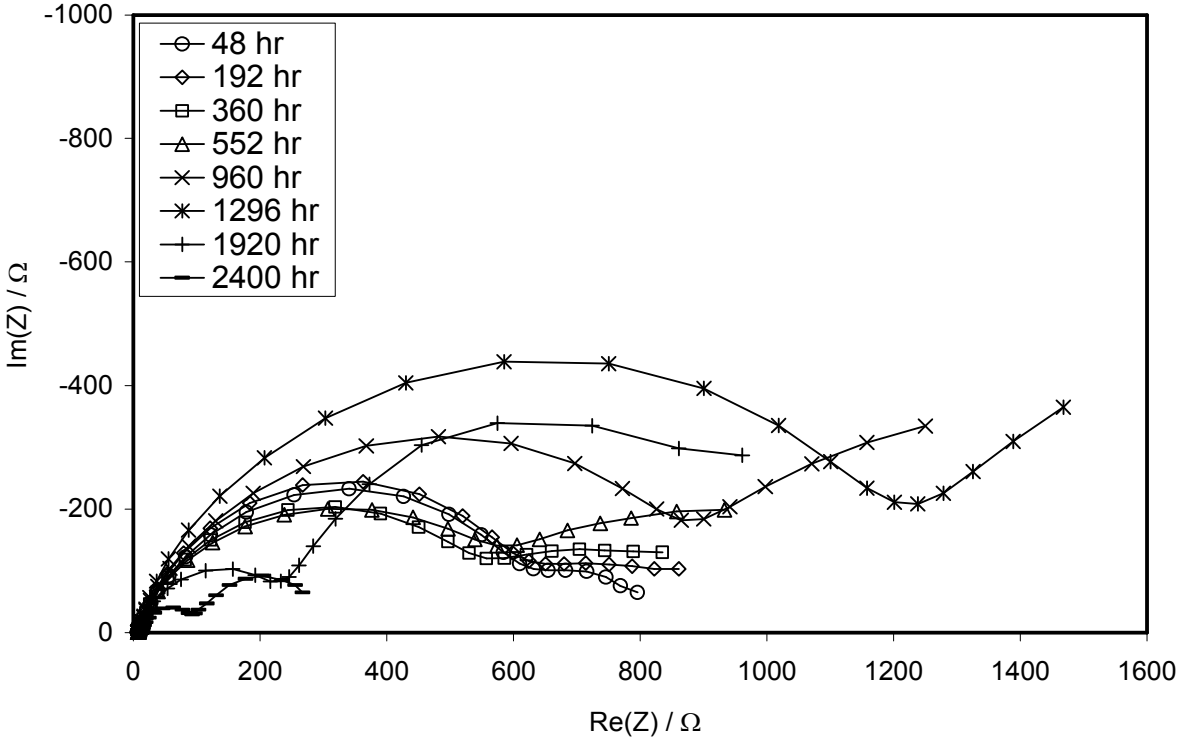

Figure 4.23: Nyquist plot of the impedance response of the LCB specimen #1 in solution P (100 KHz - 1 mHz - 5 points/decade).

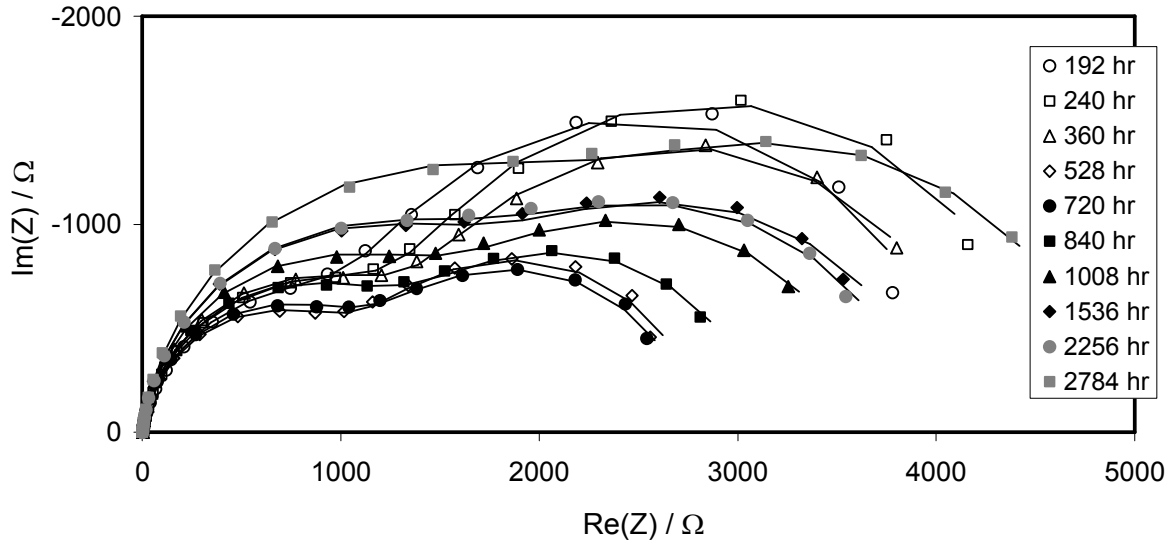

Figure 4.24: Nyquist plot of the impedance response of the LCB specimen #1 in solution SW (100 KHz - 1 mHz - 5 points/decade).

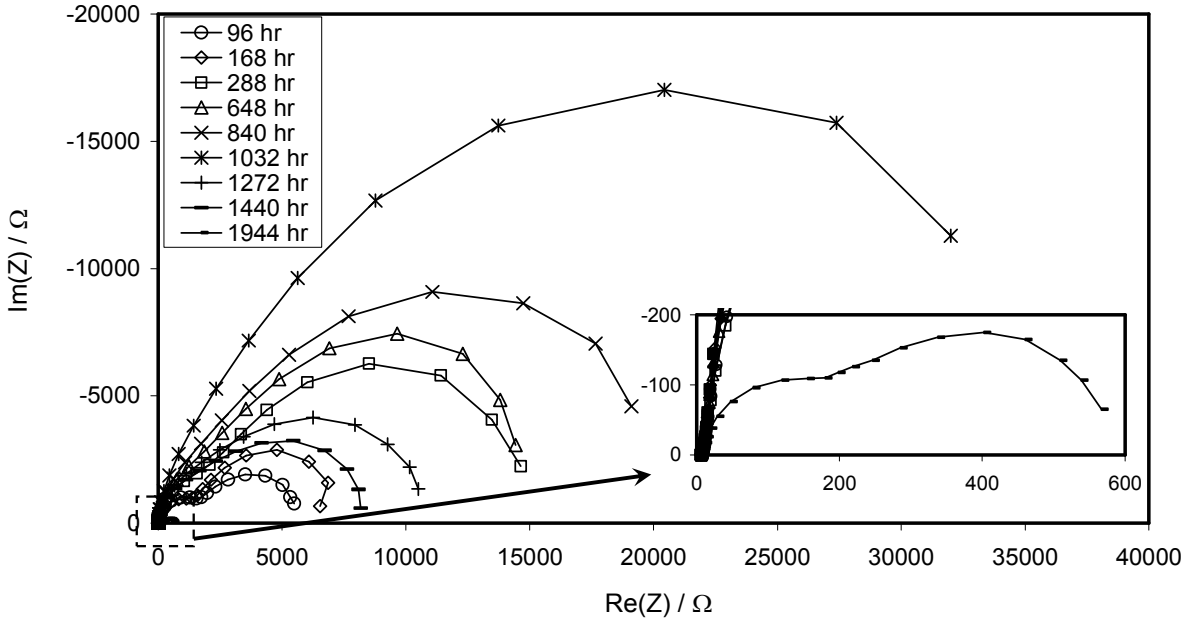

Figure 4.25: Nyquist plot of the impedance response of the SCB specimen #1 in solution NP (100 KHz - 1 mHz - 5 points/decade).

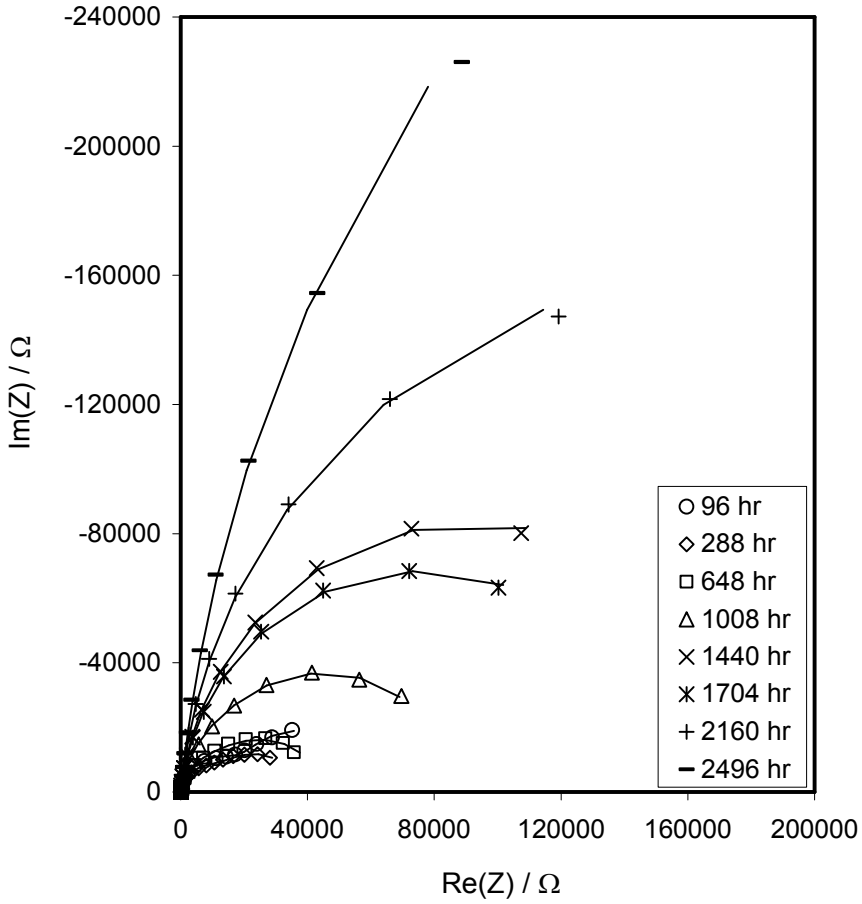

Figure 4.26: Nyquist plot of the impedance response of the SCB specimen #1 in solution P (100 KHz - 1 mHz - 5 points/decade).

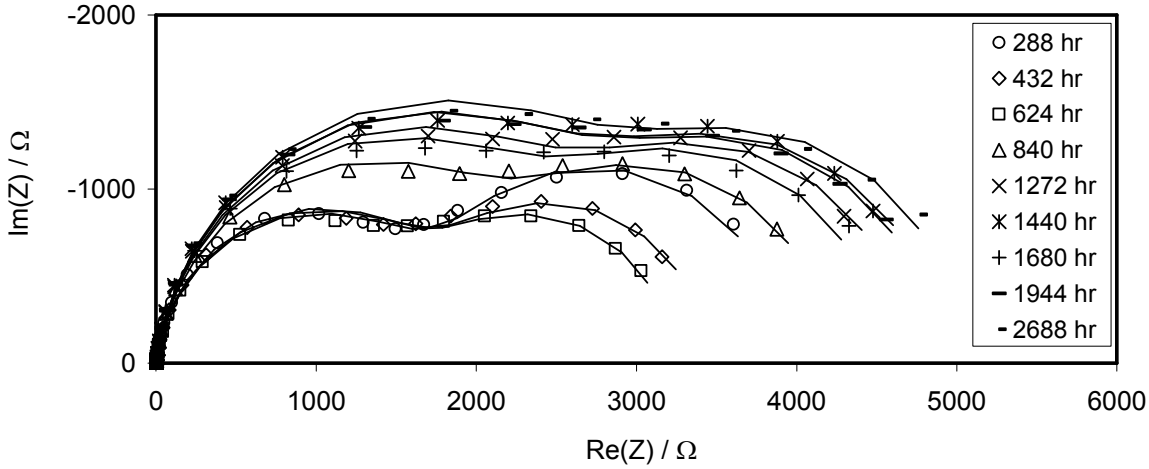

Figure 4.27: Nyquist plot of the impedance response of the SCB specimen #1 in solution SW (100 KHz - 1 mHz - 5 points/decade).

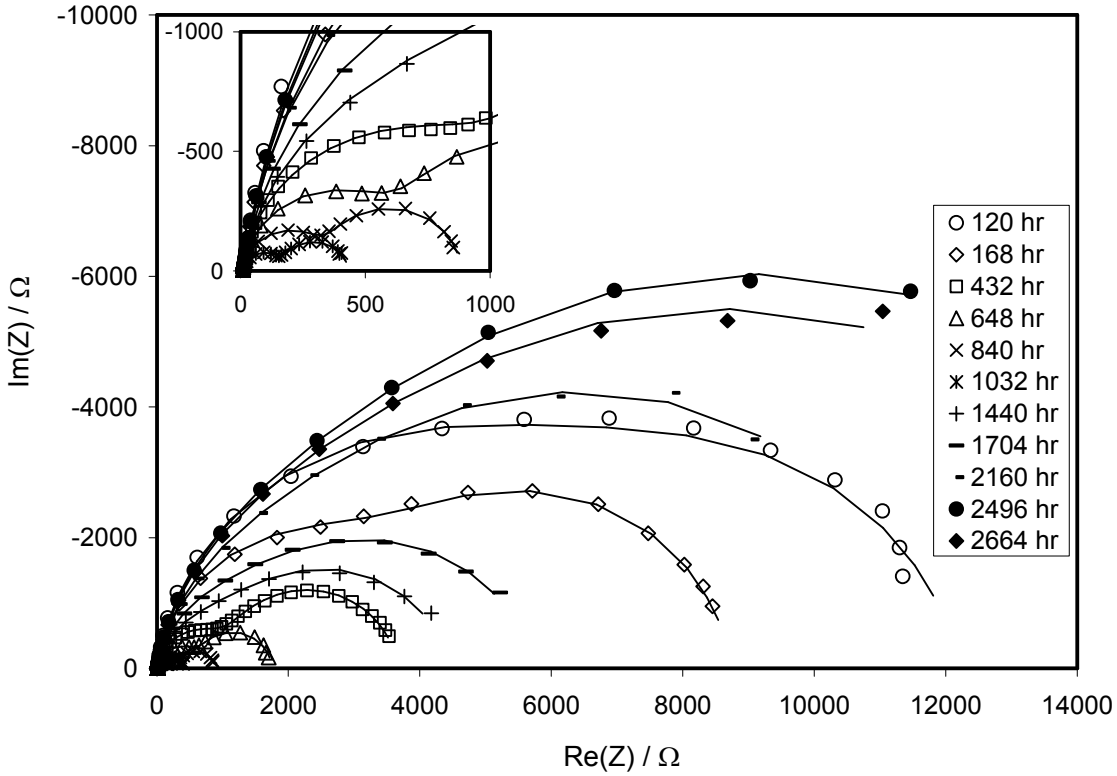

Figure 4.28: Nyquist plot of the impedance response of the SCB specimen #1 in solution C (100 KHz - 1 mHz - 5 points/decade).

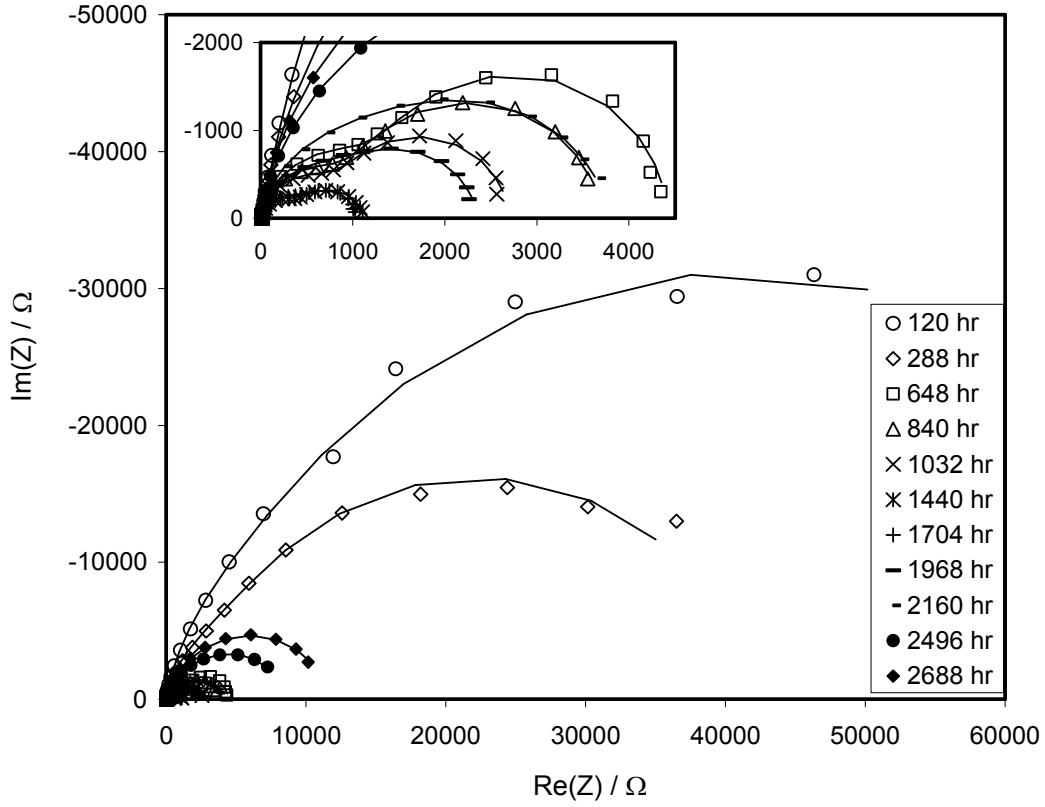

Figure 4.29: Nyquist plot of the impedance response of the SCB specimen #2 in solution C (100 KHz-1 mHz - 5 points/decade).

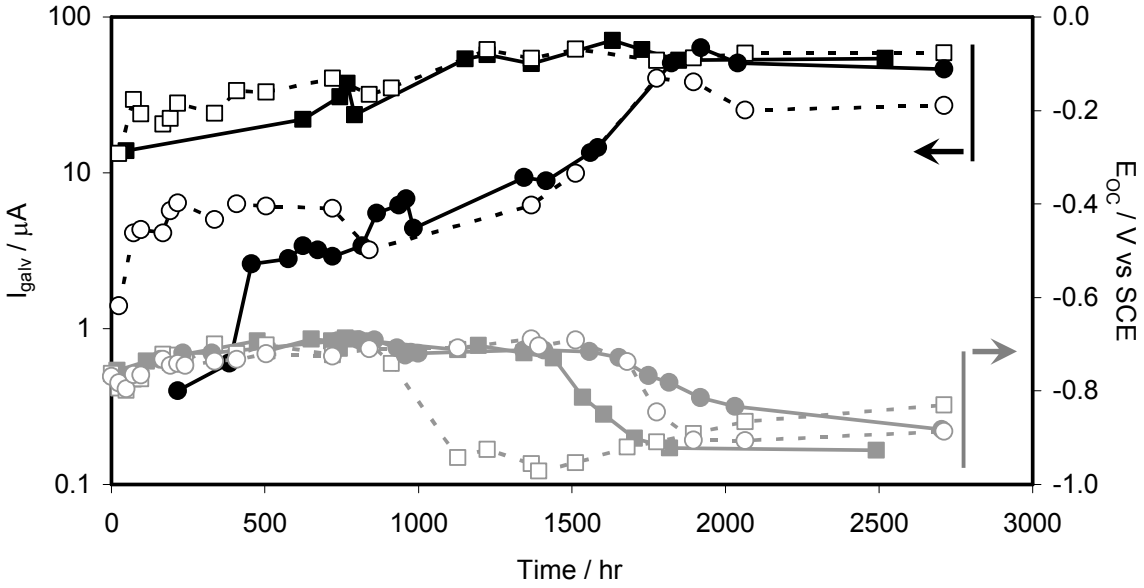

Figure 4.30: E_{OC} and galvanic current I_{galv} measurements for the macrocell assemblies exposed to solutions P (circles) and NP (squares). The steel components were always net cathodes.

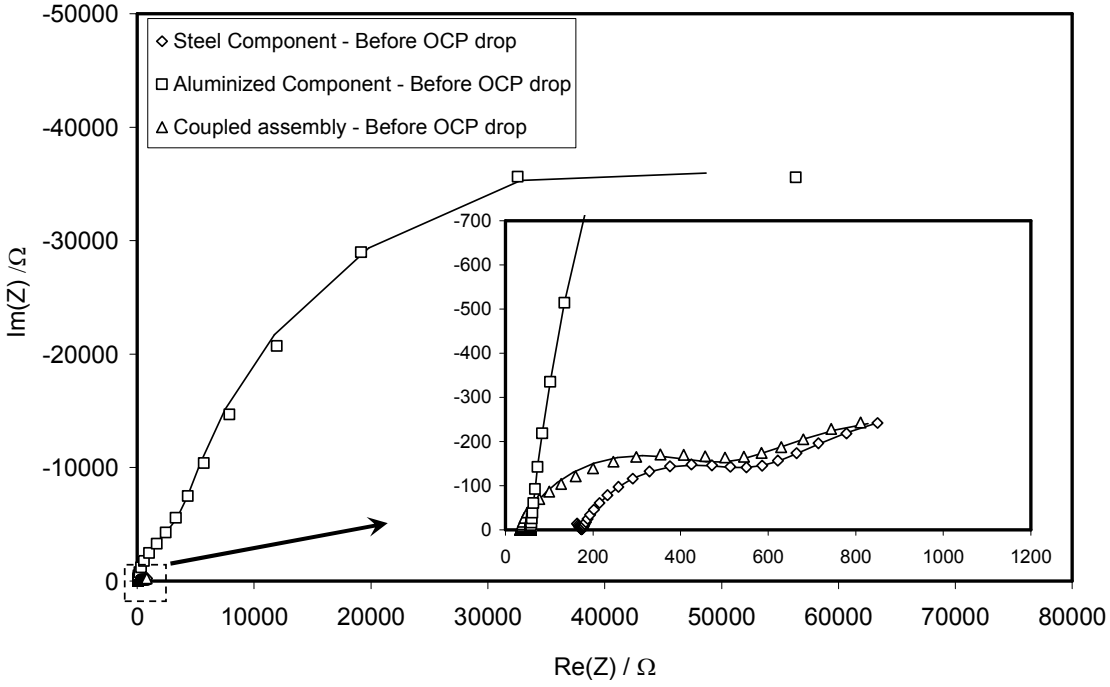

Figure 4.31: Nyquist plot of the impedance response of the macrocell assembly and the individual components exposed to solution P (100 kHz–1 mHz, 5 points/decade) before (~900 hr) the E_{OC} drop.

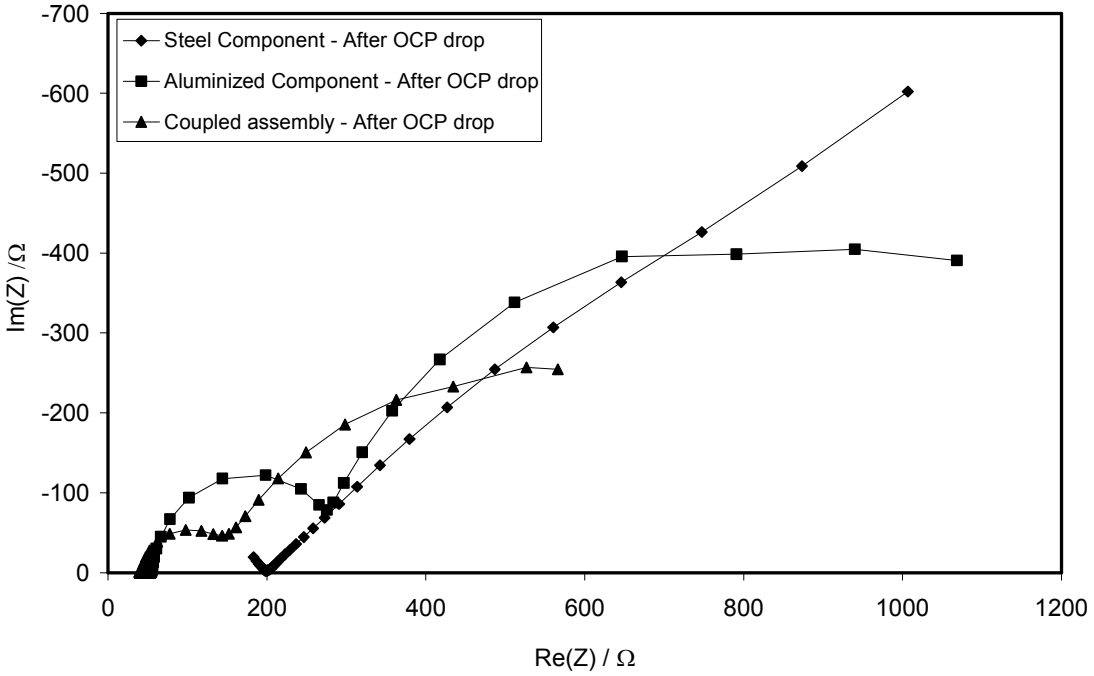

Figure 4.32: Nyquist plot of the impedance response of the macrocell assembly and the individual components exposed to solution P (100 kHz–1 mHz, 5 points/decade) after (~1,780 hr) the E_{OC} drop.

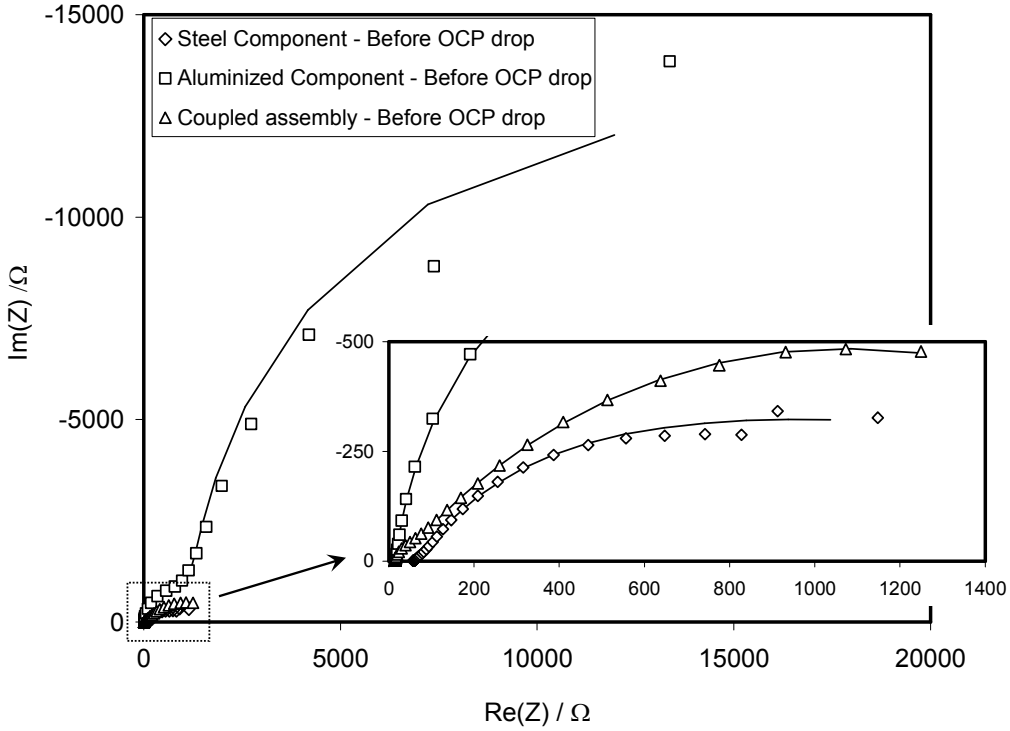

Figure 4.33: Nyquist plot of the impedance response of the macrocell assembly and the individual components exposed to solution NP (100 kHz–1 mHz, 5 points/decade) before (~900 hr) the E_{OC} drop.

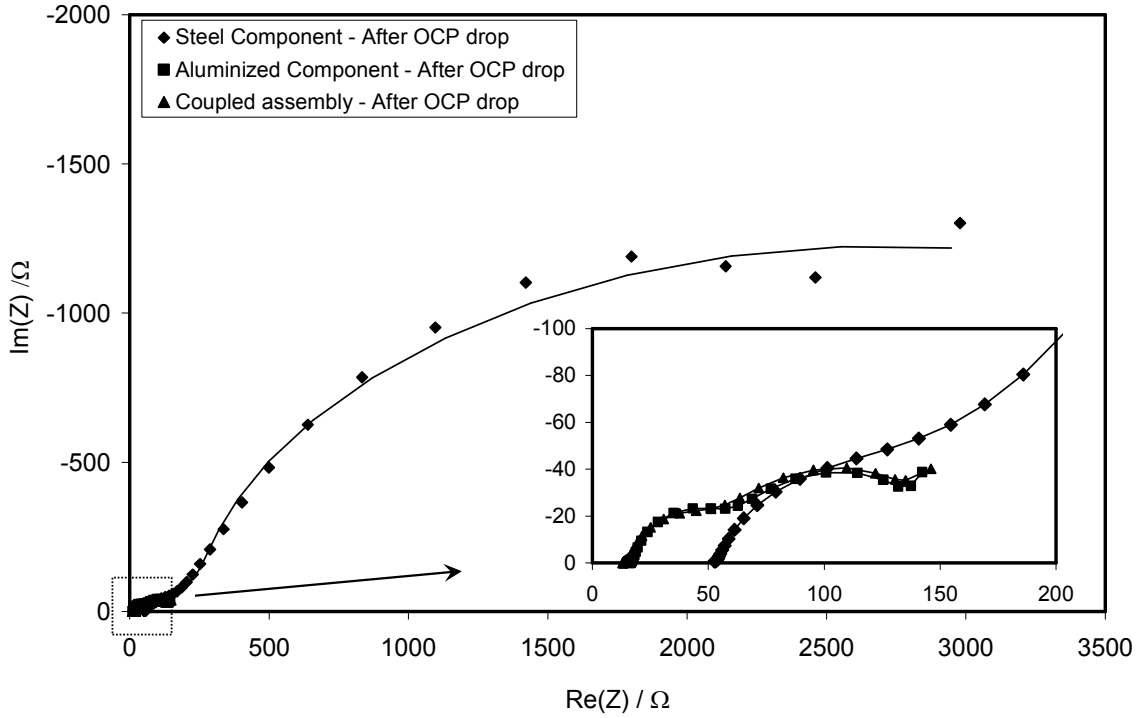

Figure 4.34: Nyquist plot of the impedance response of the macrocell assembly and the individual components exposed to solution NP (100 kHz–1 mHz, 5 points/decade) after (~1,780 hr) the E_{OC} drop.

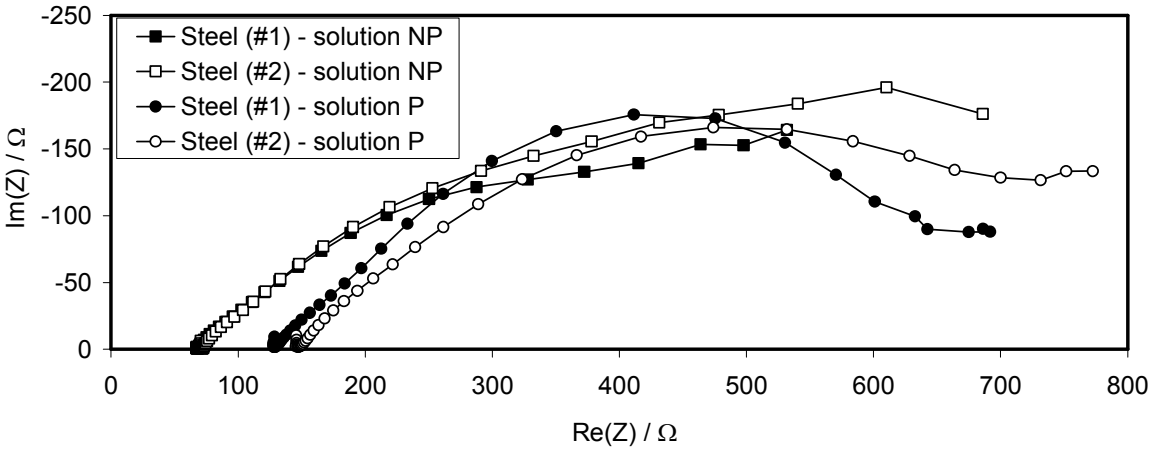

Figure 4.35: Nyquist plot of the impedance response of the replicate uncoupled steel specimens exposed to solutions NP and P (100 kHz–1 mHz, 5 points/decade).

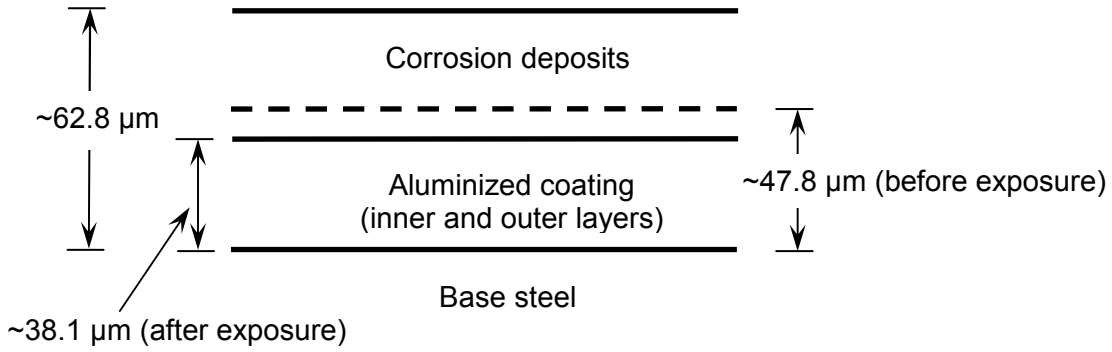

Figure 4.36: Schematic of a typical aluminized coating cross section of a LCB specimen #1 exposed to solution NP.

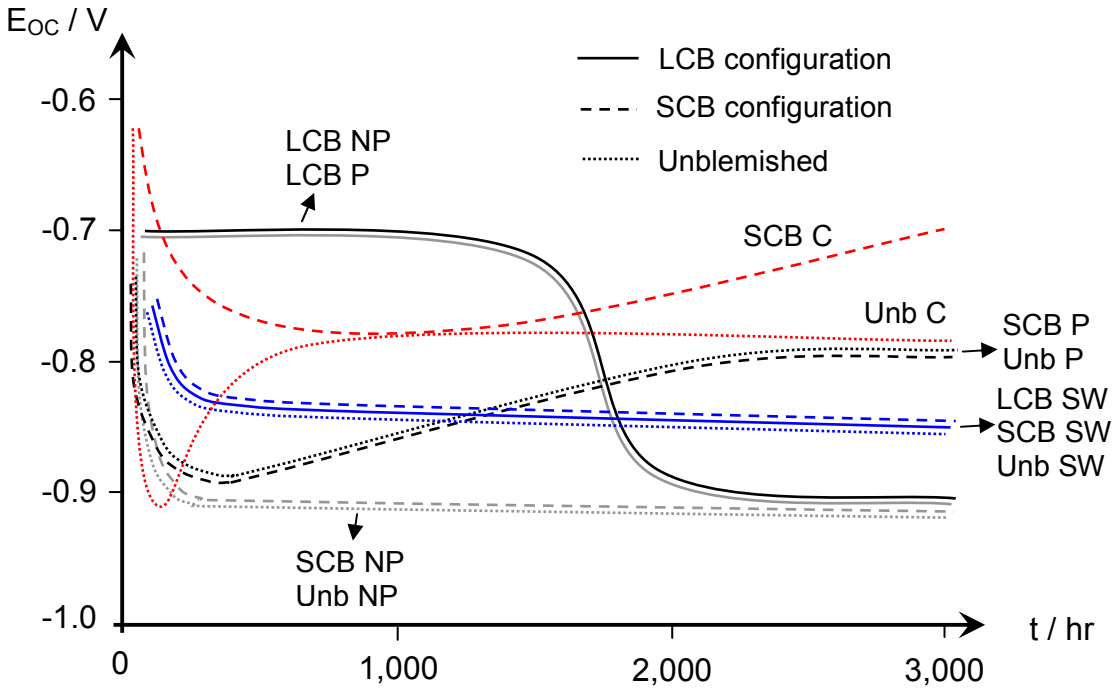

Figure 4.37: Schematic of the E_{OC} trends shown in Figures 4.5 through 4.11.

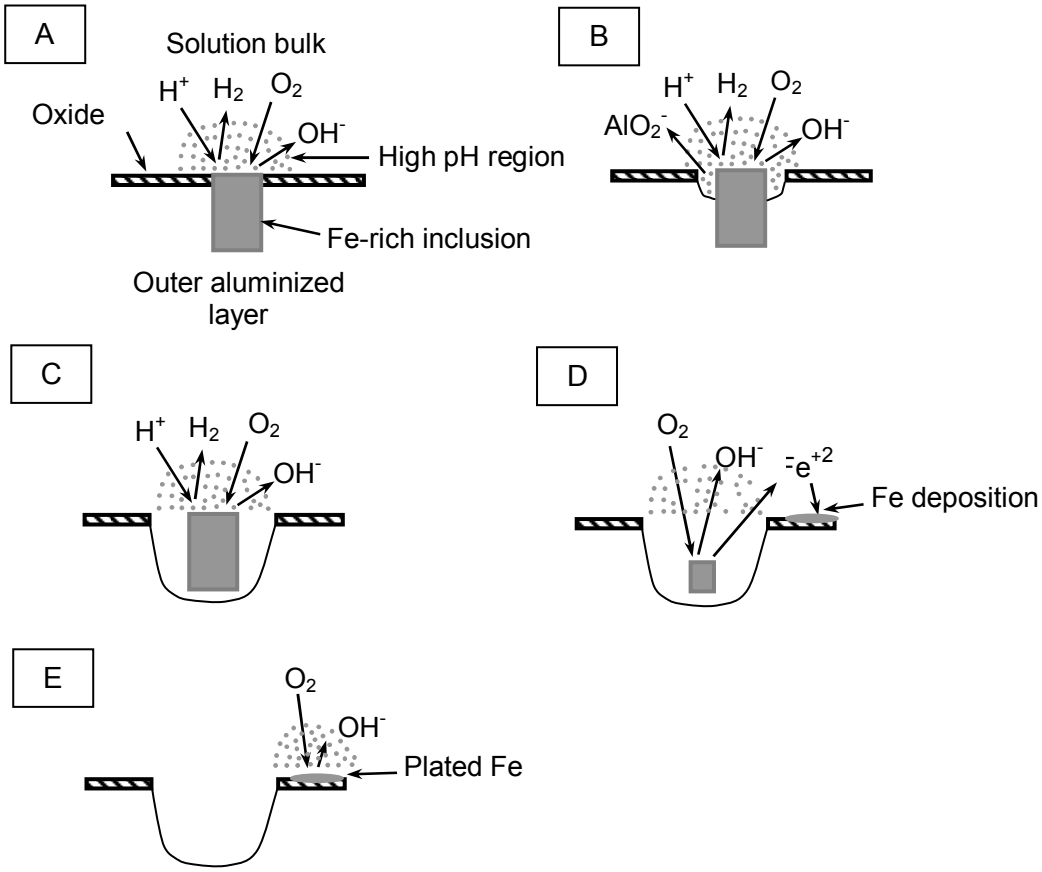

Figure 4.38: Schematic description of the corrosion mechanism of aluminized steel around the Fe-rich inclusion present in the outer aluminized layer: (A) development of high pH region around the inclusion due to the cathodic reaction, (B) corrosion initiation of the surrounding aluminum exposing larger inclusion area with consequent enhancement of the cathodic reaction, (C) detachment of the inclusion as a free particle from the aluminum matrix, (D) dissolution of the free particle and plating of Fe on aluminized surface, (E) development of a high pH region around the plated Fe (after Vukmirovic et al. (2002)).

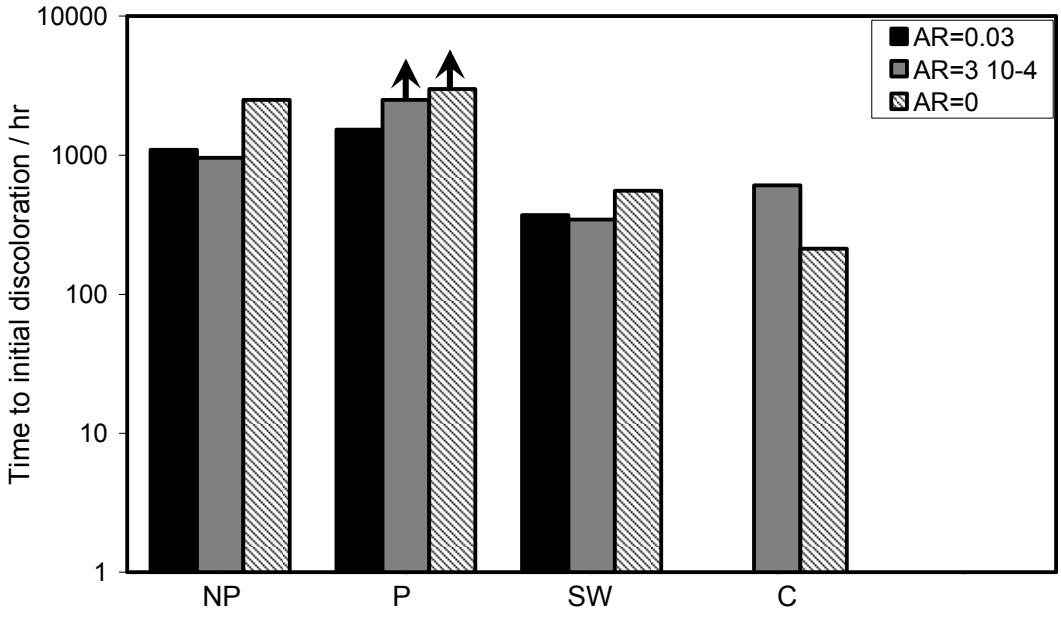

Figure 4.39: Average of the time to initial discoloration of replicate specimens as a function of A_R. Results for A_R=0 and A_R=3 10^{-4} in solution P are minimum values as indicated by the arrows.

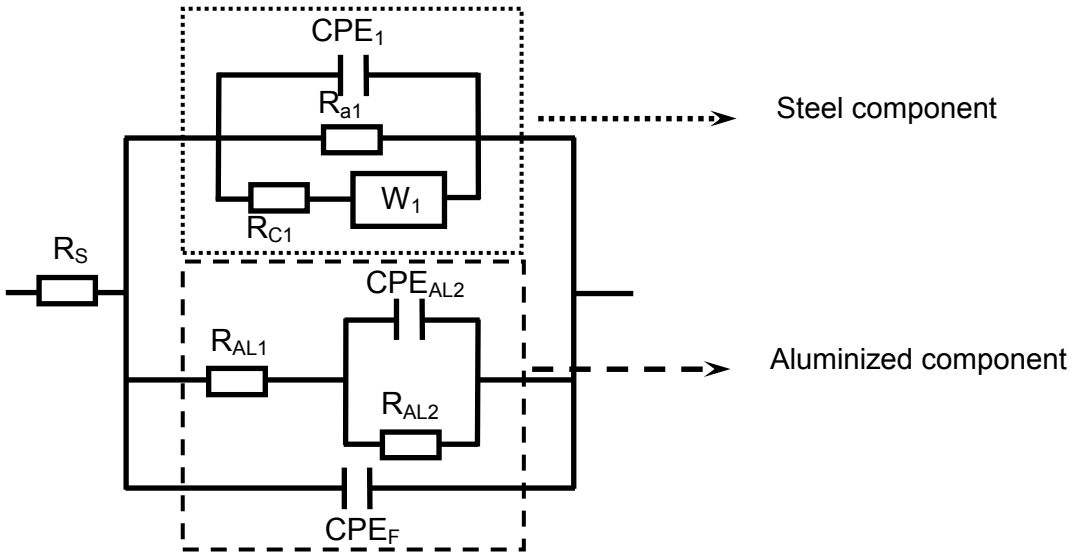

Figure 4.40: Analog equivalent circuit used to simulate the impedance response of the macrocell assemblies in solutions NP and P for the regimes before and after the E_{OC} drop.

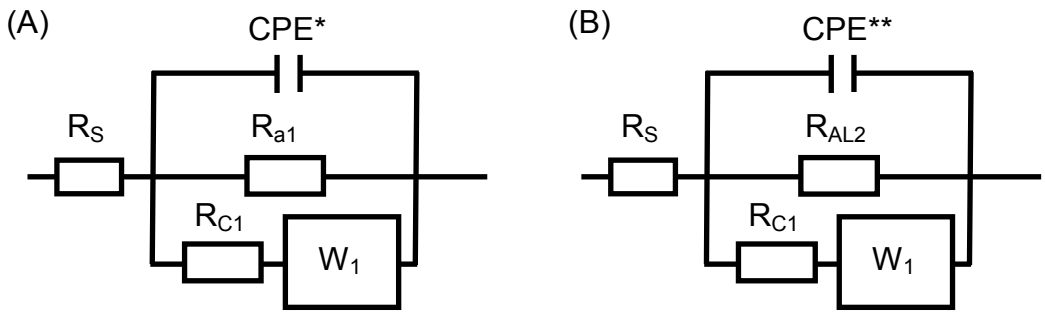

Figure 4.41: Simplified equivalent circuit used to simulate the impedance response of the LCB and SCB specimens. The circuit (A) was employed solely for the LCB specimens exposed to solutions NP and P before the E_{OC} drop. The circuit (B) was used for all solutions after the E_{OC} drop.

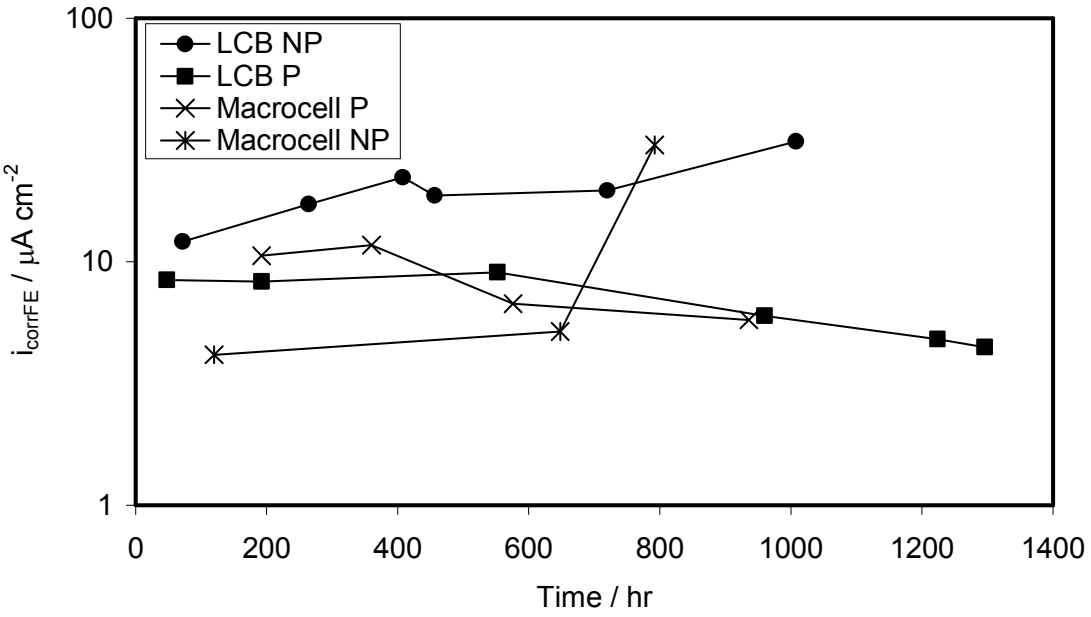

Figure 4.42: Evolution of i_{corrFE} of the exposed steel portion for the LCB specimens (#1) in solutions NP and P obtained per analog equivalent circuit shown in Figure 4.41 (A) and the steel component in the macrocell assemblies obtained per the upper branch of the analog equivalent circuit in Figure 4.40.

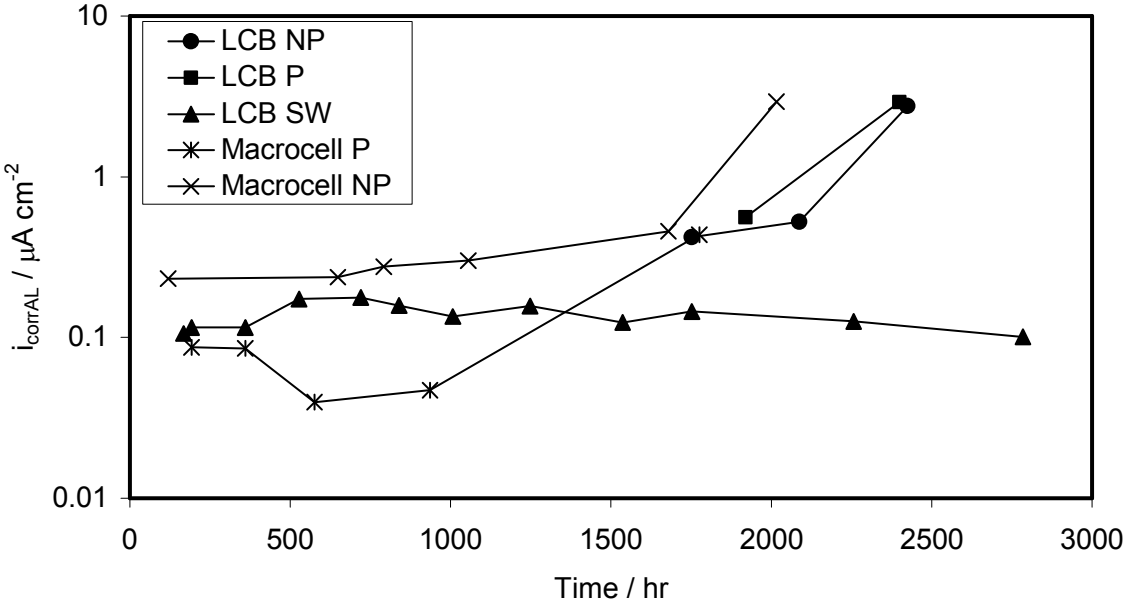

Figure 4.43: Evolution of i_{corrAL} of the aluminized portion for the LCB specimens (#1) obtained using the analog equivalent circuit shown in Figure 4.41 (B) and the aluminized component in the macrocell assemblies using the lower branch of the analog equivalent circuit shown in Figure 4.40.

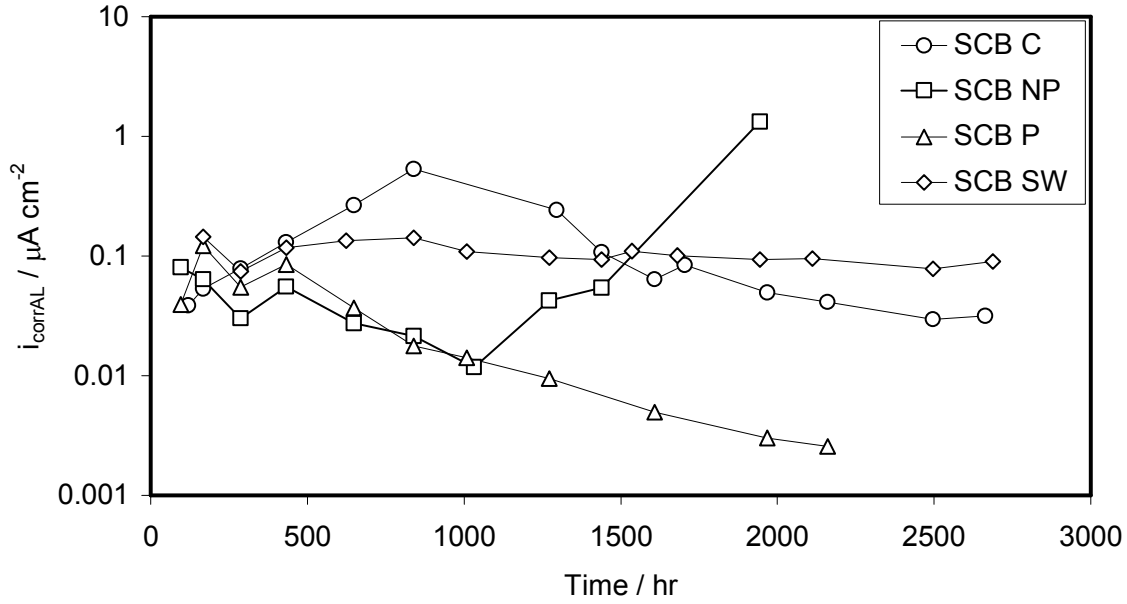

Figure 4.44: Evolution of i_{corrAL} of the aluminized portion for the SCB specimens (#1) obtained using the analog equivalent circuit shown in Figure 4.41 (B).

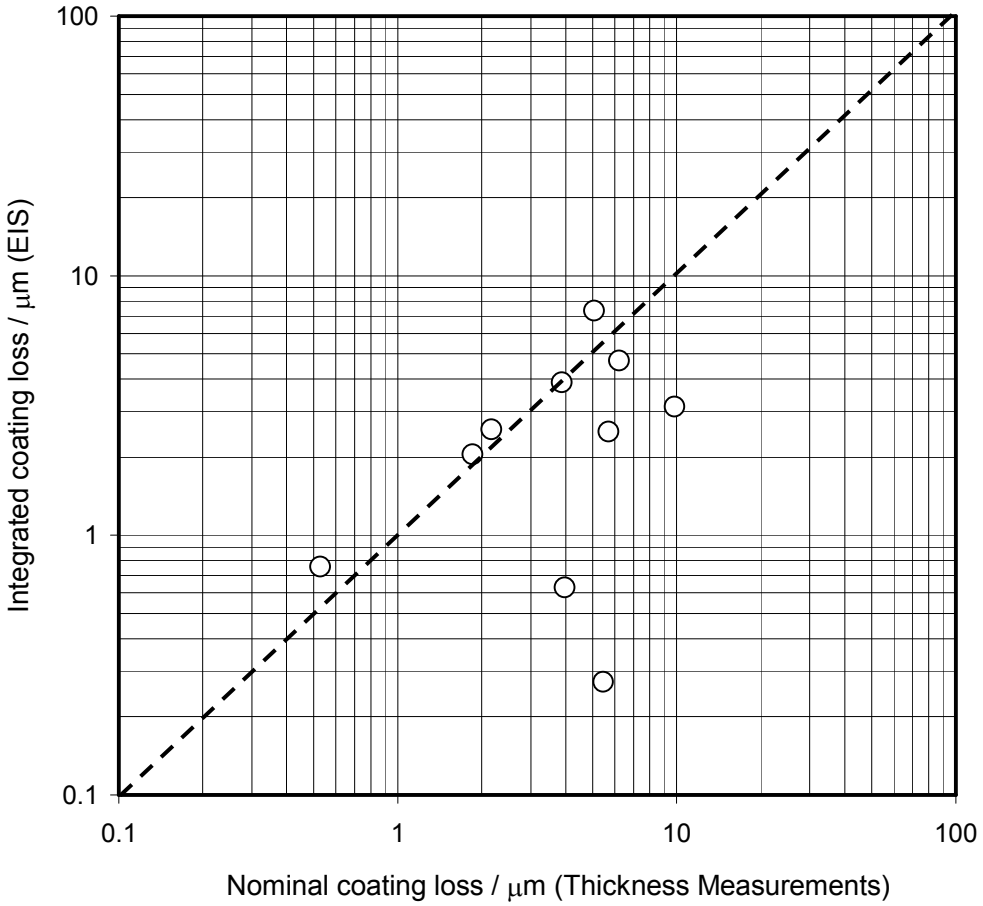

Figure 4.45: Correlation between the integrated coating loss obtained by EIS and the nominal coating thickness loss determined by magnetic coating thickness measurements for selected specimens shown in Table 4.1.

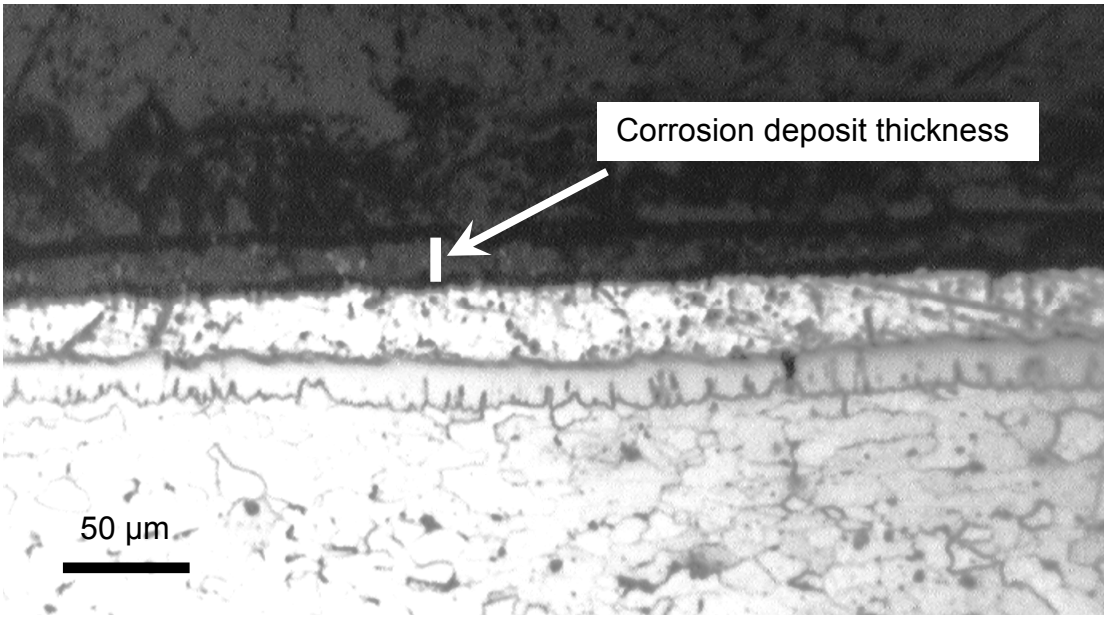

Figure 4.46: Cross section of the LCB specimen #1 exposed to solution NP. The dark outer layer covering the entire outer aluminized coating layer corresponds to corrosion deposits of ~10-15 µm thick.

Chapter 5

Computation of *ac* and *dc* Current and Potential Distributions of Aluminized Steel Type 2 with Coating Breaks

5.1 Introduction

As discussed in Chapter 2, unblemished aluminized steel showed high corrosion resistance, comparable to that of pure aluminum, in near neutral pH waters with high scaling tendencies. However, the results in Chapter 4 showed that in such environments the underlying steel exposed at aluminized coating breaks, imitating surface damage as it may be encountered in field exposure, corroded actively from the beginning of the test. Throughout the entire exposure time, the outer aluminized coating always acted as a net anode to the exposed steel, but there was initially insufficient protective macrocell galvanic action between the exposed steel and the surrounding aluminized coating, which was in passive condition early on in the exposure. Later on, larger macrocell currents were recorded suggesting a much improved protection to the exposed steel by the aluminized coating, which by that time was actively corroding.

This Chapter introduces modeling of the steady-state (*dc*) extent of galvanic action between the surrounding aluminized coating and the exposed steel as function of polarization parameters of the two metals, active/passive condition of the aluminized surface, and electrolyte conductivity. The resulting model serves as a basis for initial evaluation of the impact of some of those

variables on the effectiveness of the galvanic action beyond the conditions examined experimentally, for future expansion to address other geometric configurations that may be encountered in the field, and eventual incorporation to durability prediction models. The model system was based on the physical configuration of the LCB specimens (Chapter 4), using a two dimensional *dc* computational model solved numerically by the finite difference method. The *dc* model output was the static current and potential values at every point in the metal surface.

This Chapter also addresses modeling of behavior of the same system under *ac* conditions. As shown in previous Chapters, the EIS technique is a sophisticated experimental tool to accurately determine corrosion rates of metals by applying a small *ac* signal. However, the EIS response can be sometimes complicated to evaluate due to the presence of non uniform *ac* current and potential distributions which may lead, if not properly identified, to an inappropriate interpretation of the EIS response. Thus, it is of importance to quantify the effect of non uniform *ac* currents so that accurate estimates of corrosion rates can be achieved. The analog equivalent circuits shown in Figure 4.41 in Chapter 4, used to interpret the impedance responses of the blemished specimens, do not take into consideration the effect of uneven *ac* current distributed along the metal surface. To account for possible non uniform *ac* current distribution artifacts present under these conditions, a two dimensional (*ac)* computational model was developed. Comparison between the impedance

response calculated by the *ac* model and the experimental EIS results obtained for the LCB specimens (Chapter 4) is also presented.

5.2 The Model System

The model system, corresponding to the test cell in Figure 2.3 (Chapter 2), was cylindrically symmetric along the central axis with a disk-shaped aluminized steel Type 2 bottom of external radius r_e=5 cm for a total surface area of 95 cm^2, with total aluminized coating ~45 μm thick (of composition reported in Chapter 2). The central portion of the cell space bottom had a circular coating break of radius r_0=1 cm (matching the coating break size of the LCB configuration), exposing the underlying base steel. The electrolyte was treated as a naturally aerated homogeneous medium filling a cylindrical zone of height H=6.5 cm over the specimen surface. Constant conductivity σ and charge neutrality were assumed throughout the electrolyte. The reference electrode sensing tip was assumed to be positioned centered on the coating break. For simplicity, the counter electrode was treated as non polarizable, disk-shaped with radius r_e=5 cm, and placed at the top of the electrolyte region parallel to the specimen surface. The entire metal surface was treated as if were flat throughout so that any milling step effects of the edge and wall of the coating break were neglected.

5.2.1 The *dc* Model

Two scenarios were explored here based on the experimental observations of the LCB specimens reported in Chapter 4. The first scenario

described conditions for E_{OC} around -700 mV observed at early exposure times, when the exposed steel experienced active uniform dissolution and the surrounding aluminized surface was essentially passive (e.g. solutions NP and P). The second scenario described conditions after the onset of the E_{OC} drop (~<-850 mV) observed later on in the exposure, when the aluminized surface showed uniform discoloration with formation of small isolated pits and the exposed steel was galvanically protected by the surrounding aluminized surface.

For the first scenario, it was proposed that the prevalent cathodic reaction at the potentials of interest was O_2 reduction of the form $O_2+2H_2O+4e^-\rightarrow 4OH^-$. This reaction was assumed to obey simple Butler-Volmer kinetics, acting over the entire steel surface and to a lesser extent on the small amounts of Fe-rich inclusions present at the aluminized surface. The cathodic reaction was assumed to be under mixed activation-concentration control at the exposed steel and, because of the much lower average current density on the aluminized surface, under purely activation-limited control there. The reverse of the cathodic reaction at both places could be easily ignored since the system E_{OC} was always far below the O_2/H_2O redox potential. The transport of O_2 in the electrolyte immediately next to the exposed steel surface was assumed to proceed only by diffusion (with constant O_2 diffusivity D), limited to a thin stationary diffusional layer of thickness δ over the steel surface. The O_2 concentration elsewhere was assumed to be uniform (reflecting natural convection) and in equilibrium with the O_2 partial pressure P_{O2}=0.21 atm of the surrounding air in the test cell (Kranc and Sagüés, 1993). It is speculated that both O_2 reduction and H_2 evolution would be

part of the overall cathodic reaction at potentials ~<-850 mV, as demonstrated in Chapter 3. For the sake of simplicity, the main cathodic reaction after the E_{OC} drop is assumed to be O_2 reduction taking place mostly at the exposed steel approaching a limited-concentration control regime.

Thus, the rate of the O_2 reduction reaction at the metal surface for both scenarios is:

$$i_{Cx} = i_{0Cx} \cdot \frac{C_S}{C_B} \cdot 10^{\frac{E_{eqcx} - \Phi_S}{\beta_{Cx}}} \tag{5.1}$$

where the subscript x=1 is for the exposed steel and x=2 is for the aluminized surface, i_{0Cx} is the exchange current density for the cathodic reaction, C_S and C_B are the O_2 concentrations next to the steel surface and in the solution bulk, respectively, β_{Cx} is the cathodic Tafel slope, E_{eqcx} is the equilibrium potential for the O_2 reaction, and Φ_S is the local potential in the electrolyte adjacent to the equipotential metal surface. Per the above assumptions, the C_S/C_B ratio is equal to unity at the aluminized surface for the before and after E_{OC} drop.

Per Chapter 4, the prevalent anodic reactions for the first scenario were assumed to be uniform Fe dissolution $Fe \rightarrow Fe^{+2} + 2e^-$ at the exposed steel, and passive dissolution at the aluminized surface assumed to proceed at a potential-independent rate i_{P2}. The Fe dissolution reaction was assumed to be under activation-limited control, following simple Butler-Volmer kinetics.

Thus, the anodic current density at the exposed steel before the E_{OC} drop is given by:

$$i_{ax} = i_{0ax}\, 10^{\frac{\Phi_S - E_{eqax}}{\beta_{ax}}} \tag{5.2}$$

where the subscript x=1 is for the exposed steel, β_{ax} is the anodic Tafel slope, i_{0ax} is the exchange current density for the anodic reaction, and E_{eqax} is the equilibrium potential for the Fe/Fe^{+2} redox pair.

For the second scenario (after the E_{OC} drop), the rate of aluminum dissolution of the form $Al \rightarrow Al^{+3}+3e^{-}$ was expected to increase relative to before the E_{OC} drop, consistent with uniform discoloration of the aluminized surface noted at longer exposure times. To reflect the increase of the aluminum dissolution, it was assumed that the anodic aluminum reaction, no longer potential-independent, was under activation-limited control following simple Butler-Volmer kinetics. Then, for the second scenario the anodic current density at the aluminized surface is calculated per Eq. 5.2 substituting the subscript x=2.

At the steady-state regime, the constant σ and charge neutrality conditions imply that the potential in the electrolyte Φ for both scenarios can be stated in term of the Laplace's equation, expressed below in two dimensional cylindrical coordinates (West and Newman, 1992):

$$\frac{\partial^2 \Phi}{\partial z^2} + \frac{\partial^2 \Phi}{\partial r^2} + \frac{1}{r}\frac{\partial \Phi}{\partial r} = 0 \tag{5.3}$$

where z is the distance normal to the metal surface and r is the distance in the radial direction from the specimen center.

For both scenarios, next to the metal surface the net current density across the electrolyte must match the net rate of the electrochemical reactions. Thus, by the steel surface:

$$\sigma \cdot \left.\frac{\partial \Phi}{\partial r}\right|_{z=0} = i_{0a1}\, 10^{\frac{\Phi_S - E_{eqa1}}{\beta_{a1}}} - i_{0C1} \cdot \frac{C_S}{C_B} \cdot 10^{\frac{E_{eqc1} - \Phi_S}{\beta_{C1}}} \qquad (5.4\text{-A})$$

and by the aluminized surface:

$$\sigma \cdot \left.\frac{\partial \Phi}{\partial r}\right|_{z=0} = i_{0a2}\, 10^{\frac{\Phi_S - E_{eqa2}}{\beta_{a2}}} - i_{0C2}\, 10^{\frac{E_{eqc2} - \Phi_S}{\beta_{C2}}} \qquad (5.4\text{-B})$$

where the first term on the right hand side of the Eq. 5.4-B is equal to i_{P2} for the first scenario (before E_{OC} drop).

The remaining boundary conditions for both scenarios were provided by the lack of current density flow through all free surfaces such that:

$$\left.\frac{\partial \Phi}{\partial r}\right|_{r=0, r=r_e} = \left.\frac{\partial \Phi}{\partial z}\right|_{z=H} = 0 \qquad (5.5\text{-A})$$

and for the second scenario (after E_{OC} drop) the supply of O_2 at the exposed steel surface equaled to the amount of O_2 consumed by the cathodic reaction such that:

$$i_{C1} = n \cdot F \cdot D \cdot \left.\frac{dC}{dz}\right|_{\text{steel surface}} \qquad (5.5\text{-B})$$

for n=4 (by the reaction $O_2+2H_2O+4e^- \rightarrow 4OH^-$) and F=96,500 C/mol (Faraday constant).

5.2.1.1 Implementation of the *dc* Model

The solution to the *dc* problem consisted of finding the values of Φ at every point in the electrolyte by satisfying Eqs. (5.3-5.6) using a finite difference method. Figure 5.1 shows schematically the implementation of the *dc* model for the model system described in Section 5.2. To minimize the number of calculations while retaining good accuracy, a two dimensional cylindrical graded network with constant grid spacing in the radial Δr and normal Δz directions was generated following approach by Ozisik (1994). Other model features follow previous work by Kranc and Sagüés (1993) and Cui (2003). Per axial symmetry, only the region r>0 was modeled. For geometries matching the configuration of the LCB blemished specimens, Δr = 0.1 cm for a total of 50 nodes and Δz = 0.1 cm for a total of 65 nodes were adopted.

The implementation of the finite difference method was as follows. The normal derivative of the potential was represented using a two-node representation such that for the first scenario (before E_{OC} drop) by the steel surface is:

$$\Phi_{i,0} = \Phi_{i,1} + \frac{\Delta z}{\sigma}\left[i_{0C1} \cdot \frac{C_{i,0}}{C_B} \cdot 10^{\frac{E_{eqc1} - \Phi_{i,1}}{\beta_{C1}}} - i_{0a1} \cdot 10^{\frac{\Phi_{i,1} - E_{eqa1}}{\beta_{a1}}} \right] \qquad (5.6\text{-A})$$

and by the aluminized surface:

$$\Phi_{i,0} = \Phi_{i,1} + \frac{\Delta z}{\sigma}\left[i_{0C2} \cdot 10^{\frac{E_{eqc2} - \Phi_{i,1}}{\beta_{C2}}} - i_{P2} \right] \qquad (5.6\text{-B})$$

where $\Phi_{i,0}$ and $C_{i,0}$ correspond to the potential and O_2 concentration by the metal surface, respectively, and $\Phi_{i,1}$ and $C_{i,0}$ are the potential and O_2 concentration in

the electrolyte next to the metal surface. The subscript i here corresponds to the nodal points in the radial direction.

For the second scenario (after E_{OC} drop) by the steel surface, the normal derivative of the potential is:

$$\Phi_{i,0} = \Phi_{i,1} + \frac{\Delta z}{\sigma}\left[i_{0C1} \cdot 10^{\frac{E_{eqc1} - \Phi_{i,1}}{\beta_{C1}}} - i_{0a1} \cdot 10^{\frac{\Phi_{i,1} - E_{eqa1}}{\beta_{a1}}} \right] \tag{5.7-A}$$

and by the aluminized surface:

$$\Phi_{i,0} = \Phi_{i,1} + \frac{\Delta z}{\sigma}\left[i_{0C2} \cdot 10^{\frac{E_{eqc2} - \Phi_{i,1}}{\beta_{C2}}} - i_{0a2} \cdot 10^{\frac{\Phi_{i,1} - E_{eqa2}}{\beta_{a2}}} \right] \tag{5.7-B}$$

As stated above in the model assumptions, the O_2 transport at the exposed steel surface was assumed to follow simple linear diffusion with $\delta = \Delta z = 0.1$ cm typically found in stagnant solutions (Kaesche, 1985). Thus, in finite difference formulation, the O_2 concentration next to the steel surface is:

$$C_{i,0} = \frac{\frac{4FD \cdot C_{i,1}}{\Delta z}}{\frac{i_{0C1}}{C_B} \cdot 10^{\frac{E_{eqc1} - \Phi_{i,0}}{\beta_{C1}}} + \frac{4FD}{\Delta z}} \tag{5.8}$$

The representation of the boundary conditions at the external surfaces was carried out by creating a fictitious array of points of nodal point coordinates corresponding to the normal direction to each external surface. A symmetrical condition was applied to the grid network points located on the centerline so that $\Phi_{0,j} = \Phi_{1,j}$ where $\Phi_{0,j}$ are the potential of the grid network points located on the centerline in the direction normal to the metal surface and $\Phi_{1,j}$ are the potential of the points next to $\Phi_{0,j}$. The subscript j here is associated to the nodal points in the

z-direction to the metal surface. The symmetrical condition at the centerline obviates the need for otherwise addressing the singularity that may arise at r=0 from Eq. 5.3.

In the solution bulk, the potential values were estimated using a central difference scheme of the form:

$$\Phi_{i,j} = \frac{\dfrac{\Phi_{i,j+1}}{\Delta z^2} + \dfrac{\Phi_{i,j-1}}{\Delta z^2} + \Phi_{i+1,j}\left[\dfrac{1}{\Delta r^2} + \dfrac{1}{r_i \cdot \Delta r}\right] + \dfrac{\Phi_{i-1,j}}{\Delta r^2}}{\dfrac{2}{\Delta z^2} + \dfrac{2}{\Delta r^2} + \dfrac{1}{r_i \cdot \Delta r}} \tag{5.9}$$

The solution strategy adopted to numerically solve for Eqs. (5.6) to (5.9) made use of the Jacobi method (Burden and Faires, 1985). Such method consisted of assigning guess potential and O_2 concentration values everywhere in the solution to begin the iteration process. The guess values were placed in two arrays, one for potentials and the other for concentrations. New concentration values satisfying Eq. 5.8 were then computed from the guess arrays for each nodal point at the steel surface and stored in a companion concentration array. New potential values satisfying Eq. 5.6 (for the regime before E_{OC} drop) or Eq. 5.7 (for the regime after E_{OC} drop) were then computed, at each nodal point in the solution volume and at the boundaries, from the guess arrays except using the new values of concentration previously computed. Those new potential values were stored in a companion potential array. The companion potential and concentration array values were then used to overwrite the initial guess arrays. The process was then repeated using the overwritten guess array as the starting value. A relaxation factor α (typically with α=0.6) was used to

blend the potential value of each new generation with the previous one (Ketter and Prawel, 1969). This computation sequence was repeated for each new generation until a convergence criterion was met as shown in the next paragraph. Appropriate selection of the polarization kinetics parameters for the steel and for the aluminized components permitted obtaining the local *dc* current density for every node by the metal surface as shown below.

Figure 5.2 shows for a representative example that the computed total anodic and cathodic currents by the metal surface approached to a common terminal value as the number of iteration increased. The relative difference between the computed currents decreased to <1% after 10^5 iterations. This observation suggests that a reasonably small convergence error can be obtained after 10^5 iterations. As a result, for all model computations, a relative difference of 1% was used as a criterion to determine number of iterations needed to meet that value. All reported calculations involved at least 10^5 iterations.

5.2.1.2. Cases Studied

To examine the sensitivity to the *dc* current density and potential distributions, values of σ_{bc} = 2,000 μS/cm (base case), σ_1 = 200 μS/cm (case 1), and σ_2 = 10 μS/cm (case 2) were chosen for an exposed steel/aluminized surface area ratio A_R~0.03. The selected σ values correspond to natural waters of different aggressivity typically encountered in the invert of field metallic culvert pipes in Florida waters. The base case was chosen to represent conditions comparable to those used for experimental evaluation.

Experimental results obtained from the electrochemical measurements, where available, were used as inputs for the *dc* model. In the case of unknown polarization parameters, the following assumptions were made. Consistent with values reported in the literature, a nominal anodic Tafel slope for the steel β_{a1}=60 mV/dec (Kaesche, 1985) was assumed and i_{0a1} was chosen by adjusting its value to obtain i_{a1} that matched that obtained from the EIS measurements of the steel portion in the blemished specimens before and after the E_{OC} drop (see Chapter 4). The values of i_{0C1} and i_{0C2} were estimated consistent with the choice of the other polarization parameters. Values of D = 2 10^{-5} cm^2/sec, C_B = 3 10^{-7} mol/cm^3, and δ = 0.1 cm, representative of typical conditions in stagnant aerated systems (Kaesche, 1985), were selected. Those choices yielded a limiting current density $i_L = nFDC_B\delta^{-1}$ ~ 2.3 10^{-5} A/cm^2 for O_2 reduction on plain steel, which is also commonly observed in naturally aerated systems (Kaesche, 1985). The parameters used for the *dc* computations are summarized in Table 5.1.

5.2.2. The *ac* Model

The assumptions and configuration presented for the *dc* model are also applicable to the *ac* model. The metal surface was divided into small equal-sized elements and a local area-normalized impedance was assigned to each element. The value of the local impedance for each element was obtained from the local *dc* anodic and cathodic current densities, the area-normalized interfacial capacitance, and the geometry of the system. For simplicity, the interfacial

capacitance was taken as constant, but subject to frequency dispersion, for each metal component. Thus, the overall impedance for each element is given by:

$$Z_x(\omega) = \left[\frac{1}{Z_{ax}} + \frac{1}{Z_{Cx} + Zd_{Cx}(\omega)} + Y_x(j\omega)^{n_x} \right]^{-1} \quad (5.10)$$

where the subscript x=1 is for the bare steel and x=2 is for the aluminized surface, and Y and n are the CPE parameters representing the interfacial capacitance per unit area as defined in Chapter 2. The real components of the anodic and cathodic Faradaic impedances, envisioned here as simple resistors, are given by:

$$Z_{ax} = \left(2.3 \cdot \frac{i_{ax}}{\beta_{ax}} \right)^{-1} \quad \text{for the anodic reaction (5.11-A)}$$

$$Z_{Cx} = \left(2.3 \cdot \frac{i_{Cx}}{\beta_{Cx}} \right)^{-1} \quad \text{for the cathodic reaction (5.11-B)}$$

and the diffusional impedance component of the cathodic reaction at the exposed steel is (Sagüés (2006)):

$$Zd_{C1}(\omega) = \left[\frac{2.3}{\beta_{C1}} \cdot \frac{(i_L - i_{C1}) \cdot \sqrt{\left(j\omega \cdot \Delta z^2 \cdot D^{-1}\right)}}{\tanh\left(\sqrt{j\omega \cdot \Delta z^2 \cdot D^{-1}}\right)} \right]^{-1} \quad (5.11\text{-C})$$

To address the *ac* problem, a circuit consisting of a two-dimensional resistive network (Figure 5.3) representing the test solution for the system described in Section 5.2 was used. The values of the resistors in the network were obtained according to the system dimensions, the size of the solution element chosen, and σ. The complex impedance for the steel/aluminized coating system at each test frequency was then calculated as the ratio of the complex

potential, obtained at the location of the reference electrode sensing point, to the complex current density at the metal surface. Complex potentials and currents everywhere in the solution were computed following approach described in the next section.

5.2.2.1 Implementation of the *ac* Model

The approach presented in this Section is comparable to that used by Kranc and Sagüés (1993).

The model system was the same as that described in Section 5.2. Per axial symmetry, only the region for r>0 was modeled. The resistive network consisted of 10 resistors in the radial direction by 10 in the normal direction to the metal surface. At the solution bulk, the values of the vertical resistors were estimated as $R_V = dz\ (2\pi\ \sigma\ r\ dr)^{-1}$ and for the horizontal resistors $R_H = dr\ (2\pi\ \sigma\ r\ dz)^{-1}$ for dr = 0.50 cm and dz = 0.65 cm. At the centerline, $R_V = dz\ (\pi\ \sigma\ dr^2)^{-1}$ and $R_H = (\pi\ \sigma\ dz)^{-1}$ were established. Node equations were formulated for each point in the network by establishing a zero current balance for each node, considering the surrounding nodal points. This involved a total of 121 equations simultaneously solved using a Matlab® routine. The counter electrode was joined to the network at the upper surface by small resistors (1 Ω) to facilitate current computation. An *ac* voltage signal was then applied between the counter electrode and the metal.

Values of the admittance components for each surface element, obtained from the output of the *dc* model for the base case only, were calculated using Eq.

(5.11) following the assumptions presented in Section 5.2.1. Typical values of interfacial capacitance parameters n and Y for the aluminized and steel components were selected from previous Chapters and used here for the *ac* computations. Table 5.2 summarizes the set of parameters used for the *ac* model computations.

To examine possible non uniform *ac* current distribution on the impedance trends due to the reference electrode position, model computations were performed for reference electrode sensing tip position at three different distances from the center of the steel surface. The test frequency varied from 10^5 to 10^{-3} Hz in all cases.

5.3 Results and Discussion

5.3.1 The *dc* Model

Computed distributions of the *dc* current density and potential by the metal surface as a function of radius are shown for both scenarios (before and after E_{OC} drop) in Figures 5.4 to 5.6 for the base case and the variants shown in Table 5.1. The range of values of σ used as model input represented conditions bracketing solution conductivities commonly found in Florida inland waters, characterized by e.g. solutions P and NP. High σ as those found in natural seawater were not examined for the present set of computations.

For the first scenario (before E_{OC} drop), computation results showed little sensitivity of the anodic current density to the choice of solution conductivity (Figure 5.4). The largest and nearly constant anodic current density (~8.5

$\mu A/cm^2$) was at the exposed steel, decaying steeply to the assumed constant low anodic current density value (7 10^{-3} $\mu A/cm^2$) at the aluminized surface. The computation results were consistent with the observed i_{corr} obtained for the LCB specimens in e.g. solution P and also in agreement with the observation of uniform rust formation on the steel surface early on in the exposure, with no visual corrosion damage at the aluminized surface.

The cathodic current density for the first scenario (Figure 5.5) was greatest and nearly constant at the exposed steel (~9 $\mu A/cm^2$), and steeply decayed away from it, attaining a nearly constant value of ~9.2 10^{-4} $\mu A/cm^2$ at the aluminized surface. These results were consistent with the model assumptions and in agreement with the results obtained by cyclic polarization tests conducted on individual steel and unblemished aluminized steel specimens exposed to solutions P and NP. As before, computation results showed little sensitivity of the cathodic current density to the choice of solution conductivity.

Figure 5.6 shows the potential trends next to the metal surface as a function of radius for the first scenario. The computed potentials were nearly constant (~-715 mV) with radius with values slightly nobler at the exposed steel (~1-8 mV) for the selected σ values. The potentials for the base case were in agreement with the potential measurements recorded at several radial locations of the LCB specimens in solution P. Computations showed little sensitivity of the potential to the choice of solution conductivity.

Figure 5.7 shows the computed macrocell current as a function of σ for the first scenario (regime before the onset of the E_{OC} drop). For σ_{bc} = 2,000 μS/cm

(base case), the macrocell current was ~2 μA, in agreement with the experimental results obtained at early exposure times for the macrocell assemblies shown in Chapter 4. As expected, the macrocell currents decreased for decreasing values of σ. These results are consistent with attributing the weak galvanic action of the aluminized coating/exposed steel system early on in the exposure to the passive condition of the aluminized coating. That condition was also as manifested by large impedance moduli (>100 kΩ-cm^2) of the coating, which were exceedingly larger than those of the exposed steel (~2 kΩ-cm^2).

Figure 5.4 shows the computed anodic current density as a function of radius for all σ for the second scenario (after E_{OC} drop). For σ_{bc} = 2,000 μS/cm (base case), the nearly constant anodic current density at the exposed steel (~0.045 μA/cm^2) was approximately two orders of magnitude smaller than that obtained from the first scenario (before E_{OC} drop), in agreement with the proximity of the system potential to the equilibrium potential of the Fe/Fe^{+2} reaction, consistent with effective cathodic protection. However, increasingly larger anodic current densities at the exposed steel were noted for decreasing values of σ, suggesting limited cathodic protection in those cases. Interestingly, for σ_{bc} = 2,000 μS/cm (base case) and more noticeable for σ_1 = 200 μS/cm (case 1) and σ_2 = 10 μS/cm (case 2) the computed anodic current density at the central portion of the steel was largest (~0.45 and ~7.3 μA/cm^2 for cases 1 and 2, respectively) and smallest at the edge (~0.19 and ~2 μA/cm^2 for cases 1 and 2, respectively). The calculations are in agreement with the experimental observations of additional metal loss at the center spot of the exposed steel in

the LCB specimens exposed to solutions P and NP due to a local acidification at that spot as mentioned in detail in Chapter 4.

On the other hand, the anodic current density at the aluminized surface was largest near the steel perimeter and decreased away from the steel more noticeable for σ_1 = 200 μS/cm (case 1) and σ_2 = 10 μS/cm (case 2) and not so for σ_{bc} = 2,000 μS/cm (base case). This can be viewed as being consistent with a pH increase near the steel perimeter as a result of an enhancement of the cathodic reaction in that region. If the increase in pH is large enough, the aluminum adjacent to the steel can experience accelerated dissolution. This interpretation was confirmed by the observation of aluminized surface discoloration starting around the steel perimeter. The anodic current density computed for the aluminized portion away from the steel edge was ~1.2 μA/cm^2 for the base case and decreased slightly to ~1.0 μA/cm^2 for case 1 and to ~0.5 μA/cm^2 for σ_2 = 10 μS/cm (case 2). Those values were significantly larger than those obtained for the period before E_{OC} drop, in agreement with the observation of uniform aluminized discoloration of the LCB specimens in NP and P after the onset of the E_{OC} decay (see Chapter 4).

The cathodic current density at the exposed steel for the second scenario (after E_{OC} drop) (Figure 5.5) approached a limiting current density (~23 μA/cm^2) for all σ, in agreement with the assumption of full concentration polarization of the cathodic reaction and also consistent with the nearly straight line with slope ~0.5 (typical of a Warburg-like behavior) of the EIS spectrum obtained for the steel component in the coupled macrocell assemblies exposed to solutions NP and P

as shown in Figures 4.32 and 4.34 in Chapter 4. The cathodic current density at the aluminized surface for the second scenario (after E_{OC} drop) was considerably larger (~0.7 μA/cm^2 for all σ) than that obtained for the first scenario. The model results indicate that the aluminized surface, more specifically the Fe-rich inclusions present in the outer aluminized coating layer, becomes better cathodes than in the first scenario (before E_{OC} drop) as the system potential decreases to a constant value of ~-850 mV.

Figure 5.6 shows the potential next to the metal surface as a function of radius for the second scenario (after E_{OC} drop). The potential for the base case were nearly constant (~-850 mV) with radius and showed increasingly nobler potentials, as expected, at the exposed steel for decreasing values of σ (~-790 mV for case 1 and ~-720 mV for σ_2 = 10 μS/cm (case 2)), suggesting weak cathodic protection by the aluminized surface in extremely low conductivity environments as in case 2, especially near the central region of the steel.

Figure 5.7 shows the computed macrocell currents as a function of σ for the second scenario (after E_{OC} drop). The computed macrocell current was ~70 μA for the σ_{bc} = 2,000 μS/cm (base case), in agreement with the experimental results obtained from the macrocell assemblies as reported in Chapter 4. As expected, the macrocell currents decreased for decreasing values of σ. For the base case, the enhanced galvanic action noted for the second scenario compared to the first scenario may be related to the active corrosion of the aluminized surface, which provided nearly full galvanic protection to the exposed steel at those negative potentials.

5.3.2 The *ac* Model

The results for the *ac* model presented here represent only a preliminary evaluation step towards numerically obtaining the effect of non uniform *ac* current distribution on the EIS response in coupled aluminum/steel systems.

The results, obtained only for the base case before the E_{OC} drop, are presented as non normalized area impedance diagrams $Z_X(\omega)$ in the Nyquist form are shown in Figure 5.8 for the reference electrode placed at 0.5, 2.5, and 6.5 cm from the center of the steel surface. The EIS responses depended to some extent on the placement of the reference electrode sensing point, as the low frequency impedance limits tended to become smaller as the reference electrode was placed closer to the metal surface. But more importantly, a striking feature of the calculated impedance behavior was the presence of a conspicuous small diameter loop observable at the high frequency end as the reference electrode was placed further away from the metal surface and less noticeable otherwise.

For comparison, Figure 5.8 also shows a curve (A) representing the EIS response calculated using the same *ac* input parameters as for the other curves but assuming that the electrolyte resistance does not have any effects on the *ac* current and potential distributions, that is, all surface elements are subject to a uniform *ac* potential. The impedance response for curve (A) can then be computed by Eq. 5.10 for the integrated impedance of the steel/aluminized system in series with an effective solution resistance. Notably, the impedance response for curve (A) did not show the high frequency arc. In light of this, the

high frequency feature can indeed be attributed to a non uniform *ac* current distribution artifact that likely resulted in *ac* current constriction near the steel region at the low frequencies as detailed in Kranc and Sagüés (1993).

The overall EIS response computed by the *ac* model (for the reference electrode sensing tip located at distance from the metal surface comparable to that used in practice) was in close agreement with those obtained from the LCB specimens exposed to solutions NP and P for the period before the E_{OC} drop (Chapter 4). However, the small high frequency end loop, obtained by the model, was not observed experimentally, indicative of negligible uneven *ac* current distribution effect for the test conditions used. A possible explanation for this discrepancy is that due to the size of the reference electrode used for the experimental tests, the measured potentials, and consequently currents too, were sensed on a much broader region than that assumed by the model, resulting in average potential values over a much larger space. To corroborate if this is indeed the cause, additional experiments should be conducted using small size reference electrodes placed at various locations from the metal surface.

5.4. Conclusions

1. At E_{OC}~-700 mV (potential regime before the onset of the E_{OC} drop), the *dc* model calculations were in close agreement with the experimental results. The computations indicated slight dependence of the potential along the metal surface with solution conductivity. The *dc* model yielded small macrocell currents with larger anodic current density at the active steel

compared to that at the passive aluminized surface, consistent also with experimental observation.

2. At E_{OC}~-850 mV (potential regime after the onset of the E_{OC} drop), the *dc* model calculations were also in good agreement with the experimental observations. The model results showed a strong dependence of the potential and current distributions along the metal surface with solution conductivity. As expected, the active aluminized coating polarized the exposed steel to a potential close to the Fe/Fe^{+2} equilibrium potential, providing a nearly full galvanic protection to the steel for σ_{bc} = 2,000 μS/cm (base case). However, increasingly larger anodic current densities at the exposed steel were noted for decreasing values of σ, suggesting limited cathodic protection. In those cases, the anodic current density at the central portion of the steel was largest and smallest at the edge, in agreement with the experimental observations.
3. The *ac* model results indicated that the impedance response can be sometimes complicated to evaluate due to the presence of uneven *ac* current distribution which may lead, if not properly identified, to a misinterpretation of the impedance response. In the present system, the effect of non uniform *ac* currents was relatively small and usually not evident in the experimental results. However, caution is needed when proposing analog equivalent circuits to avoid misinterpretation.

Table 5.1: Computation parameters used for the *dc* model for all σ evaluated.

Parameter	First scenario (before E_{OC} drop)	Second scenario (after E_{OC} drop)
E_{eqa1} / V	-0.90	
E_{eqa2} / V	-	-1.50
E_{eqc1} / V	0.50	
E_{eqc2} / V	0.50	
i_{0a1} / A cm^{-2}	7 10^{-9}	
i_{0a2} / A cm^{-2}	-	5 10^{-13}
i_{0C1} / A cm^{-2}	10^{-15}	
i_{0C2} / A cm^{-2}	7 10^{-16}	5 10^{-14}
i_{P2} / A cm^{-2}	7 10^{-9}	-
β_{a1} / mV dec^{-1}	60	
β_{a2} / mV dec^{-1}	-	100
β_{C1} / mV dec^{-1}	120	
β_{C2} / mV dec^{-1}	200	

Table 5.2: Computation parameters used for the *ac* model for the base case.

Y_1 sec^n Ω^{-1}	Y_2 sec^n Ω^{-1}	n_1	n_2	R_{a1} Ω-cm^2	R_{C1} Ω-cm^2	R_{a2} Ω-cm^2	R_{C2} Ω-cm^2
3 10^{-3}	5 10^{-4}	0.75	0.95	3.24E+03	6.06E+03	6.20E+08	1.02E+08

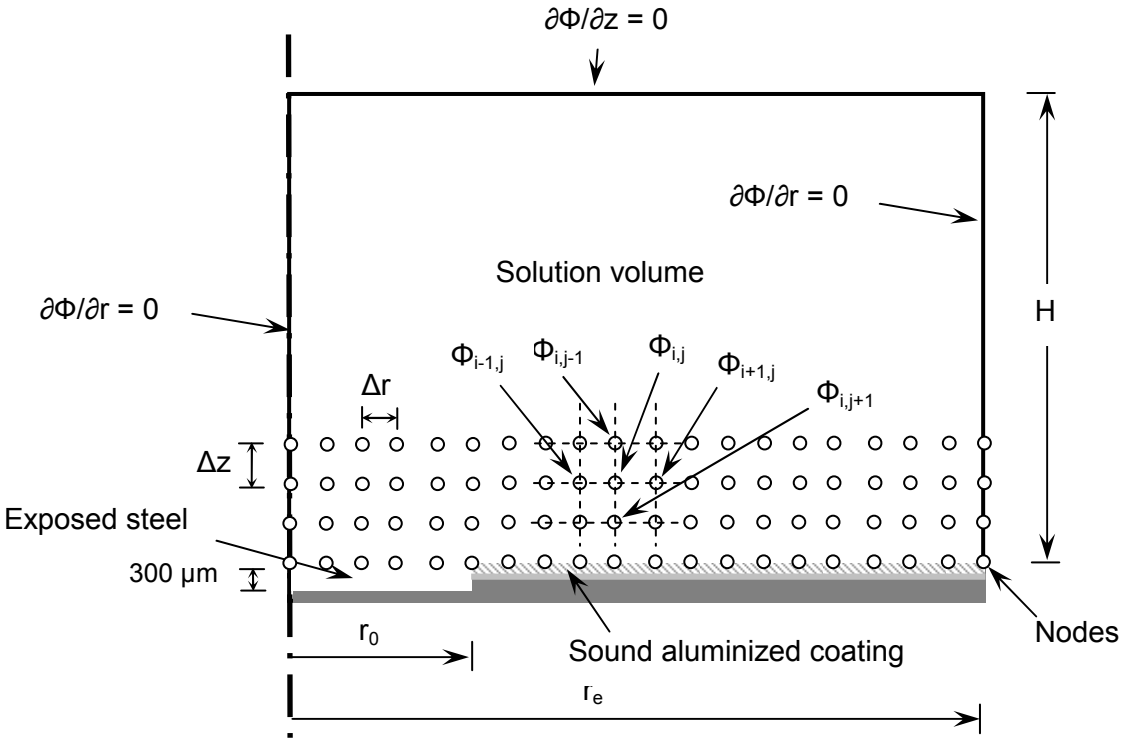

Figure 5.1: Schematic of half portion of the LCB specimen (of dimensions r_0 = 1 cm, r_e = 5 cm, and H = 6.5 cm) and the two-dimensional cylindrical graded network used for the model implementation ($\Delta r = \Delta z$ = 0.1 cm).

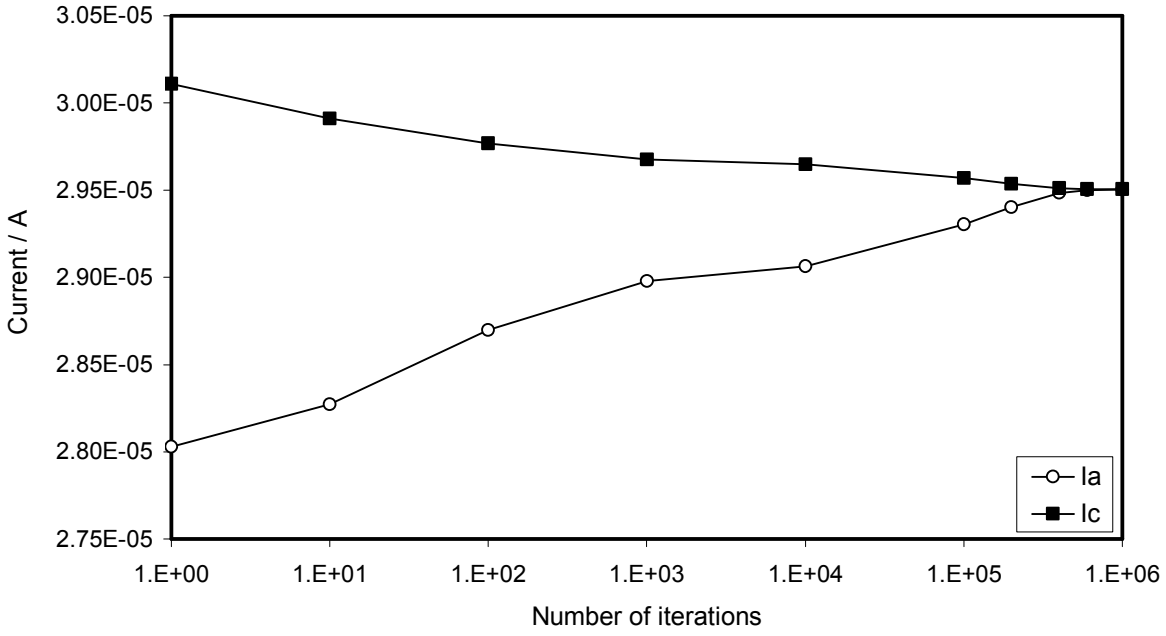

Figure 5.2: Change of the total anodic and cathodic currents I_a and I_C respectively, with the number of iterations showing convergence of the *dc* model. The calculations are for the case 1 (200 µS/cm), starting potential values = -717 mV, relaxation factor α = 0.6, and starting O_2 concentration = 3 10^{-7} mol/cm^3.

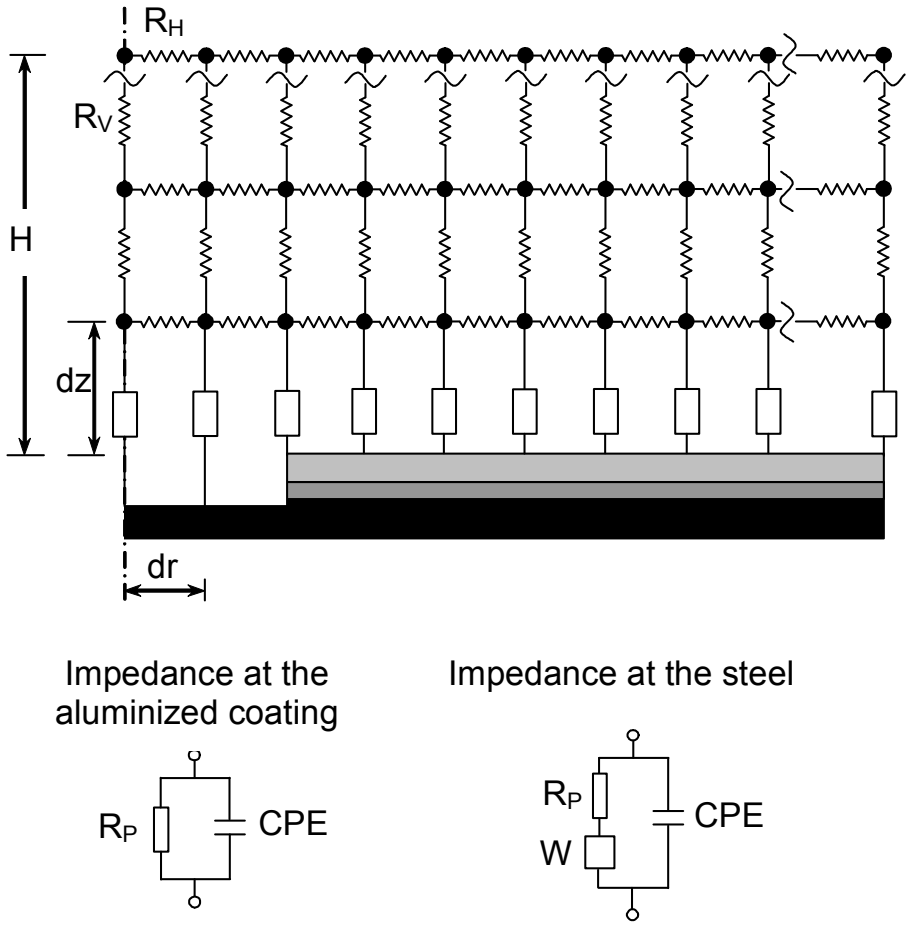

Figure 5.3: Representation of the *ac* model implementation to the LCB specimen configuration.

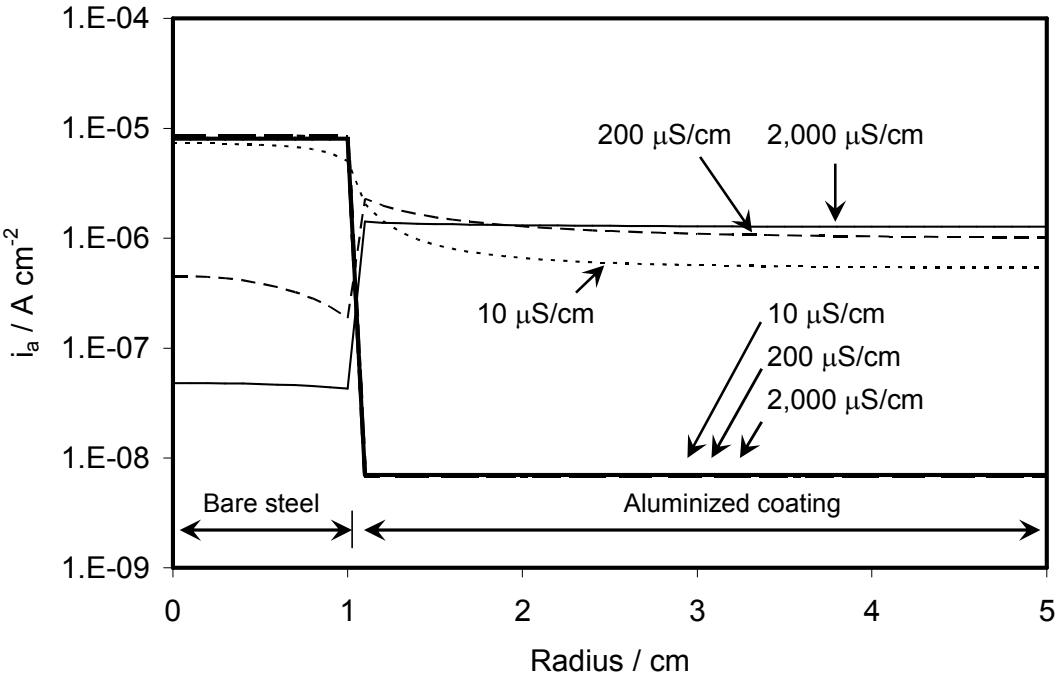

Figure 5.4: Anodic current density distribution as a function of radius (— base case (2,000 μS/cm), ---- case 1 (200 μS/cm), ···· case 2 (10 μS/cm)). Bold and light lines correspond to the period before and after the E_{OC} drop, respectively.

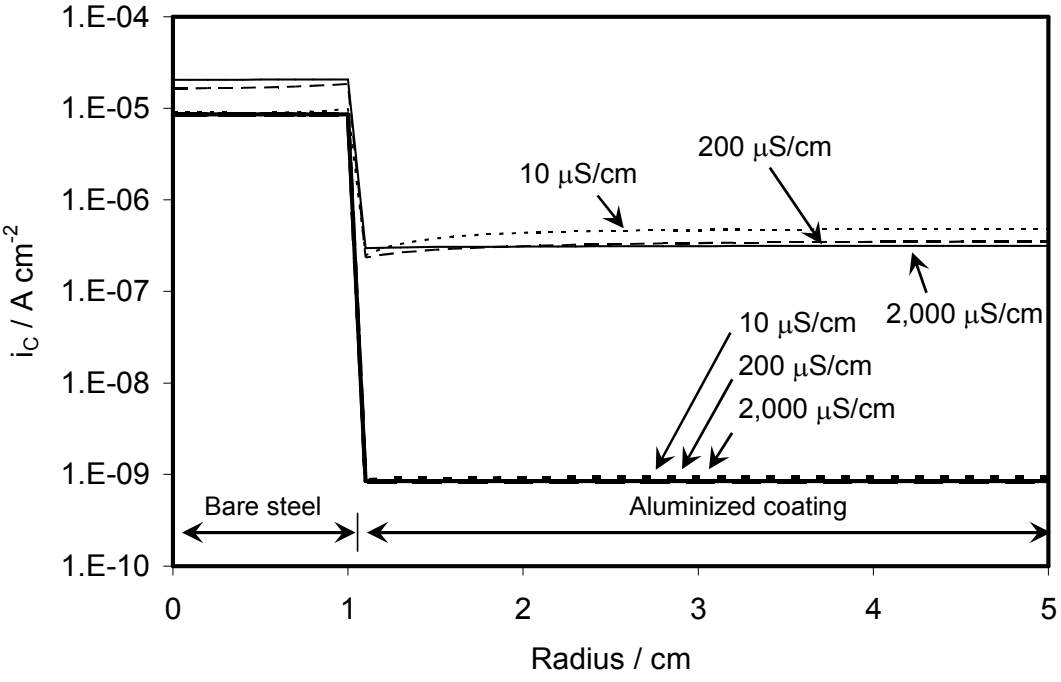

Figure 5.5: Cathodic current density distribution as a function of radius (— base case (2,000 μS/cm), ---- case 1 (200 μS/cm), ···· case 2 (10 μS/cm)). Bold and light lines correspond to the period before and after the E_{OC} drop, respectively.

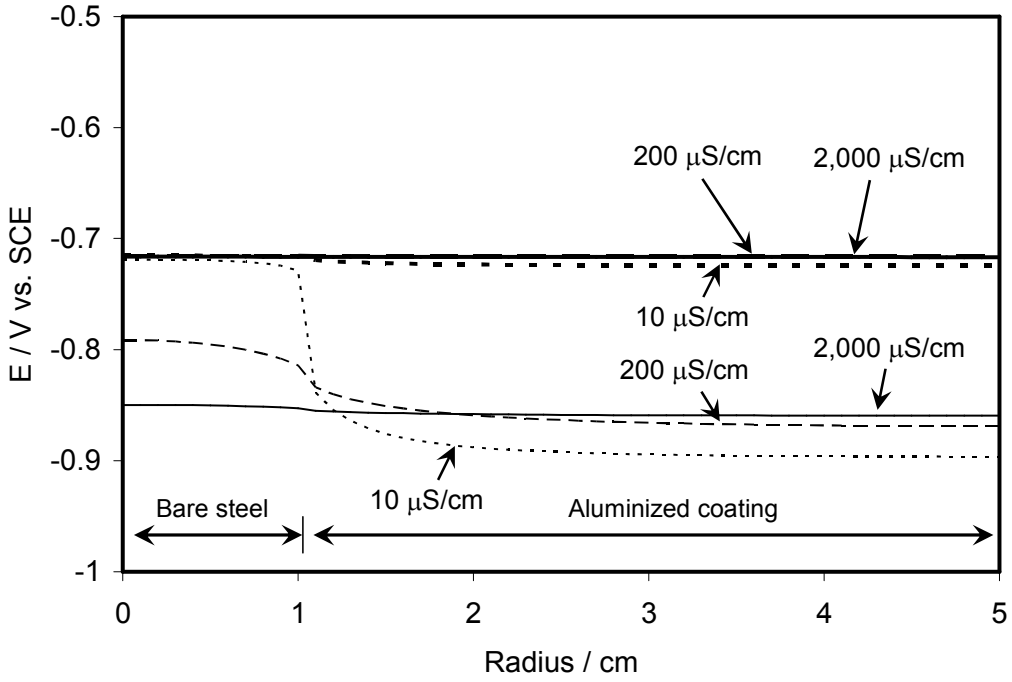

Figure 5.6: Potential distribution next to the metal surface as a function of radius. (— base case (2,000 μS/cm), ---- case 1 (200 μS/cm), ···· case 2 (10 μS/cm)). Bold and light lines correspond to the period before and after the E_{OC} drop, respectively.

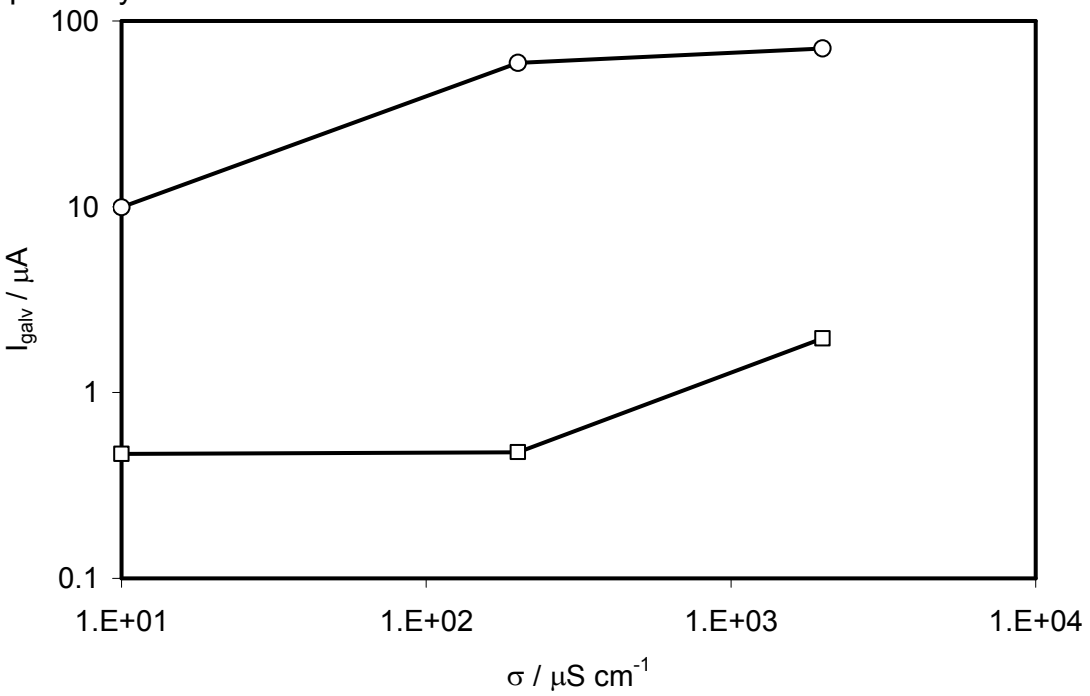

Figure 5.7: Computed macrocell currents I_{galv} as a function of σ for the first scenario (squares), before E_{OC} drop, and the second scenario (circles), after E_{OC} drop.

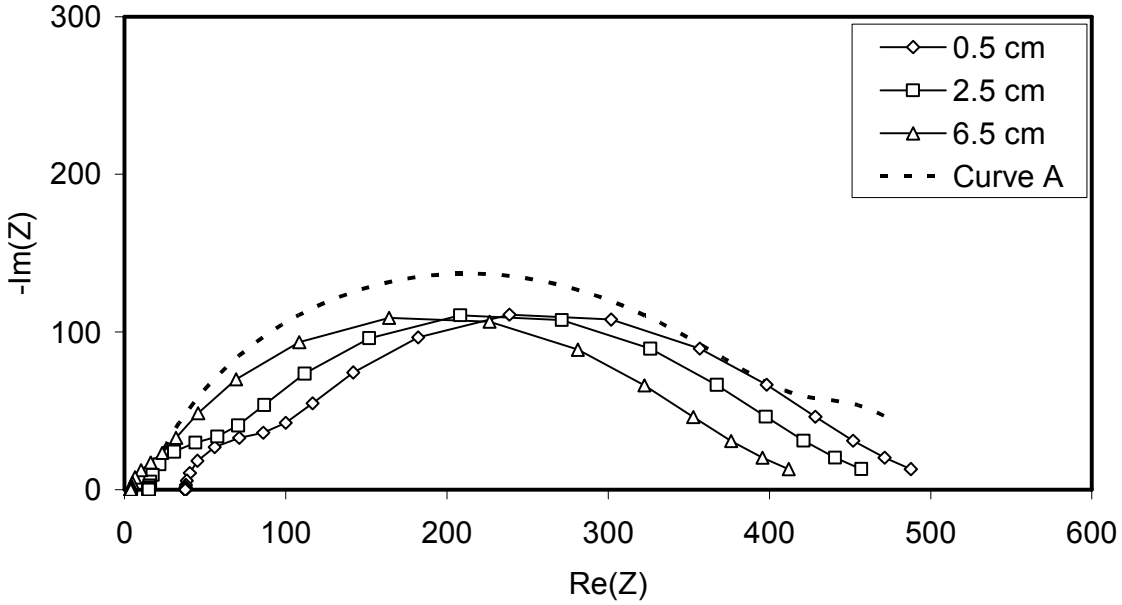

Figure 5.8: Calculated impedance shown as Nyquist diagrams for the base case for the three reference electrode positions measured from the center of the exposed steel surface (test frequency range: 10^5 to 10^{-3} Hz and 5 points per decade). Curve (A) was obtained by assuming that all surface elements in the network are subject to a uniform *ac* potential.

Chapter 6

Conclusions

The following conclusions can be drawn from this investigation:

1. For aluminized steel Type 2 without mechanical coating damage, long-term exposures in an environment with ~370 ppm chloride concentration but of high carbonate precipitating tendencies (solution P) resulted in extremely low nominal corrosion rates throughout the exposure, reaching <~0.08 μm/yr near the end. In an environment with high total alkalinity, but non-scale forming medium (solution NP), low/moderate nominal corrosion rates <~1 μm/yr were recorded for most of the test exposure increasing to ~2.2 μm/yr near the end, concurrent with the appearance of moderate uniform discoloration and increase in solution pH. In solutions of low total alkalinity and carbonate scaling tendency (solution C), early pitting followed by strong discoloration, associated with a high solution pH, were noted attaining nominal corrosion rates of ~1.3 μm/yr near the end of exposure. Tests using simulated ocean water (solution SW) of ~20,000 ppm chloride concentration revealed early formation of small pits as well as light uniform discoloration with nearly constant nominal corrosion rates of ~3 μm/yr throughout the test

exposure. Pits and surface discoloration in all cases appeared to be limited to the outer aluminized coating layer.

2. Tests conducted on aluminized steel Type 2 with coating breaks to expose the base steel (steel/aluminized area ratios A_R of ~0.03 and ~3 10^{-4}) confirmed that aluminized coating acted as an anode (and the exposed steel a cathode), providing galvanic protection to the base steel in all solutions. However, initial corrosion of the exposed steel was noted in solutions of high alkalinity and moderate chloride content with or without positive precipitating tendency, indicative of weak galvanic action early on in the exposure. Galvanic protection to the exposed steel in ocean water and in some tests in solution of moderate chloride content with low alkalinity and precipitating tendency developed early on in the exposure since little to none corrosion distress was observed at the exposed steel.
3. Integrated corrosion loss on selected blemished and unblemished specimens, computed using the corresponding analog equivalent circuits were in reasonably agreement with direct thickness measurements, supporting the validity of the impedance models chosen.
4. The results for blemished/macrocell specimens have trends that extrapolated reasonably to the limit case of unblemished aluminized surfaces (A_R=0). In that limit, the active aluminized surface condition was never reached in solution P during the 3,000 hr test. However, active conditions developed on the unblemished aluminized surfaces in the more aggressive media after

incubation times comparable to those encountered for the specimens with A_R~3 10^{-4}.

5. For the blemished and unblemished specimens experiencing aluminized surface corrosion in all test solutions except for the simulated seawater, uniform strong/moderate surface discoloration appeared to be the primary form of corrosion, while the small isolated macro pits played a secondary role. In simulated seawater, macro pitting corrosion appeared to be the primary form of corrosion. The macroscopically uniform nature of the corrosion may be a manifestation of micro pits at the scale of the finely distributed Fe-rich inclusions present in the outer aluminized coating layer. The mechanism of activation of the aluminized layer may involve local alkalinization from enhanced cathodic reaction at the inclusions (especially in the low buffering capacity solution C), which would activate aluminum in the form of micro pits at the scale of the finely distributed inclusions present in the outer aluminized coating layer. Alkalinization may have been greater next to the exposed steel region for the blemished specimens due to enhanced O_2 reduction rates there, consistent with experimental observations.
6. The impedance response for passive aluminized surface can be described by coupled cathodic reactions taking place at the Fe-rich inclusions (for the unblemished condition) and mainly at the exposed steel for the blemished case, where surface coverage by an intermediate adsorbate alters the rate of the next step. For active aluminized surface, the high frequency impedance response was dominated by the thinning or more defective aluminum oxide

film capacitance in parallel with the local ohmic resistance of all micro and macro active pits. The low frequency impedance response was mainly dominated by the discrete Faradaic polarization resistance in parallel with the interfacial capacitance at all active pits.

7. Nominal durability projections made for 16-gage unblemished aluminized steel Type 2 were >100 yr for solution P, and between 15 and 36 yr for the other media. However, for aluminized steel Type 2 with largest preexisting coating break projected durability was as low as 10 yr for solution P. For the other media, durability projections for specimens with preexisting coating breaks were between 16 and 33 yr. The results obtained in this investigation may be used as a first step in proposing refinements of presently used durability guidelines of aluminized steel Type 2 culvert pipe based on environmental composition.
8. The present findings would support retaining for the unblemished condition the present FDOT guidelines regardless of scaling tendency for environments with moderately low resistivity such as those used in the tests (e.g. ~500 Ω-cm to ~1,000 Ω-cm) and neutral to mildly alkaline conditions (e.g. ~7.5<pH<~9.0). However, for blemished aluminized steel in those same environments the results suggest that the AK Steel method may be a more appropriate alternative. The results also support exploring the use of alternative guidelines such as the AISI method for both unblemished and blemished conditions in environments with extremely high chloride contents (e.g. resistivity <50 Ω-cm) and nearly neutral pH. Eventual changes in

existing guidelines should consider not only the specific results of this investigation but also the entirety of the performance record of aluminized pipe. In addition, other corrosion processes, such as MIC, should be considered for possible inclusion in future forecasting methods.

9. The corrosion distribution in blemished coatings was investigated using 2-D *dc* and *ac* models. The *dc* model results matched well experimental trends. The *dc* model permitted to obtain corrosion rate information of the individual steel and aluminized components for solution conductivities σ beyond those examined experimentally. The *dc* results for the period before the E_{OC} drop indicated slight dependence of the potential along the metal surface with the σ values evaluated and the largest corrosion rates at the exposed steel. At more negative E_{OC} values and for the largest σ, corrosion rates at the steel were smallest, consistent with effective cathodic protection. However, increasingly larger corrosion rates at the steel were noted for decreasing values of σ, suggesting limited cathodic protection. In those cases, the corrosion rates at the central steel portion were distinctly larger than at the steel perimeter, in agreement with experiments. Before E_{OC} drop, the computed macrocell currents were smaller than those computed after E_{OC} drop, consistent with activation of the aluminized surface and nearly full cathodic protection of the exposed steel.
10. The *ac* model results indicated that the exposed steel received relatively lower *ac* current at the high frequencies, which led to the appearance of an additional loop in the impedance diagram. However, the effect was relatively

small and normally not evident in the present experimental results. Nevertheless, this possible effect should be considered when exploring other system conditions.

11. Tests conducted to study the cathodic behavior of unblemished aluminized steel Type 2 showed no conclusive evidence on the dominant cathodic reaction taking place at the Fe-rich inclusions. However, experimental results (e.g. change in open circuit potentials upon solution deaeration) permitted to speculate that O_2 reduction was the main reaction at potential of ~-900 mV and H_2 evolution reaction took over at more negative potentials. Tests also showed that for the smallest scan rate examined (0.05 mV/sec) a significant hysteresis existed between the cathodic current densities for the forward and reverse scans. The amount of hysteresis decreased for increasing scan rates (0.5 and 1 mV/sec) associated to the amount of Fe^{+2} ions being deposited during polarization. The results obtained from a simplified quantitative model were in reasonable agreement with the experimental results.

References

An J., Liu Y.B., Sun D.R. (2001), Mechanism of Bonding of Al–Pb Alloy Strip and Hot Dip Aluminised Steel Sheet by Hot Rolling, Materials Science Technology 17, pp. 451-454.

Armstrong R.D., Edmondson K. (1973), Impedance of Metals in the Passive and Transpassive Regions, Electrochimica Acta 18, pp. 937-943.

Armstrong R.D., Braham V.J. (1996), The Mechanism of Aluminum Corrosion in Alkaline Solutions, Corrosion Science 38, pp. 1463-1471.

ASM Metals Handbook (1972), Vol. 7: Atlas of Microstructures of Industrial Alloys, 8th Ed. Metals Park, OH, p.12.

Augustynski J., Frankenthal R.P., Kruger J. (Eds.) (1978), Proceedings of the Fourth International Symposium on Passivity, The Electrochemical Society, Pennington, NJ.

Ault J.P., Ellor J.A. (1996), Durability Analysis of Aluminized Type 2 Corrugated Metal Pipe, FHWA-RD-97-140, Federal Highway Administration.

Barchiche C., Deslouis C., Festy D., Gil, O. , Refait P., Touzain S., Tribollet B. (2003), Characterization of Calcareous Deposits in Artificial Seawater by Impedance Techniques - 3-Deposit of $CaCO_3$ in the Presence of Mg(II), Electrochimica Acta 48, pp. 1645-1654.

Bard J., Faulkner R. (2000), Electrochemical Methods, Fundamentals and Applications, Wiley, New York.

Beaton J.L., Stratfull R.F. (1962), Field Test for Estimating the Service Life of Corrugated Metal Pipe Culverts, State of California, Department of Public Works.

Bednar L. (1989), Galvanized Steel Drainage Pipe Durability Estimation with a Modified California Chart, Paper No. 88-0341, 68th Annual meeting, Transportation Research board, Washington, D.C.

Bednar L. (1993), Updated Environmental Limits for Aluminized Steel Type 2 Pipe Application, Transportation Research Record 1393, pp. 193-198.

Bednar L. (1998), Update of the Status of field Durability Studies on Aluminized Type 2 Drainage Pipe: Qualifying Durability of Aluminized Type 2 and Clarifying Related Issues, AK Steel research interim document.

Berzins A., Lowson R.T., Mirans K.J. (1977), Aluminum Corrosion Studies. III.Chloride Adsorption Isotherms on Corroding Aluminum, Australian Journal of Chemistry 30, pp.1891-1903.

Bessone J., Mayer C., Juttner K., Lorenz W.J. (1983), ac-Impedance Measurements on Aluminum Barrier Type Oxide Films, Electrochimica Acta 28, pp. 171.

Bessone J.B., Salinas D.R., Mayer C.E., Ebert M., Lorenz W.J. (1992), An EIS Study of Aluminium Barrier-Type Oxide Films Formed in Different Media, Electrochimica Acta 37, pp. 2283.

Bjoergum A., Sigurdsson H., Nisancioglu K. (1995), Corrosion of Commercially Pure Al 99.5 in Chloride Solutions Containing Carbon Dioxide, Bicarbonate, and Copper Ions, Corrosion 51, pp. 544-557.

Bockris J.O'.M., Kang Y. (1997), Journal Solid Sate Electrochemistry 1, pp. 17.

Bockris J.O'M., Reddy A.K.N. (1970), Modern Electrochemistry, Plenum, New York.

Bohni H., Uhlig H.H. (1969), Environmental Factors Affecting the Critical Pitting Potential of Aluminum, Journal of Electrochemical Society 116, pp. 906.

Bouche K., Barbier F., Coulet A. (1998), Intermetallic Compound Layer Growth Between Solid Iron, Materials Science and Engineering A 249, pp. 167-175.

Burden R., Faires J. (1985), Numerical Analysis, PWS-KENT Pub, Boston, pp. 402-403.

California Test 643 (1999), Method for Estimating the Service Life of Steel Culverts, Department of Transportation, State of California, Business, Transportation and Housing Agency.

Caseres L., Sagüés A.A. (2005), Corrosion of Aluminized Steel in Scale-Forming Waters, Corrosion/05, Paper no. 05348.

Castro P., Sagüés A.A., Moreno E.I., Maldonado L., Genesca J. (1996), Characterization of Activated Titanium Solid Reference Electrodes for Corrosion Testing of Steel in Concrete, Corrosion 52, p. 609.

Cerlanek W.D., Powers R.G. (1993), Drainage Culvert Service Life Performance and Estimation, State of Florida Department of Transportation Report No. 93-4A.

Chao C.Y., Lin L.F., MacDonald D.D. (1981), A Point Defect Model for Anodic Passive Films, Journal of Electrochemical Society 128, pp. 1187-1194.
Natishan P.M., McCafferty E. (1989), The Mechanism of Blister Formation and Rupture in the Pitting of Ion-Implanted Aluminum, Journal of Electrochemical Society 136, pp. 53-58.

Chu D., Savinell R. (1991), Experimental Data on Aluminum Dissolution in KOH Electrolytes, Electrochimica Acta 36, pp. 1631-1638.

Creus J., Mazille H., Idrissi H. (2000), Porosity Evaluation of Protective Coatings Electrodeposited on Steel, Surface and Coatings Technology 130, pp. 224-232.

Cui F. (2003), Corrosion Behavior of Stainless Steel Clad Rebar, Ph.D. Dissertation, University of South Florida.

Davis J.R. (1999), Corrosion of Aluminum and Aluminum Alloys, ASM International Materials Park, OH.

De Gryse R., Gomes W.P., Cardon F., Vennik J. (1975), On the Interpretation of Mott-Schottky Plots Determined at Semiconductor/Electrolyte Systems, Journal of Electrochemical Society 122, pp. 711-712.

De Levie R. (1967), Electrochemical Response of Porous and Rough Electrodes, in: P. Delaney, Ch.W. Tobias (Eds.), Advances in Electrochemical Engineering 6, Wiley, New York.

De Wit J.H.W., Lenderink H.J.W. (1996), Electrochemical Impedance Spectroscopy as a Tool to Obtain Mechanistic Information on the Passive Behaviour of Aluminum, Electrochimica Acta 41, pp. 1111-1119.

Diggle J.W. (1972), Oxides and Oxide Films, Vol. 1, Dekker, New York.

Doche M.L., Rameau J.J., Durand R., Novel-Cattin F. (1999), Electrochemical Behaviour of Aluminum in Concentrated NaOH Solutions, Corrosion Science 41, pp. 805-826.

Emregul K.C., Abbas Aksut A. (2000), The Behavior of Aluminum in Alkaline Media, Corrosion Science 42, pp. 2051-2067.

Epelboin I., Keddam M. (1970), Faradaic Impedances: Diffusion Impedance and Reaction Impedance, Journal of Electrochemical Society 117, pp. 1052-1056.

Evans U. R. (1926), Metal Ind. B, p. 481.

Morrison S.R. (1980), Electrochemistry at Semiconductor and Oxidized Metal Electrodes, Plenum Press, New York.

Fernandes J.C.S., Picciochi R., Da Cunha Belo M., Moura e Silva T., Ferreira M.G.S., Fonseca I.T.E. (2004), Capacitance and Photoelectrochemical Studies for the Assessment of Anodic Oxide Films on Aluminium, Electrochimica Acta 49, pp. 4701-4707.

Foley R.T. (1986), Localized Corrosion of Aluminum Alloys—A Review, Corrosion 42, p. 277.

Frankel G.S. (1998), Pitting Corrosion of Metals - A Review of the Critical Factors Journal of Electrochemical Society 145, pp. 2186-2198.

Furuya S., Soga N. (1990), Method for the Pitting Potential and Repassivation Potential in Crevice Corrosion of Aluminum Alloys, Corrosion 46, pp. 989-993.

Gartland P.O. (1987), Cathodic Protection of Aluminum–Coated Steel in Sea Water, Materials Performance 26, pp. 29-36.

Godard H.P., Jepson W.B., Bothwell M.R., Kane R.L. (1967), The Corrosion of Light Metals, John Wiley & Sons, Inc., New York.

Gundensen R., Nisancioglu K. (1990), Cathodic Protection of Aluminum in Seawater, Corrosion 46, pp. 279-285.

Hoar T.P., Mears, D.C., Rothwell, G.P. (1965), The Relationships between Anodic Passivity, Brightening and Pitting, Corrosion Science 5, pp. 279-289.

Handbook of Steel Drainage & Highway Construction Products (1994), American Iron and Steel Institute (AISI), Washington, DC.

Highway Design Manual, Section 850-13 (2006), California Department of Transportation, State of California.

Hoch G.M. (1974), Localized Corrosion, in: R. Staehle, B. Brown, J. Kruger, A. Agrawal (Eds.), NACE, Houston, Texas, pp. 134.

Hsu C.H., Mansfeld F. (2001), Technical Note: Concerning the Conversion of the Constant Phase Element Parameter Y_0 into a Capacitance, Corrosion 57, pp. 747-748.

Hunter M.S., Fowle P. (1956), Natural and Thermally Formed Oxide Films on Aluminum, Journal of Electrochemical Society 103, pp. 482-485.

Jakab M.A., Little D.A., Scully J.R. (2005), Experimental and Modeling Studies of the Oxygen Reduction Reaction on AA2024-T3, Journal of Electrochemical Society 152, B311-B320.

Johnsson T., Nordhag L. (1984), Corrosion Resistance of Coatings of Aluminum, Zinc and their Alloys: Results of four Years' Exposure, Interfinish.

Johnson W.K. (1971), Recent Developments in Pitting Corrosion of Aluminum, British Corrosion Journal 6, pp. 200-204.

Kaesche H. (1962), Z. Phys. Chem., Neue Folge 34, pp. 87.

Kaesche H. (1985), in Metallic Corrosion, pp. 166, National Association of Corrosion Engineers, Houston.

Kaesche H. (1974), Localized Corrosion, in: R. Staehle, B. Brown, J. Kruger, A. Agrawal (Eds.), NACE, Houston, Texas, pp. 516.

Kepaptsoglou D.M., Svec P., Janickovic D., Hristoforou E. (2007), Evolution of Lattice Parameter and Process Rates during Nanocrystallization of Amorphous Fe–Co–Si–B Alloy, Journal of Alloys and Compounds, Volumes 434-435, pp. 211-214.

Ketter R.L., Prawel S.P. (1969), Modern Methods of Engineering Computation, McGraw-Hill, Inc., New York.

Kimoto H. (1999), Corrosion Engineering 48, p. 579.

Kolics, A., Besing S., Baradlai P., Haasch R., Wieckowski A. (2001), Interaction of Chromate Ions with Surface Intermetallics on Aluminum Alloy 2024-T3 in NaCl Solutions, Journal of Electrochemical Society 148, pp. B251-B259.

Kranc S.C., Sagüés A.A. (1993), Calculation of Extended Counter Electrode Polarization Effects on the Electrochemical Impedance Response of Steel in Concrete, in Electrochemical Impedance: Interpretation and Analysis, ASTM STP 1188, D.C. Silverman, J.R. Scully and M.W. Kendig, Eds., p.365, American Society for Testing and Materials, Philadelphia.

Kranc S.C., Sagüés A.A. (1993), Polarization Current Distribution and Electrochemical Impedance Response of Reinforced Concrete When Using Guard Ring Electrodes, Electrochimica Acta 38, pp. 2055-2061.

Lasia A. (1999), in: Modern Aspects of Electrochemistry, 32, R.E. White, B.E. Conway, J.O'M. Bockris Eds., Kluwer Academic/Plenum Publishers, New York.

Lee W., Pyun S. (1999), Effects of Hydroxide Ion Addition on Anodic Dissolution of Pure Aluminum in Chloride Ion-Containing Solution, Electrochimica Acta 44, pp. 4041-4049.

Legault R.A., Pearson V.P. (1978), Kinetics of the Atmospheric Corrosion of Aluminized Steel, Corrosion 34, pp. 344-348.

Li W., Liu S., Huang Q., Gu M. (2003), Hot Dipped Aluminising (HDA) of a Low Carbon Steel Wire, Materials Science and Technology 19, pp. 1025-1028.

Lorenz W.J., Mansfeld F. (1981), Determination of Corrosion Rates by Electrochemical DC and AC Methods, Corrosion Science 21, pp. 647-672.
MacDonald D.D., Real S., Smedley S.I., Urquidi-MacDonald M. (1988), Evaluation of Aluminum-Air Batteries, Journal of Electrochemical Society 135, pp. 2410.

Mansfeld F., Lin S., Kim S., Shih H. (1990), Pitting and Passivation of Al Alloys and Al-Based Metal Matrix Composites, Journal of Electrochemical Society 137, pp. 78-82.

McCafferty E. (1995), The Electrode Kinetics of Pit Initiation on Aluminum, Corrosion Science 37, pp. 481.

McCafferty E. (2003), Sequence of Steps in the Pitting of Aluminum by Chloride Ions, Corrosion Science 45, pp. 1421-1438.

McCafferty E. (1974), Electrochemical Behavior of Iron within Crevices in Nearly Neutral Chloride Solutions, Journal of Electrochemical Society 121, pp. 1007.

Moon S., Pyun S. (1998), Faradaic Reactions and Their Effects on Dissolution of the Natural Oxide Film on Pure Aluminum during Cathodic Polarization in Aqueous Solutions, Corrosion 54, pp. 546-552.

Morris G.E., Bednar L. (1998), Comprehensive Evaluation of Aluminized Steel Type 2 Pipe Field Performance, Published by AK Steel Corporation, Middletown, Ohio.

Newman J. (1966), Resistance for Flow of Current to a Disk, Journal of Electrochemical Society 113, pp. 1235-1241.

Nguyen T.H., Foley R.T. (1979), On the Mechanism of Pitting of Aluminum, Journal of Electrochemical Society 126, pp. 1855.

Nisancioglu K., Davanger K.Y., Strandmyr O., Holtan H. (1981), Cathodic Behavior of Impure Aluminum in Aqueous Media, Journal of Electrochemical Society 128, pp. 1523-1526.

Nisancioglu K., Holtan H. (1979), Cathodic Polarization of Commercially Pure Aluminum, Corrosion Science 19, pp. 537-552.

Nisancioglu K., Holtan H. (1979), Cathodic Polarization of Aluminum in Acetate-Buffered Chloride Media, Electrochimica Acta 24, pp. 1229-1239.

Nisancioglu K. (1990), Electrochemical Behavior of Aluminum - Base Intermetallics Containing Iron, Journal of Electrochemical Society 137, pp. 69-77.

Oh S.J., Cook D.C., Townsend H.E. (1999), Atmospheric Corrosion of Different Steels in Marine, Rural and Industrial Environments, Corrosion Science 41, pp. 1687-1702.

Oltra R., Keddam M. (1988), Application of Impedance Technique to Localized Corrosion**,** Corrosion Science 28, pp. 1-18.

Park J.O., Paik C.H., Huang Y.H., Alkire R.C. (1999), Influence of Fe-Rich Intermetallic Inclusions on Pit Initiation on Aluminum Alloys in Aerated NaCl, Journal of Electrochemical Society 146, pp. 517-523.

Perkins J., Cummings J.R., Graham K.J. (1982), Morphological Studies of Occluded Cells in the Pitting of Dilute Aluminum Alloys in Seawater, Journal of Electrochemical Society 129, pp. 137-141.

Pickering H.W. (2003), Important Early Developments and Current Understanding of the IR Mechanism of Localized Corrosion, Journal of Electrochemical Society 150, K1.

Porter F.C., Hadden S.E. (1953), Corrosion of Aluminum Alloys in Supply Waters, Journal of Applied Chemistry 3, pp. 385-409.

Potter J.C., Lewandowski L., White D.W. (1991), Durability of Special Coatings for Corrugated Metal Pipe, FHWA-FLP-91-006, Federal Highway Administration.

Pourbaix M. (1974), Atlas of Electrochemical Equilibria in Aqueous Solutions, NACE, p. 389.

Pyskadlo R., Ewing J. (1987), Engineering Research and Development Bureau, New York State DOT, New York.

Pyun S.-I, Moon S.-M., Ahn S.-H, Kim S.-S (1999), Effects of Cl^-, NO_3^- and SO_4^{-2} Ions on Anodic Dissolution of Pure Aluminum in Alkaline Solution, Corrosion Science 41, pp. 653-667.

Richardson J.A., Wood G.C. (1970), A Study of The Pitting Corrosion of A1 by Scanning Electron Microscopy, Corrosion Science 10, pp. 313-323.

Rynders R., Paik C., Ke R., Alkire R.C. (1994), Use of In Situ Atomic Force Microscopy to Image Corrosion at Inclusions, Journal of Electrochemical Society 141, pp. 1439-1445.

Sagüés A.A. (2006), Lectures on Electrochemical Impedance Diagnostic Technique, Department of Civil and Environmental Engineering, University of South Florida.

Sander A., Berghult B., Elftron Broo A., Lind Johansson E., Hedberg T. (1996), Iron Corrosion in Drinking Water Distribution Systems—The effect of pH, Calcium and Hydrogen Carbonate, Corrosion Science 38, pp. 443-455.

Sasaki K., Isaacs H.S. (1990), Origins of Electrochemical Noise during Pitting Corrosion of Aluminum, Journal of Electrochemical Society 151, pp. 78-82.

Sasaki K., Isaacs H.S. (2004), Origins of Electrochemical Noise During Pitting Corrosion of Aluminum, Journal of Electrochemical Society 151, B124-B133.

Sato N. (1971), A Theory for Breakdown of Anodic Oxide Films on Metals, Electrochimica Acta 16, pp. 1683-1692.

Seri O., Furumata K. (2002), Effect of Al-Fe-Si Intermetallic Compound Phases on Initiation and Propagation of Pitting Attacks for Aluminum 1100, Materials and Corrosion 53, pp. 111-120.

Seri O., Masuko N. (1985), Journal of Japan Institute of Light Metals 35, pp. 98.

Serra E., Glasbrennner H., Perujo A. (1998), Hot-Dip Aluminum Deposit as Permeation Barrier for MANET Steel, Fusion Engineering and Design 41, pp. 149-155.

Shao H.B., Wang J.M., Zhang Z., Zhang J.Q., Cao C.N. (2003), Electrochemical Impedance Spectroscopy Analysis on the Electrochemical Dissolution of Aluminum in an Alkaline Solution, Journal of Electroanalytical Chemistry 549, pp. 145-150.

Shaw B.A., Moran P.J. (1985), Characteristics of the Behavior of Zinc-Aluminum Thermal Spray Coatings, Materials Performance 24, pp. 22-31.

Sherif E.M., Park Su-Moon (2005), Effects of 1, 5-Naphthalenediol on Aluminum Corrosion as a Corrosion Inhibitor in 0.50 M NaCl, Journal of Electrochemical Society 152, pp. B205-B211.

Snoeyink V.L., Jenkins D. (1980), Water Chemistry, John Wiley & Sons Inc., New York.

Southeastern Corrugated Steel Pipe Association (1977), Performance Evaluation of Corrugated Metal Culverts in Georgia.

Standard Methods for the Examination of Water and Wastewater (1992).

Stavros A.J. (1984), Galvalume Corrugated Steel Pipe: a Performance Summary.

Stern M., Geary A.L. (1957), Electrochemical Polarization, I. A Theoretical Analysis, Journal of Electrochemical Society 104, pp. 56.

Sullivan J.P., Dunn R.G., Barbour J.C., Wall F.D., Missert N., Buchheit R.G. (2000), Abstract 137, The Electrochemical Society Meeting Abstracts, 2000-1, Ontario, Canada.

Suter T., Alkire R.C. (2001), Microelectrochemical Studies of Pit Initiation at Single Inclusions in Al 2024-T3, Journal of Electrochemical Society 148, pp. B36-B42.

Suzuki I. (1989), Corrosion-Resistant Coatings Technology, Marcel Dekker, Inc., New York.

Szklarska-Smialowska Z. (1999), Pitting Corrosion of Aluminum, Corrosion Science 41, pp. 1743-1767.

Townsend H.E., Zoccola J.C. (1979), Atmospheric Corrosion Resistance of 55% Al–Zn Coated Sheet Steel: 13 Year Test Results, Materials Performance 18, pp. 13-20.

Townsend H.E., Borzillo A.R. (1987), Twenty-Year Atmospheric Corrosion Tests of Hot-dip Coated Sheet Steel, Materials Performance 26, pp. 37-41.

Van de Ven E.P.G.T., Koelmans H. (1976), The Cathodic Corrosion of Aluminum, Journal of Electrochemical Society 123, pp.143.

Verhoff M., Alkire R.C. (2000), Experimental and Modeling Studies of Single Corrosion Pits on Pure Aluminum in pH 11 NaCl Solutions II. Pit Stability, Journal of Electrochemical Society 147, pp. 1359-1365.

Vermilyea D.A. (1971), Concerning the Critical Pitting Potential, Journal of Electrochemical Society 118, pp. 529-531.

Vijh A.K. (1973), Pitting Potentials of Metals, Corrosion Science 13, pp. 805-806.

Vukmirovic M.B., Dimitrov N., Sieradzki K. (2002), Dealloying and Corrosion of Al Alloy 2024-T3, Journal of Electrochemical Society 149, pp. B428-B439.

West A.C., Newman J. (1992), Modern Aspects of Electrochemistry, 23, B.E. Conway et al Eds., Plenum Press, New York.

Wiersma B.J., Herbert K.R. (1991), Observations of the Early Stages of the Pitting Corrosion of Aluminum, Journal of Electrochemical Society 138, pp. 48.

Wood G.C., Richardson J.A., Abd M.F., Mapa L.M., Sutton W.H. (1978), Passivity of Metals, in: R.P. Frankenthal, J. Kruger (Eds.), Proceedings of the Fourth International Symposium on Passivity, The Electrochemical Society, Pennington, NJ.

Wong K.P., Alkire R.C. (1990), Local Chemistry and Growth of Single Corrosion Pits in Aluminum, Journal of Electrochemical Society 137, pp. 3010-3015.

Yu S.Y., O'Grady W.E., Ramaker D.E., Natishan P.M. (2000), Investigation of Chloride Interactions on Aluminum with X-ray Absorption near Edge Structure, Journal of Electrochemical Society 147, pp. 2952-2958.

Appendices

Appendix A: Results from Replicate Unblemished Specimens

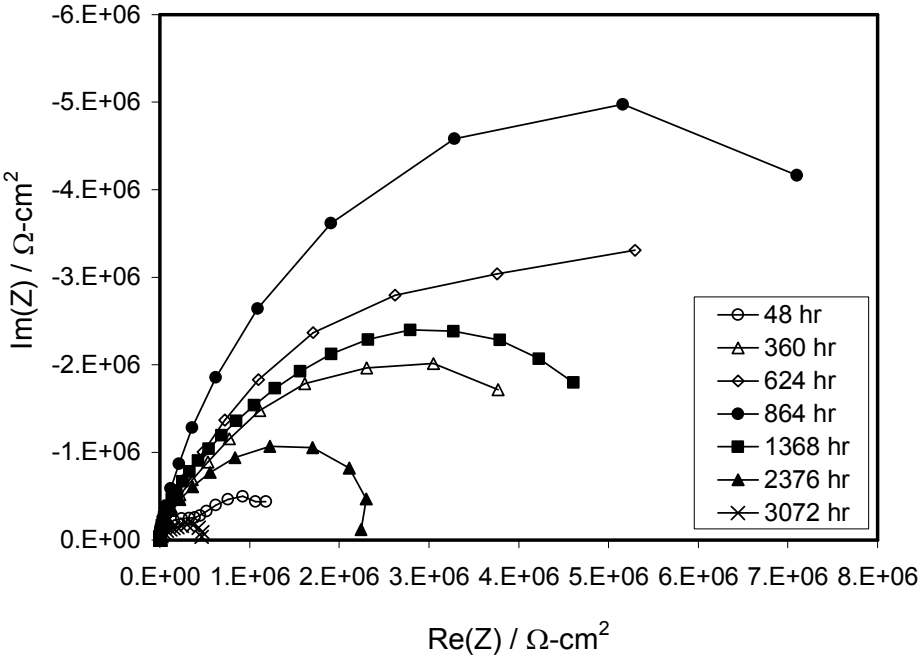

Figure A.1: EIS behavior of the unblemished specimen #2 in solution NP (100 KHz - 1 mHz - 5 points/decade unless indicated otherwise).

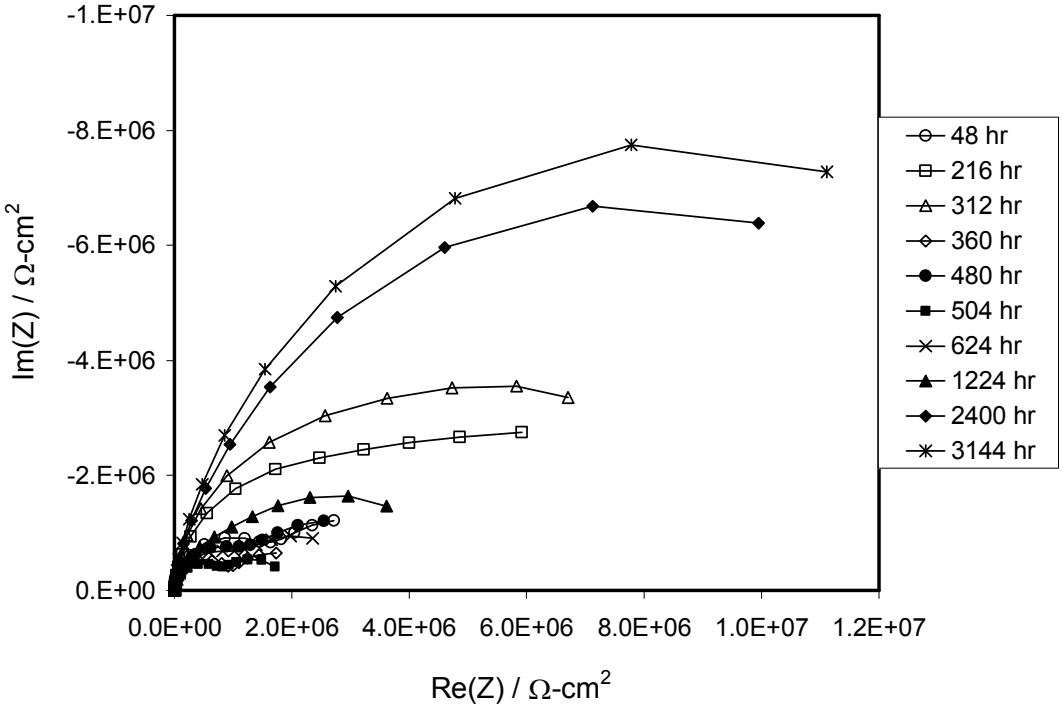

Figure A.2: EIS behavior of the unblemished specimen #2 in solution P (100 KHz - 1 mHz - 5 points/decade).

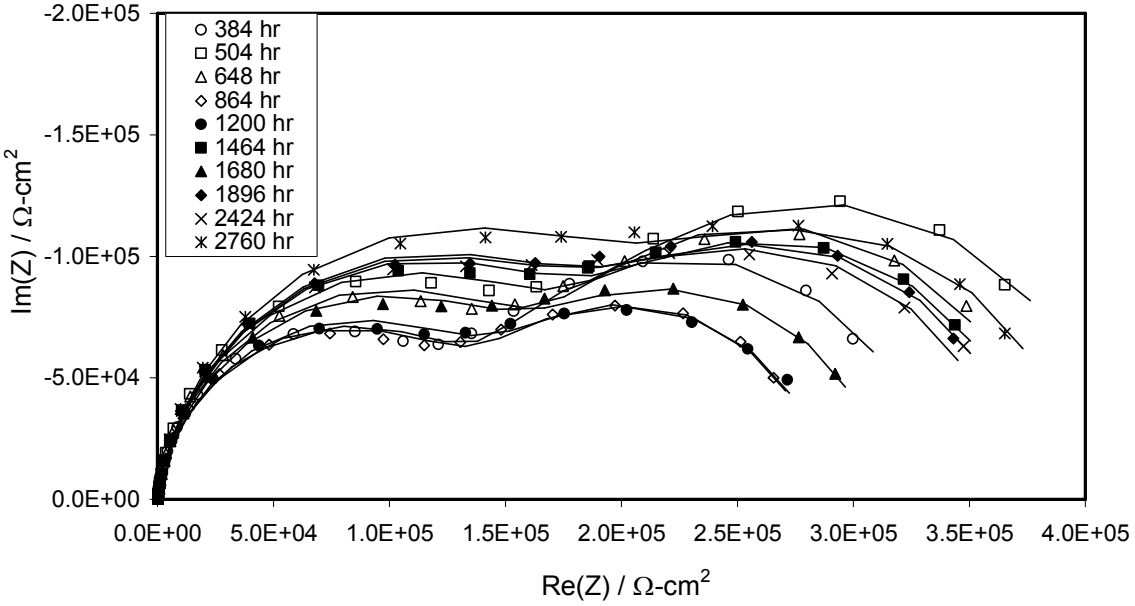

Figure A.3: EIS behavior of the unblemished specimen #2 in solution SW (100 KHz - 1 mHz - 5 points/decade).

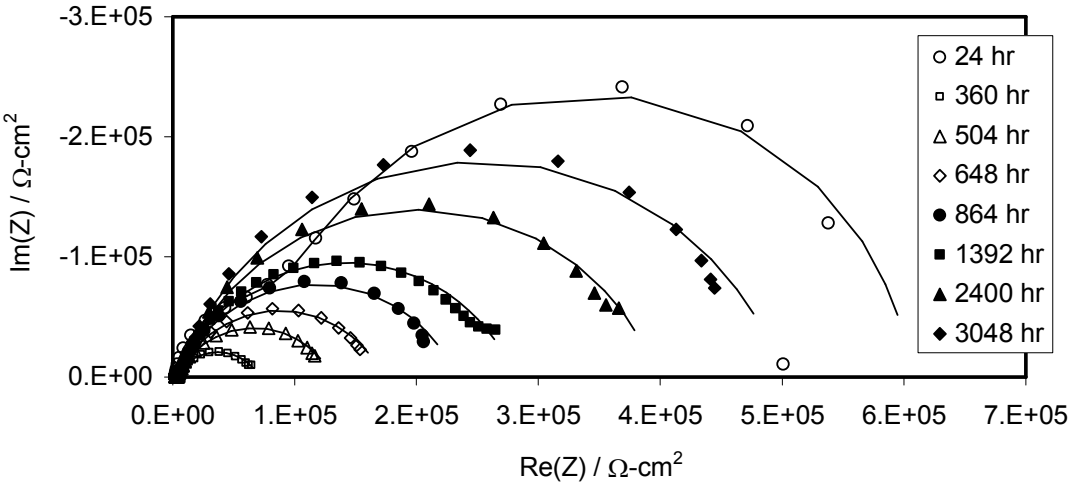

Figure A.4: EIS behavior of the unblemished specimen #2 in solution C (100 KHz - 1 mHz - 5 points/decade unless indicated otherwise).

Appendix A: (Continued)

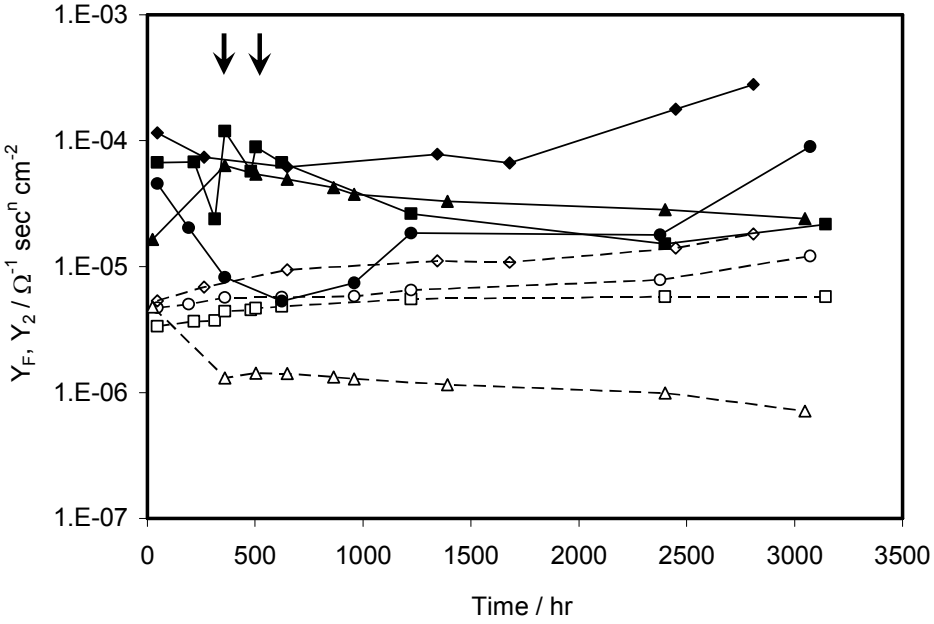

Figure A.5: Evolution of the admittance parameter as a function of time for the unblemished specimens #2 in solutions NP (circles), P (squares), C (triangles), and SW (diamonds) (--- Y_F, — Y_{AL2}). Arrows indicate $CaCO_3$ additions to solution P (#2).

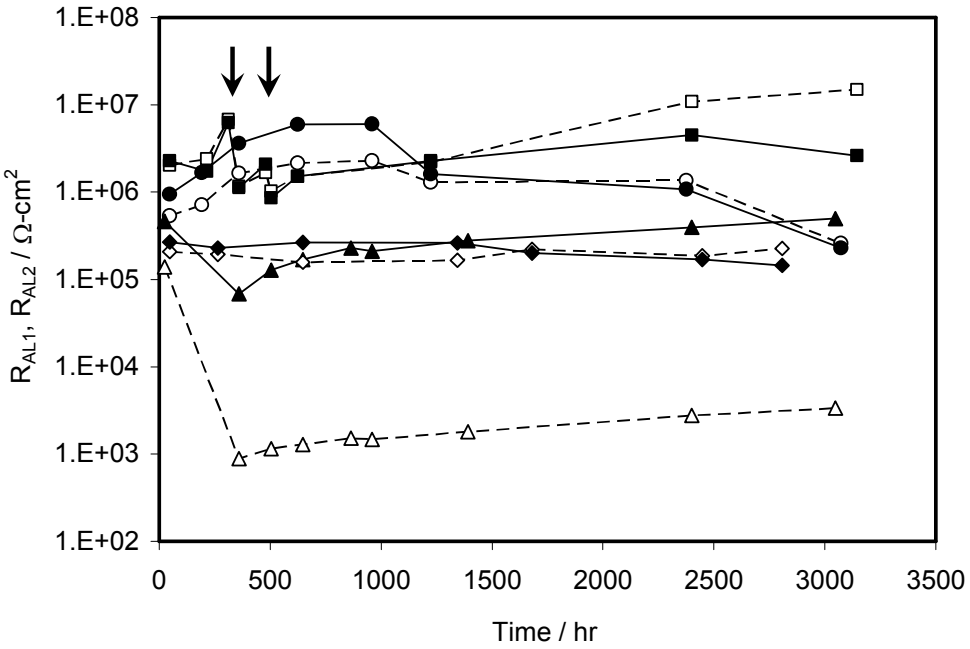

Figure A.6: Evolution of the resistive components as a function of exposure time for the unblemished specimens #2 in solutions NP (circles), P (squares), C (triangles), and SW (diamonds) (--- R_{AL1}, — R_{AL2}). Arrows indicate $CaCO_3$ additions to solution P (#2).

Appendix A: (Continued)

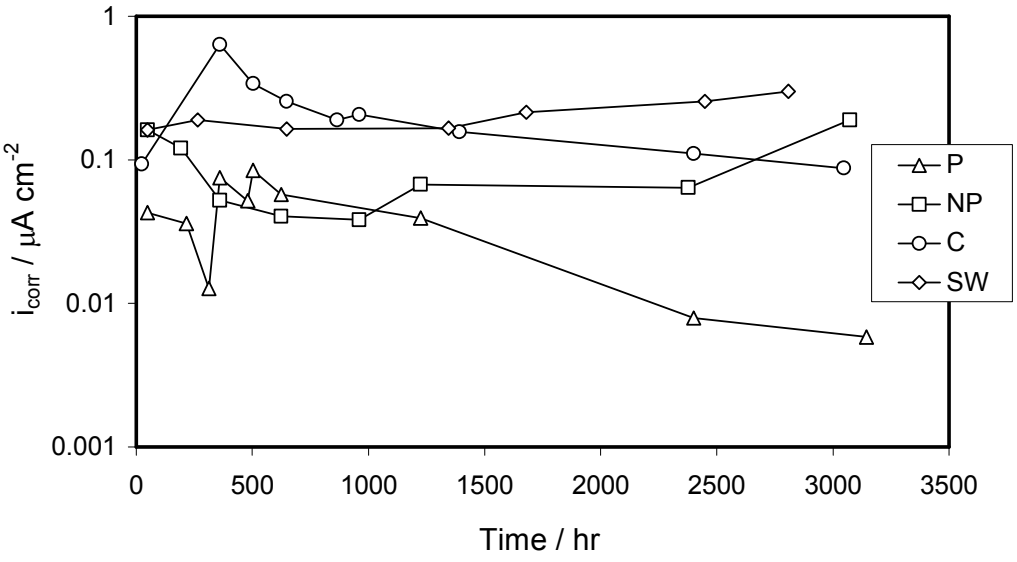

Figure A.7: Nominal corrosion current density evolution for the unblemished specimens #2.

Appendix A: (Continued)

Table A.1: Values of the equivalent circuit components in Figure 2.16 estimated from EIS data fit for the unblemished specimen #2 exposed to solution P.

Time hr	R_S Ω	R_{AL1} kΩ	Y_F s^{n_F}/Ω	n_F	R_{AL2} kΩ	Y_{AL2} $s^{n_{AL2}}/\Omega$	n_{AL2}	i_{corrAL} μA cm^{-2}
48	18.9	21.3	3.17E-04	0.94	24.1	6.37E-03	0.97	0.043
216	18.8	25.4	3.48E-04	0.94	18.3	6.39E-03	1.00	0.036
312	19.3	71.6	3.55E-04	0.94	65.9	2.27E-03	0.86	0.013
360	20.4	12.2	4.20E-04	0.94	11.8	1.13E-02	1.00	0.075
480	20.0	17.6	4.29E-04	0.94	21.9	5.42E-03	0.97	0.052
504	20.6	10.8	4.41E-04	0.94	9.0	8.46E-03	1.00	0.085
624	21.7	15.9	4.58E-04	0.94	15.9	6.37E-03	0.99	0.057
1224	21.6	23.3	5.24E-04	0.93	24.1	2.50E-03	0.97	0.039
2400	24.8	115.4	5.45E-04	0.93	47.4	1.44E-03	1.00	0.008
3144	25.0	156.8	5.45E-04	0.93	27.5	2.05E-03	1.00	0.006

Nominal specimen area A_{AL} = 95 cm^2

Table A.2: Values of the equivalent circuit components in Figure 2.16 estimated from EIS data fit for the unblemished specimen #2 exposed to solution SW.

Time hr	R_S Ω	R_{AL1} kΩ	Y_F s^{nF}/Ω	n_F	R_{AL2} kΩ	Y_{AL2} s^{nAL2}/Ω	n_{AL2}	i_{corrAL} μA cm^{-2}
48	0.49	2.6	5.07E-04	0.90	2.8	1.09E-02	1.00	0.16
264	0.43	3.1	6.53E-04	0.91	2.4	7.01E-03	1.00	0.19
648	0.44	2.6	8.96E-04	0.92	2.8	5.86E-03	1.00	0.16
1344	0.52	2.5	1.05E-03	0.91	2.7	7.39E-03	1.00	0.17
1680	0.54	2.7	1.02E-03	0.92	2.1	6.29E-03	1.00	0.22
2448	0.51	2.6	1.32E-03	0.93	1.8	1.69E-02	1.00	0.26
2808	0.50	2.6	1.72E-03	0.92	1.5	2.65E-02	1.00	0.30

Nominal specimen area A_{AL}= 95 cm^2

Table A.3: Values of the equivalent circuit components in Figure 2.16 estimated from EIS data fit for the unblemished specimen #2 exposed to solution NP.

Time hr	R_S Ω	R_{AL1} kΩ	Y_F s^{nF}/Ω	n_F	R_{AL2} kΩ	Y_{AL2} s^{nAL2}/Ω	n_{AL2}	i_{corrAL} μA/cm^2
48	14.1	5.7	4.48E-04	0.94	9.9	4.33E-03	0.92	0.16
192	13.4	7.6	4.77E-04	0.93	17.7	1.92E-03	0.93	0.12
360	13.1	17.5	5.38E-04	0.93	37.9	7.78E-04	0.85	0.05
624	12.9	22.6	5.42E-04	0.93	62.8	5.04E-04	0.85	0.040
960	13.1	23.9	5.49E-04	0.93	63.8	7.05E-04	0.94	0.038
1224	13.5	13.6	6.15E-04	0.93	16.9	1.75E-03	1.00	0.067
2376	13.1	14.2	7.43E-04	0.94	11.3	1.69E-03	1.00	0.064
3072	12.6	2.7	1.15E-03	0.94	2.4	8.48E-03	1.00	0.19

Nominal specimen area A_{AL} = 95 cm^2

Table A.4: Values of the equivalent circuit components in Figure 2.16 estimated from EIS data fit for the unblemished specimen #2 exposed to solution C.

Time hr	R_S Ω	R_{AL1} kΩ	Y_F s^{nF}/Ω	n_F	R_{AL2} kΩ	Y_{AL2} s^{nAL2}/Ω	n_{AL2}	i_{corrAL} μA/cm^2
24	17.6	1.7	4.53E-04	0.91	5.9	1.57E-03	0.91	0.08
360	15.3	0.020	1.24E-04	0.61	0.43	6.01E-03	0.71	1.05
504	16.4	0.026	1.35E-04	0.62	1.0	5.15E-03	0.73	0.44
648	17.5	0.030	1.34E-04	0.62	1.3	4.68E-03	0.73	0.37
864	18.4	0.036	1.26E-04	0.65	1.5	4.00E-03	0.75	0.31
960	18.2	0.036	1.22E-04	0.66	1.6	3.54E-03	0.76	0.29
1392	17.9	0.042	1.09E-04	0.64	2.0	3.12E-03	0.77	0.22
2400	17.4	0.043	9.38E-05	0.65	3.4	2.67E-03	0.80	0.14
3048	17.8	0.042	6.75E-05	0.66	3.6	2.29E-03	0.81	0.13

Nominal specimen area A_{AL} = 95 cm^2

Appendix B: Replicate Results of the Blemished Specimens

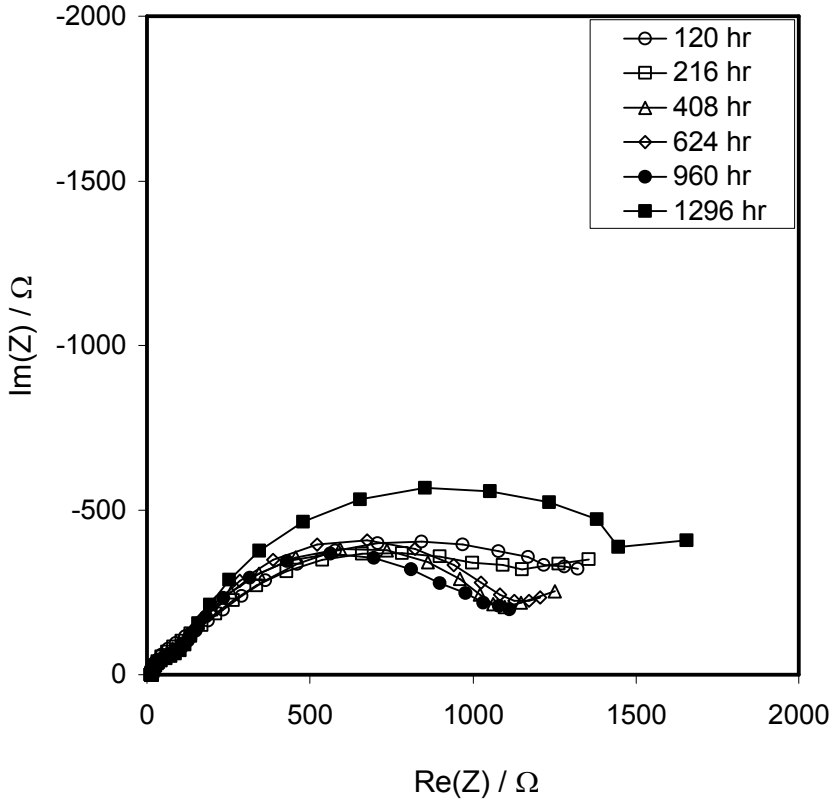

Figure B.1: Nyquist plot of the EIS response of the LCB specimen #2 in solution NP (100 KHz - 1 mHz - 5 points/decade).

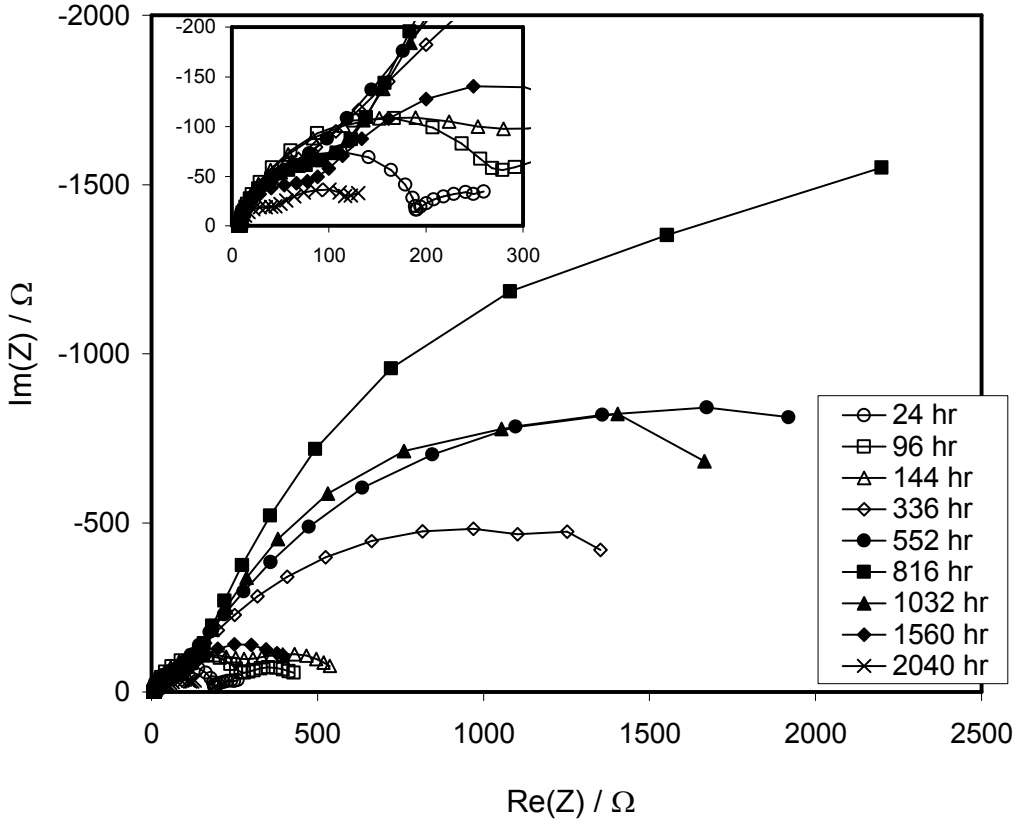

Figure B.2: Nyquist plot of the EIS response of the LCB specimen #3 in solution NP (100 KHz - 1 mHz - 5 points/decade).

Appendix B: (Continued)

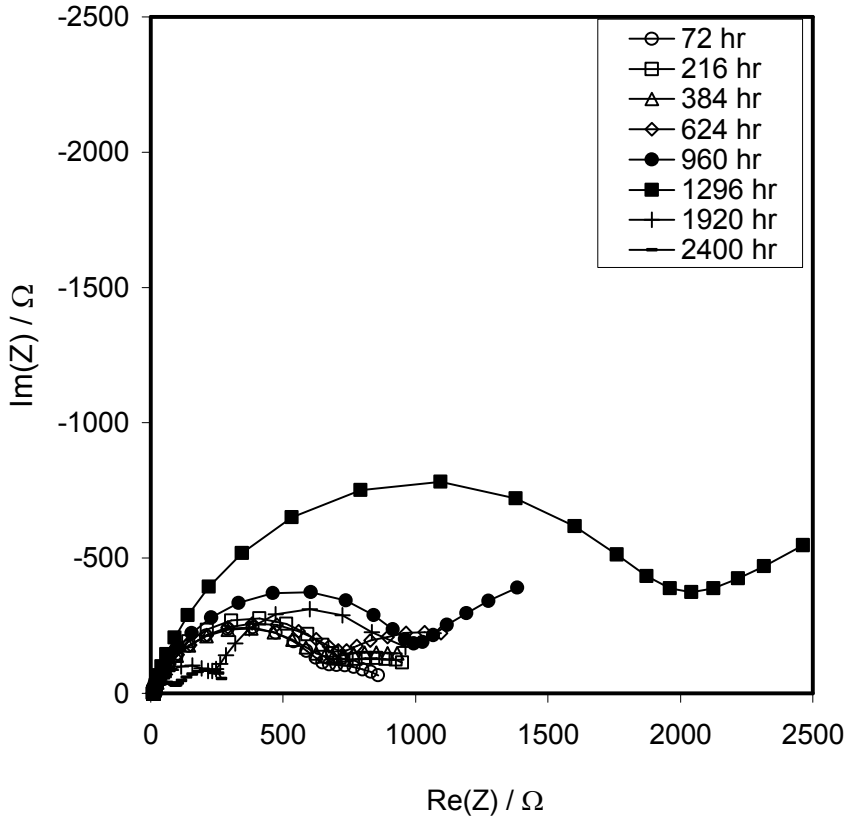

Figure B.3: Nyquist plot of the EIS response of the LCB specimen #2 in solution P (100 KHz - 1 mHz - 5 points/decade).

Appendix B: (Continued)

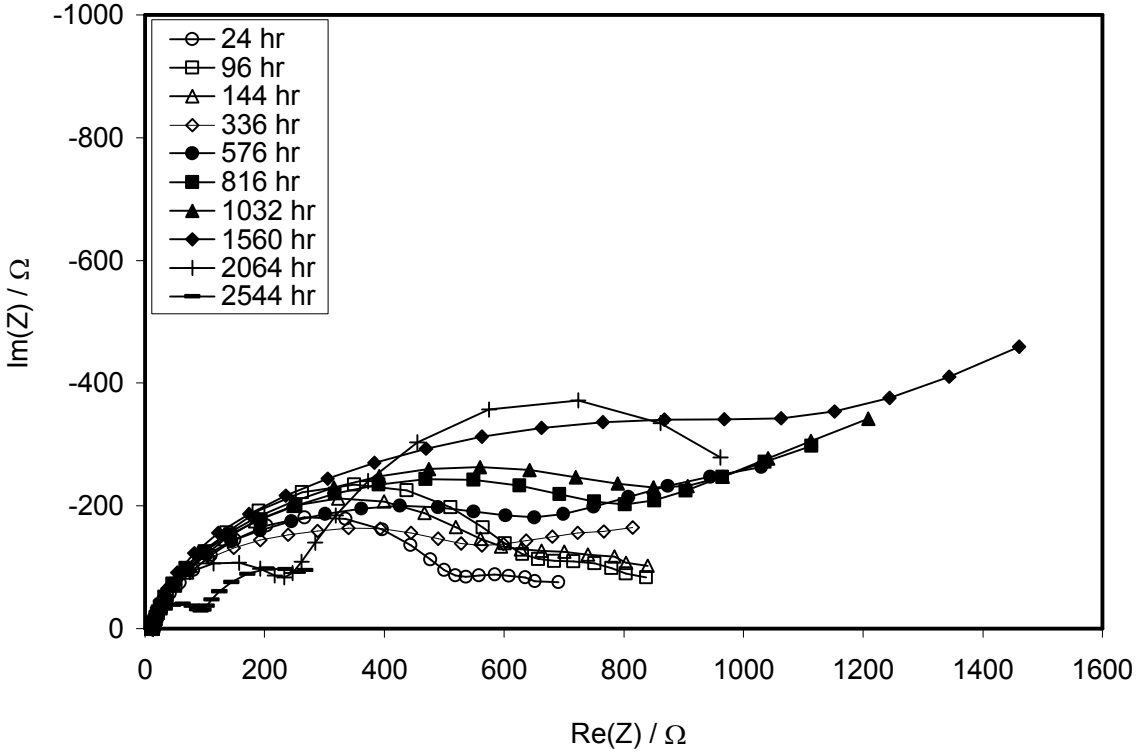

Figure B.4: Nyquist plot of the EIS response of the LCB specimen #3 in solution P (100 KHz - 1 mHz - 5 points/decade).

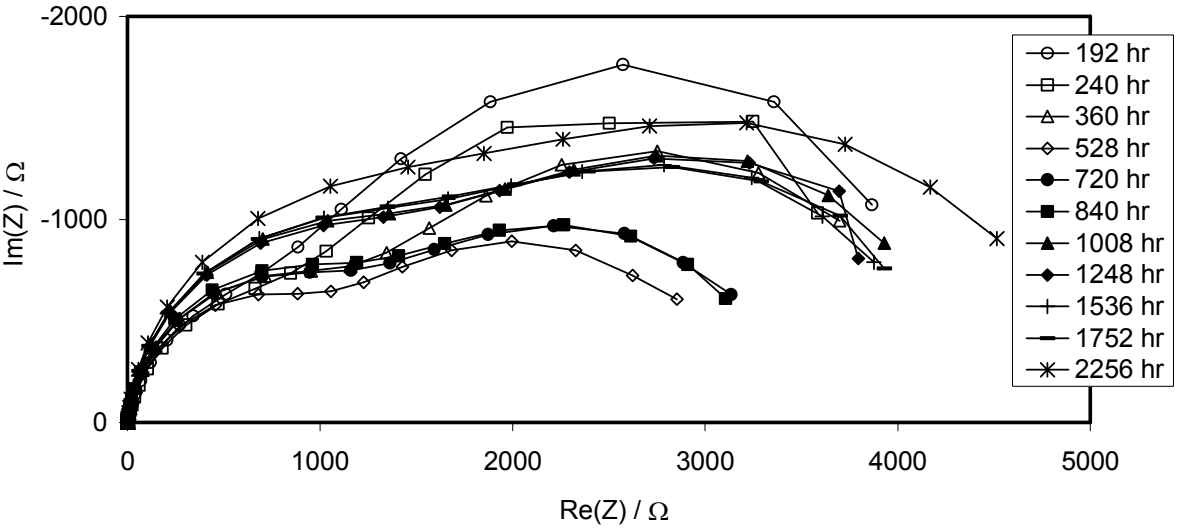

Figure B.5: Nyquist plot of the EIS response of the LCB specimen #2 in solution SW (100 KHz - 1 mHz - 5 points/decade).

Appendix B: (Continued)

Table B.1: Evolution of the nominal corrosion current density of the steel and aluminized portions for the replicate LCB specimens exposed to solution P. The parameters of the simplified equivalent circuits shown in Figure 4.41 are also included. Immune condition for the exposed steel was assumed when the system E_{OC} reached <-800 mV. Passive condition for the outer aluminized coating was assumed when the aluminized surface was bright with no visible pits.

Time hr	R_S Ω	W_1 Ω	R_{C1} Ω	R_{a1} Ω	Y* $sec^{n^*}\ \Omega^{-1}$	n*	i_{corrFE} μA cm^{-2}	i_{corrAL} μA cm^{-2}
72	8.8	49.8	3,540	856	9.01E-04	0.78	8.0	passive
216	9.0	205.6	3,188	987	8.52E-04	0.80	7.4	
960	9.3	26.7	2,642	1,731	7.78E-04	0.80	5.3	
1296	9.7	141.9	6,664	2,984	6.68E-04	0.83	2.7	

Values obtained for solution P(#2) before the E_{OC} drop.

Time hr	R_S Ω	W_1 Ω	R_{C1} Ω	R_{AL2} Ω	Y** $sec^{n^{**}}\ \Omega^{-1}$	n**	i_{corrFE} μA cm^{-2}	i_{corrAL} μA cm^{-2}
1920	9.9	3.2	361.9	801.4	3.61E-03	0.85	immune	0.6
2400	10.1	3.2	147.2	150.1	6.71E-03	0.87		3.2

Values obtained for solution P(#2) before the E_{OC} drop.

Time hr	R_S Ω	W_1 Ω	R_{C1} Ω	R_{a1} Ω	Y* $sec^{n^*}\ \Omega^{-1}$	n*	i_{corrFE} μA cm^{-2}	i_{corrAL} μA cm^{-2}
24	10.2	3.6	2,448	692	9.57E-04	0.75	10.3	passive
96	10.8	7.5	3,370	846	1.02E-03	0.76	8.2	
144	10.7	55.0	2,439	841	1.07E-03	0.76	8.9	
576	11.9	354.1	531	1,191	8.15E-04	0.83	15.1	
1344	11.8	292.3	557	1,452	1.02E-03	0.83	13.8	

Values obtained for solution P(#3) before the E_{OC} drop.

Time hr	R_S Ω	W_1 Ω	R_{C1} Ω	R_{AL2} Ω	Y** $sec^{n^{**}}\ \Omega^{-1}$	n**	i_{corrFE} μA cm^{-2}	i_{corrAL} μA cm^{-2}
2064	12.9	3.2	361.9	1,007	1.52E-03	0.89	immune	0.5
2544	13.1	1.6	147.2	288	4.55E-03	0.88		1.7

Values obtained for solution P(#3) after the E_{OC} drop.

Appendix B: (Continued)

Table B.2: Evolution of the nominal corrosion current density of the steel and aluminized portions for the replicate LCB specimens exposed to solution NP. The parameters of the simplified equivalent circuits shown in Figure 4.41 are also included. Immune condition for the exposed steel was assumed when the system E_{OC} reached <-800 mV. Passive condition for the outer aluminized coating was assumed when the aluminized surface was bright with no visible pits.

Time hr	R_S Ω	W_1 Ω	R_{C1} Ω	R_{a1} Ω	Y^* $sec^{n^*}\ \Omega^{-1}$	n^*	i_{corrFE} μA cm^{-2}	i_{corrAL} μA cm^{-2}
120	11.1	9.0	1,203	1,343	1.54E-03	0.71	8.7	passive
216	10.5	8.9	1,142	1,229	1.73E-03	0.70	9.4	
960	10.9	3.2	308.4	1,022	1.60E-03	0.72	23.4	
1296	9.5	2.2	333.3	1,640	2.20E-03	0.67	20.0	

Values obtained for solution NP(#2) before the E_{OC} drop.

Time hr	R_S Ω	W_1 Ω	R_{C1} Ω	R_{a1} Ω	Y^* $sec^{n^*}\ \Omega^{-1}$	n^*	i_{corrFE} μA cm^{-2}	i_{corrAL} μA cm^{-2}
24	6.8	15.4	732.3	263	1.01E-03	0.82	28.7	passive
96	7.1	30.7	913.9	429.7	1.44E-03	0.81	18.9	
144	6.8	268.9	388.7	555.5	1.41E-03	0.82	24.2	
552	6.5	48.1	533.6	2,243	3.18E-03	0.69	12.8	

Values obtained for solution NP(#3) before the E_{OC} drop.

Time hr	R_S Ω	W_1 Ω	R_{C1} Ω	R_{AL2} Ω	Y^{**} $sec^{n^{**}}\ \Omega^{-1}$	n^{**}	i_{corrFE} μA cm^{-2}	i_{corrAL} μA cm^{-2}
816	7.0	5.2	226	2,940	2.72E-03	0.78	immune	0.2
1032	7.2	8.2	232	1,817	2.95E-03	0.80		0.3
1560	7.6	5.7	166	400.8	5.17E-03	0.83		1.2
2040	7.9	9.4	102	125	1.31E-02	0.78		3.8

Values obtained for solution NP(#3) after the E_{OC} drop.

Appendix B: (Continued)

Table B.3: Evolution of the nominal corrosion current density of the aluminized portion for the replicate LCB specimens exposed to solution SW. The parameters of the simplified equivalent circuits shown in Figure 4.41 are also included. Immune condition for the exposed steel was assumed when the system E_{OC} reached <-800 mV.

Time hr	R_S Ω	W_1 Ω	R_{C1} Ω	R_{AL2} Ω	Y** sec^{n**} Ω^{-1}	n**	i_{corrFE} μA cm^{-2}	i_{corrAL} μA cm^{-2}
192	0.38	6.9	4,910	4,667	3.38E-03	0.81		0.10
240	0.38	5.5	3,028	4,222	2.37E-03	0.84		0.11
360	0.38	5.3	3,112	4,061	1.59E-03	0.90		0.12
528	0.36	5.4	2,980	2,981	1.66E-03	0.91		0.16
720	0.38	5.8	3,646	3,282	1.65E-03	0.91		0.14
840	0.38	18.8	3,963	3,289	1.66E-03	0.91	immune	0.14
1008	0.40	15.0	5,042	4,277	1.63E-03	0.91		0.11
1248	0.38	9.5	4,850	4,246	1.65E-03	0.91		0.11
1536	0.39	10.0	5,410	4,148	1.66E-03	0.91		0.11
1752	0.38	10.3	5,534	4,168	1.67E-03	0.91		0.11
2256	0.38	11.3	6,861	4,782	1.62E-03	0.91		0.10

Values obtained for solution SW(#2) after the E_{OC} drop.

Appendix B: (Continued)

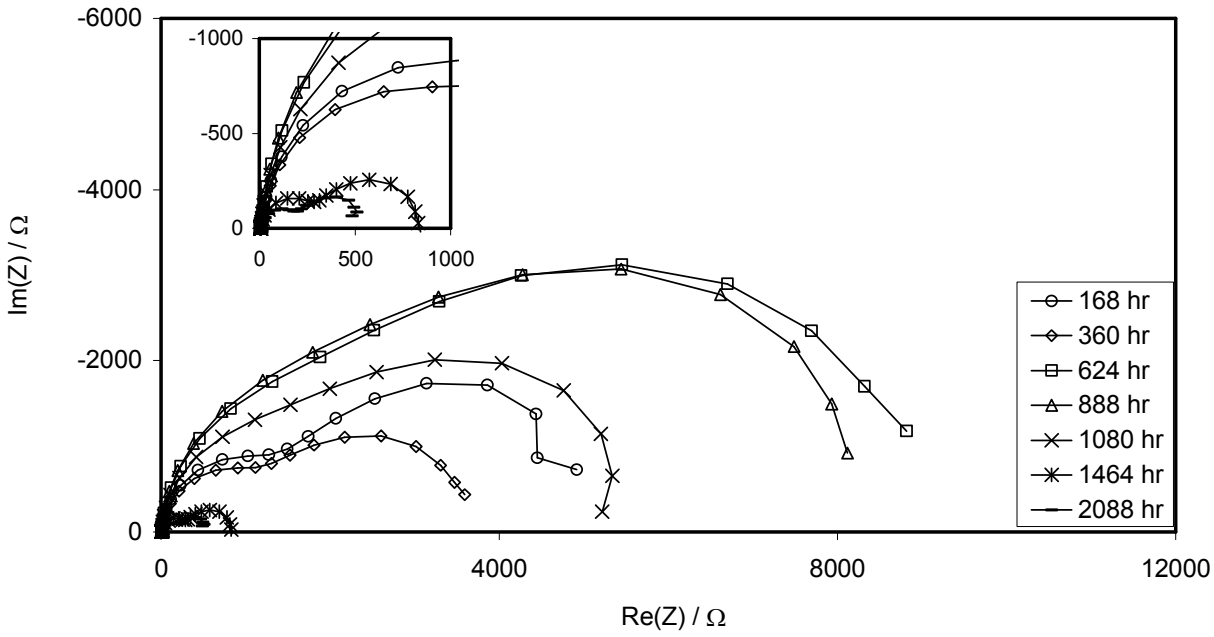

Figure B.6: Nyquist plot of the EIS response of the SCB specimen #2 in solution NP (100 KHz - 1 mHz - 5 points/decade).

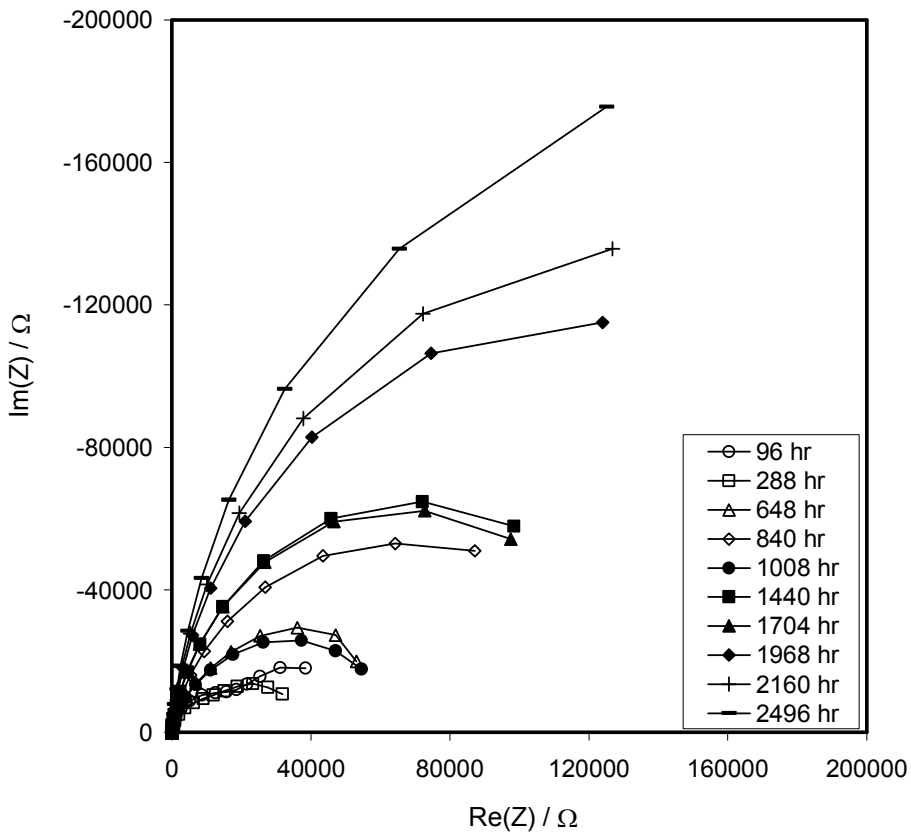

Figure B.7: Nyquist plot of the EIS response of the SCB specimen #2 in solution P (100 KHz - 1 mHz - 5 points/decade).

Appendix B: (Continued)

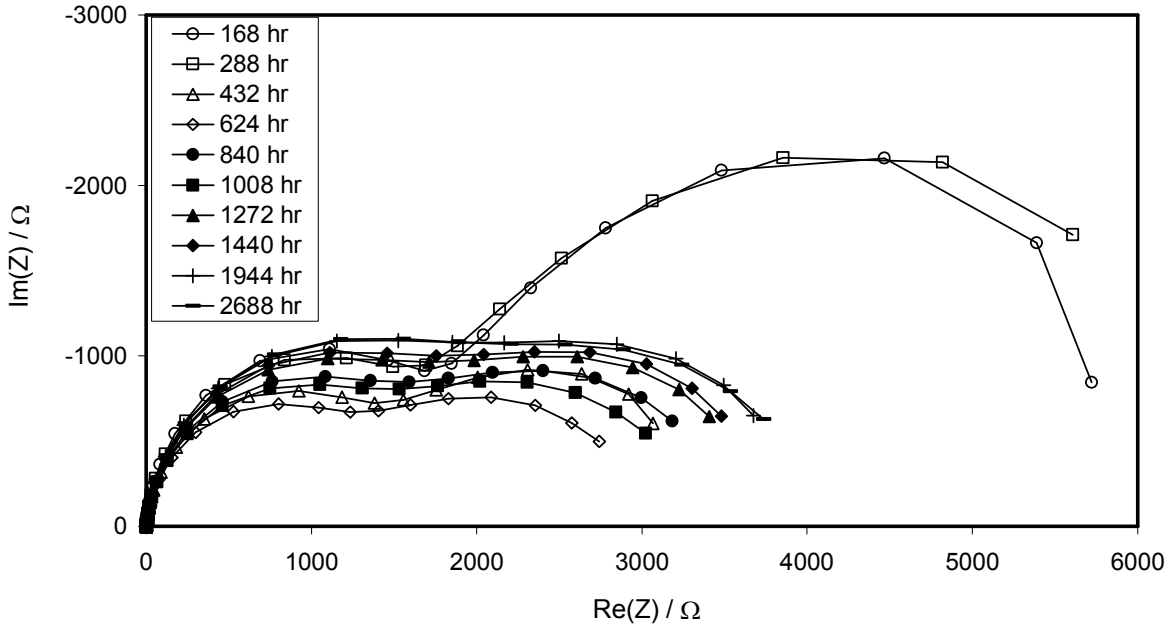

Figure B.8: Nyquist plot of the EIS response of the SCB specimen #2 in solution SW (100 KHz - 1 mHz - 5 points/decade).

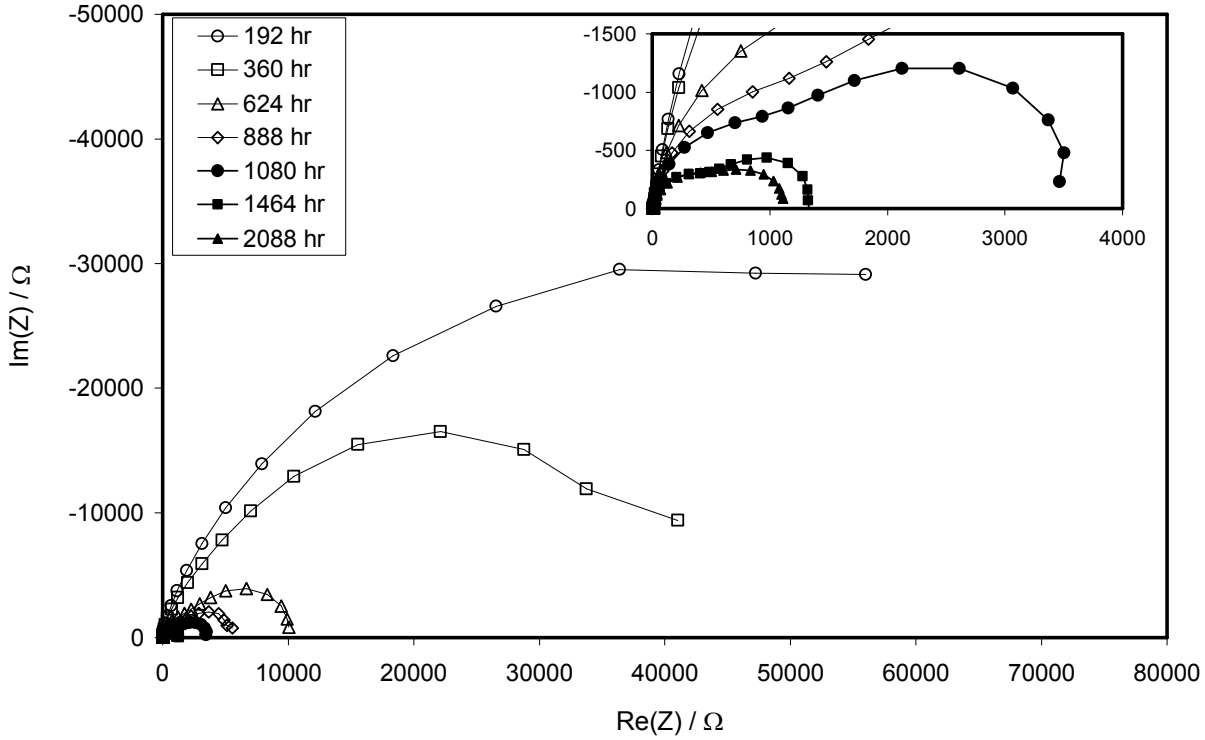

Figure B.9: Nyquist plot of the EIS response of the SCB specimen #3 in solution C (100 KHz-1 mHz - 5 points/decade).

Appendix B: (Continued)

Table B.4: Evolution of the nominal corrosion current density of the aluminized portion for the replicate SCB specimens exposed to solution NP. The parameters of the simplified equivalent circuits shown in Figure 4.41 are also included. Immune condition for the exposed steel was assumed when the system E_{OC} reached <-800 mV.

Time hr	R_S Ω	W_1 Ω	R_{C1} Ω	R_{AL2} Ω	Y** sec^{n**} Ω^{-1}	n**	i_{corrFE} μA cm^{-2}	i_{corrAL} μA cm^{-2}
72	6.6	170	5,363	6,542	5.32E-04	0.92	immune	0.07
168	6.4	242	3,410	4,974	7.03E-04	0.92		0.09
360	6.5	92	3,299	3,613	7.91E-04	0.92		0.13
624	6.5	174	9,270	8,835	8.20E-04	0.92		0.05
888	6.6	254	11,140	8,408	8.93E-04	0.92		0.05
1080	6.5	229	6,878	5,508	9.76E-04	0.92		0.08
1464	6.2	66	627	822	1.57E-03	0.92		0.56
2088	6.9	38	435	522	3.04E-03	0.89		0.88

Values obtained for solution NP(#2) after the E_{OC} drop.

Table B.5: Evolution of the nominal corrosion current density of the aluminized portion for the replicate SCB specimens exposed to solution P. The parameters of the simplified equivalent circuits shown in Figure 4.41 are also included. Immune condition for the exposed steel was assumed when the system E_{OC} reached <-800 mV.

Time hr	R_S Ω	W_1 Ω	R_{C1} kΩ	R_{AL2} Ω	Y** sec^{n**} Ω^{-1}	n**	i_{corrFE} μA cm^{-2}	i_{corrAL} μA cm^{-2}
96	7.1	74.5	44.5	55,350	3.59E-04	0.92	immune	0.017
168	7.5	62.2	16.1	15,800	4.25E-04	0.92		0.058
288	7.9	121.1	38.7	35,080	4.67E-04	0.93		0.026
432	7.9	64.7	27.2	20,280	5.03E-04	0.92		0.045
648	8.2	100.6	79.7	43,640	5.15E-04	0.91		0.021
840	8.1	170.4	288.9	71,990	5.18E-04	0.92		0.013
1008	8.1	157.4	533.4	86,920	5.09E-04	0.92		0.011
1272	8.3	291.3	2E3	112,500	5.06E-04	0.92		0.008
1440	8.5	539.1	2E3	189,100	4.94E-04	0.92		0.005
1704	7.9	292.6	3E3	156,400	4.98E-04	0.92		0.006
2160	8.2	335.2	5E3	372,200	4.83E-04	0.93		0.002

Values obtained for solution P(#2) after the E_{OC} drop.

Appendix B: (Continued)

Table B.6: Evolution of the nominal corrosion current density of the aluminized portion for the replicate SCB specimens exposed to solution SW. The parameters of the simplified equivalent circuits shown in Figure 4.41 are also included. Immune condition for the exposed steel was assumed when the system E_{OC} reached <-800 mV.

Time hr	R_S Ω	W_1 Ω	R_{C1} Ω	R_{AL2} Ω	Y** $sec^{n**}\ \Omega^{-1}$	n**	i_{corrFE} μA cm^{-2}	i_{corrAL} μA cm^{-2}
96	0.29	3.3	3,295	3,746	6.55E-04	0.91	immune	0.12
168	0.31	3.3	3,952	6,128	7.64E-04	0.91		0.07
288	0.29	2.8	3,776	6,344	9.95E-04	0.91		0.07
432	0.29	1.7	4,474	3,344	1.33E-03	0.90		0.14
624	0.29	1.2	4,428	2,903	1.53E-03	0.90		0.16
840	0.30	1.7	5,870	3,429	1.63E-03	0.89		0.13
1008	0.30	2.9	5,665	3,210	1.65E-03	0.89		0.14
1272	0.30	2.5	7,012	3,683	1.65E-03	0.90		0.12
1440	0.30	3.0	7,503	3,772	1.64E-03	0.89		0.12
1536	0.30	1.6	6,572	3,213	1.65E-03	0.90		0.14
1680	0.30	1.8	6,538	3,412	1.63E-03	0.90		0.13
2112	0.30	2.1	7,654	3,617	1.58E-03	0.90		0.13
2496	0.31	3.3	10,280	4,496	1.53E-03	0.90		0.10
2688	0.30	1.9	8,598	3,962	1.54E-03	0.90		0.12

Values obtained for solution SW(#2) after the E_{OC} drop.

Table B.7: Evolution of the nominal corrosion current density of the aluminized portion for the replicate SCB specimens exposed to solution C. The parameters of the simplified equivalent circuits shown in Figure 4.41 are also included. Immune condition for the exposed steel was assumed when the system E_{OC} reached <-800 mV.

Time hr	R_S Ω	W_1 Ω	R_{C1} Ω	R_{AL2} Ω	Y** $sec^{n**}\ \Omega^{-1}$	n**	i_{corrFE} μA cm^{-2}	i_{corrAL} μA cm^{-2}
192	9.2	343.1	90,530	76,610	3.88E-04	0.89	immune	0.01
360	8.1	143.8	33,170	41,050	4.20E-04	0.90		0.01
624	8.7	66.4	7,444	10,290	5.69E-04	0.91		0.04
888	8.8	42.2	4,119	5,574	8.30E-04	0.92		0.08
1080	8.4	15.0	3,090	3,570	1.01E-03	0.93		0.13
1464	8.5	18.0	1,276	1,343	1.55E-03	0.94		0.34
2088	9.8	16.4	1,798	1,121	2.40E-03	0.91		0.41

Appendix B: (Continued)

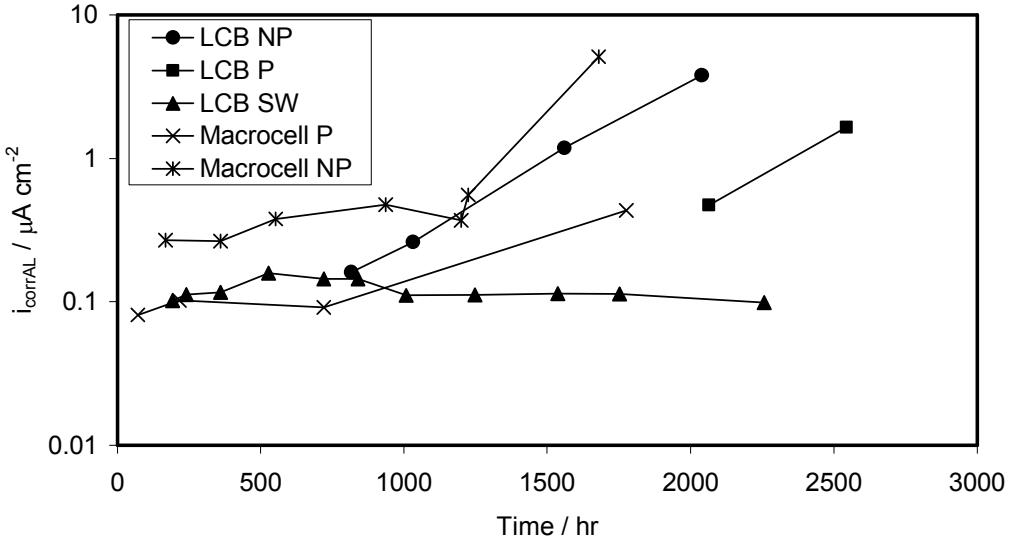

Figure B.10: Evolution of i_{corrAL} of the aluminized portion for the replicate LCB and macrocell assemblies.

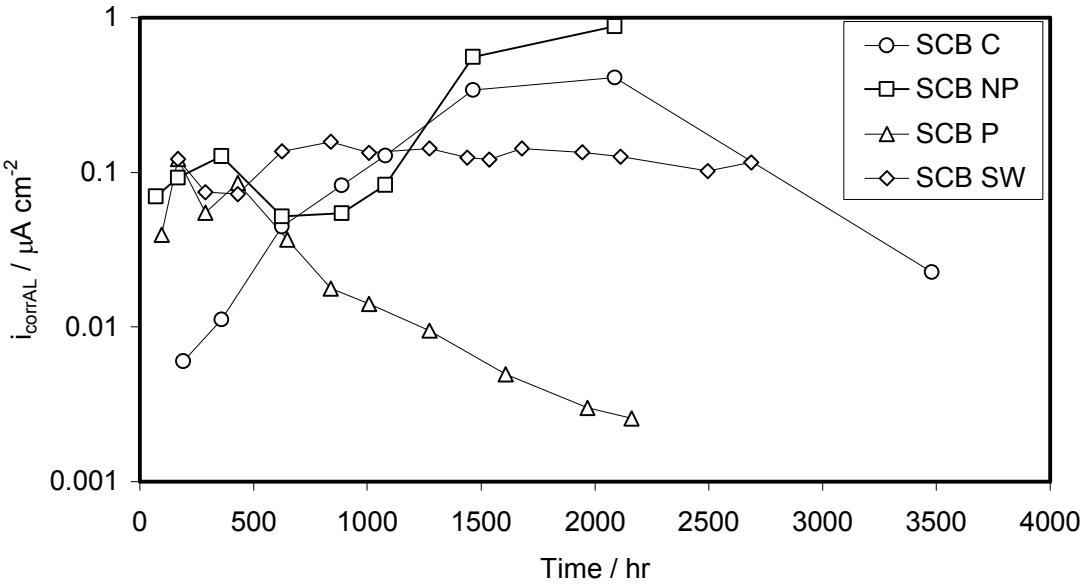

Figure B.11: Evolution of i_{corrAL} of the aluminized portion for the replicate SCB specimens.

Appendix B: (Continued)

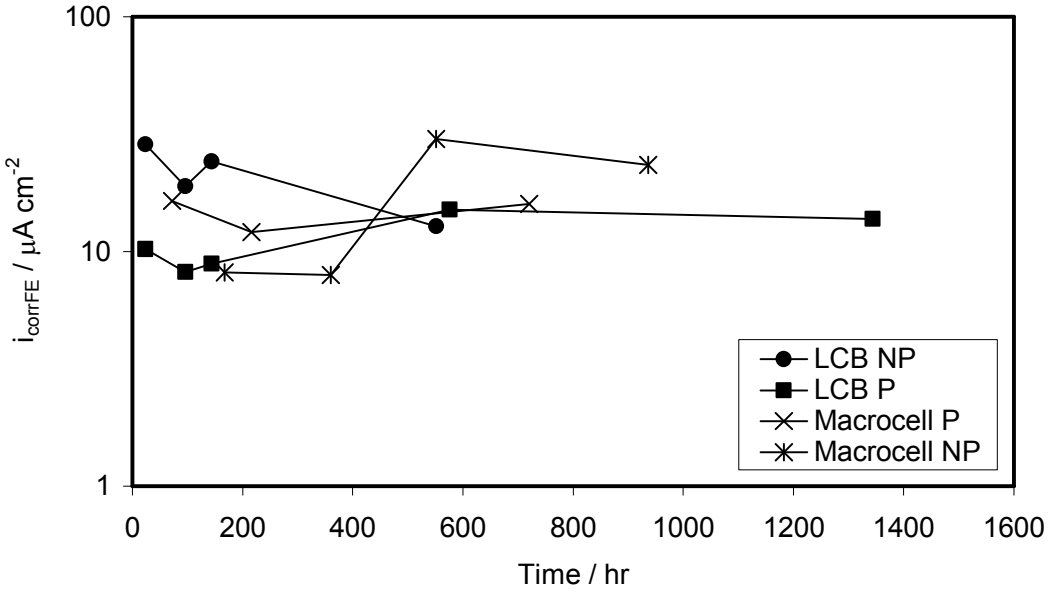

Figure B.12: Evolution of i_{corrFE} of the exposed steel portion for the replicate LCB specimens in solutions NP and P obtained per equivalent circuit shown in Figure 4.41-A.

Appendix C: Interpretation of the Two-Step Reaction Mechanism

This Appendix deals with systems where the surface composition or arrangement of phases changes as a result of the *ac* excitation polarization. This treatment is adapted from Sagüés (2006) which follows along general lines established by Epelboin (1970). The generalized conceptual interpretation of the system to be modeled is as follows. Species A reacts at the metal surface yielding an intermediate species B that resides on a fraction θ of the surface area as an adsorbate formerly suitable for reaction of species A which can react only on an area fraction (1-θ). Species B undergoes further reduction to become species C, which then detaches from the metal surface. As the potential is varied from the E_{OC}, the rates of formation and decomposition of species B change, leading in general to change in coverage from the steady state condition.

Assuming that the system is at a steady state potential E_0 and that the decomposition of species B to yield species A is neglected near E_0, thus:

$$A + n_A e \rightarrow B_{adsorbed} \quad (C.1)$$
$$B_{adsorbed} + n_B e \rightarrow C \quad (C.2)$$

where n_A and n_B are electrons involved in each reaction step.

The reaction rates per unit area are assumed to be potential dependent such as:

$$r_A = a_1 k_1 (1-\theta) \quad (C.3)$$
$$r_B = a_2 k_2 \theta \quad (C.4)$$

where k_1 and k_2 are the rate constants for the reactions (C.1) and (C.2) of the form $k = k_0 \exp(-2.3 (E-E_0)/\beta)$, respectively expressed in moles per unit time, a_1 is the activity of species A assumed to be constant with applied potential, and a_2 represents the number of moles per unit area of the area covered by species B. The parameters k_0 and β are the rate constants at the steady state ($r_{A0}=r_{B0}$) and the cathodic Tafel slope, respectively. The difference between r_A and r_B is equal to $(r_1-r_2) = dm/dt = a_2\, d\theta/dt = a_1\, k_1\, (1-\theta) - a_2\, k_2\, \dot{\theta}$ where m is number of moles of species B per unit area.

The corresponding cathodic current per unit area (negative by convention) is a function of the potential and θ such as:

$$I_C = -F\,(n_A\, a_1\, k_1\, (1-\theta) + n_B\, a_2\, k_2\, \theta) \qquad (C.5)$$

Taking the total derivative of the cathodic current to Eq. (C.5), one gets:

$$d(I_C) = (\partial I_C/\partial\theta)_E\, d\theta + (\partial I_C/\partial E)_\theta\, dE \qquad (C.6)$$

Differencing respect to the potential E, one finds the overall admittance Y of the coupled reactions:

$$Y = -(\partial I_C/\partial\theta)_E\, d\theta/dE - (\partial I_C/\partial E)_\theta \qquad (C.7)$$

Now, taking the derivative of Eq. (C.5) of I_C with respect to θ around E_0, one gets the first term of Eq. (C.7):

$$(\partial I_C/\partial\theta)_{E0} = F\,(n_A\, k_{10}\, a_1 - n_B\, k_{20}\, a_2) \qquad (C.8)$$

where k_{10} and k_{20} are the reaction rate constants at the steady state potential for each coupled reaction.

The term $(\partial I_C/\partial E)_\theta$ is obtained by differentiating Eq. (C.5) with respect to E:

$$(\partial I_C/\partial E)_\theta = F\,(n_A\, a_1\, (1-\theta)\, \partial k_{10}/\partial E - n_B\, a_2\, \theta\, \partial k_{20}/\partial E) \qquad (C.9)$$

Recalling that $k = k_0 \exp(-2.3\,(E-E_0)/\beta)$, then its derivative with respect to E for each reaction is:

$$(\partial k/\partial E)_\theta = -k_0 \exp(-2.3\,(E-E_0)/\beta)\,(2.3/\beta) = -2.3\,k/\beta \qquad (C.10)$$

Replacing Eq. (C.10) into Eq. (C.9), one obtains:

$$(\partial I_C/\partial E)_\theta = -F\,(2.3\, n_A\, a_1\, (1-\theta)\, \beta_1^{-1} + 2.3\, n_B\, a_2\, \theta\, \beta_2^{-1}) \qquad (C.11)$$

Around the steady state condition $\theta_0 = a_1\, k_{10} / (a_1\, k_{10} + a_2\, k_{20})$ so that Eq. (C.11) can then be written as:

$$(\partial I_C/\partial E)_{\theta 0} = -2.3\, a_1\, a_2\, F\, k_{10}\, k_{20}\, (n_A\, \beta_1^{-1} + n_B\, \beta_2^{-1})/(a_1\, k_{10} + a_2\, k_{20}) \qquad (C.12)$$

For EIS measurements, the small amplitude *ac* potential varies harmonically with the excitation frequency ω, and as a result the area coverage fraction θ deviates from θ_0 following a time-dependent sinusoidal excitation. Thus,

$$\theta - \theta_0 = A_0 \exp(j\omega t) \qquad (C.13)$$

where A_0 is a complex number that accounts for the phase difference between $(\theta-\theta_0)$ and the excitation potential. Hence,

$$d(\theta - \theta_0)/dt = d\theta/dt = j\omega\,(\theta - \theta_0) \qquad (C.14)$$

Recalling that $d\theta/dt = a_1/a_2\, k_1\, (1-\theta) - k_2\, \dot{\theta}$ and replacing into Eq. (C.14), one obtains:

$$j\omega\,(\theta - \theta_0) = (a_1/a_2)\, k_1\, (1-\theta) - k_2\, \theta \qquad (C.15)$$

Appendix C: (Continued)

Taking the derivative of both sides with respect to E:

$$j\omega\, d\theta/dE = -(d\theta/dE)\,(a_1/a_2\, k_1+k_2)-\theta\,(a_1/a_2\, dk_1/dE+dk_2/dE)+a_1/a_2\, dk_1/dE \qquad (C.16)$$

which at around θ_0 yields:

$$(d\theta/dE)_{\theta 0}=(2.3\, a_1\, a_2\, k_{10}\, k_{20}/(a_1\, k_{10}+a_2\, k_{20}))\,(\beta_1^{-1}-\beta_2^{-1})/(j\, a_2\, \omega+(a_1\, k_{10}+a_2\, k_{20})) \qquad (C.17)$$

Replacing Eqs. (C.8), (C.12), and (C.17) into Eq. (C.7), the overall admittance for excitation potentials around E_0 is:

$$Y=2.3\, I_C\,(n_A+n_B)^{-1}\,(n_A\,\beta_1^{-1}+n_B\,\beta_2^{-1}+(n_B\, I_2-n_A\, I_1)(\,\beta_1^{-1}-\beta_2^{-1})/(jFa_2\,\omega\,(n_A+n_B)+I_1+I_2) \qquad (C.18)$$

where $I_1 = F\, a_1\, k_{10}\,(n_A+n_B)$ and $I_2 = F\, a_2\, k_{20}\,(n_A+n_B)$.

In the simplest case of $\beta_1=\beta_2=\beta$ or $n_A\, a_1\, k_{10} = n_B\, a_2\, k_{20}$, the admittance reduces to the so-called frozen polarization resistance or charge transfer resistance ($R_{CT} = \beta\,(2.3\, I_C)^{-1}$) in the time domain. Under this condition, the area coverage fraction θ remains constant and no phase difference between $(\theta-\theta_0)$ and the excitation potential exists since at the high frequency limit the surface coverage does not have time to respond to the excitation signal.

For the usual case of $\beta_1\neq\beta_2$ and depending on the sign of $(\beta_1-\beta_2)$ and $(n_BI_2-n_AI_1)$, the system may have a capacitive or inductive behavior reaching at the low frequency limit a so-called relaxed polarization resistance or simply polarization resistance R_P of the form:

$$R_P=(2.3\, I_C\,(n_A+n_B)^{-1}\,(n_A\,\beta_1^{-1}+n_B\,\beta_2^{-1}+(n_B\, I_2-n_A\, I_1)(\,\beta_1^{-1}-\beta_2^{-1})/(I_1+I_2))^{-1} \qquad (C.19)$$

When the product $(\beta_1-\beta_2)(n_BI_2-n_AI_1)$ is positive, then $R_{CT}<R_P$ and the behavior is capacitive, resembling the usual behavior of a Randles circuit if the effects of interfacial capacitance are ignored. Otherwise, the system is inductive.

Appendix C: (Continued)

Inputting typical values of β_1, β_2, n_B, I_2, n_A, I_1, and a_2, values of R_{CT} and R_P were ~10^6 Ω-cm^2 comparable to those obtained experimentally for passive unblemished aluminized steel in NP and P solutions.

About the Author

Leonardo Caseres earned his B.S. degree in Chemical Engineering in 1998 from the Universidad Nacional del Centro de la Provincia de Buenos Aires (Olavarria campus), Buenos Aires, Argentina. From 1997 to 1998, he worked as a junior researcher at the Universidad Nacional del Centro de la Provincia de Buenos Aires working under the direction of Dr. Mirta Barbosa.

He came to United States in 1999 to pursue his M.S. in Civil and Environmental Engineering at the University of South Florida. He completed his M.S. degree in Civil and Environmental Engineering in 2002 and embarked on the Ph.D. program in 2003. From 1999 to 2007, he worked as a graduate assistant under the direction of Dr. Alberto Sagüés at the Corrosion Engineering Laboratory. His research interests are in the areas of corrosion of reinforcing steel in concrete, corrosion inhibitors, corrosion of metals, corrosion electrochemistry, and performance of metallic coatings. During the past few years, he has published one referred journal paper and another under revision at present, four international conference papers, and participated in the preparation of a report. He received the Third Place in the Mars Fontana Corrosion Engineering category in the student poster session at the annual meeting of NACE International in Denver, 2002. He is currently a student member of NACE International and the Electrochemical Society.